AN ABSTRACT OF THE DISSERTATION OF

Thomas K. Bauska for the degree of Doctor of Philosophy in Geology presented on October 8, 2013.

Title: Carbon Cycle Variability during the Last Millennium and Last Deglaciation

Abstract approved: _____

Edward J. Brook

The exchange of carbon on earth is one of the fundamental processes that sustains life and regulates climate. Since the onset of the Industrial Revolution, the burning of fossil fuels and anthropogenic land conversion have altered the carbon cycle, increasing carbon dioxide in the atmosphere to levels that are unprecedented in the last 800,000 years. This rapid rise in atmospheric carbon dioxide is driving current climate change and further increases are projected to dominate future climate change. However, the fate of the carbon cycle in response to climate change remains uncertain.

Insight into how the carbon cycle may change in the future can come from an understanding how it has changed in the past. Key constraints on past carbon cycle variability come from the concentration and stable isotopic composition of atmospheric carbon dioxide recorded in polar ice cores, but reconstructing these histories has been a significant analytical challenge. This thesis presents a new, more precise method for measuring the stable isotopic composition of carbon in carbon dioxide ($\delta^{13}C$ of CO_2) from polar ice. The new method is then used to reconstruct the atmospheric history of $\delta^{13}C$ of CO_2 during the last millennium (~770-1900 C.E.) and last deglaciation (~20,000-10,000 years before present).

Previously, methods for measuring the $\delta^{13}C$ of CO_2 had been limited to precision of

greater than ±0.05‰. The method presented here combines an ice grater air extraction method and micro-volume equipped dual-inlet mass spectrometer to make high-precision measurements on very small samples of fossil CO_2. The precision as determined by replicate analysis is ±0.018‰. The method also provides high-precision measurements of the CO_2 (±2 ppm) and N_2O (±4 ppb).

A new high-resolution (~20 year spacing) record of the $\delta^{13}C$ of CO_2 from 770-1900 C.E is presented that suggests land carbon controlled atmospheric CO_2 variability prior to the Industrial Revolution. A deconvolution of the CO_2 fluxes to the atmosphere provides a well-constrained estimate of the evolution of land carbon stocks. The relationship between climate and land carbon for this time period constrains future climate-carbon cycle sensitivity, but an additional process affecting land carbon is required to explain the data. This missing process may be related to early anthropogenic land cover change or patterns of drought.

A long-standing problem in the field of paleoclimatology is a complete mechanistic understanding of the 80 ppm increase in atmospheric CO_2 during the last deglaciation. A horizontal ice core on the Taylor Glacier in Antarctica allowed for the recovery of well-dated, large ice samples spanning the last deglaciation. From this unique archive, a new $\delta^{13}C$ of CO_2 of very high resolution (50-150 year spacing) is reconstructed. A box model of the carbon cycle is used to construct a framework of the evolution of the carbon cycle during deglaciation. During the Last Glacial Maximum, the lower CO_2 concentration accompanied by only a minor shift in $\delta^{13}C$ of CO_2 relative to the early Holocene is consistent with a more efficient biological pump in the Southern ocean, limited air-sea gas exchange around Antarctica, and colder ocean temperatures. The temporal evolution of these factors, as informed by timing of proxy data, reconciles the non-linear relationship between CO_2 and $\delta^{13}C$ of CO_2 from the Last Glacial Maximum to the pre-Industrial. However, the data also reveal very fast changes in $\delta^{13}C$ of CO_2 that suggest a rapid emission of depleted carbon to the atmosphere on the centennial timescale that is not captured in current models.

Carbon Cycle Variability during the Last Millennium and Last Deglaciation

by
Thomas K. Bauska

A DISSERTATION
submitted to
Oregon State University

in partial fulfillment of
the requirements for the
degree of
Doctor of Philosophy

Presented October 8, 2013
Commencement June 2014

Doctor of Philosophy dissertation of Thomas K. Bauska presented October 8, 2013

APPROVED:

Major Professor, representing Geology

Dean of the College of Earth, Ocean, and Atmospheric Sciences

---

Dean of the Graduate School

I understand that my dissertation will become part of the permanent collection of Oregon State University libraries. My signature below authorizes release of my dissertation to any reader upon request.

Thomas K. Bauska, Author

ACKNOWLEDGEMENTS

This thesis benefits from innumerable and immeasurable contributions from friends, family and colleagues. First and foremost, I thank my advisor Ed Brook for his support, encouragement and advice. I think I have benefited from his method of mentoring which (in my opinion) strikes a near-perfect balance between hands-off management and constant support - fostering both independent and critical thinking. I thank Alan Mix for showing me how to challenge my own assumptions and his creativity in the laboratory. I think the improvements in the method are due in large part to his input and expertise. I would estimate his contribution quantitatively but he probably wouldn't be satisfied unless I could also state the one-sigma uncertainty. Andreas Schmittner and Peter Clark have fostered my development in the classroom and their service on my committee is greatly appreciated. I also thank Harry Yeh for acting as the Graduate Council Representative.

I am especially indebted to fellow students Shaun Marcott, Jeremy Shakun, Logan Mitchell and Julia Rosen for their support and the countless hours spent discussing science.

Of all the colleagues that have contributed to this thesis, Daniel Baggenstos probably stands above the rest if person-hours were being tallied. He has devoted three seasons and counting in Antarctica to understanding the stratigraphy of the Taylor Glacier and his thesis work fundamental underpins the results in Chapter 5.

For years now, Andy Ross has been my primary sounding board when troubleshooting technical issues. I can't count the number of times I've made the trek from the basement of Wilkinson to the third floor of Burt to consult with him. Even when one of the mass specs is in pieces on the floor he'll stop what he's doing to take time for even the most mundane issues.

Finally, I must thank the most important people in my life: my sister, Emily; and my parents, Scott and Kathleen. You have supported me since the day I was born (Emily only from ages ~2.5 years to present). Words on a page can't express what you mean to me, but I think you know.

CONTRIBUTIONS OF AUTHORS

Chapter 3: E. J. Brook and A.C. Mix helped design the methodology. A. Ross provided expertise in the mass spectrometry techniques and was instrumental in making many of measurements during the early experimental design phase.

Chapter 4: E. J. Brook helped design the study. F. Joos hosted T.K. Bauska and oversaw the modeling work with help from R. Roth. A.C. Mix provided the technical expertise related to the stable isotopic measurement. J. Ahn provided CO_2 data. All authors contributed to the manuscript preparation.

Chapter 5: E.J. Brook and J.P. Severinghaus designed the larger goals of the Taylor Glacier Project. D. Baggenstos provided data and helped interpret the stratigraphy of the site. A.C. Mix provided the technical expertise related to the stable isotopic measurement. V.V. Petrenko and H. Schaefer through their expertise in blue ice zones aided in the design of the study and provided assistance in the field. J. Lee made most of the methane measurements and also helped in the field.

TABLE OF CONTENTS

TABLE OF CONTENTS (Continued)

TABLE OF CONTENTS (Continued)

Page

LIST OF FIGURES

LIST OF FIGURES (Continued)

LIST OF TABLES

Nothing is too wonderful to be true, if it be consistent with the laws of nature.

Michael Faraday

We had discovered an accursed country. We had found the Home of the Blizzard.

Douglas Mawson

1 Introduction

1.1 Forward

This dissertation covers three studies related to the measurement and interpretation of past changes in the atmospheric concentration and stable isotopic composition of CO_2 as recorded in polar ice cores. As a preface to the studies that follow, background information on stable isotopes, their measurement and their application to understanding the carbon cycle is presented in Chapter II.

Because direct observations of carbon dioxide are limited to the past few decades, the ancient air archived in ice core records is needed to extend our knowledge of the early Industrial Period and expand our understanding of the pre-Anthropogenic natural variability. However, measurements of ice core air are technically challenging and analytical advancements remain important to providing better data constraints. Chapter III provides a detailed, technical description of a new method for high-precision measurements of the stable isotopes of CO_2 from air occluded in polar ice.

The ocean and terrestrial biosphere are the major sinks for anthropogenic CO_2 and therefore essential for the natural mitigation of future climate change. Yet the way in which these systems will respond to climate change is not well known. The paleorecord offers an opportunity to observe the carbon cycle response to past climate change, but the mechanisms that drive natural carbon cycle variability remain unconstrained. In particular, the interplay between multi-decadal climate and CO_2 variability during the last millennium has spurred debate about the sensitivity of the carbon cycle to climate change (Frank et al., 2010) and the role early anthropogenic land-use change (Ruddimann, 2003). Chapter IV presents a new high-resolution record of the stable isotopic composition of CO_2 from about 770-1900 C.E. that attempts to constrain the dominant mechanisms behind multi-decadal CO_2 variability in the pre-Industrial.

Understanding how carbon dioxide acts as both a forcing and feedback on climate change is essential for constraining future climate change. Fundamental questions persist about the mechanisms behind the large variations in atmospheric CO_2 that occurred coeval with changes in temperature and ice volume that characterize the glacial-interglacial cycles of the late-Pleistocene (Sigman and Boyle, 2000). While it is highly certain the rising levels of CO_2 were important as a climate forcing during the last deglaciation (Shakun et al., 2012), an incomplete understanding what drove CO_2 changes precludes a mechanistic understanding of glacial-interglacial climate cycles. Chapter V presents record a new record of the stable isotopes of CO_2 spanning the last deglaciation (~22,000 to 10,000 years B.P.). The data are discussed in light of some of the current theories for glacial-interglacial CO_2 and a framework of the evolution of the carbon cycle during deglaciation is constructed with a box model.

Appendix A and B provide supplementary material for Chapters IV and V, respectively.

1.2 References

Frank, D. C., et al. (2010), Ensemble reconstruction constraints on the global carbon cycle sensitivity to climate, *Nature*, *463*(7280), 527-U143.

Ruddiman, W. F. (2003), The anthropogenic greenhouse era began thousands of years ago, *Clim. Change*, *61*(3), 261-293.

Sigman, D. M., and E. A. Boyle (2000), Glacial/interglacial variations in atmospheric carbon dioxide, *Nature*, *407*(6806), 859-869.

Shakun, J. D., et al. (2012), Global warming preceded by increasing carbon dioxide concentrations during the last deglaciation, *Nature*, *484*(7392), 49-54.

2 Background on the Carbon Cycle

2.1. Stable Isotope Systematics

Elemental carbon has three naturally occurring isotopes. Most of the carbon on earth, about 99%, is in the stable form of carbon-12 (^{12}C). The remaining 1% is comprised primarily of stable carbon-13 (^{13}C). The abundance of ^{12}C is a product of the unique stellar nuclear synthesis process whereby three alpha particles (^{4}He) combine to form ^{12}C via an intermediate and highly unstable ^{8}Be. Once ^{12}C is formed, it acts as a major building block for synthesis of higher mass elements via further alpha processes. Additionally, ^{12}C is integral as the catalysis in the conversion of hydrogen to helium in the carbon-oxygen-nitrogen (CNO) cycle. ^{13}C is produced as an intermediate step in the CNO cycle as a product of the betaplus decay of ^{13}N. An extremely rare radioisotope, carbon-14 (^{14}C), is found in some carbon reservoirs on earth at the parts per trillion level. Produced primarily in the atmosphere by interactions of nitrogen and cosmic rays, it decays relatively rapidly on geologic timescales with a half-life of about 5730 years. The abundance of (^{14}C) in any given reservoir is thus a product of the production rate in the atmosphere and the residence time of the reservoir with respect to the atmosphere. The $\delta^{13}C$-CO_2 is a measure of the relative abundances of the stable isotopes ^{13}C and ^{12}C in CO_2 gas. More specifically, convention dictates that isotopic values are reported as the relative per mil difference between a sample and a known standard such that:

$$\delta^{13}C = \left(\frac{R^{13}_{\text{sample}}}{R^{13}_{\text{standard}}} - 1 \right) * 1000 \qquad (1)$$

where R^{13} denotes the ratio of ^{13}C to ^{12}C in a compound.

$$R^{13} = \frac{^{13}C}{^{12}C} \qquad (2)$$

The canonical standard used in reporting $\delta^{13}C$ is the Pee Dee Belemnite (PDB) (Craig, 1953), but this standard is no longer in existence and for practical purposes values are typically referenced to the ”Vienna”-PDB. Values are often described as heavy/enriched and light/depleted, where positive values of $\delta^{13}C$ indicate heavy samples with more ^{13}C than the standard and light samples with less ^{13}C.

Most commonly, $\delta^{13}C$-CO_2 is determined by gas-source isotope ratio mass spectrometry (IRMS). Briefly, gaseous CO_2 is ionized by electron bombardment in vacuum, focused into a stream of ions, and accelerated through a magnetic field. The magnetic field separates the stream by their mass-to-charge ratio (m/z). The strength of each ion beam is then measured by a dedicated collector. The masses 44,45, and 46 are measured simultaneously and the ratio of enriched masses relative to mass 44 (R^n) can be determined with very high precision. The ratio of measured masses is related to the isotopic ratios by:

$$R^{45} = \frac{\left(^{13}C^{16}O^{16}O\right) + \left(^{12}C^{17}O^{16}O\right)}{\left(^{12}C^{16}O^{16}O\right)} = R^{13} + 2R^{17} \qquad (3)$$

$$R^{46} = \frac{\left(^{12}C^{18}O^{16}O\right) + \left(^{13}C^{17}O^{16}O\right) + \left(^{12}C^{17}O^{17}O\right)}{\left(^{12}C^{16}O^{16}O\right)} = 2R^{18} + 2R^{13}R^{17} + \left(R^{17}\right)^2 \qquad (4)$$

where R^{18} denotes:

$$R^{18} = \frac{^{18}O}{^{16}O} \qquad (5)$$

In these two equations there are two knowns, the measured R^{45} and R^{46}, and three unknowns, R^{13}, R^{17}, and R^{18}. Solving for the desired unknowns R^{13} and R^{18} requires an assumption about the abundance of O^{17} relative to O^{18}. R^{17} is related to R^{18} by terms derived from the abundance O^{17} in the reference material (K) and the fractionation observed in most natural systems (a).

$$R^{17} = \frac{^{17}O}{^{16}O} = K\left(R^{18}\right)^{a} \qquad (6)$$

Conversion of the ratio of ion beam strength to the ratio of $\delta^{13}C$ requires a precise measurements of the ion ratio relative to a known standard, correction for isobaric interference from other masses, and the quantification of the relationship between ion beam strength and inlet pressure.

2.2 An Isotopic Perspective on the Carbon Cycle

Carbon is distributed through the earth system in variety of reservoirs that are constantly exchanging with one another. Essentially all carbon reservoirs on earth will exchange with the atmosphere on timescales from minutes to millions of years. While the atmosphere contains a relatively small amount of carbon at about 600 gigatons of carbon (GtC), it is a major conduit for exchange between the other much larger reservoirs. As a gauge on the carbon cycle, the atmosphere is an excellent integrator of information. On the other hand, because the atmosphere is strongly sensitive to so many different carbon cycle processes, the information provided by the atmosphere alone does not provide a complete mechanistic understanding of the carbon cycle.

Most of the carbon on earth is stored in the lithosphere (10^8 GtC). The lithosphere exchanges carbon with the atmosphere by volcanic emissions, chemical weathering, and the formation of sediments. The exchange rate is very slow, on the order of a few tenths of a GtC per year, and only affects the atmosphere on timescales greater than about 10^4-10^5 years. The sources and sinks for CO_2 on timescales ranging from months to glacial-interglacial cycles are dominated by the terrestrial biosphere (2500 GtC) and the ocean (38,000 GtC). The residence time of carbon in the terrestrial biosphere is determined primarily by the rate of uptake by gross primary production and loss by soil respiration, which at steady-state is about 100 GtC yr^{-1}. The terrestrial biosphere is in turn composed of distinct carbon pools, each with their

respective turn-over time, ranging from a few years for ground vegetation, decades for soil carbon, and thousands for years for permafrost and peatland.

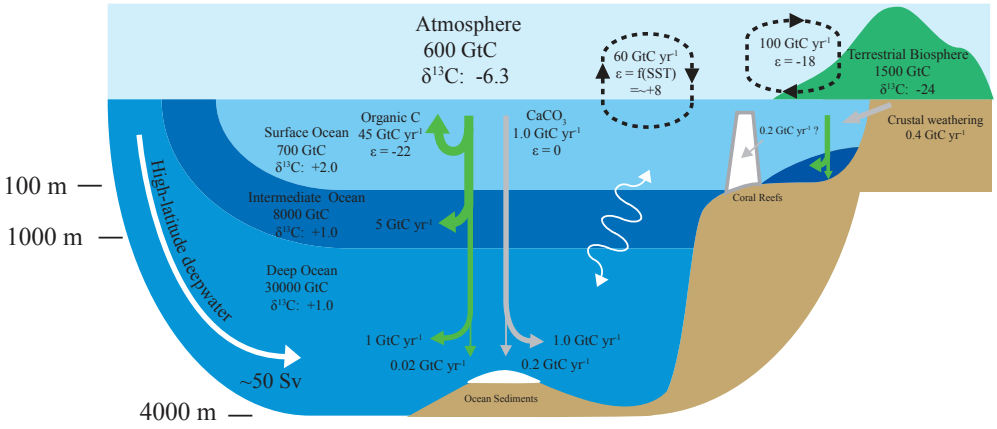

Figure 2.1 An Overview of the Carbon Cycle
The carbon cycle with some of the major reservoirs, fluxes and isotopic compositions. Figure is based on data primarily from *Sarmiento and Gruber, 2006* and the author's calculations.

Carbon in the surface ocean (700 GtC) exchanges in the atmosphere through air-sea gas exchange (60 GtC yr^{-1}) on timescales a few years, but mixing of water across the thermocline is typically more rapid, which leads to a surface ocean that can be out of equilibrium with the atmosphere. Carbon entrained in deep ocean by deep water formation, export of organic matter, and $CaCO_3$ dissolution, exchanges with the atmosphere on timescales of hundred to thousands of years, though abrupt changes in this exchange by reorganizations of ocean circulation or changes in nutrient utilization can have immediate impacts on the atmosphere.

Isotopic fractionation during some of these exchanges leads to different $\delta^{13}C$ compositions of some reservoirs. The two most common processes that alter the isotopic composition of different carbon reservoirs are kinetic fractionation during photosynthesis and equilibrium fractionation during chemical exchange between the atmosphere and surface ocean. Because photosynthesis and air-sea gas exchange dominate the atmospheric carbon budget, the $\delta^{13}C$-CO_2 is strongly sensitive to many different carbon cycle processes. In the broadest sense, $\delta^{13}C$-CO_2 can be interpreted

as an indicator of mean ocean temperature and the amount of respired carbon in the atmosphere.

2.3 Inorganic Carbon Chemistry

CO_2 is a special species as it is both soluble in and reactive with water. CO_2 is almost an order of magnitude more soluble in seawater than most of the major and trace gases (N_2O and CCl_4 are the notable exceptions) with solubility decreasing with increasing temperature. After dissolution, $CO_{2(aq)}$ disassociates in water to $[HCO_3^-]$, $[CO_3^{2-}]$and [H+]. The dissolution and disassociation can be described with he following equation:

$$CO_2 + H_2O \Leftrightarrow H_2CO_3 \Leftrightarrow HCO_3^- + H^+ \Leftrightarrow CO_3^{2-} + H^+ \qquad (7)$$

where H_2CO_3 signifies sum of aqueous CO_2 and carbonic acid. The equilibrium constants for each reaction are as follows with the brackets indicating the concentration of a given species:

$$K_0 = \frac{[H_2CO_3]}{pCO_2} \qquad (8)$$

$$K_1 = \frac{[HCO_3^-][H^+]}{[H_2CO_3]} \qquad (9)$$

$$K_2 = \frac{[CO_3^{2-}][H^+]}{[HCO_3^-]} \qquad (10)$$

Seawater is typically is comprised of about 0.5% H_2CO_3, 86.5% HCO_3^-, and 13% CO_3^{2-}, though the exact partitioning depends on temperature and salinity. Because only a minor fraction of the carbon in the ocean exists as CO_2, the rate at which

carbon can enter or leave the ocean is limited by exchange via this small pool. Additionally, the amount of carbon that ocean can uptake depends not simply on the solubility of CO_2, but rather the complex interaction of many different species.

To understand some the major processes that affect the ocean carbon cycle it is useful to define two parameters: dissolved inorganic carbon (DIC) and (carbonate) alkalinity (ALK):

$$DIC = [H_2CO_3] + [HCO_3^-] + [CO_3^{2-}] \qquad (11)$$

$$ALK = [HCO_3^-] + 2[CO_3^{2-}] + \left([OH^-]\right) - [H^+] + [B(OH)_4^- + \text{minor bases}\right) \qquad (12)$$

Figure 2.2 shows how pCO_2 increases non-linearly with increasing DIC and decreasing ALK. This non-linearity has major implications for the carbon cycle. It is best described by sensitivity of CO_2 to changes in DIC.

$$\gamma DIC = \frac{DIC}{pCO_2}\frac{\partial pCO_2}{\partial DIC} = \frac{\partial \ln pCO_2}{\partial \ln DIC} \approx 9 - 13 \qquad (13)$$

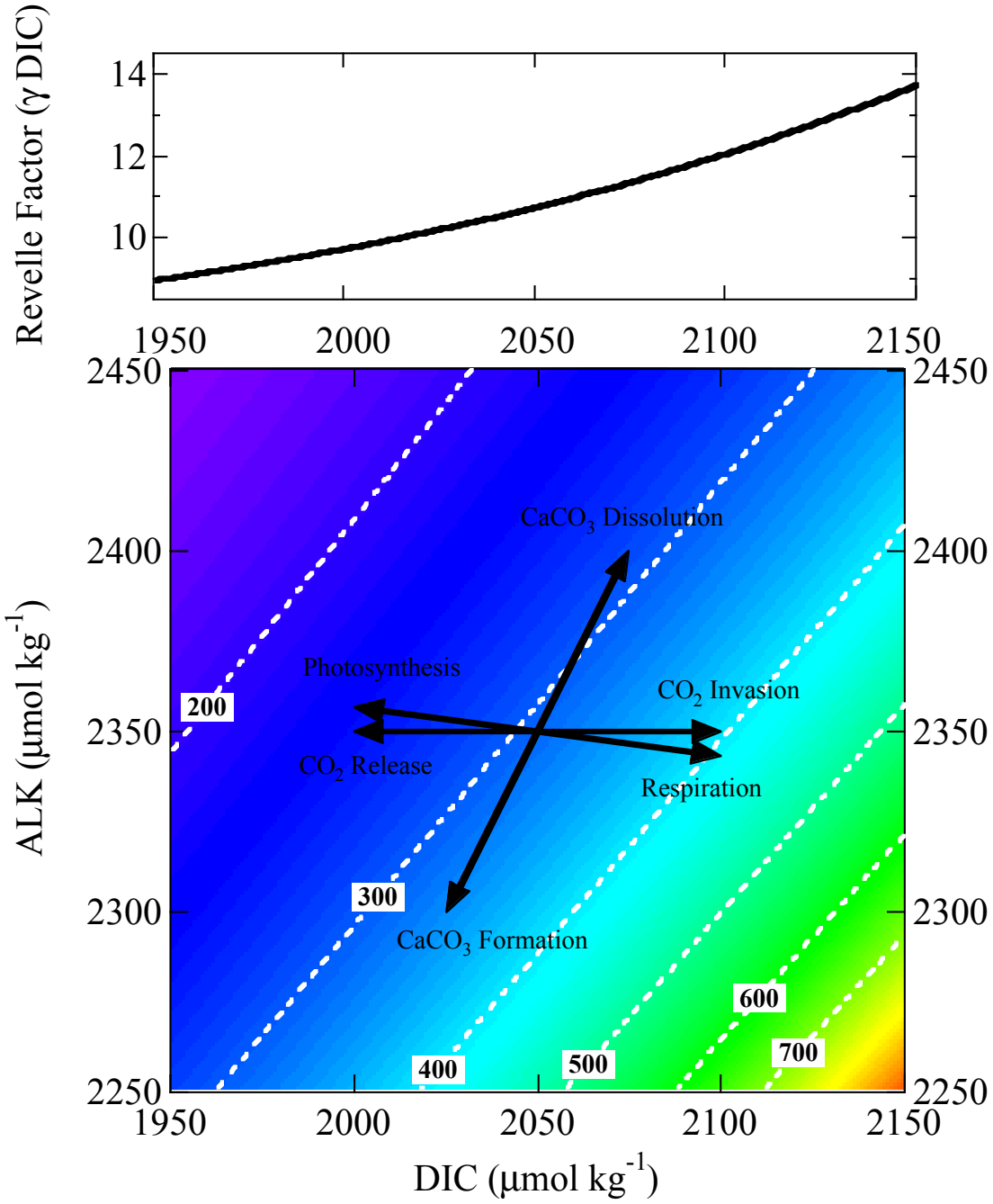

Figure 2.2 The carbonate system
The partial pressure of CO_2 (ppm) as a function of DIC and ALK at constant temperature (18°C) and salinity (34.17). Black arrows indicated the effect of different closed system processes on the carbon system. The top panel shows the Revelle factor at constant ALK (2350 µmol kg^{-1}) and variable DIC. The figure form follows the presentation in (Zeebe and Wolf-Gladrow, 2001). The CO_2 was calculated using modified Matlab code provided as supplement to the text.

This factor γDIC is commonly referred to as the "Revelle factor" after the pioneering chemical oceanographer Roger Revelle who first described its importance for the carbon cycle (Revelle and Suess, 1957). A Revelle factor of 10 implies that a 10% increase in pCO_2 will result in only a 1% increase in DIC. Or put another way, ocean DIC needs only change by 1% to affect the atmosphere by 10%. This implies that while the ocean is a huge reservoir for carbon, it is not an unlimited sink for increasing level of CO_2 in the atmosphere. Moreover, as greater amounts of carbon are taken up by the ocean, DIC increases but the Revelle factor also increases, leading to an ocean that progressively loses the ability to uptake more carbon.

2.4 Air-Sea Gas Exchange

The flux of carbon across the air-sea boundary per unit area is proportional to concentration and piston velocity. The piston velocity, which is typically inferred from observations, is likely proportional to the square root of the windspeed at the boundary layer (Wanninkhof, 1992) but other power dependences are possible (Wanninkhof and McGillis, 1999). When a difference in the partial pressures is established the net flux into the ocean Φ will be:

$$\Phi = k_g \left(pCO_{2atm} - pCO_{2ocn} \right) \qquad (14)$$

where k_g is in units of velocity and solubility concentration from Henry's Law.

The solubility of CO_2 decreases with temperature. With tropical surface waters reaching > 20 °C and the sources of deep water near the poles at close to the freezing point, the heterogeneity in surface ocean CO_2 is in part due the temperature structure of the ocean. If the ocean were abiotic, deepwater formation near the poles would draw down CO_2. When this water is up-welled and warmed in tropical regions, the CO_2 would be released back to the atmosphere. The amount of CO_2 the ocean can

hold from the "solubility pump" is weighted to the surface ocean temperature at the site of deepwater formation, though the exact magnitude of this effect also depends in the timescales for ocean mixing and the degree to which the surface ocean is in equilibrium with the atmosphere (Broecker et al., 1999). This effect suggests that CO_2 can covary with climate and changes in ocean circulation that impact the heat budget of the ocean on a variety of timescales.

The sensitivity of CO_2 to temperature change can be approximated by:

$$\frac{1}{pCO_2}\frac{\partial pCO_2}{\partial T} \approx 0.0423 T(^\circ C)^{-1} \qquad (15)$$

If seawater is saturated at 300 ppm, a 1°C increase in ocean temperature will increase CO_2 by about 13 ppm. For the same temperature change in colder waters (with the same DIC and ALK) where CO_2 is, for example, 150 ppm, the resultant increase will only be about 6.5 ppm.

Isotope fractionation during air-sea gas exchange is large and dependent on temperature. Measurements indicate that fractionations are as follows (Zhang et al., 1995) (with $\varepsilon_{a\text{-}b} = \delta_a - \delta_b$).

$$\varepsilon([HCO_3^-] - pCO_2) = -0.1141\, T(^\circ C) + 10.78 \qquad (16)$$

$$\varepsilon(CO_{2(aq)} - pCO_2) = +0.0049\, T(^\circ C) - 1.31 \qquad (17)$$

At equilibrium these two fraction factors lead to an atmosphere that is about 8‰ more depleted than the surface ocean. The relationship between temperature and fractionation is linear. For about a 1°C increase in ocean temperature, $\delta^{13}C\text{-}CO_2$ will become about 0.1‰ more enriched.

Unlike most gases, the equilibration time for both pCO_2 and $\delta^{13}C\text{-}CO_2$ is not simply a product of this exchange alone. For example, given typical piston velocities across the air-sea interface (k_w = 5 m d^{-1}) and mixed layer depth (z_{ml} = 50 m), a soluble gas like O_2 will equilibrate in about 10 days. The timescale for this equilibration for pCO_2 and $\delta^{13}C\text{-}CO_2$, however, is a function of air-sea gas exchange, chemical equilibria, and ocean mixing.

To reach a new steady-state, CO_2 needs to equilibrate with the entire DIC pool. In the case of isotopes, this equilibration is function of the air-sea exchange time (≈10 days) and the DIC/pCO_2 ratio (≈ 200) (Lynch-Stieglitz et al., 1995).

$$\tau_{\delta^{13}CO_2} = \frac{z_{ml}}{k_w}\frac{DIC}{pCO_2} \approx (10 \text{ days})\ (200)\ \approx 6 \text{ years} \qquad (18)$$

Unlike the isotopes, pCO_2 does not need to exchange with the entire DIC pool before it reaches chemical equilibrium. Here again, the buffering capacity of the ocean plays a role.

$$\tau_{CO_2} = \frac{z_{ml}}{k_w}\frac{DIC}{pCO_2}\frac{1}{\gamma DIC} \approx (10 \text{ days})\ (200)\left(\frac{1}{10}\right) \approx 0.6 \text{ years} \qquad (19)$$

In regions of the surface ocean with strong, deep convection, the renewal of water masses is often more rapid than air-sea gas exchange, particularly for the full equilibration of isotopes. The surface ocean and atmosphere are often out of equilibrium. Windspeed over the deep water formation areas of the Southern Ocean and North Atlantic can have a significant leverage on the $\delta^{13}C\text{-}CO_2$. For example, stronger windspeed over the typically depleted Southern Ocean waters will likely slightly increase the CO_2 and drive the $\delta^{13}C\text{-}CO_2$ of the atmosphere towards depleted values.

Changes in salinity also affect the solubility of CO_2. While the heterogeneities in the surface ocean salinity are of minimal importance for the air-sea flux, the waxing and waning of land ice on glacial-interglacial variations can lead salinity variations on the order of 3%. The sensitivity of CO_2 to salinity can be approximated by (Sarmiento and Gruber, 2006).

$$\frac{S}{pCO_2}\frac{\delta pCO_2}{\delta S} \approx 1 \qquad (20)$$

A lowering of sea-level by about 130 meters (Clark et al., 2009) during the Last Glacial Maximum would lead to an increase in salinity of 3‰ and about an 8 ppm increase in atmospheric CO_2.

2.5 The Terrestrial Biosphere

Fractionation during photosynthesis on land is jointly controlled by diffusion via stomatal openings ($\varepsilon = -4$) and the non-reversible carboxylation reaction ($\varepsilon = -28$) (O'Leary, 1981). Fractionation in C3 plants is mostly limited by the carboxylation step and therefore exhibit a strong fractionation during photosynthesis, with typical delta values on the order of - 28‰. C4 plants are more limited by diffusion, exhibiting a weaker fractionation and delta values of about -14‰. Given the prevalence of C3 plants, the mean fractionation during photosynthesis is typically on the order of -18‰. A similar fractionation is observed in marine biota.

Gross primary production by vegetation on land and respiration, primarily in soils, each proceed at about 100 GtC yr^{-1}. Any imbalance in these fluxes will alter the CO_2 and $\delta^{13}C$-CO_2 content of the atmosphere. Increased storage of carbon on land will lower CO_2 and enrich $\delta^{13}C$-CO_2, while a loss of land carbon to the atmosphere will increase CO_2 and deplete $\delta^{13}C$-CO_2.

The isotopic signal from the loss or uptake of carbon from the atmosphere by the terrestrial biosphere does not exhibit closed system mixing because the atmosphere is constantly exchanging with the surface ocean. In the case of a terrestrial source, the depleted carbon added to the atmosphere will begin to exchange with the carbon in the surface ocean as well as "re-exchange" with the terrestrial biosphere, effectively diluting the isotopic signature of the source in the atmosphere throughout the carbon system. Additionally, the isotopic signature that has mixed into the other reservoirs will itself affect the isotopic signature returned to the atmosphere. The isotopic disequilibria will persist on the timescale of mixing for the entire reservoir. This combination of effects overwhelms the closed system equilibration time of the surface ocean described in section 4.2 and the isotopic composition of the atmosphere will generally equilibrate faster than the concentration (Siegenthaler and Oeschger, 1987).

2.6 The Ocean's Organic Carbon Pump

In the ocean, production of organic carbon in the mixed layer (45 GtC yr^{-1}) and subsequent remineralization at depth establishes a gradient of DIC and δ^{13}C-DIC in the water column. Export of about 6 GtC yr^{-1} carbon across the thermocline, primarily through sinking particles, leaves the surface ocean depleted in DIC and enriched in δ^{13}C-DIC. As the particles sink to the seafloor they are slowly remineralized. Most of the remineralization occurs in the high-nutrient, low-oxygen waters that underlie the productive tropical ocean. Consequently, δ^{13}C-DIC is generally highly correlated to apparent oxygen utilization (AOU), remineralized nutrient levels and, to a lesser extent, DIC. A more efficient biological pump would lower CO_2 levels by establishing a stronger DIC gradient in the ocean, leading to lighter δ^{13}C-DIC in the deep ocean and heavier δ^{13}C in the surface ocean and atmosphere.

Most of the surface ocean is nutrient limited, whereby the production of organic material proceeds until a particular nutrient (typically either NO_3, PO_4, $Si(OH)_4$, Fe)

is drawn down to near zero, at which point no additional carbon can be fixed. Delivery of remineralized material to the surface by upwelling from below is typically balanced by the export of particulate material to back down to deep ocean. In this ideal regime, the rate of upwelling would not affect the net export of CO_2.

One route for changing the efficiency of the biological pump is to rearrange the flux of limiting nutrients. Because not all nutrient are drawn down to zero at the surface, some of the nutrient content of the deep ocean will be set by the unique conditions at the surface sites of deepwater formation. The initial nutrient content of a newly subducted water mass is referred to as the performed nutrient content. A low-efficiency biological pump (high atmospheric CO_2) would be characterized by a deep ocean with a high preformed nutrient content. One way to think about this is to consider that for every nutrient that evades the biological pump and is instead subducted, there is a corresponding amount of CO_2 that also escapes export to the deep ocean and will remain in the surface ocean/atmosphere (solubility effects aside). Because the deep ocean is largely filled by regions in the North Atlantic (lower preformed nutrient) and the Southern Ocean (higher preformed nutrient), the relative contribution of these water masses to the entire deep ocean will control CO_2 levels. For example, if the formation of North Atlantic Deepwater were to cease, the ocean would mostly be sourced from the higher preformed nutrient waters of the Southern Ocean. The biological pump would become less efficient and CO_2 levels in the atmosphere would increase.

Alternate ways to changes nutrient limitation are via changes in the type of productivity that occurs at the surface. For example, the degree to which diatoms or coccolithophorids dominate productivity in Southern Ocean can be influence the export of Si(OH)4 into intermediate waters and subsequently impact the drawdown of CO_2 in the tropics (Brzezinski et al., 2002). Additionally, the flux of the Fe from atmospheric dust has been hypothesized to change the nutrient limitation in the Southern Ocean with significant implications for local CO_2 drawdown (Martin,

1990).

A small amount of organic carbon makes its way to seafloor and is incorporated into sediments, with the bulk of burial occurring at shallow continental margins. Net burial of organic carbon would lower CO_2 and enrich the atmosphere and the whole ocean δ^{13}C-DIC would enrich homogeneously.

2.7 $CaCO_3$ Cycling

The cycling of $CaCO_3$ controls CO_2 by altering the DIC and ALK gradients of the ocean and regulating the long-term ALK balance. The immediate impact of $CaCO_3$ production, in both coral reefs and the open ocean, has the somewhat counter intuitive effect of raising CO_2 levels in the atmosphere. This is clear when looking at the ALK, DIC, and CO_2 relationship (Figure 2.2). $CaCO_3$ formation lowers DIC by one unit, which would otherwise decrease CO_2, but also lowers ALK by two units, leading to an overall increase in CO_2.

The balance between deposition and dissolution in the deep ocean can also have a major impact on CO_2 on timescales related to the long-term weathering flux of alkalinity to the ocean (10^5 years). The primary source of ALK to the ocean is the riverine input of continental weathering products, while the burial of $CaCO_3$ is the main route by which the ocean loses ALK. The amount of $CaCO_3$ that is eventually entombed in sediments on the seafloor depends on dissolution in the water column and sediments. Calcite and aragonite solubility increases with depth, primarily because of the increase in pressure, with the concentration at saturation defined as $[CO_3^{2-}]_{sat}$. Because variation in the concentration of $[Ca^{2+}]$ in the ocean are minor, the saturation state of $CaCO_3$ (Φ) depends primarily on the concentration of $[CO_3^{2-}]$ such that:

$$\Phi = \frac{[CO_3^{2-}]}{[CO_3^{2-}]_{sat}} \qquad (21)$$

Variations in $[CO_3^{2-}]$ can be approximated as a function of ALK and DIC by rearranging the equations (11) and (12):

$$[CO_3^{2-}] \approx ALK - DIC \qquad (22)$$

In the upper ocean, the organic pump dominates the $[CO_3^{2-}]$ saturation by depleting the surface waters in DIC while enriching intermediate waters, with only a minor effect on ALK. Surface waters are typically high in $[CO_3^{2-}]$ and supersaturated, while intermediate waters are undersaturated. In the deep ocean, the dissolution of $CaCO_3$ begins to become equally important to the remineralization of organic material. Dissolution of $CaCO_3$, with the effect of raising DIC by one unit and ALK two units, increases $[CO_3^{2-}]$ with depth and competes with remineralization to drive $CaCO_3$ towards a more saturated state. Once $CaCO_3$ reaches the seafloor, dissolution can occur as a complex function of respiration, diagenesis and porosity. The interaction of all these components is complex and not necessarily intuitive. Two examples that facilitate a cursory understanding are the effect of fossil fuel invasion of the ocean and a decrease in $CaCO_3$ export.

As fossil CO_2 enters the ocean, DIC increases following the Revelle Factor but ALK would initially be constant, and therefore $[CO_3^{2-}]$ decreases in the whole ocean. As $[CO_3^{2-}]$ decreases, the depth at which $CaCO_3$ dissolves shoals and the burial of $CaCO_3$ subsequently slows (additionally some previously deposited $CaCO_3$ may dissolve). The outpacing of riverine input of ALK over burial and the increased dissolution of $CaCO_3$ replenishes the $[CO_3^{2-}]$, further buffering the fossil CO_2. As $[CO_3^{2-}]$ increases, the saturation horizon deepens, and the system eventually returns to steady-state. In another scenario, $CaCO_3$ export from the surface ocean decreases. The immediate

effect of decreased $CaCO_3$ export is to increase surface ALK and lower CO_2. At depth, the decreased $CaCO_3$ burial will increase whole ocean ALK and $[CO_3^{2-}]$, further lowering CO_2. Higher $[CO_3^{2-}]$ leads to a deeper saturation horizon and eventually a steady-state where burial $CaCO_3$ is once again in balance with the riverine input (i.e. with the flux of $CaCO_3$ per unit area lowered by decreased export, the area must increase to balance the constant riverine input).

Because carbon isotope fractionation between $[CO_3^{2-}]$ and $CaCO_3$ is thought to be minor, the impact of changes in the ALK and $CaCO_3$ on $\delta^{13}C$-CO_2 are relatively small.

2.8 Previous Work

Harmon Craig performed the first work on the stable isotopes of carbon during the 1950's at Harold Urey's lab at the University of Chicago (Craig, 1953). Craig made some of the very first quality measurements of $\delta^{13}C$ on a suite of different samples. Craig was able to demonstrate that the major carbon bearing components on the earth (e.g. $CaCO_3$, CO_2 gas, plant tissue, fossil fuel, etc,) are distinct in their isotopic composition. Furthermore, he showed that many of these different carbon components had measurable heterogeneities within each reservoir. Craig was thus able to demonstrate the potential power of $\delta^{13}C$ as a tool for discerning processes occurring both within and between the earths major biogeochemical systems. Following Craig's lead, $\delta^{13}C$ has been applied broadly across many different fields, from studies of the air intake by the stomata of plants to the timing of the origin of life on earth.

The precise measurement of $\delta^{13}C$-CO_2 has been a major challenge for the ice core community. Because the measurement requires large volumes of air and fractionation of the isotopes in the multi-step extraction process is difficult to control, very few records have been produced.

The first record $\delta^{13}C\text{-}CO_2$ was produced by a team of Swiss scientist in Bern lead by Bernhard Stauffer and Hans Oeschger. The Swiss used a milling device on Siple Station ice to produce a record from onset of Industrial Revolution to the present (Friedli et al., 1986). The authors were able to show that the anthropogenic release of CO_2 by fossil fuel burning had been occurring since the mid-19th century. The overall uncertainty in their measurements was estimated to be 0.15‰.

The Swiss then produced a record extending back to the glacial period using the Byrd ice core. The record stands as the longest to date, extending back to about 40 ka with a resolution ranging from 1-3 ka excluding notable gaps in the measurements from 20 to 14 ka and 9 to 1 ka (Leuenberger et al., 1992). Precision was calculated to be about 0.10‰. Their interpretation was based on existing theories of the biological pump and ocean alkalinity, though their results could not single out which was the primary mechanism.

In the last 1990s an Australian ice core group begin working on making high-precision gas measurements from Law Dome. Their team developed new methods for dry gas extraction from large samples, most notably their design of an ice grater which moves a large piece of ice across a number of knife edges to grate the ice into snow and release the trapped air. By measuring large air samples and employing high-precision dual-inlet mass spectrometry, they were able to produce a record for the last 1,000 years with an uncertainty of 0.05‰ (Francey et al., 1999). The record has a resolution of about 100 years from 1000 BP to 1700 BP. The resolution increases through the industrial revolution from about 10 years in 1850 to about 3 years by 1978. The remaining measurements up to 1996 were made on firn air and archival air from Cape Grim.

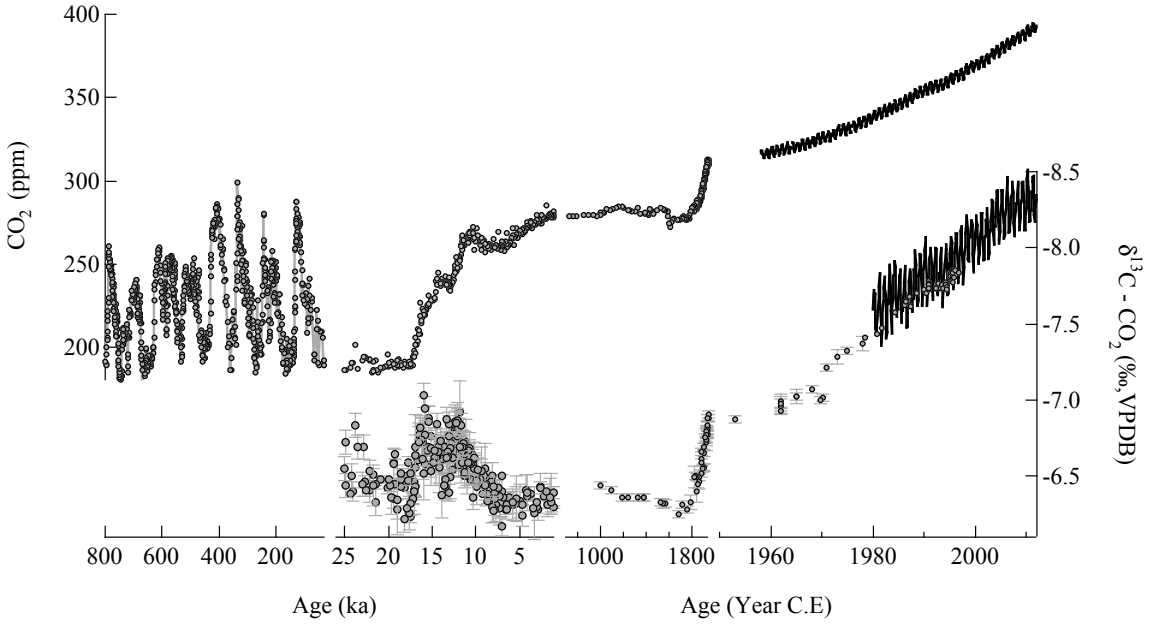

Figure 2.3 Timescales for CO_2 variability
A compilation of CO_2 and $\delta^{13}C$-CO_2 records from 800,000 years ago to present for a variety of timescales. The carbon cycle exhibits variability from glacial-interglacial to seasonal timescales. Note that the age axis is divided into 4 segments each with different resolutions and the $\delta^{13}C$-CO_2 is inverted. Data are compiled from many different ice core, firn air, and atmospheric studies (Elsig et al., 2009, Francey et al., 1999, Lourantou et al., 2010, Luthi et al., 2008, MacFarling Meure et al., 2006, Monnin et al., 2001, 2004, Petit et al., 1999, Schmitt et al., 2012, Siegenthaler et al., 2005, Smith et al., 1999, Welp et al., 2011)

Resolution of the last deglaciation and Holocene was improved by *Smith et al., 1999* and *Indermuehle et al., 1999*, but precision remained relatively low at about 0.08‰. More recently, gas-chromatographic IRMS methods have significantly decreased the required sample size, which allows for greater sampling resolution and less complicated mechanical crushers. Precision with these techniques remains low at 0.1‰ (Elsig et al., 2009, Lourantou et al., 2010, Schaefer et al., 2011). A novel method that employs sublimation to release the occluded air and GC-IRMS measurement techniques has made significant improvement to the precision obtained from small samples (Schmitt et al., 2011). By combining the available data with some new measurements, Schmitt et al. 2012 produced an aggregate record with largely low-precision but high sampling resolution measurements covering the LGM to the late Holocene, sourced primarily from the low-accumulation EPICA Dome C ice

core. The millennial-scale signal recovered in this study is a substantial step-forward. Yet the inherent smoothing of the gas records in low-accumulation ice cores and the signal processing needed to extract information from the low-precision measurements leaves a great deal of room for improvement.

2.9 References

Broecker, W., et al. (1999), How strong is the Harvardton-Bear Constraint?, *Global Biogeochemical Cycles*, *13*(4), 817-820.

Brzezinski, M. A., et al. (2002), A switch from $Si(OH)_4$ to NO_3, depletion in the glacial Southern Ocean, *Geophysical Research Letters*, *29*(12), 5-1-5-4.

Clark, P. U., et al. (2009), The Last Glacial Maximum, *Science*, *325*(5941), 710-714.

Craig H. (1953), The geochemistry of the stable carbon isotopes *Geochimica et Cosmochimica Acta*, *3*, 53-92.

Elsig, J., et al. (2009), Stable isotope constraints on Holocene carbon cycle changes from an Antarctic ice core, *Nature*, *461*(7263), 507-510.

Francey, R. J., et al. (1999), A 1000-year high precision record of $\delta^{13}C$ in atmospheric CO_2, *Tellus Series B-Chemical and Physical Meteorology*, *51*(2), 170-193.

Friedli, H., Fischer, H., Oeschger, H., Siegenthaler, U., , and B. Stauffer (1986), Ice core record of the $^{13}C/^{12}C$ ratio of atmospheric CO_2, in the past two centuries, *Nature*, *324*(20), 237-238.

Indermühle, A., et al. (1999), Holocene carbon-cycle dynamics based on CO_2 trapped in ice at Taylor Dome, Antarctica, *Nature*, *398*(6723), 121-126.

Leuenberger, M., et al. (1992), Carbon isotope composition of atmospheric CO_2 during the last ice-age from an Antarctic ice core, *Nature*, *357*(6378), 488-490.

Lourantou, A., et al. (2010), Constraint of the CO_2 rise by new atmospheric carbon isotopic measurements during the last deglaciation, *Global Biogeochemical Cycles*, *24*, 15.

Luthi, D., et al. (2008), High-resolution carbon dioxide concentration record 650,000-800,000 years before present, *Nature*, *453*(7193), 379-382.

Lynch-Stieglitz, J., et al. (1995), The influence of air-sea exchange on the isotopic composition of oceanic carbon: Observations and modeling, *Global Biogeochemical Cycles*, *9*(4), 653-665.

MacFarling-Meure, C., et al. (2006), Law Dome CO_2, CH_4 and N_2O ice core records extended to 2000 years BP, *Geophysical Research Letters*, *33*(14).

Martin, J. H. (1990), Glacial-interglacial CO_2 change: The Iron Hypothesis, *Paleoceanography*, *5*(1), 1-13.

Monnin, E., et al. (2001), Atmospheric CO_2 concentrations over the last glacial termination, *Science*, *291*(5501), 112-114.

Monnin, E., et al. (2004), Evidence for substantial accumulation rate variability in Antarctica during the Holocene, through synchronization of CO_2 in the Taylor Dome, Dome C and DML ice cores, *Earth and Planetary Science Letters*, *224*(1-2), 45-54.

O'Leary, M. H. (1981), Carbon isotope fractionation in plants, *Phytochemistry*, *20*(4), 553-567.

Petit, J. R., et al. (1999), Climate and atmospheric history of the past 420,000 years from the Vostok ice core, Antarctica, *Nature*, *399*(6735), 429-436.

Revelle, R., and H. E. Suess (1957), Carbon Dioxide Exchange Between Atmosphere and Ocean and the Question of an Increase of Atmospheric CO_2 during the Past Decades, *Tellus*, *9*(1), 18-27.

Sarmiento, J. L., and N. Gruber (2006), *Ocean biogeochemical dynamics*, Princeton University Press.

Schaefer, H., et al. (2008), On the suitability of partially clathrated ice for analysis of concentration and $\delta^{13}C$ of palaeo-atmospheric CO_2, *Earth and Planetary Science Letters*, *307*(3-4), 334-340.

Schmitt, J., et al. (2012), Carbon Isotope Constraints on the Deglacial CO_2 Rise from Ice Cores, *Science*.

Schmitt, J., et al. (2011), A sublimation technique for high-precision measurements of $\delta^{13}CO_2$ and mixing ratios of CO_2 and N_2O from air trapped in ice cores, *Atmos. Meas. Tech.*, *4*(7), 1445-1461.

Siegenthaler, U., and H. Oeschger (1987), Biospheric CO_2 emissions during the past 200 years reconstructed by deconvolution of ice core data, *Tellus B*, *39B*(1-2), 140-154.

Siegenthaler, U., et al. (2005), Stable carbon cycle-climate relationship during the late Pleistocene, *Science*, *310*(5752), 1313-1317.

Sigman, D. M., and E. A. Boyle (2000), Glacial/interglacial variations in atmospheric

carbon dioxide, *Nature*, *407*(6806), 859-869.

Smith, H. J., et al. (1999), Dual modes of the carbon cycle since the Last Glacial Maximum, *Nature*, *400*(6741), 248-250.

Trudinger, C. M., et al. (2002), Kalman filter analysis of ice core data - 2. Double deconvolution of CO_2 and delta C-13 measurements, *J. Geophys. Res.-Atmos.*, *107*(D20).

Wanninkhof, R. (1992), Relationship between wind speed and gas exchange over the ocean, *Journal of Geophysical Research: Oceans*, *97*(C5), 7373-7382.

Wanninkhof, R., and W. R. McGillis (1999), A cubic relationship between air-sea CO_2 exchange and wind speed, *Geophysical Research Letters*, *26*(13), 1889-1892.

Welp, L. R., et al. (2011), Interannual variability in the oxygen isotopes of atmospheric CO_2 driven by El Nino, *Nature*, *477*(7366), 579-582.

Zeebe, R., and D. Wolf-Gladrow (2001), *CO_2 in Seawater: Equilibrium, Kinetics, Isotopes* 346 pp., Amsterdam.

Zhang, J., et al. (1995), Carbon isotope fractionation during gas-water exchange and dissolution of CO_2, *Geochimica et Cosmochimica Acta*, *59*(1), 107-114.

3 High precision dual-inlet IRMS measurements of the stable isotopes of CO_2 and the N_2O/CO_2 ratio from polar ice core samples

Thomas Bauska, Ed Brook, Alan Mix, Andy Ross

College of Earth, Ocean and Atmospheric Sciences, Oregon State University, Corvallis, OR 97330, USA

3. 1 Abstract

Past variations in the concentration and stable isotopic composition of carbon dioxide illuminate the interaction between climate and biogeochemical cycles. More specifically, the covariation between carbon dioxide and climate on glacial-interglacial timescales is one of the most distinctive, yet enigmatic observations in the field of paleoclimatology. An important constraint on carbon cycle variability is provided by the stable isotopic composition of carbon in atmospheric carbon dioxide ($\delta^{13}C$-CO_2), but obtaining very precise measurements from air trapped in polar ice have proven to be a significant analytical challenge. Here we describe a new technique that can determine the $\delta^{13}C$ of CO_2 at exceptional precision, as well as the CO_2 and N_2O mixing ratios. Fossil air is extracted from relatively large ice samples (~400 grams) with a dry-extraction "ice-grater" device. The liberated air is cryogenically purified to a CO_2 and N_2O mixture and analyzed with a micro-volume equipped dual-inlet IRMS (Thermo MAT 253). We demonstrate very precise dual-inlet IRMS measurements, largely free of non-linear effects, on the limited amounts of CO_2 that a typical ice core can provide. Our experiments show that minimizing water vapor pressure in the extraction vessel by housing the grating apparatus in a ultra-low temperature freezer (-60°C) improves the precision and decreases the experimental blank of the method. We describe techniques for accurate calibration of

small samples and the novel application of a mass spectrometric method based on source fragmentation for reconstructing the N_2O history of ice core samples. The oxygen isotopic composition of CO_2 is also described, which confirms previous observations of oxygen exchange between gaseous CO_2 and solid H_2O within the ice archive. The data offer a possible constraint on oxygen isotopic fractionation during H_2O and CO_2 exchange below the H_2O bulk melting temperature.

3.2 Introduction

The air occluded in polar ice is an outstanding archive of the ancient atmosphere. Over the past few decades, highly specialized analytical methods have yielded excellent records of climate and biogeochemical processes. Ice cores now provide a record of the paleoatmosphere to nearly 800,000 years before present (Lüthi et al., 2008). Currently, the field is pushing to resolve very fine-scale features with continuous and high-throughput discrete measurements in the deep ice cores as well as identifying ablation zone archives that offer the opportunity of essentially unlimited sampling across select time horizons.

3.3 Previous $\delta^{13}C$-CO_2 methodology

Measuring the gases in ice core samples present a number of significant technical challenges, most notably how to extract the air from the ice without significantly altering the in situ composition, and how to make accurate and precise measurements on limited amounts of air.

Early attempts to analyze carbon isotope ratios of CO_2 in ice cores using milling devices on large samples with dual-inlet IRMS measurements (Friedli et al., 1986; Leuenberger et al., 1992) obtained precision on the order of 0.1‰. Subsequently, dual-inlet IRMS measurements improved the constraints on the last glacial termination and Holocene history (Smith et al., 1999; Indermuehle et al., 2003), but precision remained relatively low, around 0.08‰. More recently, gas-

chromatographic IRMS (GC-IRMS) methods have significantly decreased the required sample size, which allows for greater sampling resolution and less complicated mechanical crushers. However, precision with these techniques is still on the order of 0.1‰ (Leuenberger et al., 2003; Elsig et al., 2009; Lourantou et al., 2010; Schaefer et al., 2011). A novel method that employs sublimation to release the occluded air followed by GC-IRMS measurement techniques has made significant improvement to the precision obtained from small samples (0.05-0.09‰) (Schmitt et al., 2011; 2012). The highest precision measurements (0.025-0.05‰) to date were obtained from the Law Dome ice core spanning the last millennium using an large volume ice grater and dual-inlet technique (*Francey et al., 1999*). However, this record was recently revised, including a significant shift in the mean values of many of the measurement and a reevaluation of the uncertainty (including the accuracy and not necessarily the precision) of individual measurements to encompass a much broader range on the order 0.1‰ (*Rubino et al., 2013)*.

Because of the limited nature of ice sampling, many methods are designed to minimize sample consumption, possibly at the expense of precision for an individual measurement. Sometimes this lower precision can be balanced by ability to collect larger numbers of replicates or higher resolution sampling schemes. As such, GC-IRMS techniques, that require very small samples, have come to dominate ice core $\delta^{13}C\text{-}CO_2$ measurements. Our technique approaches the problem from a different perspective and aims to increase the precision of the measurement with larger samples such that fewer measurements are required to extract a low-noise signal from the ice core.

While dual-inlet IRMS typically offers better precision than GC-IRMS, it also presents distinct problems. N_2O in ice core samples, generally atmospheric in origin but occasionally produced *in situ* in large amounts, interferes isobarically with CO_2. With changes in the N_2O-to-CO_2 ratio up to 30% over a glacial- interglacial cycle, the magnitude of the $\delta^{13}C\text{-}CO_2$ correction can range from about 0.2-0.3‰, introducing a

systematic error. N_2O can be readily separated from CO_2 by a GC, but is practically impossible to separate from CO_2 cryogenically or in a chemically destructive manner without altering the isotopic composition of the CO_2.

Dual-inlet mass spectrometry measurements thus require an accurate estimate of the N_2O-to-CO_2 ratio in the ion beam. Previous methods derived the N_2O-to-CO_2 ratio by offline measurements, sometimes from an aliquot of the same sample air (*Francey et al., 1999*) or from an interpolation of separate data sets to the depths of the samples used for isotopic measurements (*Jesse-Smith et al., 1999*). We utilize a method that measures the $^{14}N^{16}O$ fragment produced in the mass spectromer source to determine the abundance and ionization efficiency of N_2O (*Assonov and Brenninkmeijer, 2006*). We demonstrate the method is very precise for estimating the interference correction and provides, as a novel byproduct, a robust record of the ice core N_2O history.

Contamination by drilling fluid containing hydrodcarbons is minimized by GC cleanup in GC-IRMS methods but could cause major problems for dual-inlet measurement if the catenated molecules, highly susceptible to fragmentation, reach the ion source. We observed drilling fluid contamination in a few samples based on strong signals on m/z 45,47,48 and 49 cups installed in our instrument for measurements of the "clumped isotope" ratios of CO_2 for other projects. The highly sensitive clumped isotope detectors proved effective for monitoring contamination and additional cleaning steps (described below) completely mitigated the problem in high-quality ice.

Our method has the virtue of simplicity. The extraction vessel utilizes no moving parts under vacuum, other than the ice block itself. The gas extraction and most of the purification proceeds in one step and does not involve any chemical traps. The sample is effectively measured immediately after extraction, limiting complications experienced during storage like sample loss or contamination. Dual-inlet IRMS

measurements with a micro-volume cold finger are a well established, with relatively minor non-linear effects, albeit not always utilized for such small samples amounts.

3.4 Ice Archives

Three ice archives were utilized in this study (Table 3.1). The Taylor Glacier archive is a "horizontal " ice core from an ablating section of ice on the Taylor Glacier, McMurdo Dry Valleys, Antarctica (77.75 S, 161.75 E). The section encompasses a complete stratigraphic section of the last deglaciation from about 20,000 to 10,000 years before present (1000 years = 1 ka). WDC05A is a relatively shallow depth (~300 m) core from the West Antarctic Ice Sheet (WAIS) Divide Ice Core Site (79.467 S, 112.085 W) and spans that last 1000 years (Mitchell et al., 2011). WDC06A is the main deep core from WAIS Divide, but the data presented here only cover an interval from about 250-350 meters (1250-750 years B.P.).

3.5 Ice Grater Apparatus Design

The ice grater extraction vessels are constructed from a stainless steel, electropolished cylinder of about 25 cm in length and capped on both ends with copper gasket sealed, 6-3/4 inch CF Flanges (Kurt Lesker Company). The flanges have been machined to remove excess weight from the exterior and bored to allow for a 3/8 inch outlet. The interior of the ice grater contains a perforated stainless steel sheet, molded to form a semi-cylinder, and attached to the walls of the ice grater with welds. The perforations resemble the abrasive surface one finds on a household cheese grater used to finely grate a spice or hard cheese.

Most of the components on the extraction line are stainless steel and are joined with either tungsten inert gas welds or copper gasket-sealed fittings (Swagelok VCR). The combination of both welds and gasket fittings lowers the chance of leaks but also

maintains modularity. All the valves are bellows-sealed with spherical metal stem-tips (majority are Swagelok BG series).

During air extraction, the ice grater chamber is housed in an ultra-low temperature freezer at -60°C (So-low, Inc.) with custom-built pass-through ports. The grater rests on an aluminum frame fixed to a linear slide apparatus which is driven by a pneumatic piston (SG Series; PHD, Inc). A pneumatic valving system allows the operator to control the stroke length of the motion and the frequency. The pneumatic piston sits outside the freezer and the ice grater cradle slides on steel rods with teflon coated bushings. The combination of keeping the greased pneumatic piston outside of the freezer and replacing the standard lubricated ball bearings with teflon bushings proved effective in keeping the moving parts of the ice grater shaker from seizing up in the cold.

3.6 Experimental Procedure

3.6.1 Air Extraction

About 14 hours prior to the first analysis, ice samples stored in a -25°C freezer are cut and shaped with a bandsaw. The dimensions of the cut sample are typically 5x6x15cm or slightly larger with masses ranging between 400 to 550 grams depending on the availability and quality of sampling. Additionally, about 1-3 mm of ice from the surface of the sample is removed with a ceramic knife as a precautionary cleaning step.

Ice samples from coring campaigns that did not use drill fluid (WDC05A and Taylor Glacier in this study) required very minor cleaning. However, samples exposed to drilling fluid composed of HCFC-141B and Isopar-K (WDC06A) required an extensive cleaning procedure which involved removing about 1 cm the exterior of the ice core to avoid micro-fractures filled with drill fluid.

After cleaning, two samples are each loaded and sealed in their respective ice grater. The graters are placed into the -60°C freezer, attached to the extraction line (Figure 3.1) via an opening in the freezer wall, and pumped to vacuum at about 0.02 Torr (in the presence of water vapor) in about 30 minutes. The ice graters are detached from the vacuum line, but remain sealed under vacuum in the freezer for a period of about 12 hours. This is important for letting the ice completely cool down and minimizes the amount of water vapor in the extraction vessel during grating. Also, a small amount of sublimation and subsequent condensation on the ice grater walls occurs during the relaxation periods which may induce further cleaning of the ice surface and passivation of the interior surface of the vessel with water vapor.

Prior to the sample analysis at least three aliquots of standard air are processed and measured like a sample, with the exception of exposure to the ice grater portion of the system (see description of air extraction below). After the initial standard runs are completed, the first ice grater is reattached to the vacuum line, checked to make sure no significant leaks developed during storage, and pumped for an additional 45 minutes. The ice grater is then detached and placed on the pneumatic slide.

To grate the ice, the pneumatic piston drives the ice grater horizontally with a translation of 20 cm at around 2 Hz for 30 minutes. This is sufficient to grate about 75% of the ice into <1cm fragments. Typically, an ellipsoid shaped piece of about 100 grams remains intact, which can be used at a later date for additionally analysis. Based on manometric measurements of the air extracted from a bubble ice sample, and typical total air content for ice (0.1 cc per gram), the overall air extraction efficiency is on the order of 60%. This is on the low end many dry extraction methods and an area for future improvement. Moreover, experiments with fully and partially clathrated ice showed marked decreases in the grating efficiency (that is, the ice was still grated finely, but the piece remaining intact after a long period of time was very large), and the measurements were deemed too impractical.

After grating, the ice grater is re-coupled to the extraction line (Figure 3.1). At this point, the ice grater contains about 5 Torr of sample air. A small aliquot of the sample, <1 cc STP, is isolated from the ice grater in the extraction line (volume between Valves 1 and 15). The air sample is cyropumped through a coiled, stainless steel trap held at 170 K (with liquid nitrogen cooled ethanol) to remove water vapor and condensed at 11K in a 7 cc sample tube held in a closed-cycle cryocooler (10K-CCR, Janis Research Company). This air sample is warmed to room temperature and stored for a few hours before being analyzed with a Agilent 7890A GC to determine the CO_2 mixing ratio. The CO_2 measurement is very similar to the method described in *Ahn, Brook and Howell, 2009*, whereby CO_2 is separated with a Porapak Q 80/100 mesh column, reduced to CH_4 with a nickel catalyst, and measured with a flame ionization detector (FID). However, whereas the *Ahn, Brook and Howell, 2009* method uses a manometer in the sample loop to determine the total air injected into the GC, we employ a thermal conductivity detector (TCD) to measure amount of O_2 and N_2 in the sample. This design minimizes the volume required for sample injection. Standard gases calibrated by NOAA on 2007 WMO Mole Fraction Scale are used to reference the sample mixing ratio (Table 3.2) (Zhao, Tans, and Thoning, 1997).

In order to extract the CO_2 and N_2O from the remaining air sample, the "w" shaped stainless steel trap is cooled with liquid nitrogen to 80 K (Figure 3.1, between valves 10 and 12). The rest of the sample air is passed over the coiled water trap (~170 K) and the “w” CO_2-N_2O trap (~80 K) by pulling the air from the ice grater through the extraction line with a turbo-molecular pump. The flow is regulated using a spherical stem-tip valve to remain less than 5 cm^3 per minute. After about 5 minutes of regulating the flow with about 80% of the air extracted, the valve is fully opened and sample extraction continues for an additional 15 minutes until about 99% of the air has been removed (air pressure remaining about 0.05 Torr). The "w" shaped trap, with the liquid nitrogen only submerging the lower portion of the trap, effectively has two closely spaced "u" traps. This proved useful in preventing the loss of CO_2 in the

fast moving stream of air, without greatly decreasing the conductance of the vacuum line. Though the cryocooler also showed promise as an effective air pump and would have allowed for the additional analysis of the CO_2 and N_2O free air, the turbo-molecular pumping system ultimately proved more efficient at extracting the last few percent of sample without any significant isotopic fractionation.

With the CO_2 and N_2O held in the "w" trap, valves 7 and 12 are closed (Figure 3.1) to isolate the sample from the portion of the extraction line exposed to water vapor. The "w" trap is warmed to 170 K by replacing the liquid nitrogen dewar with a chilled ethanol dewar. This releases the CO_2 and N_2O but secures any water that may have passed through the primary water trap. The amount of CO_2 and N_2O is then is determined manometrically (MKS Baratron). The sample amount is used to predict the subsequent sample inlet pressure on the dual-inlet and pre-adjust the reference bellows accordingly. To transfer the now dry CO_2 and N_2O to the dual-inlet system, a small stainless steel tube attached to the line with a VCR fitted valve is immersed in liquid nitrogen for about 1 minute, allowing the gases to condense in the tube. This tube is removed from the extraction line and placed on the sample side of the dual-inlet prior to analysis.

3.6.2 Dual-Inlet IRMS Measurement

The dual-inlet portion of the analysis is a computer controlled routine (Thermo Fisher Scientific, Inc.), modified slightly to accommodate the small samples and the measurement of the m/z 30 beam. The CO_2 and N_2O bypass the sample bellow and are condensed in 150 µl cold finger known as the “micro-volume” for a period of 120 seconds. Valves are closed so that the microvolume bleeds only to the changeover valve via a crimped capillary. The microvolume is warmed to 28°C to allow the CO_2 and N_2O to leak into the ion source.

With the reference side pre-adjusted to the expected sample size, the automated bellow adjustment period is typically minimal. Once the reference beam is within about 100 mV of the sample intensity, typically by the time the sample beam intensity is about 3000 mV, the reference side "pseudo" micro-volume (also 150 µl) is isolated from the bellows, and the dual-inlet measurement begins. The operating range for the dual-inlet pressure was between about 0.01-0.015 bar, equivalent to about a sample size of 1.5-2.25 bar µl. The measurement is comprised of eight dual-inlet cycles, each with an integration time of 8 seconds and idle time for changeover switching of 15 seconds. By the end of the measurement, the sample beam is typically on the order of 1000-2000 mV. A careful balance of the reference and sample capillary crimps and pre-adjustment of the reference bellows was required to keep the difference between the reference and sample beam both small and consistent (mean = 77 mV, 1-sigma standard deviation = 40 mV).

After the CO_2 analysis is complete, the instrument peak jumps to m/z 30 and measures the intensity on the sample and reference beams. The O^{17} abundance correction follows the formulation of *Santrock et al., 1985*. All traps are heated to about 50°C and pumped before the start of the next analysis.

3.7 Calibration

In order to calibrate the sample measurement, a working reference gas of pure CO2 (Oztech) was measured on a daily basis against at least six aliquots of a NOAA standard air (typically NOAA1). The "NOAA" standards were calibrated by the INSTAAR Stable Isotope Lab, University of Colorado to the VPDB-CO_2 scale with the primary reference as NBS-19 (see Table 3.2). The NOAA standard gas aliquots were processed with the sample extraction line both before and after the samples were analyzed. Typically, the mean of all six NOAA standard gas measurements was used as one-point calibration for the working reference gas. All the standard gas

measurements, relative to a fixed working reference gas value are shown in Figure 3.2.

Over the analysis period, the 1-sigma standard deviation of the NOAA1 standard was 0.027 and 0.13‰, for $\delta^{13}C$ and $\delta^{18}O$ respectively. However, the signal is not completely random, the $\delta^{13}C$ and $\delta^{18}O$ co-vary on the order of a few days ($R^2 = 0.13$; slope = 1.78; intercept = 7.42) (Figure 3.2). Often, the standard appears to become more depleted, or alternatively, the working reference gas become more enriched, by about 0.075‰ in $\delta^{13}C$ over the course of a few days, with the trend reversed when the working reference gas is replenished. This trend was confirmed during early experimentation and sample analysis by occasionally measuring the reference bellow against the same gas in the sample bellow that was only lightly consumed of the course of analysis. Assuming no leaks were present, this suggests that the gas in the reference bellows was becoming more enriched if not replenished.

Reference gas enrichment over time may be at least partially due to a mass dependent distillation process operating as the gas in reference bellow is consumed. Because the amount of gas in the bellows has to be very small to accommodate the lower sample size (e.g. 10 mbar at 100% expansion ≈ 0.25 mbar ml), the gas is quickly consumed over a few days of analysis, typically on the order of 10% per day. Given Rayleigh distillation, this would roughly correspond to a fractionation factor of about 1‰ for $\delta^{13}C$ and 2‰ for $\delta^{18}O$. While much smaller than the expected $\delta^{13}C$ fractionation if molecular flow dominated the flow-regime (~11‰) (Halstead and Nier, 1950), it does suggests the flow is not completely viscous at all times. Ultimately, the effect on precision of the sample measurements is negligible because the working reference gas is calibrated to the NOAA standard every day. From a practical standpoint, it requires that the working reference gas is replenished about every other day and gas consumption is minimized.

Additional experiments with a second NOAA standard of similar $\delta^{13}C$-CO_2 (-8.106‰) but very different $\delta^{18}O$-CO_2 (-0.777‰), CO_2 (~150 ppm) and N_2O (~321 ppb), as well as another working references gases with very different $\delta^{13}C$ (-3.58) were made to test the validity of a one-point calibration (see Table 3.2). The accuracy of the NOAA calibration scale was also checked by measuring the working reference gases against the carbonate standard NBS-19 with a Kiel Device, allowing for an independent in-house calibration of the NOAA standards (reported in Table 3.2). With the NOAA1 standard being measured over 400 times against the working reference, the INSTAAR-SIL and in-house calibration converge within 0.001‰ for $\delta^{13}C$-CO_2. The difference between the calibrations for the NOAA2 standard $\delta^{13}C$-CO_2 (0.034‰) is probably a product of the significantly less frequent measurement of the NOAA2 standard, which was used almost exclusively to calibrate the N_2O measurement.

3.8 N_2O Measurement

To correct the IRMS measurements for isobaric interference of N_2O, we employ a method that uses the fragmentation of N_2O in the source to estimate both the N_2O-to-CO_2 ratio and the ionization efficiency of N_2O (Assonov and Brenninkmeijer, 2006). Briefly, m/z 30, composed primarily of $^{14}N^{16}O^+$ derived from N_2O and $^{12}C^{18}O^+$ derived from CO_2, is measured relative to the m/z 44 intensity in both the sample (a unknown mixture of N_2O and CO_2) and the reference (pure CO_2). The difference between m/z 30 signal of the sample and the reference is a measure of the N_2O in sample that is has been ionized in the source. More completely, the fragmentation yield of $^{14}N^{16}O^+$ from N_2O (^{30}Intensity/^{44}Intensity of N_2O = ^{30}R-N_2O) and the ionization efficiency of N_2O (E-N_2O) must be determined in order to completely estimate the N_2O-to-CO_2 ratio. Idealized experiments with pure N_2O and/or N_2O diluted in an inert gas can be performed to quantify these parameters. For practical purposes, we calibrate the method using two NOAA calibrated standards with very different N_2O-to-CO_2 ratios (0.00091 and 0.00214) to estimate the two unknowns.

Our initial calibration found effective values of $^{30}R\text{-}N_2O = 0.19$ and $E\text{-}N_2O = 0.70$. The difference in $^{30}R\text{-}N_2O$ from the ~0.30 value reported in *Assonov and Brenninkmeijer, 2006* is mostly because our parameter is uncorrected for the decay of the signal during peak jumping.

We report N_2O in terms of ppb, rather than the more cumbersome N_2O-to-CO_2 ratio that is directly measured. To calculate the N_2O and associated errors of the NOAA standard measurements in terms of ppb we use a constant CO_2 concentration known from the NOAA calibration. For the samples, we use the CO_2 concentration measured on our GC system, introducing a source of error from the offline analysis.

Because only the NOAA1 standard was analyzed on a day-to-day basis, only one single N_2O-to-CO_2 ratio was used to monitor the drift in the calibration, and occasionally make small adjustments. Generally the drift over the course of weeks was negligible, on the order of the noise in the measurement (±1.7 ppb) (Figure 3.3). However, following a re-tuning of the source parameters after 6 months of heavy use measuring the clumped isotopes of CO_2, the calibration was reevaluated and observed to have changed significantly. Without the re-calibration using the two NOAA standard gases, the inferred N_2O would have been about 25 ppb lower than expected (see open squares in Figure 3.3). The two-point calibration check is thus essential after any change in the source conditions or after many weeks of analysis.

Ultimately, the N_2O measurements from the ice core samples proved very effective with a sample reproducibility of ±4.35 ppb (Table 3.1), which corresponds to uncertainty in the isobaric correction of ±0.0045‰ for $\delta^{13}C\text{-}CO_2$. Additionally, a comparison between the m/z 30 reconstruction and an independent N_2O record derived from an N_2O isotopic method on essentially the same samples from the Taylor Glacier archive show remarkable agreement (*Adrian Schilt, personal communication*). During periods with no in situ production, the mean difference between the two records is only 1±4ppb.

3.9 Linearity

With a dual-inlet system, careful balancing of the capillaries and precise pressure adjustment mitigates most non-linearity. During the periods of analysis, the linearity of the method is demonstrated by relationship between intensity and measured $\delta^{13}C$ and $\delta^{18}O$ values relative to the working reference standard (Figure 3.4). Because the gas for these standard measurements was passed through the gas extraction line, they offer a measure of the overall non-linearity of the system.

$\delta^{13}C$-CO_2 increases modestly at about 0.021±0.008‰ per volt and $\delta^{18}O$-O_2 shows very little trend relative to the noise 0.003±0.039‰. The standard error of a given measurement (internal precision) shows a slight trend towards decreased precision with small sample size ($\delta^{13}C$-CO_2 s.e. = -0.0016‰ per volt; $\delta^{18}O$-CO_2 s.e. = -0.0042‰ per volt).

Because most measurements fell with a relatively narrow range (~750 mVolts), no non-linearity correction was made to the data. In the rare instance that the sample size was significantly less than expected (<2000 mVolt) a series of standard measurements were completed in that range and a separate calibration for the sample was constructed.

3.10 Accuracy

Evaluating the accuracy of ice core gas measurements is a significant challenge, primarily because it is impractical to manufacture an artificial ice sample with a known gas composition. As an alternative, we performed experiments with the system in which a gas free piece of ice mimics an ice core sample and the introduction of a known standard gas emulates the release of occluded air. Initially, when using a standard freezer capable of housing the grater at -25°C, we found that standard gas became more depleted in $\delta^{13}C$-CO_2 than expected when grating the ice

or when the ice was warmed in the absence of any grating. This depletion, or "blank" appears to be proportional to the water vapor pressure after air extraction (and by inference the temperature of the ice block) (Figure 3.5).

After obtaining an ultra-low temperature freezer (operated at -60°C), we were able to minimize the water vapor to about 50 mTorr after a complete grating. Less water vapor lowered and decreased the scatter in blanks experiments to -0.066±0.036‰, though blanks up to -0.11‰ were observed on vigorously grated ice blocks.

We could not differentiate by experiment whether this effect was dominated by the amount of the water vapor in the grater itself or the flux of water vapor from the ice grater into the extraction line. Based on these experiments we chose to correct all measurement with a constant blank by +0.11‰. Note that the accuracy of the method is less than the precision, given the potentially unconstrained errors introduced by the experimental procedure.

3.11 Precision

Precision is estimated by performing replicate analyses on a selection of samples for the various archives. In the case of WDC05A, the sampling allows for true duplication, that is two samples from the same exact depth. Otherwise, as is the case with WDC06A and Taylor Glacier, duplicates are from adjacent depths. Given the degree of gas smoothing in the firn and the depth-age relationship at these sites, the adjacent depths should record nearly identical atmospheric values. However, variability in the chemistry of the ice is present on these length scales (e.g. annual layers in WDC cores). Replicate analysis from adjacent depths for species that can be subject to in situ production in the ice, most notably N_2O, could therefore bias our estimates to artificially large uncertainties.

The pooled standard deviation of all the $\delta^{13}C\text{-}CO_2$ duplicate analyses is 0.018‰ (Table 3.1). This is modest improvement of about 30% compared the CSIRO method (reported as mostly 0.025‰ error in Francey et al., 1999), at least a 60% improvement on the sublimation technique of Schmitt et al., 2011 (minimum ~0.05‰) and nearly an order of magnitude better than most of the GC-IRMS techniques. Parsed by ice archive, the estimated precisions are very similar, with perhaps larger uncertainty in the Taylor Glacier study, which encompasses CO_2 values across the complete glacial-interglacial range.

3.12 Oxygen Isotopic Fractionation

The oxygen isotopic composition of atmospheric CO_2 is primarily controlled by the exchange of oxygen between CO_2 and H_2O during photosynthesis in plant leaves and respiration in soils (Keeling, 1995). Atmospheric $\delta^{18}O\text{-}CO_2$ therefore offers a unique constraint on gross of primary production and the hydrological cycle on a global scale (Welp et al., 2011). However, the atmospheric signal of $\delta^{18}O\text{-}CO_2$ in ice core gas is probably compromised by exchange of oxygen with the surrounding ice (Siegenthaler et al., 1988). The process by which this exchange occurs is somewhat enigmatic as it most likely requires the interaction of CO_2 and liquid water at sub-freezing temperatures. Though liquid water in very small amounts is probably ubiquitous in polar ice, specifically at the triple junctions of grains *(*Nye, 1973; Mader, 1992), its influence on the preservation of gas records is not well known. A better understanding of the interaction of gas and ice is important for constraining any possible diffusion of atmospheric signals in the very old (>1 million years ago) and very warm basal ice that may be recovered as part of "Oldest Ice" project (Fischer et al., 2013).

Observations of ice core $\delta^{18}O\text{-}CO_2$ have previously been reported and discussed from low-resolution measurements from ice cores at Siple Dome, South Pole and Byrd (Siegenthaler et al., 1988; hereafter *Siegenthaler*) and high-precision measurements

from firn sampling campaigns at Dome C, Dronning Maud Land, and Berkner Island (Assonov, Brenninkmeijer and Joeckel, 2005; hereafter *ABJ*). *Siegenthaler* observed $\delta^{18}O\text{-}CO_2$ values about 20 to 30‰ more depleted than typical atmospheric values and correlated to the $\delta^{18}O$ of the surrounding ice matrix. *ABJ* observed $\delta^{18}O\text{-}CO_2$ becoming more depleted relative to the atmosphere as the age of the CO_2 increases with depth in the firn.

We also observe very highly correlated $\delta^{18}O\text{-}CO_2$ and $\delta^{18}O\text{-}H_2O$ (Figures 3.6 and 3.7). Most notably, the high (~3 cm) resolution $\delta^{18}O\text{-}H_2O$ data from the WDC05A core (Steig et al., 2013) allows to accurate determine the mean $\delta^{18}O$ surrounding each gas sample (Figure 3.6). $\delta^{18}O\text{-}H_2O$ measurements from Taylor Glacier are only available in nearby samples so the $\delta^{18}O\text{-}H_2O$ data was smoothed to and interpolated before comparison with the gas data. The apparent fractionation (ε) between CO_2 and H_2O is determined by taking the difference between $\delta^{18}O\text{-}CO_2$ and $\delta^{18}O\text{-}H_2O$ on a sample-by-sample basis. Note that $\varepsilon_{a\text{-}b} = 1000 \ln(\alpha_{a\text{-}b}) \approx \delta_a\text{-}\delta_b$.

The mean and 1-sigma standard deviation of the apparent $\varepsilon(CO_2\text{-}H_2O_{(s)})$ is 47.43±0.45 and 44.42±1.34‰, for WDC05A and Taylor Glacier, respectively (Table 3.3). With the ice temperature of WDC05A about 11K colder than Taylor Glacier, there appears to be an increase in fractionation for decreasing temperature. The higher noise in the Taylor Glacier $\delta^{18}O\text{-}CO_2$ data is probably related to the aliasing of high-frequency $\delta^{18}O\text{-}H_2O$ variability. The $\varepsilon(CO_2\text{-}H_2O_{(l)})$ show no discernible trend with time. Even the youngest sample at WAIS Divide (gas age = 1915 C.E.) is only about 1‰ heavier than the mean $\varepsilon(CO_2\text{-}H_2O_{(l)})$ for the entire core, appearing to be mostly equilibrated with the surrounding ice. This is probably consistent with the observation of the rate of exchange in the firn. *ABJ* calculate the equilibration proceeds with a half-life of about 23 years at the Berkner Island Site, which at -26°C is only slightly warmer than WAIS Divide, suggesting that youngest WAIS Divide sample should be about on the order of 90% equilibrated.

Siegenthaler proposed that apparent fractionation between the ice matrix and gaseous CO_2, could be described by temperature dependent fractionation at thermodynamic equilibrium between gaseous CO_2 and the solid, liquid and vapor phases of the H_2O as follows:

$$\alpha\left(CO_2 - H_2O_{(s)}\right) = \alpha\left(CO_2 - H_2O_{(l)}\right)\alpha\left(H_2O_{(l)} - H_2O_{(g)}\right)\alpha\left(H_2O_{(g)} - H_2O_{(s)}\right) \quad (1)$$

The left hand side of the equation is the accepted fractionation between gaseous CO_2 and solid water - what we would expect to see in the ice core. The fraction factors on the right hand side of the equation have been estimated by theoretical and experimental work, but for reasons of practicality and applicability, $\alpha(CO_2\text{-}H_2O_{(l)})$ and $\alpha(H_2O_{(l)}\text{-}H_2O_{(g)})$ have not been determined below the freezing point of water. The $\alpha(H_2O_{(g)}\text{-}H_2O_{(s)})$ has been determined over a wide range of sub-freezing temperatures because of its relevance in interpreting oxygen isotope records from polar ice. However, estimates of $\alpha(H_2O_{(g)}\text{-}H_2O_{(s)})$ at very cold temperature (~<240 K) are not well constrained. *Siegenthaler* used $\alpha(CO_2\text{-}H_2O_{(l)})$ from *Bottinja, 1968* and $\alpha(H_2O_{(l)}\text{-}H_2O_{(g)})$ and $\alpha(H_2O_{(g)}\text{-}H_2O_{(s)})$ from *Majoube, 1971*. Table 3.4 summarizes these and other fractionation factors discussed here, and provides shorthand for the formulations.

Using the fractionation factors from *Siegenthaler*, we find our data are about 1.19 and 1.58 more depleted than would be expected from complete equilibration in WAIS Divide and Taylor Glacier, respectively (Table 3.3). Given the uncertainties is determining the apparent fractionation from the noisy data and accurately measuring $\delta^{18}O\text{-}CO_2$, the new data are mostly in agreement with previous data and proposed model for $\delta^{18}O\text{-}CO_2$ equilibration (Figure 3.8).

The uncertainties in the ice core data, however, are probably slightly smaller than the uncertainties in the experimentally and theoretically derived temperature dependence of fractionation. Including additional estimates of fractionation factors suggests that

the predicted $\alpha(CO_2\text{-}H_2O_{(s)})$ appears relatively insensitive to changing $\alpha(CO_2\text{-}H_2O_{(l)})$ and $\alpha(H_2O_{(l)}\text{-}H_2O_{(g)})$ (black band, Figure 3.8) . However, the convergence of the expected fractionation from various studies does not necessarily equate to accuracy because these formulations are extrapolated below the freezing point. On the other hand, $\alpha(CO_2\text{-}H_2O_{(s)})$ appears very sensitive to different $\alpha(H_2O_{(g)}\text{-}H_2O_{(s)})$ predictions from experimental observations (*Majoube, 1971; Ellehoj et al., 2013*) and theoretical work (*Méheut et al., 2007*), showing a large divergence at very cold temperatures (dot and dash-dot lines, Figure 3.8) . Though $\alpha(H_2O_{(g)}\text{-}H_2O_{(s)})$ can probably be better constrained by controlled experiment in the laboratory, ice core $\delta^{18}O\text{-}CO_2$ may offer a unique, naturalistic experiment to observe this process over long time periods.

Finally, by combining our data with the results from *Siegenthaler*, we derive a relationship for $\alpha(CO_2\text{-}H_2O_{(s)})$ and temperature with the form:

$$\varepsilon = 1000\ln(\alpha) = \frac{K_2(10^6)}{T^2} - \frac{K_1(10^3)}{T} + K_0 \qquad (3)$$

With temperature in absolute degrees, $K_2 = 19.5\pm27.6$, $K_2 = -145\pm226$ and $K_0 = 312\pm461$. The relationship remains fairly under constrained (light grey band in Figure 3.8 shows 95% C.I. of the fit), so additional data from ice archives with different temperature are needed, especially at sites with very cold temperatures. Additionally, laboratory experiments and modeling of $CO_2\text{-}H_2O_{(s)}$ interactions may illuminate the processes at play on the micro-scale of liquid water layers in the ice.

3.13 Conclusions

The new method presented here advances the methodology for measuring the $\delta^{13}C\text{-}CO_2$ from polar ice. While not a radically new or complicated method, the external precision of 0.018‰ obtained with the system is a marked improvement on most other methods. More generally, this study describes the rigorous testing and careful

analytical procedures, including source tuning, linearity testing, and daily calibration that are required to obtain high-precision with a dual-inlet technique on very small samples (~1 bar μL). By demonstrating a method for accurately correcting for isobaric interference of N_2O on small sample, a significant barrier for dual-inlet measurement of ice core or other limited atmospheric sampling studies of CO_2 has been mitigated. Moreover, the method provides a means for determining the CO_2 and N_2O mixing ratios on the same fossil air sample, albeit from much larger ice samples than is typically warranted. Finally, the $\delta^{18}O$-CO_2 data presented here constrain the fractionation of oxygen isotopes during what appears to be an exchange of oxygen between CO_2 and solid ice. Future improvement could focus on increasing the grating efficiency, which should be make the method suitable for clathrated ice.

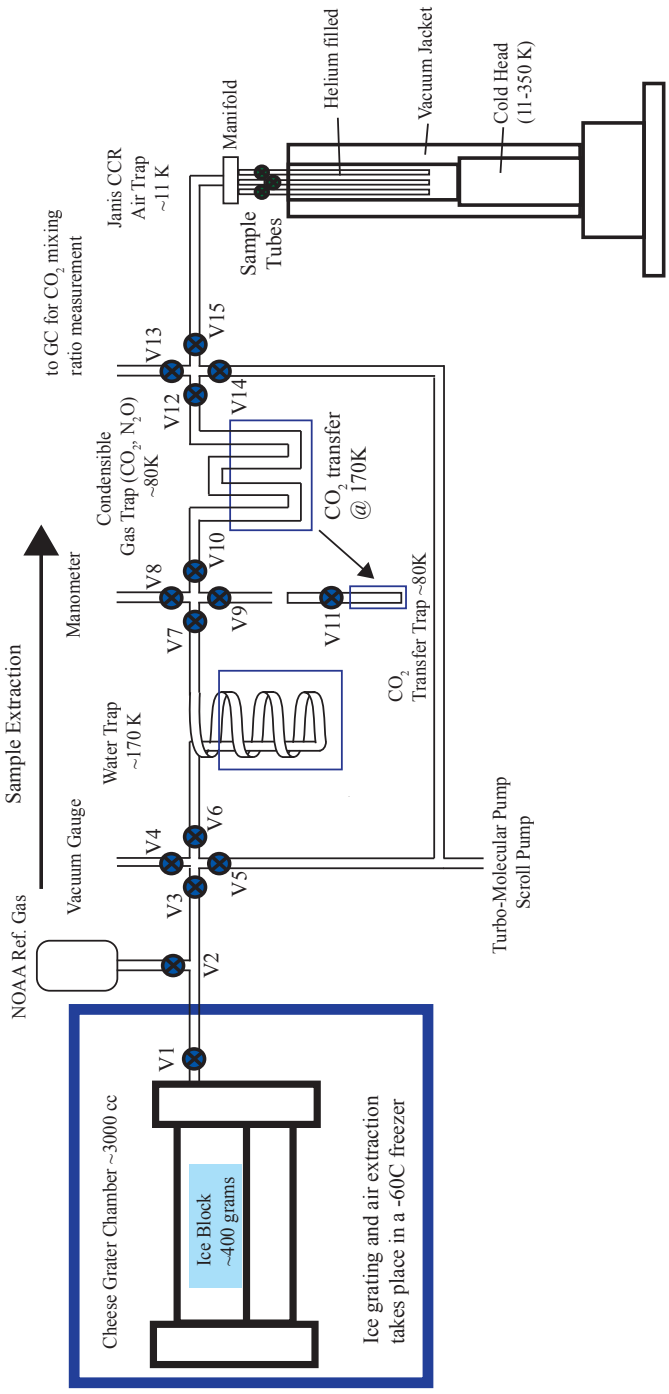

Figure 3.1 Extraction Line
A simplified schematic of the ice core air extraction vacuum line. The blue circles with crosses represent bellows sealed valves.

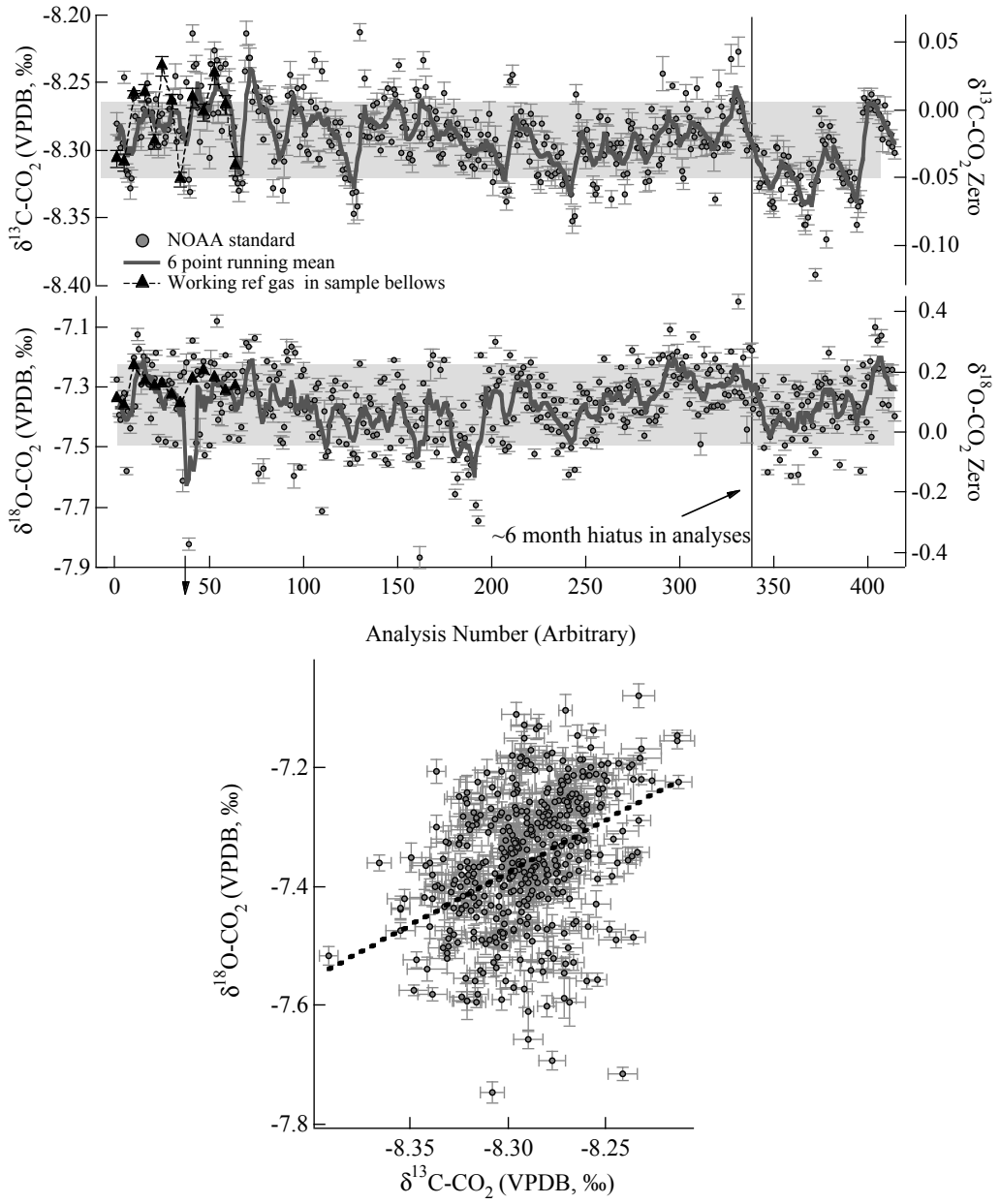

Figure 3.2 Standard Measurement Reproducibility
Upper Panel: All measurements of the NOAA1 standard gas over the course of a number of measurement campaigns encompassing about 5 months time in total. The $\delta^{13}C$ and $\delta^{18}O$-CO_2 are reported relative to the working reference gas. Note that there are a few analyses of the same working reference gas that was stored in the sample bellows (black triangles) while the gas in the reference bellows was being depleted (plotted on the "zero" axis). The gray bars represent the 1-sigma standard deviation of the NOAA1 standard over the entire period. Lower Panel: $\delta^{13}C$-CO_2 covariation with $\delta^{18}O$-CO_2.

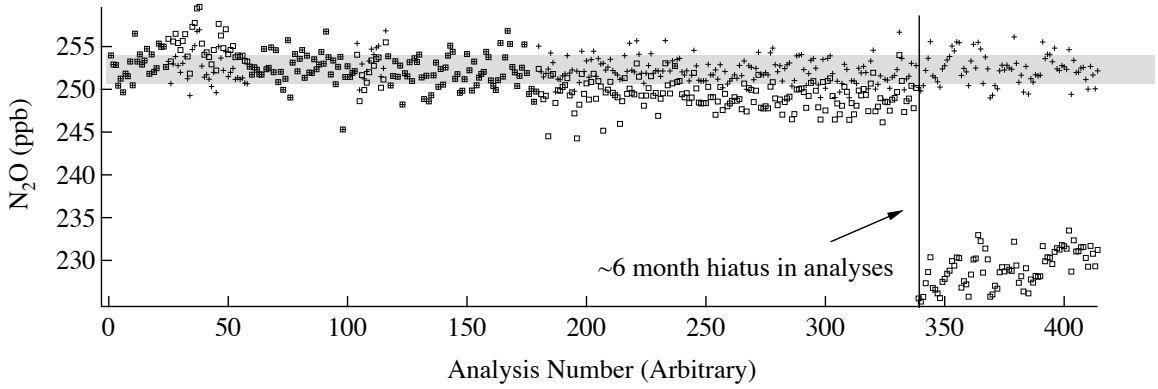

Figure 3.3 N_2O Standard Reproducibility
The reproducibility and drift in the N_2O calibration of the same period of analysis as in Figure 2. The black crosses are the N_2O of the NOAA1 standard as determined by the daily calibration. The open squares represent the same data if the calibration was fixed to a set value at the beginning of analysis (time 0). This shows both a small drift from about number 0 to 300 (~4 months) and a major shift in the values around 340, which represents a 6 month hiatus and retuning of the source.

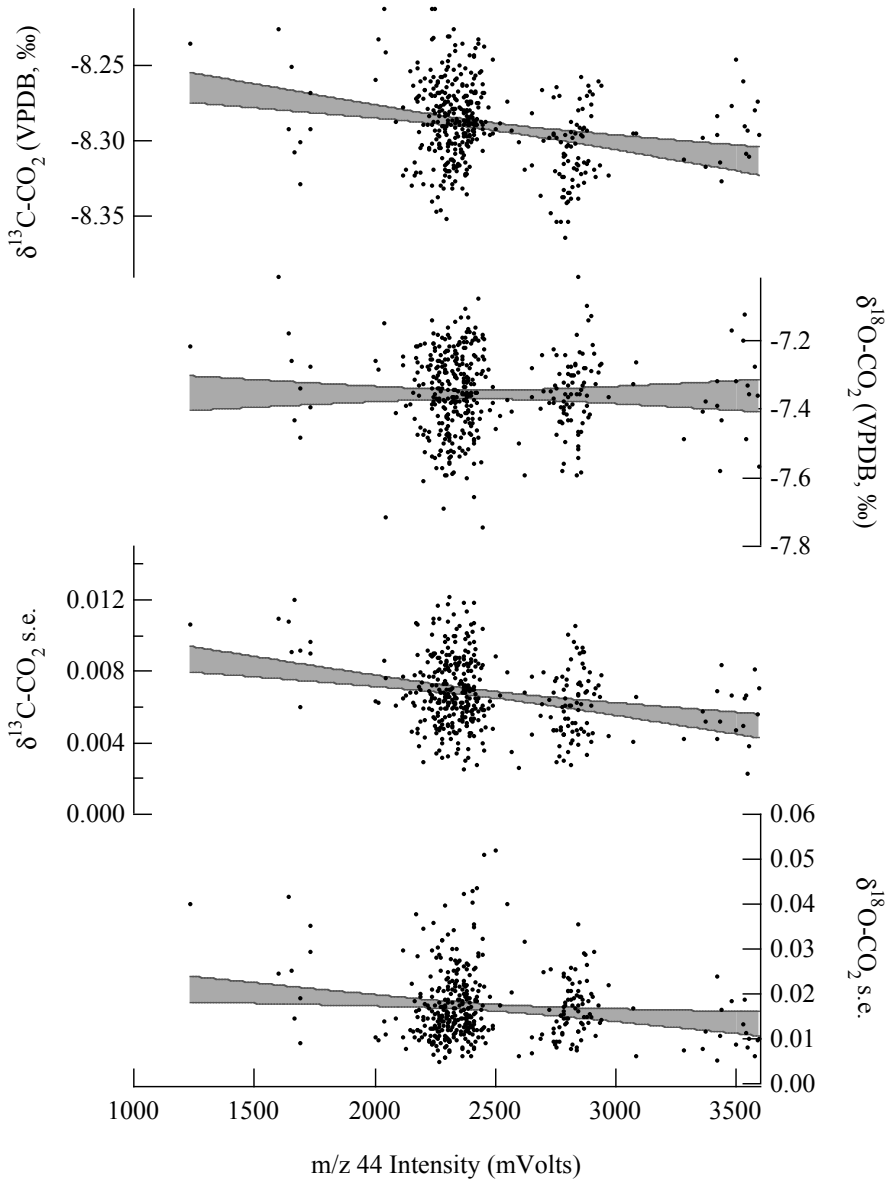

Figure 3.4 Linearity and Precision of Standard Measurements
The linearity and internal precision of the measurement versus m/z 44 intensity as recorded by measurements of the NOAA1 standard during the period of analysis. $\delta^{13}C$ and $\delta^{18}O$-CO_2 are reported relative to the working reference gas (upper two panels) and the internal precision is reported as 1-sigma standard error of the eight dual-inlet measurements (lower two panels). The grey shading represents the 95% confidence intervals for a linear fit to the data.

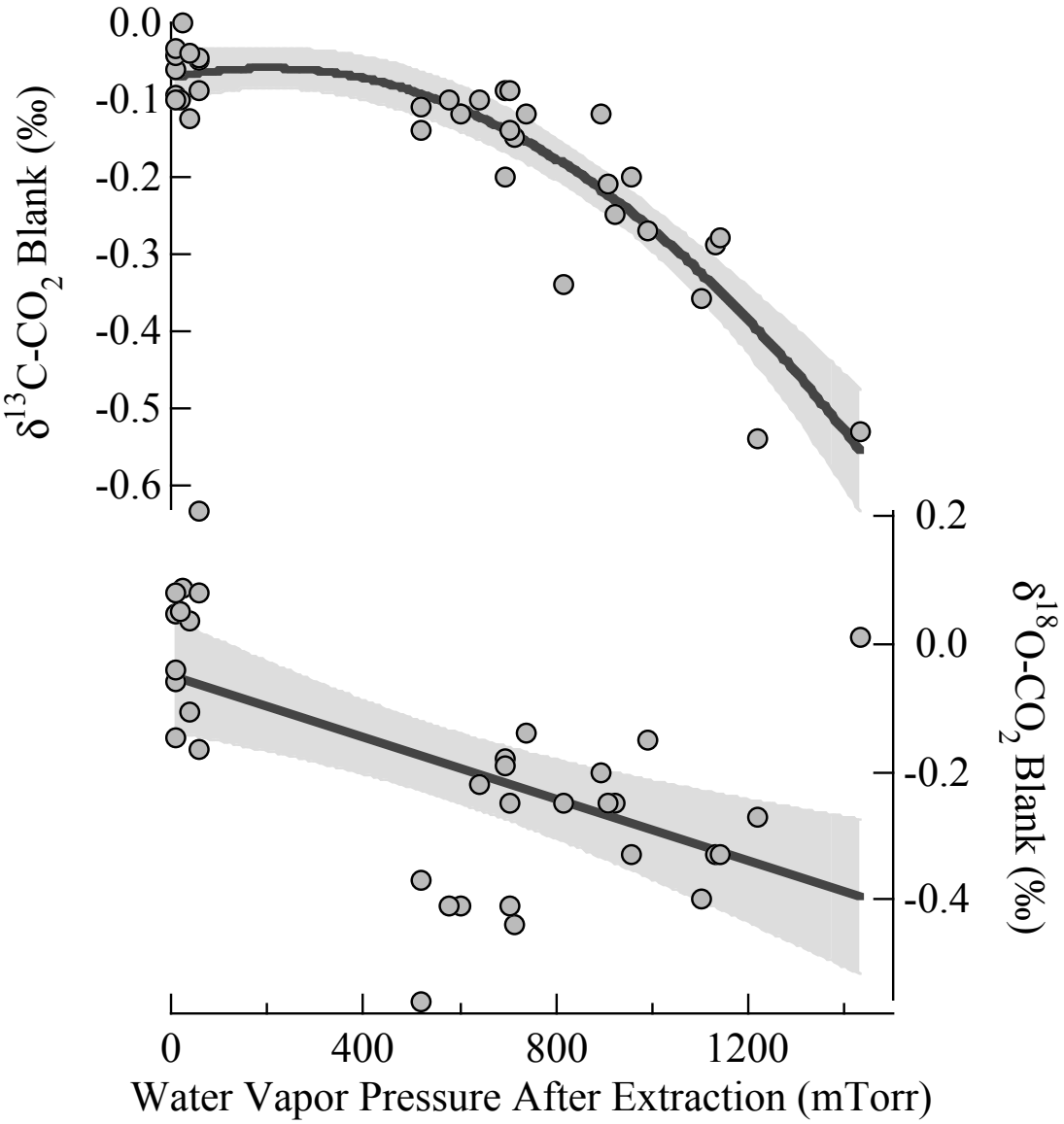

Figure 3.5 Procedural Blank Experiments
Measurements of the procedural blank of the system and its relationship to water vapor pressure. Blank is reported as the difference of the expected δ-value (from the NOAA calibration) to the measured value when ice grating and air extraction is simulated. Negative blanks indicate that the standard air become more negative during the simulation. The grey shading indicates 3rd order polynomial fit to the $\delta^{13}C\text{-}CO_2$ with 95% confidence intervals and linear fit to the $\delta^{18}O\text{-}CO_2$.

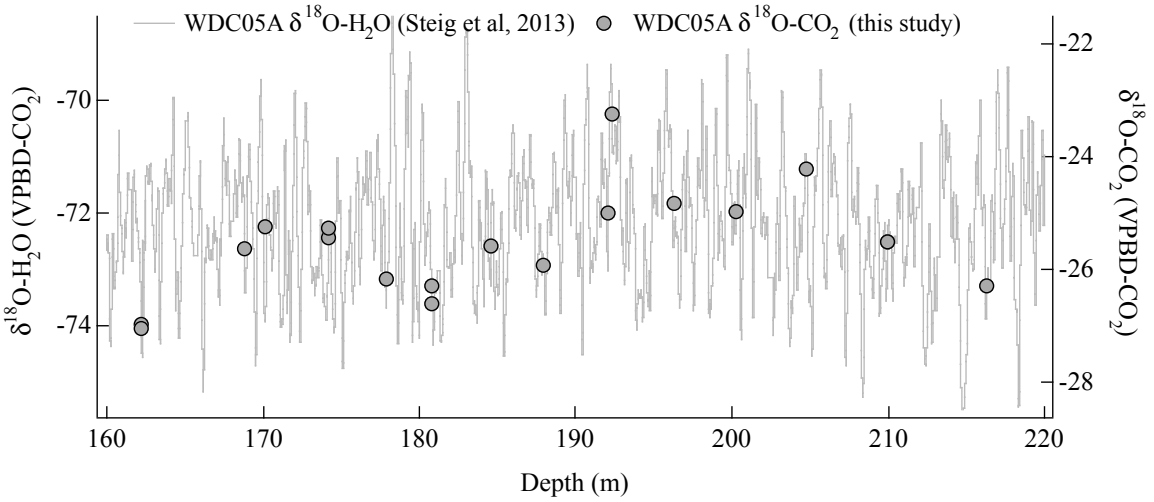

Figure 3.6 WAIS Divide $\delta^{18}O\text{-}CO_2$ and $\delta^{18}O\text{-}H_2O$
A short selection of the $\delta^{18}O\text{-}CO_2$ and $\delta^{18}O\text{-}H_2O$ data on the depth scale from the WDC05A core. The two vertical axes are of the same magnitude but offset to show the relatively good ability of $\delta^{18}O\text{-}CO_2$ to capture and integrate the fine scale $\delta^{18}O\text{-}H_2O$.

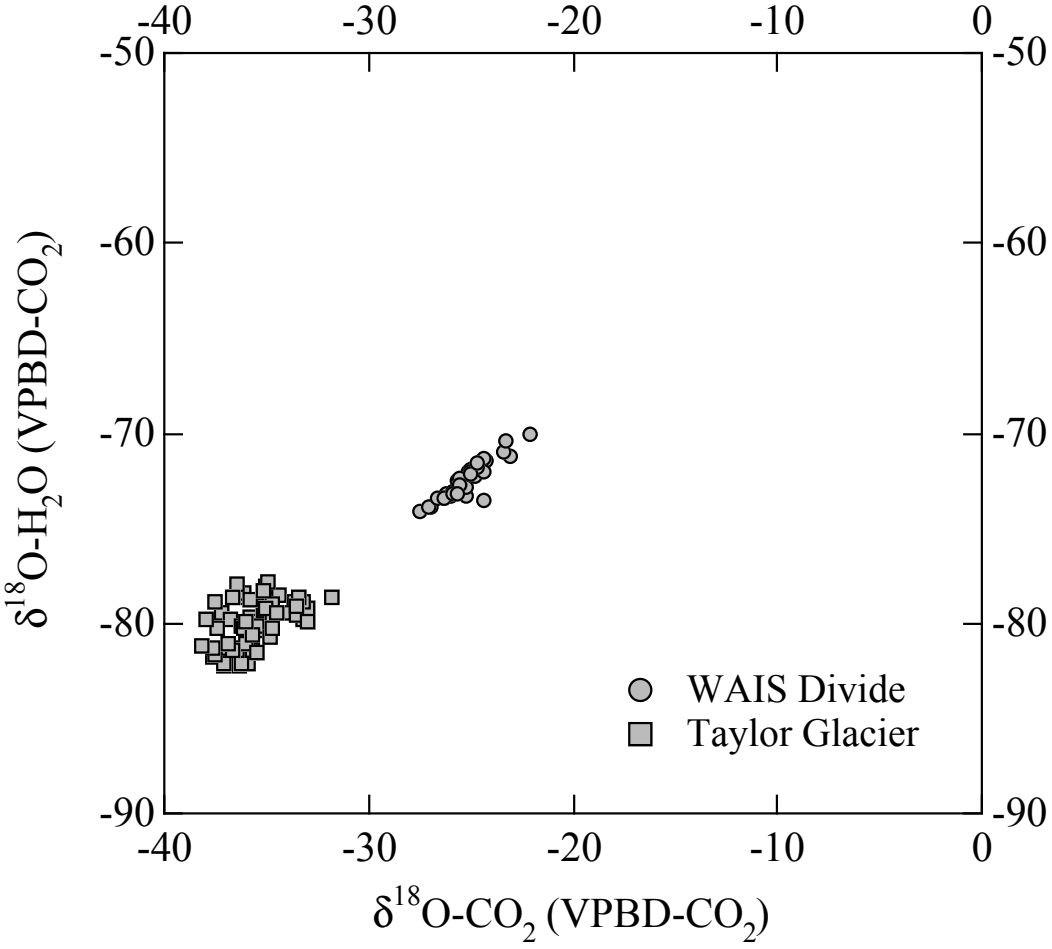

Figure 3.7 $\delta^{18}O\text{-}CO_2$ and $\delta^{18}O\text{-}H_2O$ correlation
$\delta^{18}O\text{-}CO_2$ plotted against $\delta^{18}O\text{-}H_2O$ from the WAIS Divide and Taylor Glacier archives.

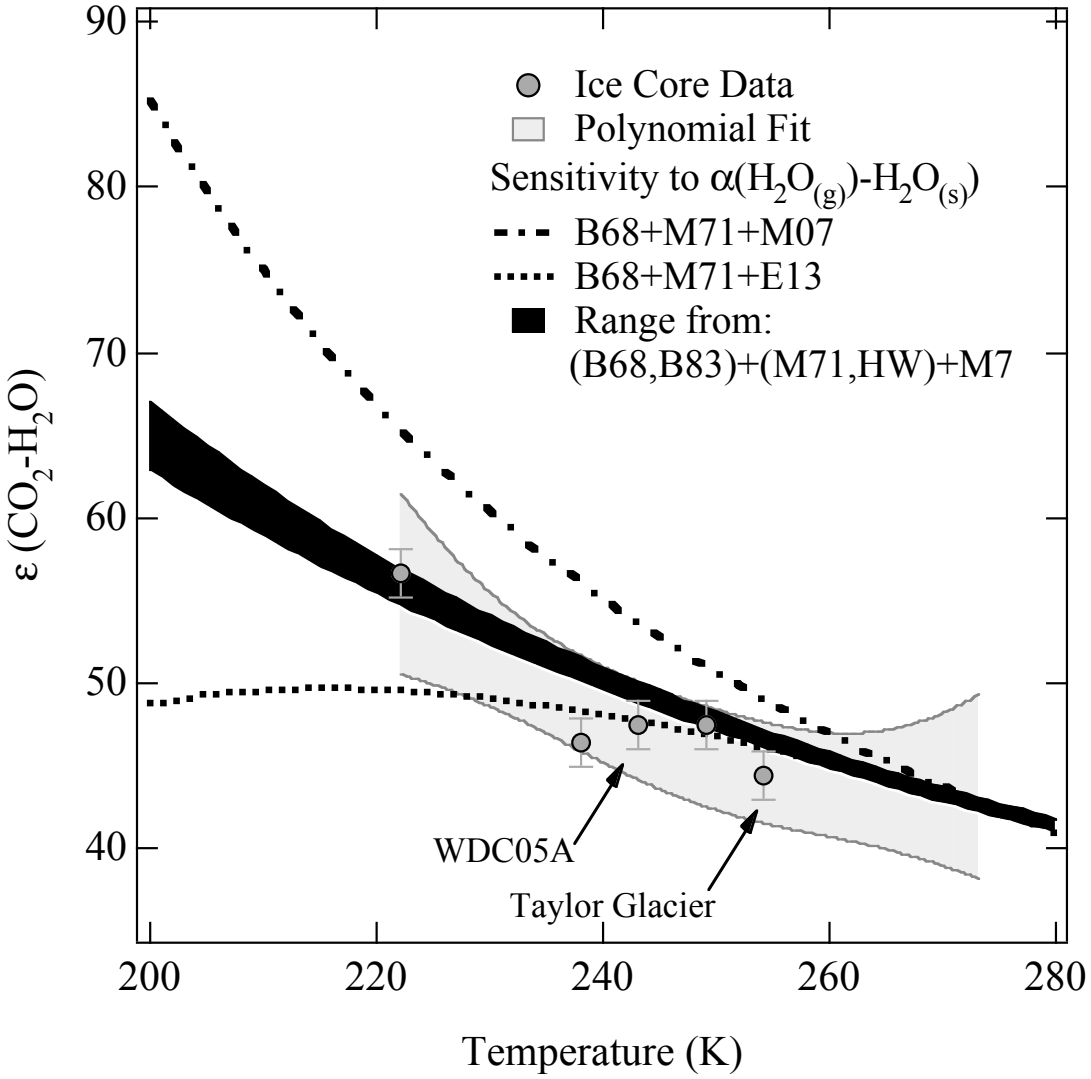

Figure 3.8 Temperature dependence of oxygen isotope fractionation
The relationship between ice core $\delta^{18}O$-CO_2 gas fractionation $\varepsilon(CO_2\text{-}H_2O_{(s)})$ (grey circles) from this study (indicated with arrows) and *Siegenthaler et al., 1988.* The light grey shading indicates a 3rd order polynomial fit to the data. The curves indicated the predicated fraction in thermodynamic equilibrium of gaseous CO_2 with H_2O vapor, liquid and solid (Equation 1). The black banding uses a range of determinations for $\alpha(CO_2\text{-}H_2O_{(l)})$ and $\alpha(H_2O_{(l)})\text{-}H_2O_{(g)})$ (Table 3.4) but only M71 for $\alpha(H_2O_{(g)})\text{-}H_2O_{(s)})$. The dot-dashed line uses only B68 for $\alpha(CO_2\text{-}H_2O_{(l)})$ and M71 for $\alpha(H_2O_{(l)})\text{-}H_2O_{(g)})$ but M07 for $\alpha(H_2O_{(g)})\text{-}H_2O_{(s)})$. The doted line also uses only B68 for $\alpha(CO_2\text{-}H_2O_{(l)})$ and M71 for $\alpha(H_2O_{(l)})\text{-}H_2O_{(g)})$ but E13 for $\alpha(H_2O_{(g)})\text{-}H_2O_{(s)})$ (See Table 3.4 for a description of the fractionation formulas).

Table 3.1 Ice archives utilized in this study with their respective precisions from replicate analysis

				1-sigma pooled standard deviation		
Ice Archive	Drill Fliud	Type of Replicates	n	$\delta^{13}C\text{-}CO_2$ (‰)	CO_2 (ppm)	N_2O (ppb)
WDC05A	none	true	8	0.016	2.18	3.83
WDC06A	Isopar-K, HCFC-141b	adjacent depths	6	0.014	1.04	2.4
Taylor Glacier	none	adjacent depths	9	0.022	1.3	5.23
Overall			23	0.018	1.9	4.35

Table 3.2 Reference gases used in calibration scheme

	Mixing Ratio			Isotopic Composition			
	Reference Scale	CO_2 (ppm) (s.d)	N_2O (ppb) (s.d)	Analysis Facility	Primary Ref. Material	$\delta^{13}C\text{-}CO_2$ (VPDB-CO_2)	$\delta^{18}O\text{-}CO_2$ (VPDB-CO_2)
NOAA1	2007 WMO MOLE FRACTION SCALE (CO_2), NOAA-2006 (N_2O)	277.04 (0.03)	252.6 (0.2)	INSTAAR-SIL	NBS-19	-8.288	-7.171
				OSU	NBS-19	-8.287	-7.58
NOAA2		150.01 (0.01)	321.96 (0.2)	INSTAAR-SIL	NBS-19	-8.135	-0.578
				OSU	NBS-19	-8.101	-0.934
Working Ref.	n.a.	pure	n.a.	Oztech		-10.39	-9.84
				OSU	NBS-19	-10.51	-10.06

Table 3.3 Observed $\delta^{18}O$ fractionation results from this study and other studies

Core	Study	Age Interval	$\delta^{18}O$-CO_2 (VPD-CO_2)	$\delta^{18}O$-H_2O (VPD-CO_2)	Temperature (K)	ε CO_2-H_2O (Observed)
WAIS Divide	this study	1.25-0.1 ka	-25.17	-72.41	243.15	47.43±0.45
Taylor Glacier		23-11 ka	-35.58	-80.00	254.15	44.42±1.34
Siple Dome	Siegenthaler et al., 1988	0.3-0.1 ka	-20.40	-67.86	249.15	47.46
South Pole		0.9-0.4 ka	-31.70	-88.31	222.15	56.61
Byrd		~50 ka	-31.80	-78.23	238.15	46.43

Table 3.4 $\delta^{18}O$ Fractionation Factors

α(A-B)	1000 ln(α) =	Reference	Shorthand
$\alpha(CO_2\text{-}H_2O_{(l)})$	$-\frac{0.021(10^6)}{T^2}+\frac{17.99(10^3)}{T}-19.97$	Bottinga (1968)	B68
	$\frac{17.6(10^3)}{T}-17.93$	Brenninkmeijer, et al. (1983)	B83
$\alpha(H_2O_{(l)}\text{-}H_2O_{(g)})$	$\frac{1.137(10^6)}{T^2}-\frac{0.42(10^3)}{T}-2.07$	Majoube (1971)	M71
	$\frac{0.35(10^9)}{T^3}-\frac{1.666(10^6)}{T^2}+\frac{6.71(10^3)}{T}-7.68$	Horita & Wesolowski (1994)	HW94
$\alpha(H_2O_{(s)}\text{-}H_2O_{(g)})$	$\frac{11.84(10^3)}{T}-28.22$	Majoube (1971)	M71
	$-0.0016799x^3-.00721x^2+1.675x-2.685$ where $x=\frac{10^6}{T^2}$	Méheut, et al. (2007)	M07
	$\left(\frac{8312.5}{T^2}-\frac{49.192}{T}+0.0831\right)\times 1000$	Ellehoj et al., 2013	E13

3.13 References

Ahn, J., et al. (2009), A high-precision method for measurement of paleoatmospheric CO2 in small polar ice samples, J. Glaciol., 55(191), 499-506.

Assonov, S. S., and C. A. M. Brenninkmeijer (2006), On the N_2O correction used for mass spectrometric analysis of atmospheric CO_2, Rapid Communications In Mass Spectrometry, 20(11), 1809-1819.

Assonov, S. S., et al. (2005), The ^{18}O isotope exchange rate between firn air CO_2 and the firn matrix at three Antarctic sites, Journal of Geophysical Research: Atmospheres (1984‚Äì2012), 110(D18).

Bottinga, Y., and H. Craig (1968), Oxygen isotope fractionation between CO_2 and water, and the isotopic composition of marine atmospheric CO_2, Earth and Planetary Science Letters, 5, 285-295.

Brenninkmeijer, C. A. M., et al. (1983), Oxygen Isotope Fractionation Between CO_2 and H_2O, Isotope Geoscience, 1(2), 181-190.

Ellehoj, M. D., et al. (2013), Ice-vapor equilibrium fractionation factor of hydrogen and oxygen isotopes: Experimental investigations and implications for stable water isotope studies, Rapid Communications In Mass Spectrometry, 27(19), 2149-2158.

Elsig, J., et al. (2009), Stable isotope constraints on Holocene carbon cycle changes from an Antarctic ice core, Nature, 461(7263), 507-510.

Fischer, H., et al. (2013), Where to find 1.5 million yr old ice for the IPICS "Oldest Ice" ice core, Clim. Past Discuss., 9(3), 2771-2815.

Francey, R. J., Enting, I.G., Leuenberger, M., Langenfelds, R.L., Michel, E., Steele, L.P., Allison, C.E., Etheridge, D.M., Trudinger, C.M. (1999), A 1000-year high precision record of $\delta^{13}C$ in atmospheric CO_2, Tellus, Series B: Chemical and Physical Meteorology, 51(2), 170-193.

Friedli, H., Fischer, H., Oeschger, H., Siegenthaler, U., , and B. Stauffer (1986), Ice core record of the $^{13}C/^{12}C$ ratio of atmospheric CO_2 in the past two centuries, Nature, 324(20), 237-238.

Halsted, R. E., and A. O. Nier (1950), Gas Flow through the Mass Spectrometer Viscous Leak, Review of Scientific Instruments, 21(12), 1019-1021.

Horita, J., and D. J. Wesolowski (1994), Liquid-vapor fractionation of oxygen and hydrogen isotopes of water from the freezing to the critical temperature, Geochimica et Cosmochimica Acta, 58(16), 3425-3437.

Indermuhle, A., et al. (1999), Holocene carbon-cycle dynamics based on CO_2 trapped in ice at Taylor Dome, Antarctica, Nature, 398(6723), 121-126.

Keeling, R. F. (1995), The atmospheric oxygen cycle: The oxygen isotopes of atmospheric CO_2 and O_2 and the O_2/N_2 ratio, Rev. Geophys., 33(S2), 1253-1262.

Leuenberger, M., et al. (1992), Carbon isotope composition of atmospheric CO_2 during the last ice-age from an Antarctic ice core, *Nature*, *357*(6378), 488-490.

Leuenberger, M. C., et al. (2003), High-resolution delta C-13 measurements on ancient air extracted from less than 10 cm(3) of ice, *Tellus Series B-Chemical and Physical Meteorology*, *55*(2), 138-144.

Lourantou, A., et al. (2010), Constraint of the CO_2 rise by new atmospheric carbon isotopic measurements during the last deglaciation, Global Biogeochemical Cycles, 24, 15.

Luthi, D., et al. (2008), High-resolution carbon dioxide concentration record 650,000-800,000 years before present, Nature, 453(7193), 379-382.

Mader, H. M. (1992), Observations of the water-vein system in polycrystalline ice, J. Glaciol., 38(130), 333-347.

Majoube, M. (1971), Oxygen-18 and Deuterium Fractionation Between Water and Steam, *Journal De Chimie Physique Et De Physico-Chimie Biologique*, *68*(10), 1423-1436.

Meheut, M., et al. (2007), Equilibrium isotopic fractionation in the kaolinite, quartz, water system: Prediction from first-principles density-functional theory, Geochimica et Cosmochimica Acta, 71(13), 3170-3181.

Mitchell, L. E., et al. (2011), Multidecadal variability of atmospheric methane, 1000-1800 CE, Journal of Geophysical Research-Biogeosciences, 116.

Nye, J. F., and F. C. Frank (1973), Hydrology of the intergranular veins in a temperate glacier, paper presented at Symposium on the Hydrology of Glaciers.

Rubino, M., et al. (2013), A revised 1000 year atmospheric $\delta^{13}C$-CO_2 record from Law Dome and South Pole, Antarctica, Journal of Geophysical Research: Atmospheres, 118(15), 8482-8499.

Santrock, J., et al. (1985), Isotopic analyses based on the mass-spectrum of carbon-dioxide Analytical Chemistry, 57(7), 1444-1448.

Schaefer, H., et al. (2008), On the suitability of partially clathrated ice for analysis of concentration and $\delta^{13}C$ of palaeo-atmospheric CO_2, Earth and Planetary Science Letters, 307(3,Äì4), 334-340.

Schmitt, J., et al. (2012), Carbon Isotope Constraints on the Deglacial CO_2 Rise from Ice Cores, Science.

Schmitt, J., et al. (2011), A sublimation technique for high-precision measurements of δ13CO2 and mixing ratios of CO2 and N2O from air trapped in ice cores, Atmos. Meas. Tech., 4(7), 1445-1461.

Siegenthaler, U., et al. (1988), Stable-isotope ratios and concentration of CO_2 in air from polar ice cores, Annals of Glaciology, 10, 151-156.

Smith, H. J., et al. (1999), Dual modes of the carbon cycle since the Last Glacial Maximum, Nature, 400(6741), 248-250.

Welp, L. R., et al. (2011), Interannual variability in the oxygen isotopes of atmospheric CO_2 driven by El Nino, Nature, 477(7366), 579-582.

Zhao, C. L., et al. (1997), A high precision manometric system for absolute calibrations of CO_2 in dry air, Journal of Geophysical Research: Atmospheres, 102(D5), 5885-5894.

4 Pre-industrial atmospheric carbon dioxide controlled by land carbon during the last millennium

Thomas K. Bauska[1], Fortunat Joos[2], Raphael Roth[2], Alan C. Mix[1], Jinho Ahn[3], Edward J. Brook[1]

[1]College of Earth, Ocean, and Atmospheric Sciences, Oregon State University, Corvallis, OR 97331

[2]Climate and Environmental Physics, Physics Institute and Oeschger Center for Climate Change Research, University of Bern, Bern, Switzerland

[3]School of Earth and Environmental Science, Seoul National University, Seoul 151-742, Korea

4. 1 Abstract

The history of carbon cycle responses to climate change provides an important constraint on future climate-carbon feedbacks (Cox and Jones, 2008; Frank et al., 2010). In the coming centuries, warming climate may turn the land carbon reservoir into a net source of carbon to the atmosphere (Raich and Schlesinger, 1992; Davidson and Janssens, 2006), but long-term, global-scale observations of this process are difficult (Trumbore and Czimczik, 2008; Hopkins et al., 2012) making model projections of future CO_2 levels uncertain (Friedlingstein et al., 2006; Arora et al., 2013). We present a high-resolution, high-precision record of the stable isotopic composition of atmospheric carbon dioxide ($\delta^{13}C$-CO_2) that suggests land carbon controlled atmospheric CO_2 variability from 770-1850 C.E., and a deconvolution of the atmospheric CO_2 and $\delta^{13}C$-CO_2 that provides a well-constrained estimate of the evolution of land carbon stocks. The relationship between temperature and land carbon for this time period is consistent with land carbon decreasing by about 60 gigatons for every one degree of Northern Hemisphere warming, in agreement with most models projecting future climate-carbon cycle feedbacks. However, we also find that an additional process affecting land carbon is required to explain our data.

This missing process may be related to patterns of drought or early anthropogenic land cover change.

4.2 Introduction

Atmospheric CO_2 constantly exchanges with carbon reservoirs on land and in the surface ocean. During these exchanges, the isotopes of carbon are fractionated, allowing the sources and sinks for CO_2 to be differentiated. During photosynthesis, ^{12}C is preferentially taken up into biological carbon reservoirs relative to ^{13}C. If more biological carbon is stored on land or exported to the deep ocean, atmospheric CO_2 decreases and becomes more enriched in ^{13}C. When this carbon is respired and returns to the atmosphere, atmospheric CO_2 increases and becomes more depleted in ^{13}C (i.e. more negative $\delta^{13}C\text{-}CO_2$).

Fractionation during air-sea gas exchange also alters the atmospheric $^{13}C/^{12}C$ ratio. The net effect of kinetic and thermodynamic fractionations during exchange between CO_2 in the atmosphere and dissolved inorganic carbon in the surface ocean establishes an atmosphere that is more depleted in ^{13}C relative to the surface ocean, with the magnitude of the fractionation determined primarily by sea surface temperature (SST). If the ocean becomes colder, the solubility of CO_2 increases along with the magnitude of fractionation, leading to an atmosphere with lower CO_2 and more negative $\delta^{13}C\text{-}CO_2$ (essentially the opposite sign of biologically driven changes). Additionally, changes in the rate of air-sea gas exchange can affect atmospheric $\delta^{13}C\text{-}CO_2$. Enhancing air-sea gas exchange in the cold, high-latitude ocean (e.g. increasing windstress or decreasing sea ice cover) will gradually fill the deep ocean with enriched carbon, leading to a more depleted atmosphere.

The $\delta^{13}C\text{-}CO_2$ thus reflects the surface ocean carbon isotopic composition, global mean SST, and the balance between photosynthesis and respiration. For timescales on the order of the mixing time of the ocean ($>10^2$ years), changes in ocean circulation,

the strength of the biologic pump and gas exchange can govern $\delta^{13}C\text{-}CO_2$. On timescales shorter than the mixing time of the ocean, $\delta^{13}C\text{-}CO_2$ can respond strongly to changes in the source/sink history of the terrestrial biosphere.

Changes in the amount of carbon stored on land are believed to be driven by climate and CO_2 concentration. On glacial-interglacial timescales, the colder conditions and growth of Northern Hemisphere ice sheets probably lead to a decrease in land carbon (Ciais et., 2012). Re-growth of the terrestrial biosphere following climate amelioration in the Holocene took place over millennia with some processes, such as the gradual buildup of peatlands, probably still underway (MacDonald et al., 2006; Yu, 2012). On shorter timescales, relevant to future climate change, higher CO_2 levels are thought to enhance the uptake of carbon by the land biosphere, primarily by increased efficiency of plant water-use, the so-called "CO_2 fertilization effect". However, land carbon might decrease as the climate warms by enhancing soil respiration at the expense of photosynthesis (Raich and Schlesinger, 1992; Davidson and Janssens, 2006). Empirical evidence for these effects have relied on experiments (in both the laboratory and in nature) over relatively short time-scales with respect to the climate change projected over the coming centuries (Trumbore and Czimzik, 2008; Hopkins et al., 2012). Therefore, the competition between the impacts of rising CO_2 and increasing temperature on the current and future land carbon budget remains a point of debate. To test the hypothesis that climate can drive land carbon, we reconstruct carbon cycle changes prior to the Industrial Revolution when natural climate variations, rather than CO_2 fertilization and anthropogenic land conversion, may have dominated the carbon cycle budget.

4.3 Results

A new record of $\delta^{13}C\text{-}CO_2$ (presented here) and an extended high-resolution CO_2 record (Ahn et al., 2012) were constructed using samples from the Antarctic WAIS Divide Ice Core (West Antarctic Ice Sheet, 79.467 S, 112.085 W, ice elevation 1769

m) spanning the period of 770-1930 C.E. with an average resolution of 20 and 10 years and precision of ±0.016‰ and 0.8 ppm, respectively (see Appendix A).

The records of CO_2 and $\delta^{13}C$-CO_2 covary (R^2=0.54) with increasing CO_2 associated with decreasing $\delta^{13}C$-CO_2 from about 770-1870 C.E. (Figure 4.1). This relationship rules out ocean temperature changes as the sole driver of carbon cycle changes and strongly suggests variations in a ^{13}C-depleted reservoir as the primary control on atmospheric CO_2.

The 5-6 ppm increase in CO_2 between 950-1100 C.E is associated with a 0.08‰ ^{13}C depletion. For the following 400 years, CO_2 levels in the atmosphere were stable, or gradually declined, with a small step change to slightly lower CO_2 and more ^{13}C enriched values around 1250 C.E. Around 1400 C.E., atmospheric CO_2 began to decrease and ^{13}C became more enriched, but this trend quickly reversed with a rapid 3-4 ppm increase in CO_2 and a 0.1‰ depletion between 1470-1510 C.E. At about 1550 C.E. the atmosphere became more enriched in ^{13}C by about 0.2‰, followed by a sharp decrease in CO_2 levels around 1580 C.E. A broad minima in CO_2 and maxima in ^{13}C is reached between ~1600 and 1700 C.E. After 1700 C.E., CO_2 rose and became more depleted in ^{13}C, with a significant rate increase at the onset of Industrial period around 1850 CE.

4.4 Interpretation

The decreasing trend of CO_2 and enrichment in $\delta^{13}C$-CO_2 from around 1200 C.E. to 1700 C.E. is correlated with the gradual cooling in the Northern Hemisphere (NH) and Southern Hemisphere (SH) over the last millennium (PAGES 2k Consortium, 2013; Mann et al., 2008). While less clear, the $\delta^{13}C$-CO_2 from 950-1100 C.E. may also be correlated to NH temperature (the so-called Medieval Climate Anomaly, MCA) (Moberg et al., 2005; Christiansen and Ljungqvist, 2012) For example, the $\delta^{13}C$-CO_2 correlates with the *Moberg et al., 2005* low-frequency NH temperature

reconstruction ($R^2 = 0.27$), with a maximum correlation reached when the carbon cycle changes are lagging the temperature variations by about 100 years ($R^2 = 0.60$). However, the rapid excursion (increase in CO_2 and decrease in $\delta^{13}C\text{-}CO_2$) spanning 1500-1580 CE is more associated with some of the coldest conditions in the NH, suggesting a different relationship with NH temperature during this interval and complicating the interpretation of the lag correlation.

The covariation of NH climate and $\delta^{13}C\text{-}CO_2$, whereby increases in NH temperature are associated with more respired CO_2 in the atmosphere, is inconsistent with the formation rate of NADW as the primary moderator of climate (Broecker, 2000) and the preformed nutrient and carbon content of the ocean (with the exception of the CO_2 increase at ~1500 CE, though this would require a corresponding warming in the SH). Assuming that NH temperature and sea-ice covaried, and the retreat of NH sea ice would promote CO_2 invasion of the deep ocean (Chikamoto et al., 2012), the phasing is also inconsistent with NH sea ice as the dominant control on CO_2. On the other hand, the gradual cooling of Antarctica over the last millennium could contribute to a slow drawdown of CO_2 (and gradual enrichment of $\delta^{13}C\text{-}CO_2$) by way of extended sea ice cover, but likely not the more rapid CO_2 increases.

The centennial-scale, globally extensive temperature variations that appear to covary and possibly lead CO_2 and $\delta^{13}C\text{-}CO_2$, are consistent with climate driving small changes in the carbon cycle (with a relatively minor feedback by way of radiative impact of CO_2). Given this relationship and the rapidity and magnitude and sign of the $\delta^{13}C\text{-}CO_2$ variations, our observations are consistent with the terrestrial biosphere as the primary moderator of atmospheric CO_2.

To further interpret the data we derived a suite of land-atmosphere and ocean-atmosphere flux histories from a double deconvolution (Joos and Bruno, 1998) using the High-Latitude Exchange/Interior Diffusion-Advection (HILDA) ocean model coupled to 4-box model of the terrestrial biosphere (see Appendix A). The double

deconvolution reveals multi-decadal scale land carbon variability with intervals of net sources to the atmosphere from 975-1100, 1460-1540, and 1775-1850 C.E. (after which $\delta^{13}C$-CO_2 is no longer fully resolved in this record) and net sinks from 1375-1460 and 1550-1725 C.E (Figure 4.2). Broadly, land carbon lost 20 GtC from 950-1100 C.E. and then gained 55 GtC from 1200-1750 C.E..

The new estimate of land carbon stocks, when combined with records of land temperature, provides an opportunity to test the land-carbon climate sensitivity hypothesis in the pre-Industrial period (land-carbon climate sensitivity is defined as $\gamma_L = \Delta C/\Delta T$, where ΔC is the change in carbon stocks due a temperature change ΔT, all other things being equal). Because the changes in the CO_2 concentration are small (~5 ppm) over this time interval, we neglect the minor effect of CO_2 fertilization (~1 GtC ppm^{-1}) (Friedlingstein et al., 2006).

Using a similar approach to an analysis of CO_2 and northern hemisphere (NH) temperature sensitivity (Frank et al., 2010) the land carbon stocks were linearly regressed against a reconstructed NH temperature from 1000-1800 C.E. (Frank et al., 2010) and 770-1800 C.E. (Moberg et al., 2005; Mann et al., 2008) (hereafter: FK10, MG05, MN08, respectively) with a lag of 100 years. The slope of the regression line is the estimate of γ_L, capturing the transient response of the carbon cycle to temperature variations. A one-box model of the terrestrial biosphere was also used in which the response of land carbon stocks to temperature approaches equilibrium with an e-folding time of 50 years. This acts as a low-pass filter based on single global turnover time of carbon in soil and vegetation. Uncertainty is evaluated by using a monte-carlo approach of multiple land carbon stock deconvolutions (n = 1000) with each temperature time-series varied within its stated error with high-correlated red noise (Ar = 0.95, n = 1000).

Nearly all the regressions explain a significant ($p < 0.01$) but partial (R^2 =0.28-0.71) portion of the land carbon variability. All approaches indicate a negative γ_L and

converge on a median value of -61 GtC K^{-1} (Figure 4.3) in good agreement with the mean of CMIP5 estimates (-58 GtC K^{-1}) (Arora et al., 2013). Considering the large uncertainty and simplicity of the analysis, we can only state that γ_L is unlikely to be positive (i.e. a negative feedback on temperature change) or very sensitive (<-110 GtC K^{-1}) (Figure 4.3 and Table S.1).

4.5 Discussion

While suggesting that climate is an important driver of land carbon, the regression analysis also opens at least three distinct possibilities: errors in the data prevent accurate description of the relationship between the carbon cycle and temperature, the carbon cycle responds to temperature in a non-linear fashion not captured by the simple statistical models used in this analysis, or temperature is not the only process affecting land carbon. Reduction of data errors (primarily in the temperature reconstructions) and more complex modeling will require further work. We focus on outlining three additional carbon cycle processes that may be integrated into the land carbon signal.

First, the gradual re-growth of peatland throughout the Holocene is thought to be significant sink for atmospheric CO_2 (MacDonald et al., 2006; Yu, 2012). Second, variability in precipitation can drive multi-decadal scale changes in land carbon (van der Molen et al., 2011; Schwalm et al., 2012). Third, population expansion (contraction) can drive land conversion (abandonment) and a decrease (increase) in land carbon stocks (Ruddiman, 2003).

To evaluate the potential magnitude of missing processes we assume that peatland accounted for 30 to 50 GtC of uptake per thousand years and land carbon-climate sensitivity, driven by MG05 ($R^2 = 0.60$), varied between -25 and -125 GtC K^{-1}. These processes are then subtracted from the total land carbon stocks to obtain the variability that remains unexplained under these assumptions and uncertainties

(Figure 4.3). Closing the budget would require a 35 GtC loss of land carbon from 1000-1300, a 30 GtC loss from 1450-1550, a 35 GtC uptake from 1550-1750, and a 50 GtC loss after 1800 C.E.

During the late Holocene, precipitation variability is characterized by zonally and meridionally asynchronous changes, likely driven by changes in the strength or position of the intertropical convergence zone. Western North America (Cook et al., 2004), central America (Kennet et al., 2012), and northern Europe (Helama et al., 2009) experienced prolonged droughts during the MCA. The Asian Monsoon regions (Cook et al., 2010; Sinha et al., 2011) and northern South America (Haug et al., 2001) experienced drought conditions in the LIA. Some regions, like Equatorial Africa, experienced droughts in both the MCA and LIA (Shanahan et al., 2009) or fine-scale spatial heterogeneities (Russell and Johnson, 2007). Drought could therefore be responsible for some of the land carbon loss during the warming in the MCA as well as the sharp loss at around 1450-1550 C.E. during an interval of cooling in the LIA.

Estimates of anthropogenic land cover change (ALCC) readily explain the decrease in land carbon after 1800 C.E, but the contribution of ALCC further in the past remains unconstrained and controversial. Due to uncertainties in per capita land-use and the disparate effects of land conversion on vegetation and soil carbon pools, the exact relationship between population, land conversion, and carbon stocks is not well-constrained but is likely non-linear and time variant.

World population is estimated to have increased from 1000-1200 C.E., followed by near zero growth from about 1200-1400 C.E. due primarily to population contractions in Europe and Asia associated with the Black Death and Mongol Invasions, respectively (Goldewijk et al., 2011) (Figure 4.3). Around 1500 C.E., population growth resumed and continued largely unabated into the Industrial Period. These two intervals of population growth appear to correspond to times of significant land carbon loss, but significant uncertainties in population estimates preclude establishing

a conclusive relationship. Additionally, a shift to colder climate and peatland uptake can account for most of the trend in land carbon uptake between 1400-1700 C.E., but fails to account for the magnitude or timing of the sharp uptake at around 1600 C.E., which may be associated with a poorly constrained post-Colombian New World population decrease.

Model-based estimates of the impact of ALCC on carbon stocks do not simulate most of the features in total land carbon stocks and are therefore inconsistent with the data if ALCC is assumed to be the sole driver of land carbon. Emissions based on constant per capita land-use mostly fall within the uncertainty of the residual but simulate no centennial-scale features (Stocker, Strassmann and Joos, 2011). Emissions driven by population density are generally too large but do predict some similar second order features (Kaplan et al., 2011). When temperature and peatland effects are accounted for, we can speculate, with much less certainty, that the data are consistent with a small, steady increase in ALCC during the preindustrial, possibly punctuated by periods of enhanced land carbon loss/storage possibly driven by pandemics and warfare.

4.6 Conclusions

By extending our observations of the $\delta^{13}C\text{-}CO_2$ into the past with unprecedented precision and resolution, we demonstrate that temperature and land carbon are coupled on multi-decadal to centennial timescales. This strongly supports the hypothesis that future climate warming will drive a loss of carbon from the terrestrial biosphere. However, we also observe new variability in the carbon cycle that is not readily explained by the temperature changes alone. Our new observations present a challenging benchmark for models attempting to simulate the climate and carbon cycle of the past in order to understand the projections for the future.

4.7 Methods Summary

$\delta^{13}C\text{-}CO_2$ was measured using a new dry extraction technique coupled to a dual-inlet system and gas-source isotope ratio mass spectrometer (Thermo MAT 253) (Chapter 2). Measurement uncertainty derived from the pooled standard deviation of replicate analyses is ±0.016‰ - a significant improvement on previously published techniques. The average 1-sigma uncertainty of a CO_2 concentration is 0.8 ppm based on the standard error for each depth. The gas age scale is derived from a layer-counted ice age timescale with an absolute age uncertainty of ±10 years within the time interval considered here. The high accumulation rate at the site (~22 cm yr^{-1}) allows us to resolve multi-decadal variability in atmospheric gases. Gravitational fractionation in the firn was accounted for using $\delta^{15}N$ of N_2 data from approximately the same depth interval for each sample (Jeffrey Severinghaus, personal communication). Diffusive fractionation, estimated using the formulation from *Buziert et al., 2013* is negligible for the interval of interest (maximum range of 0.04 per mil).

The double deconvolution technique assumes that land carbon and ocean temperature are the only drivers of CO_2 and uses the known CO_2 and ^{13}C atmospheric composition to solve the unknown net land and ocean fluxes. The HILDA ocean model is used to estimate the isotopic disequilibrium flux and variations in the air-sea gas fractionation due to changes in SST. To drive the temperature dependent ocean flux, we employ the only globally extensive land and ocean temperature reconstruction covering the Common Era (Mann et al., 2008), though other temperature histories that resolve Northern Hemisphere land were explored (Appendix A). The impact of random uncertainties is evaluated by running Monte Carlo simulations (n = 1000) in which the data input (CO_2 $\delta^{13}C\text{-}CO_2$), SST, and the photosynthetic fractionation factor were varied within their estimated error.

The Monte Carlo simulations demonstrate that the timing and structure of the features in the flux history are insensitive to uncertainty in the prescribed SST, ocean mixing parameters or photosynthetic fractionation factor. However, a significant portion of

the long-term trend in land carbon stocks (~25 GtC) depends on a SST cooling into the Little Ice Age (LIA) (Figure A.4). Assuming that the land-biased temperature reconstruction used to drive the model SST captures the true long-term global SST trend, land carbon stocks would have lost 20 GtC from 950-1100 C.E. and then gained 55 GtC from 1200-1750 C.E (Figure 4.2).

4.8 Acknowledgements

This work was supported by NSF grant 0839078. We appreciate the support of the WAIS Divide Science Coordination Office for the collection and distribution of the WAIS Divide ice core (Kendrick Taylor (Desert Research Institute of Reno Nevada), NSF Grants 0230396, 0440817, 0944348; and 0944266 - University of New Hampshire). The work was also partially supported by Korea Meteorological Administration Research and Development Program under grant CATER 2012-7030. F.J and R.R. thank for financial contributions by the Swiss National Science Foundation, including contributions through the Sinergia Project iTree (project 136295), and by the European Commission through the FP7 project CARBOCHANGE (grant no. 264879) and Past4Future (grant no. 243908).

The NSF also funds the Ice Drilling Program Office, Ice Drilling Design and Operations group which leads coring activities and The National Ice Core Laboratory which curates the core and performs core processing. We thank Jeff Severinghaus for providing $\delta^{15}N$ of N_2 data, Raytheon Polar Services for logistics support in Antarctica, and the 109th New York Air National Guard for airlift in Antarctica.

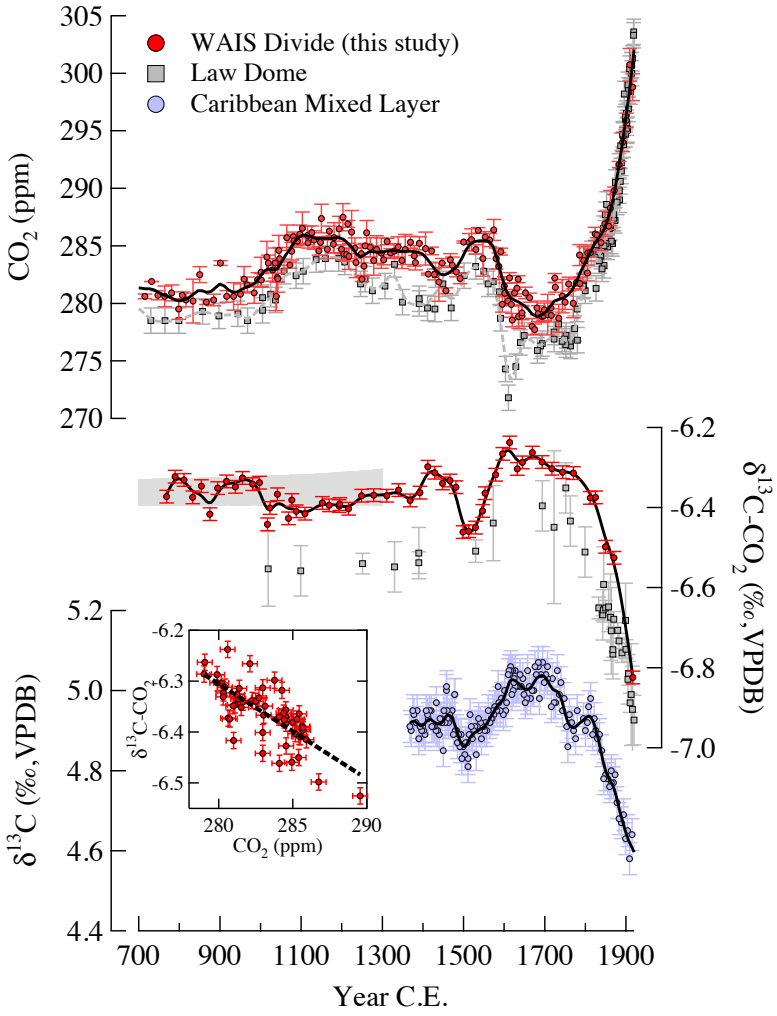

Figure 4.1 Carbon Cycle Variability of the Last Millennium
CO_2 and $\delta^{13}C$-CO_2 (red markers, this study) from the WAIS Divide Ice Core with earlier reconstructions from the Law Dome ice core (grey markers) (Francey et al., 1999; MacFarling Meure et al., 2006), with the $\delta^{13}C$-CO_2 plotted as recently revised in (Rubino et al., 2013), a small portion of glacial-interglacial reconstruction by *Schmitt et a 2012* (grey shading), and a pristine coral record from the near surface Caribbean (25 meters water depth, 78°57'W, 17°32'N) (Böhm et al., 2002). Compared to Law Dome, the higher resolution and precision of our new data allows for a more robust definition of small changes in the carbon cycle, yet the accuracy of pre-Industrial $\delta^{13}C$-CO_2 requires further study (see Appendix A for further discussion).

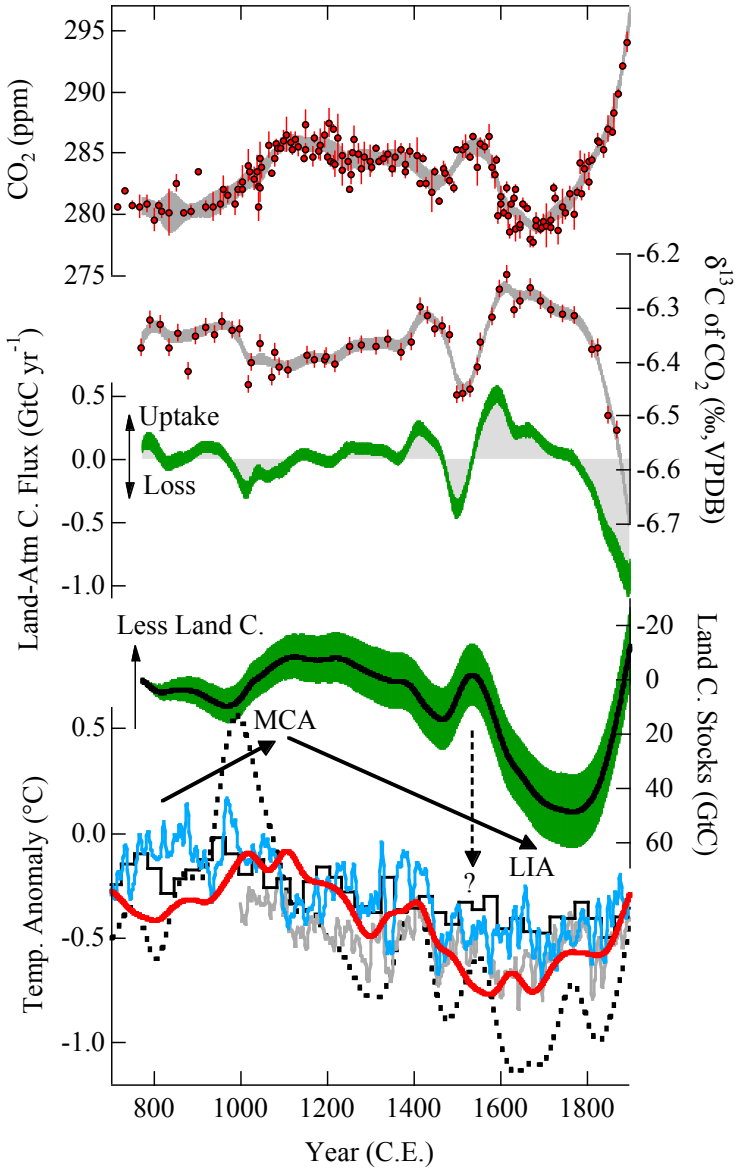

Figure 4.2 Climate Carbon-Cycle Relationship
Temperature reconstructions of the following: global temperature from the PAGES 2k (solid black) and MN08 (solid blue); northern hemisphere land from MG05 (solid red); northern hemisphere extra-tropical land (Christiansen and Ljungqvist, 2012) (dashed black); or a suite of 521 northern hemisphere land reconstructions with a variety of calibrations from FK10 (grey line, representing the median). Land carbon stocks (the cumulative sum of the flux history) with the 1-sigma uncertainty (green band) on an inverted y-axis.

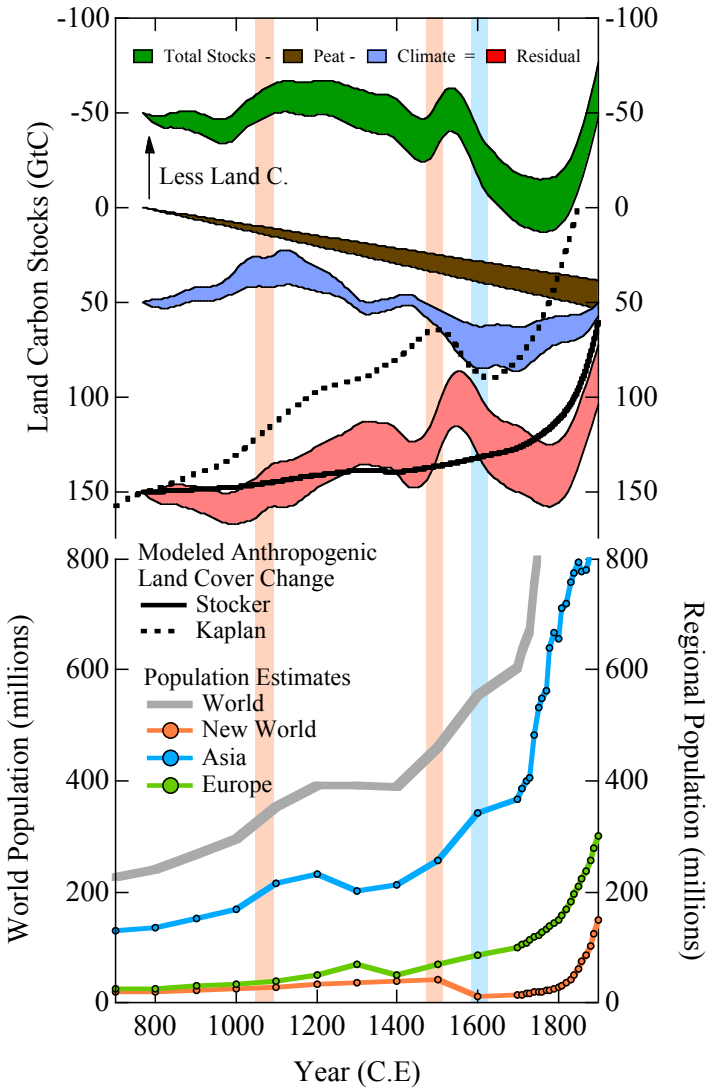

Figure 4.3 Land Carbon Processes
An estimate of the processes at play in the land carbon stock reconstruction on an inverted y-axis. The green shading is the land carbon stock estimate. The brown shading is effect of peatland uptake and the blue shading is the effect of temperature. These two histories are subtracted (with propagation of uncertainty) from the reconstructed land carbon stocks to estimate the unexplained variability (the red banding). The shading shows the 1-sigma uncertainty and the curves have been offset from each other on the y-axis for clarity. The solid black line shows the effect of ALCC on land carbon stocks when modeled with constant per-capita land-use (Stocker, Strassmann and Joos, 2011) and the dashed black lines shows the a model estimates with variable per-capita land-use (Kaplan et al., 2011). Also plotted are world and regional population estimates. Note that the markers indicate the coarse, century resolution of the population curves. The bars highlight the onset of land carbon loss (red) or uptake (blue).

4.9 References

Ahmed, M., et al. (2013), Continental-scale temperature variability during the past two millennia, *Nature Geoscience*.

Ahn, J., et al. (2012), Atmospheric CO_2 over the last 1000 years: A high-resolution record from the West Antarctic Ice Sheet (WAIS) Divide ice core, *Global Biogeochemical Cycles*, *26*.

Arora, V. K., et al. (2013), Carbon-Concentration and Carbon-Climate Feedbacks in CMIP5 Earth System Models, *J. Clim.*, *26*(15), 5289-5314.

Böhm, F., et al. (2002), Evidence for preindustrial variations in the marine surface water carbonate system from coralline sponges, *Geochem. Geophys. Geosyst.*, *3*, 13.

Broecker, W. S. (2000), Was a change in thermohaline circulation responsible for the Little Ice Age?, *Proceedings of the National Academy of Sciences*, *97*(4), 1339-1342.

Buizert, C., et al. (2013), Assessment of diffusive isotopic fractionation in polar firn, and application to ice core trace gas records, *Earth and Planetary Science Letters*, *361*(0), 110-119.

Chikamoto, M. O., et al. (2012), Quantifying the ocean's role in glacial CO_2 reductions, *Climate of the Past*, *8*(2), 545-563.

Christiansen, B., and F. C. Ljungqvist (2012), The extra-tropical Northern Hemisphere temperature in the last two millennia: reconstructions of low-frequency variability, *Climate of the Past*, *8*(2), 765-786.

Ciais, P., et al. (2012), Large inert carbon pool in the terrestrial biosphere during the Last Glacial Maximum, *Nature Geosci*, *5*(1), 74-79.

Consortium, P. k. Continental-scale temperature variability during the past two millennia, *Nature Geosci*, *6*(5), 339-346.

Cook, E. R., et al. (2010), Asian Monsoon Failure and Megadrought During the Last Millennium, *Science*, *328*(5977), 486-489.

Cook, E. R., et al. (2004), Long-term aridity changes in the western United States, *Science*, *306*(5698), 1015-1018.

Cox, P., and C. Jones (2008), Illuminating the Modern Dance of Climate and CO_2, *Science*, *321*(5896), 1642-1644.

Davidson, E. A., and I. A. Janssens (2006), Temperature sensitivity of soil carbon decomposition and feedbacks to climate change, *Nature*, *440*(7081), 165-173.

Francey, R. J., et al. (1999), A 1000-year high precision record of $\delta^{13}C$ in atmospheric CO_2, *Tellus, Series B: Chemical and Physical Meteorology*, *51*(2), 170-193.

Frank, D. C., et al. (2010), Ensemble reconstruction constraints on the global carbon cycle sensitivity to climate, *Nature*, *463*(7280), 527-U143.

Friedlingstein, P., et al. (2006), Climate-carbon cycle feedback analysis: Results from the C(4)MIP model intercomparison, *J. Clim.*, *19*(14), 3337-3353.

Goldewijk, K. K., et al. (2011), The HYDE 3.1 spatially explicit database of human-induced global land-use change over the past 12,000 years, *Glob. Ecol. Biogeogr.*, *20*(1), 73-86.

Haug, G. H., et al. (2001), Southward migration of the intertropical convergence zone through the Holocene, *Science*, *293*(5533), 1304-1308.

Helama, S., et al. (2009), Multicentennial megadrought in northern Europe coincided with a global El Nino-Southern Oscillation drought pattern during the Medieval Climate Anomaly, *Geology*, *37*(2), 175-178.

Hopkins, F. M., et al. (2012), Warming accelerates decomposition of decades-old carbon in forest soils, *Proceedings of the National Academy of Sciences*, *109*(26), 1753-1761.

Joos, F., and M. Bruno (1998), Long-term variability of the terrestrial and oceanic carbon sinks and the budgets of the carbon isotopes C-13 and C-14, *Global Biogeochemical Cycles*, *12*(2), 277-295.

Kennett, D. J., et al. (2012), Development and Disintegration of Maya Political Systems in Response to Climate Change, *Science*, *338*(6108), 788-791.

MacDonald, G. M., et al. (2006), Rapid early development of circumarctic peatlands and atmospheric CH4 and CO2 variations, *Science*, *314*(5797), 285-288.

Mann, M. E., et al. (2008), Proxy-based reconstructions of hemispheric and global surface temperature variations over the past two millennia, *Proc. Natl. Acad. Sci. U. S. A.*, *105*(36), 13252-13257.

Moberg, A., et al. (2005), Highly variable Northern Hemisphere temperatures reconstructed from low- and high-resolution proxy data, *Nature*, *439*(7079), 1014-1014.

Raich, J. W., and W. H. Schlesinger (1992), The global carbon-dioxide flux in soil respiration and its relationship to vegetations and climate, *Tellus Series B-Chemical and Physical Meteorology*, *44*(2), 81-99.

Rubino, M., et al. (2013), A revised 1000 year atmospheric $\delta^{13}C$-CO_2 record from Law Dome

and South Pole, Antarctica, *Journal of Geophysical Research: Atmospheres*, *118*(15), 8482-8499.

Ruddiman, W. F. (2003), The anthropogenic greenhouse era began thousands of years ago, *Clim. Change*, *61*(3), 261-293.

Russell, J. M., and T. C. Johnson (2007), Little Ice Age drought in equatorial Africa: Intertropical Convergence Zone migrations and El Nino-Southern Oscillation variability, *Geology*, *35*(1), 21-24.

Schmitt, J., et al. (2012), Carbon Isotope Constraints on the Deglacial CO_2 Rise from Ice Cores, *Science*, *336*(6082), 711-714.

Schwalm, C. R., et al. (2012), Reduction in carbon uptake during turn of the century drought in western North America, *Nature Geoscience*, *5*(8), 551-556.

Shanahan, T. M., et al. (2009), Atlantic Forcing of Persistent Drought in West Africa, *Science*, *324*(5925), 377-380.

Sinha, A., et al. (2011), A global context for megadroughts in monsoon Asia during the past millennium, *Quaternary Science Reviews*, *30*(1-2), 47-62.

Stocker, B. D., et al. (2011), Sensitivity of Holocene atmospheric CO_2 and the modern carbon budget to early human land use: analyses with a process-based model, *Biogeosciences*, *8*(1), 69-88.

Trumbore, S. E., and C. I. Czimczik (2008), An Uncertain Future for Soil Carbon, *Science*, *321*(5895), 1455-1456.

van der Molen, M. K., et al. (2011), Drought and ecosystem carbon cycling, *Agric. For.*

Meteorol., *151*(7), 765-773.

Yu, Z. C. (2012), Northern peatland carbon stocks and dynamics: a review, *Biogeosciences*, *9*(10), 4071-4085.

5 Stable isotopes of CO_2 support iron fertilization and Antarctic sea ice as the dominant control on the carbon cycle during the deglaciation

Thomas K. Bauska[1], Daniel Baggenstos[2], Edward J. Brook[1], Jeffrey P. Severinghaus[2], Alan C. Mix[1], Vasillii V. Petrenko[3], Hinrich Schaefer[4] and James E. Lee[1].

[1]College of Earth, Ocean, and Atmospheric Sciences, Oregon State University, Corvallis, OR 97331
[2]Scripps Institution of Oceanography, University of California San Diego, La Jolla, CA 92093
[3]Department of Earth and Environmental Sciences, University of Rochester, Rochester, NY 14627
[4]National Institute of Water and Atmospheric Research Ltd, Wellington, New Zealand.

5.1 Abstract

We present a record of the stable isotopic composition of carbon in CO_2 ($\delta^{13}C$ of CO_2) from a horizontal ice core on the Taylor Glacier, Antarctica that spans the last deglaciation. This unique ice archive provides very large samples and allows measurement of $\delta^{13}C$ of CO_2 at very high precision (~0.02 per mil) and resolution (200-50 years). The data strongly confirm earlier reconstructions but illuminate previously unobserved changes in the carbon cycle during the abrupt climate transitions. We use a box model to construct a framework of the evolution of the carbon cycle during deglaciation. During the LGM, the lower CO_2 concentration

accompanied by only a minor shift in $\delta^{13}C$ of CO_2 relative to the early Holocene is consistent with a more efficient biological pump drivng by iron fertilzation in the Southern ocean, limited air-sea gas exchange around Antarctica from extended sea ice, and colder ocean temperatures. The temporal evolution of these factors, as informed by timing of proxy data, reconciles the non-linear relationship between CO_2 and $\delta^{13}C$ of CO_2 from the LGM to the pre-Industrial. However, we observe some very fast changes in $\delta^{13}C$ of CO_2 that suggest a rapid emission of ^{13}C-depleted carbon to atmosphere on the centennial timescale that is not captured in current models.

5.2 Introduction

The covariation of atmospheric carbon dioxide (CO_2), temperature and ice volume during glacial-interglacial cycles is one of the fundamental characteristics of late-Pleistocene climate, yet a complete understanding of the mechanisms that drive CO_2 remains elusive. The stable isotopic composition of carbon in atmospheric CO_2 is sensitive to many key carbon cycle processes because fractionation during photosynthesis and air-sea gas exchange (which is temperature dependent), differentiates the isotopic composition of some of the sources and sinks of carbon to the atmosphere.

Broadly, the $\delta^{13}C$ of CO_2 is influenced by the temperature and air-sea gas equilibrium state of the surface ocean and the amount of organic carbon bound up on the land and in the deep ocean. Colder ocean temperatures allow more CO_2 to dissolve in seawater and increase fractionation during air-sea gas exchange, leading to an atmosphere with lower CO_2 and more depleted $\delta^{13}C$ of CO_2. Increased storage of photosynthetically fixed, depleted carbon on lands lowers atmospheric CO_2 and enriches $\delta^{13}C$ of CO_2. More entrainment of organic carbon in the deep ocean leads to a stronger surface-to-deep gradient in total carbon and $\delta^{13}C$, also lowering CO_2 and enriching the atmosphere. The $\delta^{13}C$ of CO_2 is thus sensitive, in not necessarily unique

ways, to many different changes in the carbon cycle. Though not a panacea, $\delta^{13}C$ of CO_2 offers unique information about the globally integrated state of the carbon cycle.

While improvements in paleorecords of carbon cycle processes and advancements in biogeochemical modeling have winnowed the range of possible glacial-interglacial CO_2 mechanisms, direct hypothesis testing has been limited, primarily by the complexity of the carbon cycle, but also by the paucity of high-precision $\delta^{13}C$ of CO_2 measurements. The technical difficulties in the extraction of large quantities of CO_2 from ice core air without significant contamination or fractionation and the sample size limitations imposed by ice core archives have made high-precision, high-resolution, measurements challenging.

A complete understanding of the fundamental glacial-interglacial carbon cycle processes ultimately requires a comprehensive approach that integrates a broad range of proxy data and state-of-the-art biogeochemical modeling. As a step forward, we first present new data that significantly increase the carbon isotope constraint on carbon cycle budget of last deglaciation. We then construct a framework of the evolution of the carbon cycle during the deglaciation using a simplified modeling scheme that highlights both the complexities and possibilities presented in the interpretation of $\delta^{13}C$ of CO_2.

5.3 Results

5.3.1 Taylor Glacier Blue Ice Samples

The gas records were constructed from an ablating section of ice on the Taylor Glacier in McMurdo Dry Valleys of Antarctica (77.75 S,161.75 E). A complete deglacial stratigraphic section crops out on the surface of the glacier with isochrones extending for hundreds of meters, offering large amounts of ice for sampling. The age of the section was initially identified by numerous CH_4 measurements in the field,

followed by more complete lab-based measurements on the deglacial section presented here. The resolution of the transect varies from 1 meter to 10 meter spacing, with higher resolution near the periods of abrupt CH_4 transitions (see Appendix B).

The age model was constructed by CH_4 synchronization to the WAIS Divide Ice Core (WAIS Divide Community Members, 2013; Marcott et al., in prep) and confirmed by comparison of CO_2, N_2O and $\delta^{18}O$ of O_2 (Baggenstos et al., in prep) to other well-dated ice cores. The record spans an interval from the Last Glacial Maximum (LGM) to the Preboreal (PB) with excellent coverage during Heinrich stadial 1 (HS1, ~18-15 ka), the Bølling-Allerød (BA) and the Younger Dryas (YD). The age resolution varies between about 200 to 50 years for most of the deglacial section. The age uncertainty relative to other gas time-scales is estimated to be very low for most the record (±50 years), with the exception of the LGM and the early part of deglacial CO_2 rise, where CH_4 and $\delta^{18}O$ of O_2 tie-points are limited (±500 years).

Occluded air from large ice samples (400-500 grams) was extracted using an ice grater dry extraction technique (Chatper 3). $\delta^{13}C$ of CO_2 was determined by cryogenic separation of CO_2 from air followed by measurement with a micro-volume equipped, dual-inlet isotope ratio mass spectrometer (MAT 253). The CO_2 was measured on an aliquot of the sample air by separation with gas chromatography and quantification with a flame ionization detector. The one-sigma pooled standard deviation of replicate analyses was 0.022‰ and 1.3 ppm for $\delta^{13}C$ of CO_2 and CO_2, respectively.

5.3.2 Data Description

The LGM carbon cycle is characterized by relatively constant CO_2 concentration around 195 ppm but a trend in $\delta^{13}C$ of CO_2 from a maximum of -6.35‰ around 22.5 ka to nearly -6.50‰ around 20-18 ka prior to deglaciation (Figure 5.1). Around 17.8 ka, CO_2 begins to increase at about 2 ppm per century, reaching 225 ppm around 16.3

ka. The $\delta^{13}C$ of CO_2 is somewhat ambiguous as to the nature of the initial 10 ppm CO_2 rise (17.8-17.4 ka), but on average there is little change. The subsequent 20 ppm rise (17.4-16.3 ka) is accompanied by a rapid 0.35‰ depletion. A decrease in CO_2 growth rate to about 1 ppm per century around 16.3 ka is accompanied by a sharp enrichment of $\delta^{13}C$ of CO_2 of at most 0.15‰. At the onset of the BA, marked by a rapid rise in CH_4, the CO_2 growth rate accelerates to 4-5 ppm per century and $\delta^{13}C$ of CO_2 becomes more enriched by about 0.1‰. After CO_2 growth stagnates around 244 ppm in the BA, $\delta^{13}C$ of CO_2 continues to rise by about another 0.1‰. At the BA-YD transition, the CO_2 growth resumes at about 2 ppm per century and $\delta^{13}C$ of CO_2 rapidly becomes more depleted by ~0.15‰. During the YD, $\delta^{13}C$ of CO_2 returns to near BA values after CO_2 has increased by about 15 ppm rise (by 12.0 ka). As CH_4 rises at the YD-PB boundary, CO_2 growth again returns to 4-5 ppm per century, and $\delta^{13}C$ of CO_2 records a brief 0.075‰ enrichment in the form of an excursion.

Our record of $\delta^{13}C$ of CO_2 is in excellent agreement within stated 1-sigma uncertainty in the spline fit reconstruction of *Schmitt et al., 2012*, but the higher-precision and resolution (in most intervals) reveals new modes of variability on the sub-millennial timescale. Additionally, the record provides a robust signal of subtle changes in $\delta^{13}C$ of CO_2 relative to rapid variations in CH_4 (and by extension abrupt climate change). The CO_2 record is systematically about 5-6 ppm higher than the data reported for the Dome C ice core, but in good agreement with results obtained at the OSU laboratory for the WAIS Divide Ice Core (*Shaun Marcott, personal communication*).

To our knowledge, this is the first detailed CO_2 record extracted from a blue ice region. The high-precision and measurement of CO_2 and $\delta^{13}C$ of CO_2 on the same sample adds significantly to the interpretive power of the records, especially for subtle but rapid inflection points in the CO_2 record.

5.4 Interpretation

A standard approach in paleoclimatolgy is to compare time-series in order to construct a statistical model or test a hypothesis in a qualitative manner. The non-linearities replete in the carbon cycle make direct comparison of $\delta^{13}C$ of CO_2 to proxy records challenging. An alternate approach is to build a hypothesis into a quantitative model of the carbon cycle that can control for a various factors and provide quantitative, testable predictions. We use a box model comprised of an atmosphere, terrestrial biosphere and 11-box ocean that traces phosphate, oxygen, alkalinity and the isotopes of carbon (see Appendix B and Figure B.1 for a description and representation of the model).

The approach we use involves two related constraints. We attempt to determine a suite of processes that can both lower CO_2 levels to glacial levels and explain the timing and structure of deglacial rise. This approach relies on the assumption that the same carbon cycle processes that drove glacial inception are mostly responsible for the deglaciation. Similar approaches have been used before (Kohler et al., 2005; Lourantou et al., 2010; Bouttes et al., 2011; Bouttes et al., 2012) but using data sets that could not resolve the precise timing of changes in the deglaciation.

This approach is not without uncertainty. The timing of changes in some proxies is well-constrained, such as the change in ssNa flux to Antarctica and $\delta^{18}O$ of precipitation over Greenland, but highly uncertain in their translation to physical processes like sea-ice extent and temperature of deepwater formation, respectively. Additional uncertainty arises in translating these changes into CO_2 variability with a carbon cycle model that has many tunable parameters, particularly a box model that will not accurately capture many transient features such as abrupt changes in ocean circulation. Finally, our limited understanding of some fundamental processes that could affect $\delta^{13}C$ of CO_2, such as changes in the photosynthetic fractionation in marine biota, further impede a complete interpretation of the $\delta^{13}C$ of CO_2 record (see *Broecker and McGee, 2013* for a more complete treatment of uncertainty for

reconciling glacial CO_2 and $\delta^{13}C$ of CO_2). None-the-less, we believe the alternate approach relying on direct comparison of proxies to $\delta^{13}C$ of CO_2 is fraught with too many non-linear and time-dependent parameters to form a robust empirical model. The results we present also highlight that caution should be exercised when comparing any single proxy record to $\delta^{13}C$ of CO_2.

The analysis is structured as follows: first we describe processes and their effect on the carbon cycle that have reasonable constraints on both their magnitude and timing, such as SST, land carbon, and reef building; then the processes that only have constraints on their timing during the deglaciation are discussed with a focus on iron fertilization, sea ice, and ocean circulation. For each process, we first describe the impact on the LGM budget (Figure 5.2) and then describe the evolution from the LGM to late Holocene (Figures 5.3 and 5.4).

5.4.1 Ocean Temperature

During the LGM, CO_2 would be more soluble in the colder ocean, lowering CO_2 in the atmosphere. Because the deep ocean is primarily sourced from the near-freezing high-latitude waters and a significant amount of upwelling occurs in the low-latitudes, the exact magnitude of this effect depends largely on the temperature change near the poles and the degree to which the high and low latitude waters are equilibrated with the atmosphere (Broecker et al, 1999).

The LGM to pre-Industrial temperature difference of the surface ocean is partially constrained by latitudinal temperature stacks (Shakun et al, 2012; Marcott et al, 2013), weighted for the area they represent. During the LGM, low-latitude surface boxes and the Subantarctic are 2.8°C and 4.5°C colder, respectively. North Atlantic and Southern Ocean water are cooled by 4.5 and 3.0°C, respectively, to reach a minimum during the LGM near the freezing point of seawater. The subsequent deep ocean temperature change would be within the uncertainty but near the upper-bound

of porewater based estimates (Adkins, McIntyre, and Schrag, 2002). The global surface ocean glacial-interglacial temperature change prescribed in the box model is about 3.0°C, consistent with the *Shakun et al 2012* and within error, but probably at the upper-end of the more spatial-resolved reconstructions of MARGO (-1.9±1.8°C) (MARGO Project Members, 2009) and CLIMAP (-2.3°C) (CLIMAP Project Members, 1976).

Because atmospheric CO_2 is tied mostly to the temperature of the deep ocean while $\delta^{13}C$ of CO_2 is controlled primarily by air-sea gas exchange at the surface, atmospheric CO_2 is dominated by the temperature of the polar oceans, and the $\delta^{13}C$ of CO_2 follows mean global surface temperature. The colder ocean during LGM leads to a drawdown of about 40 ppm, at the higher end of estimates, with an enrichment in $\delta^{13}C$ of CO_2 of 0.25‰ (Figure 5.2).

The LGM to pre-Industrial temperature history is mostly driven by the latitudinal stacks. In the case of the North Atlantic and Antarctic Ocean, the glacial-interglacial temperature differences are scaled to proximal ice core records NGRIP *(*NGRIP Community Members, 2004) and a composite of Antarctic records (Pedro et al, 2011), respectively (Figure 5.3). During the deglaciation, CO_2 rises slowly associated with the gradual warming of the deep ocean, though the sharp warming of the North Atlantic at the onset of BA and the PB may account for some the rapid CO_2 growth rate (Figure 5.4). This is supported by the $\delta^{13}C$ of CO_2 which shows a small enrichment at both boundaries, possibly indicating that ocean temperature drove CO_2 change in the stadial-to-interstadial transitions.

5.4.2 Sea Level and Salinity

With sea level 120-135 meters lower than present during the LGM (*Clark and Mix, 2002*), increased salinity would decrease the solubility of CO_2 in the ocean and drive about a 7 ppm increase in atmospheric CO_2. During the deglaciation, the sea level

history based on benthic $\delta^{18}O$ (Waelbroeck et al, 2002) used in the model accounts for a small decrease in atmospheric CO_2 during the later half of the deglaciation and early Holocene.

5.4.3 Land Carbon

The amount of carbon stored on land was likely lower during the LGM. Estimates of the loss vary, but generally range between 0-700 gigatons of carbon (GtC) (see *Ciais et al, 2012* for review). We reconcile the LGM carbon budget using an estimate that places 500 GtC of carbon in the ocean during the LGM (Figure 5.2). In the model, the land carbon is released to the ocean over a period for 4000 years and then allowed to approach a new steady-state for an additional 15,000 years. This change by itself would cause about a 10 ppm increase in CO_2 with a isotopic shift in the atmosphere and all ocean basins of about -0.3 per mil.

During the deglacation, carbonate ion and deep ocean $\delta^{13}C$ reconstructions support regrowth of the biosphere that lags the initial CO_2 rise with little uptake by 14 ka followed by 400 GtC of uptake between 14-10 ka (Yu et al, 2010). We choose to drive land carbon re-growth as a function of rising CO_2 concentration (CO_2 fertilization 1.35 GtC/CO_2 ppm) (Friedlingstein et al, 2006) as well as the loss of land ice and general climate amelioration into the Holocene (Kaplan et al, 2002). From 18-10 ka, about 200 GtC had returned to land, with most of the remaining 300 GtC of regrowth occurring between 10-7 ka. The detailed timing of this later stage of uptake is not well-constrained by an independent data set. In this case, the trend of decreasing CO_2 and enriching $\delta^{13}C$ of CO_2 in the early Holocene is probably a better constraint on the exact timing of the land carbon uptake, and we tune the timing of the land carbon changes to fit the data.

5.4.4 Reef Building and $CaCO_3$ Compensation

$CaCO_3$ reef building likely increased as the continental shelves were flooded by sea level rise during the deglaciation. The removal of alkalinity in the surface ocean by formation of $CaCO_3$ would increase CO_2 in the atmosphere. But with negligible carbon isotopic fractionation during $CaCO_3$ precipitation, $CaCO_3$ formation or dissolution would have only a minor effect on $\delta^{13}C$ of CO_2. To drive the CO_2 input from reef building in the model, we use data based estimates of shallow water $CaCO_3$ production (Vecsei and Berger, 2004). With the bulk of reef building lagging sea level rise, the CO_2 source to the atmosphere is mostly important in the later part of the deglaciation, particularly the early Holocene.

The transfer of carbon from the ocean to the atmosphere and terrestrial biosphere during the deglaciation would lead to an excess carbonate ion concentration in the deep ocean, temporarily deepening the saturation horizon of $CaCO_3$ and increasing preservation. The increased preservation would slowly remove alkalinity from the ocean, increasing atmospheric CO_2 (with small changes in $\delta^{13}C$ of CO_2), and eventually bring the carbonate ion concentration back to equilibrium. Using a response function for deep-sea sediment carbon fluxes (Archer, Kheshgi, Maier-Reimer, 1997; Joos et al., 2004), we find excellent agreement with the gradual CO_2 rise in the Holocene that is associated with only minor changes in $\delta^{13}C$ of CO_2. The combination of $CaCO_3$ compensation and reef building reconciles the Holocene carbon cycle budget without any significant input from anthropogenic sources (Figure 5.3).

5.4.5 Summary of Constrained Processes

The effects from salinity, temperature and land carbon during the LGM lead to an atmosphere with slightly lower CO_2 (~250 ppm) and a significantly depleted $\delta^{13}C$ of CO_2 (~-6.9) relative to the pre-Industrial (Figure 5.2). This suggests that additional mechanisms required to drawdown CO_2 should enrich the atmosphere, by about 0.5‰. During the deglaciation, the timing of this combination of changes in salinity, temperature and land carbon would lead to a modest increase in CO_2 and a large

enrichment in $\delta^{13}C$ of CO_2. Assuming accurate simulation of these factors, the broad isotopic minimum associated with the atmospheric CO_2 rise requires that missing mechanisms must largely precede the changes in salinity, temperature and land carbon.

5.4.6 Uncertainty of Constrained Processes

To estimate the uncertainty and possible biases in this approach, a Monte Carlo analysis was performed by varying the land carbon loss by 200 GtC (1-sigma standard deviation), with steady-state relaxation times between 5,000 and 15,000 years, and the prescribed global surface ocean temperature glacial-interglacial difference between 2-3°C. Assuming that the land carbon and temperature errors are uncorrelated, the uncertainty in the atmospheric CO_2 and $\delta^{13}C$ of CO_2 is on the order of ±7 ppm and ±0.13‰, respectively (Figure 5.2). Uncertainty in model parameters would significantly enhance this range, possibly with a non-random distribution. Most notably, changes in the routes and rates of deepwater formation can significantly alter the amount of CO_2 that can be draw down by increased solubility. This cursory uncertainty analysis demonstrates that a mechanistic partitioning from atmospheric CO_2 and $\delta^{13}C$ of CO_2 alone remains significantly limited. Though we employ additional constraints when outlining the possible evolution during the deglaciation, most notably oceanic $\delta^{13}C$ and radiocarbon, we stress that the accuracy of these results are affected by these large, underlying uncertainties.

5.4.7 Efficiency of the Southern Ocean Biological Pump

A change in the efficiency of the biological pump, possibly due to a variable flux of dust to the iron limited surface of the Southern Ocean, is a leading hypothesis for glacial-interglacial CO_2 changes (Martin, 1990). The timing of the flux of dust and trace elements to Antarctica is fairly well constrained by high-resolution ice core records (Figure 5.3), but the corresponding flux to the Southern Ocean and the possible effects on nutrient utilization remain speculative (Fischer et al, 2007).

None-the-less, a key constraint on the magnitude of the effect may come from the tight coupling between dust and CO_2 from about 18-16 ka, with the initial 20-30 ppm rise in atmosphere CO_2 and depletion in $\delta^{13}C$ of CO_2 closely associated with a significant decrease in the dust and iron flux.

To simulate the possible effects of iron fertilization in the Southern Ocean during the LGM we decrease the restoring PO_4 level (preformed nutrient content) in the Subantarctic surface box to the low-latitude nutrient limitation levels (0.2 mmol m^{-3}). In the LGM, this accounts for an atmospheric CO_2 decrease of about 25 ppm and $\delta^{13}C$ of CO_2 enrichment of 0.2‰ relative to the pre-Industrial (Figure 5.2), with the drawdown carbon largely stored in the deep Southern Ocean and Pacific basins. Further CO_2 drawdown by even greater efficiency of the biological pump is possible, but achieving glacial levels CO_2 from this effect alone probably leads to deep ocean anoxia.

During the deglaciation, the glacial-interglacial range in restoring PO_4 in the Subantarctic box is scaled to the nssCa flux from the EDML ice core on a timescale consistent with the Greenland ice core chronology (Lemieux-Dudon et al., 2010). The efficiency of the biological pump in the Southern Ocean rapidly decreases to near interglacial levels during the first half of HS1 (18-16ka) (Figure 5.3). The subsequent release of carbon from the deep ocean dominates the initial CO_2 rise and $\delta^{13}C$ of CO_2 depletion (Figure 5.4).

Schmitt et al., 2012 called upon Southern Ocean upwelling to drive the initial CO_2 rise and depletion. We offer iron fertilization as an alternate or additional hypothesis. However, $\delta^{13}C$ of CO_2 alone probably cannot discriminate between iron fertilization and Southern Ocean stratification. The box model binds up depleted carbon in the deep ocean by increasing the efficiency of the Southern Ocean biological pump, but stratification would probably have a very similar effect on the carbon isotope budget (Bouttes et al., 2012). While ocean circulation changes are also modeled during the

deglaciation (see below), the restoring PO_4 scheme used in the box model may impose an unrealistic limitation on the variability explained by upwelling. For example, Southern Ocean upwelling with fixed carbon export would release much more depleted carbon to the atmosphere than would be expected if biological processes are allowed to respond (Lee et al., 2011).

5.4.8 Sea Ice

Limiting air-sea gas exchange in the Southern Ocean has been suggested as a possible mechanism for lowering CO_2 (Stephens and Keeling, 2000). It is an attractive option because it allows entrainment of CO_2 into deepwater without a significant impact on deep ocean O_2 levels (gas-equilibration of O_2 proceeds about 20 times faster than CO_2 because O_2, unlike CO_2, is only soluble in, and not reactive with seawater). We drive the deglacial evolution by roughly scaling the area of sea ice in the Antarctic surface ocean box to a record of ssNa flux, a possible proxy for sea ice extent (Fischer et al., 2007) (Figure 5.3). The exact scaling is not conclusive, but probably a log-like dependence is reasonable. We find a consistent history if sea ice lowers CO_2 by about 25 ppm in the LGM (Figure 5.2) and subsequently accounts for roughly 10 ppm of HS1 rise with the remaining 15 ppm occurring during the YD (Figure 5.4).

Stephens and Keeling demonstrated that greater lowering of CO_2 by sea-ice is possible, but this has been questioned, as it requires almost complete isolation of the deep ocean from the atmosphere (Archer et al., 2003). Though sea ice nearly covers the entire Antarctic Ocean box in our model, some mixing occurs across the Antarctic Convergence, allowing the deep Southern Ocean to communicate with sea-ice free surface, possibly abating this effect and setting a more realistic upper limit to the amount of CO_2 sequestered by sea-ice. More importantly, we argue that the sea-ice driven $\delta^{13}C$ of CO_2-to-CO_2 relationship is so steep, a larger fraction of glacial CO_2 explained by sea ice is difficult to reconcile with the atmospheric record, unless the

temperature effect is underestimated. For example, *Stephens and Keeling*, using the lower resolution $\delta^{13}C$ of CO_2 available at the time, reconcile the LGM atmospheric budget using a 500 GtC loss of land carbon and a large and possibly unrealistic 5°C decrease in surface ocean temperature (albeit less in the near-freezing high-latitude ocean boxes).

With Southern Ocean sea-ice dominating the CO_2 rise during the YD, the $\delta^{13}C$ of CO_2 would shift toward values that are probably too depleted by the onset of the PB. We speculate that some of the millennial-scale CO_2 features could be driven by an advancement of North Atlantic sea-ice at the expense of Antarctica Sea during the stadials, particularly in the YD, when there is little change in $\delta^{13}C$ of CO_2 between the start and end of the stadial. By simultaneously closing one of the primary sinks for CO_2 in the North Atlantic while releasing CO_2 from the Southern Ocean in the model, this "sea-ice see-saw" drove CO_2 levels in the atmosphere slightly higher, while dampening the effect of the depleted isotopic signature from Southern Ocean sea-ice. Alternatively, the effect of rising SST during the YD could be underestimated and should account for a larger portion of the CO_2 rise and a stronger enrichment that offsets the sea ice effect. Alternatively, an increase in the volcanic input, which has little effect on $\delta^{13}C$ of CO_2, may have played a role in the later part of the deglaciation (Huybers and Langmuir, 2009; Roth and Joos, 2012)

5.4.9 Ocean Circulation

Changes in ocean circulation are likely important for CO_2 on glacial-interglacial and millennial timescales, predominately by influencing the preformed nutrient content of the ocean, and thus the efficiency of the biological pump. During the deglaciation, abrupt reorganizations of ocean circulation probably drove millennial-scale climate variations and their influence on the carbon cycle cannot be neglected.

We reconcile some of the major observations of the LGM ocean by switching the flow of North Atlantic Deepwater (NADW) in the deep ocean basins. In the modern ocean, most of the NADW that reaches Antarctica is transformed by Circumpolar Deepwater (CDW) to denser water and routed into the Pacific Basin or returned in to the deep Atlantic. Under LGM conditions, when NADW is likely shoaled, but still vigorous (Curry and Oppo, 2005; McManus et al., 2004), we allow more northern sourced waters to upwell in the Southern Ocean in the Subantarctic box (~north of the Antarctic convergence) where they are routed to the intermediate, rather than the deep waters of the ocean.

Under these LGM conditions, the zone of ^{13}C depleted carbon, high nutrient/carbon and low oxygen waters migrates from the intermediate ocean to the deep ocean. The deep ocean basins become more poorly ventilated with relatively more waters sourced from the south and influenced by Antarctic sea ice formation. With NADW decreased from 18 to 14 Sv and Antarctic Bottom Water (AABW) to the Atlantic ramped up from 6 Sv to 16 Sv, the deep Atlantic shifts from being about a 3:1 to a 1:1 mix of northern and southern sourced waters, respectively (Figure B.1 and Table B.1).

Though this effect alone has only a minor influence on LGM CO_2 (~ 4 ppm lower) and $\delta^{13}C$ of CO_2 (~0.12‰ depletion), it does reconcile some of the major observations of the LGM ocean. The combination of iron fertilization, sea ice, and circulation changes leads to the deep ocean basins that are more ^{13}C depleted in carbon with the Pacific, Atlantic and deep Southern sourced waters becoming about 0.4, 0.6, and 1.0‰ more depleted, in good agreement with well-resolved benthic records (Figure 5.6 and Table B.1). The oxygen poor conditions in the deep Indo-Pacific, at the expense the increased oxygen at intermediate depths, agrees with qualitative reconstructions (Jaccard et al., 2011). The increased radiocarbon age in the deep ocean basins is in agreement with some reconstructions of North Pacific, AABW, and NADW (Galbraith et al., 2007, Barker et al., 2010, Thornalley et al.,

2011), but the extreme aged water in lower CDW (Skinner et al., 2010) remain difficult to explain without anoxia emerging (Figure 5.6).

During the deglaciation, roughly following the Pa/Th proxy data (McManus et al., 2004) the model NADW slows to about 4 Sv during HS1, increases to near modern values in the BA, slows to 9 Sv during the YD, ramps up to 14 Sv during the PB, followed by a gradual rise to modern values in the early Holocene (Figure 5.3). Additionally, the strength of southern overturning increases in the model when northern overturning is slowed based on evidence that a shift or strengthening in the southern westerlies may have increased overturning in the stadials (Anderson et al., 2009). Modeled CO_2 is relative insensitive to these abrupt changes in ocean circulation, with increases of about 8 ppm during stadials (Figure 5.4), in agreement the sign but not necessarily the larger magnitude simulated with intermediate complexity models (Marchal, Stocker and Joos, 1998; Schmittner and Galbraith, 2008). Modeled $\delta^{13}C$ of CO_2 shows a strong depletion on the order of about 0.2‰ after the onset of stadial conditions (and a similar enrichment during NADW resumption).

The data cannot rule out that an abrupt weakening of NADW played a role in the sharp $\delta^{13}C$ of CO_2 depletions at the onset of HS1 and the YD, however, that lack of any large shift in $\delta^{13}C$ of CO_2 at the onset of the BA and the PB suggests that $\delta^{13}C$ of CO_2 is relatively insensitive to the resumption of NADW. Alternatively, a mechanism is needed that shifts ocean circulation during HS1 and the YD, such that $\delta^{13}C$ of CO_2 is strongly affected by the slowing of NADW but only weakly sensitive to the re-invigoration. This asymmetric response may be reconciled by the re-emergence of NADW ventilation of the deep Indo-Pacific, possible as westerly wind-stress shifts to the south. In the model, interglacial circulation conditions are partially re-established prior to the onset of the BA. When NADW abruptly strengthens during the BA, it ventilates the deep Indo-Pacific via CDW, leading to a major shift in the water mass properties, most notably the radiocarbon age, but with a tempered

effect on $\delta^{13}C$ of CO_2 such that atmosphere only records a small enrichment during the onset of interstadial circulation.

5.5 Rapid $\delta^{13}C$ of CO_2 Variability

Though the primary goal of the analysis is to demonstrate a possible data-consistent deglacial scenario, we also employ the modeling scheme to highlight that, even with most of the variability explained by previously hypothesized mechanisms, a few enigmatic features emerge. The sharp isotopic minimum at 16.3 ka corresponds to an inflection point in the CO_2 rise with the growth rate slowing from about 2 to 1 ppm/century (Figure 5.1). This could reflect a decrease in an isotopically depleted source or an abrupt emergence of a strong depleted sink for CO_2. A similar minimum is observed at the onset of the YD; in this case at an inflection point in CO_2 located at the resumption of growth at about 2 ppm/century.

The pattern of sharp depletion and enrichment seen at 16.3 ka and to a lesser extent in the YD presents a conundrum: do the minima represent major mode shifts in the carbon cycle or events? While we argue that the drivers behind the HS1 rise and the YD are different because iron fertilization may only be important during HS1, the minima about halfway through the stadials may be related.

If the minima are indicative of a source of depleted carbon, they may be caused by a rapid release of land carbon to the atmosphere on the order of a 50 GtC over a few hundred years, followed by regrowth (as modeled in Figure 5.4). Alternatively, an abrupt enhancement of air-sea gas exchange driven by increase in wind-stress over the Southern Ocean could also drive $\delta^{13}C$ of CO_2 to depleted values and cause some additional outgassing of CO_2. If the features are more indicative of the emergence of sink for CO_2, a mechanism may be needed that strongly moderates the release of depleted carbon to atmosphere about mid-way through the stadials. This may be related to switch in ocean circulation or a tipping point that brings high-nutrient

waters into contact with a region with a more efficient biological pump, such as the tropical ocean. This would predict that carbon export to the deep ocean lagged the sharp $\delta^{13}C$ of CO_2 depletions. Many low-latitude records show incursions of high-nutrient water or increases in export during periods of CO_2 rise (Calvo et al, 2011; Hendry et al, 2012; Meckler et al, 2013) but better age control is probably needed before conclusions can be drawn about the phasing with respect to $\delta^{13}C$ of CO_2.

5.6 Conclusions

The specific combination of factors presented is very consistent with the carbon isotope budget and the timing of proxy variability, yet not necessarily accurate, because of the many free parameters and non-linear uncertainties in the carbon cycle and the model. As a final step, we outline a possible evolution of climate and carbon cycle changes during deglaciation to demonstrate that this series of mechanisms is internally consistent. The primary assumption in this conceptual model is that the position of the westerlies and the sea-ice front moved in lock-step, driven by both rapid millennial-scale climate changes and more gradual glacial-interglacial transition. A depiction of the evolution is presented in Figure 5.5.

During the LGM, the equatorward contraction of the westerlies shifted the Southern Hemisphere westerlies off the Drake Passage and onto the continental land masses (Lamy et al, 1999). Stronger winds or drying over the continents increased the dust loading to the Southern Ocean, while decreased windstress over the Southern Ocean limited upwelling and/or air-sea gas exchange (Figure 5.5: LGM). The wind delivered iron to the Southern Ocean, increasing the efficiency of the biological pump by causing greater export of carbon to the deep Ocean basins. The area covered by sea-ice, at least in the winter (Gersonde et al., 2005), was greatly expanded, partially decoupling the Southern Ocean from the atmosphere thereby preventing the evasion of respired carbon to the atmosphere.

During the early part of HS1, the collapse of AMOC decreased heat transport to the North Atlantic. In response, large areas of Northern Hemisphere cooled and Southern Hemisphere warmed, driving sea ice retreat and ocean warming, releasing some CO_2. In particular, the nearly constant $\delta^{13}C$ of CO_2 during the first 10 ppm rise suggests a large role for rising SST (Figure 5.4). In conjunction with the inter-hemisphere temperature gradient, the ITCZ and Southern Hemisphere westerlies shifted southward (Wang et al., 2004; Cheng et al., 2009; Denton et al., 2010). The southward shift of the westerlies off the continents lead to a precipitous decline in dust delivery over the Southern Ocean, driving the bulk of the CO_2 rise from about 17.4-16.0 ka. Simultaneously, the sea ice front retreated, augmenting the deep ocean carbon evasion. The southward migration of the ITCZ lead to a drying in parts of the Northern Hemisphere possibly causing a loss of land carbon, most notably around 16.3 ka, near the minimum observed in the Hulu $\delta^{18}O$. Alternatively, or additionally, the shifting Southern Hemisphere westerlies reached a tipping point around 16.3 ka, where windstress realigned with the Southern Ocean, leading to enhanced air-sea gas exchange. During the later half of HS1, dust deposition had effectively reached interglacial levels, and the CO_2 rise was driven by retreating sea ice and warming ocean temperatures.

In response to the resumption of AMOC at the onset of the BA, the North Atlantic warmed, driving some of the rapid CO_2 rise at the transition. The westerlies shifted back towards the equator and the sea ice front expanded, but not back to glacial levels. Most importantly, the westerlies may have been prevented from returning to a full glacial state by the increased CO_2 levels (Toggweiler, Russell and Carson, 2006), and were unable to reinvigorate dust sources.

In the BA, the temperature rise and sea ice retreat in Southern Hemisphere stagnated, leading to steady CO_2, with a trend in $\delta^{13}C$ of CO_2 towards enriched values related to the regrowth of the terrestrial biosphere and the gradual filling of the deep ocean with North Atlantic sourced waters.

After the slowing of AMOC during the YD the CO_2 increase was dominated by changes in sea ice and ocean temperature, in similar fashion to the later half of HS1, though $CaCO_3$ compensation and reef building became important during this interval. The rapid cooling and drying in the Northern Hemisphere at the onset of the YD may have also triggered a second loss of land carbon, or depression of Southern Hemisphere westerlies, leading again to enhanced air-sea gas exchange.

At the onset of the PB, the resumption of AMOC lead to a temperature driven CO_2 rise. In the early part of the Holocene, the decrease in CO_2 was driven by regrowth of the biosphere. The steady rise in CO_2 during the later Holocene was related to reef building and $CaCO_3$ compensation triggered by the deglaciation.

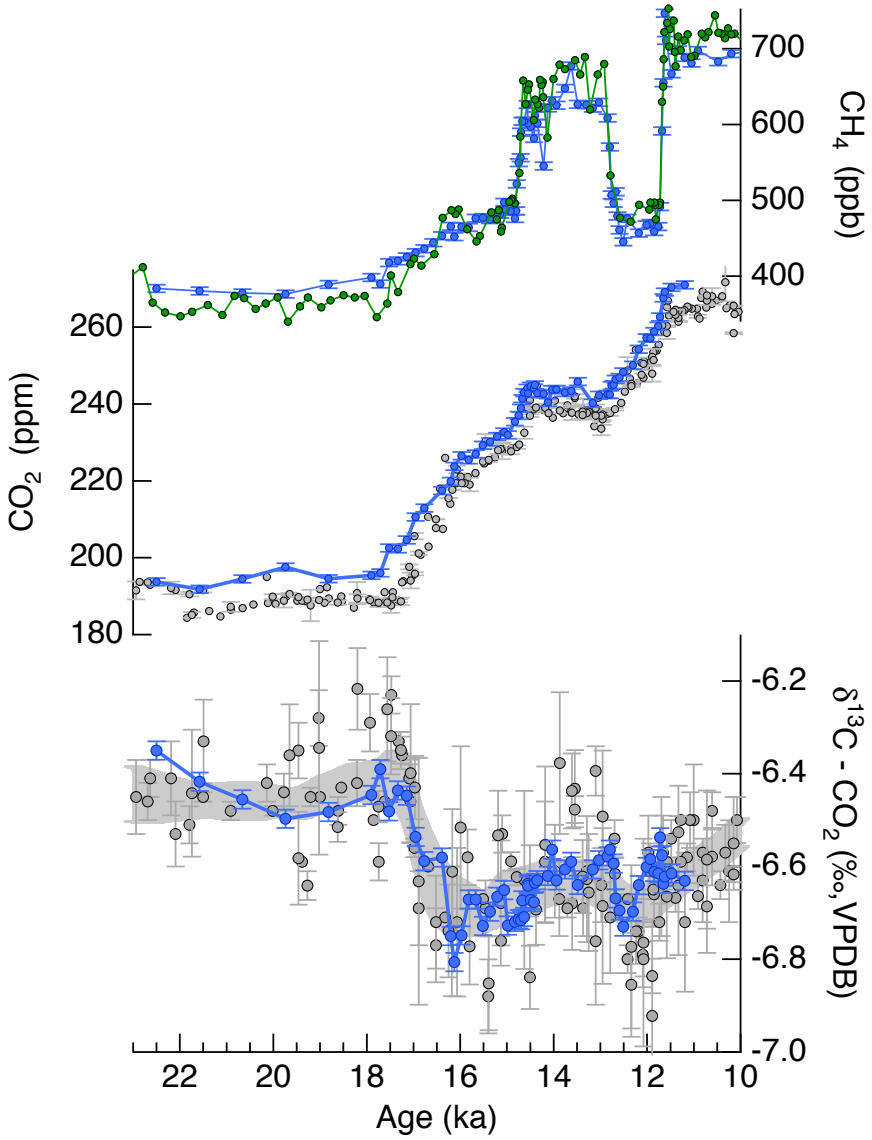

Figure 5.1 Taylor Glacier Gas Records
The CH_4, CO_2, and $\delta^{13}C$ of CO_2 records from Taylor Glacier (blue symbols) with other well-dated ice core records. The age model is constructed by wiggle matching to composite of Greenland CH_4 on the GICC05 timescale (Blunier et al., 2007). The one-sigma error bars the pooled standard deviation from replicate experiments on a subset of samples. The $\delta^{13}C$ of CO_2 strongly confirms the spline-fit reconstruction (one-sigma uncertainty in grey shading) of previously published data (grey symbols) sourced primarily from the EPICA Dome C (EDC) ice core (Schmitt et al., 2012) but provides a much more detailed constraint. Also shown is a composite of CO_2, also EDC on the same timescale (Monnin et al., 2001; Lourantou et al., 2010) and Taylor Dome (Monnin et al., 2004).

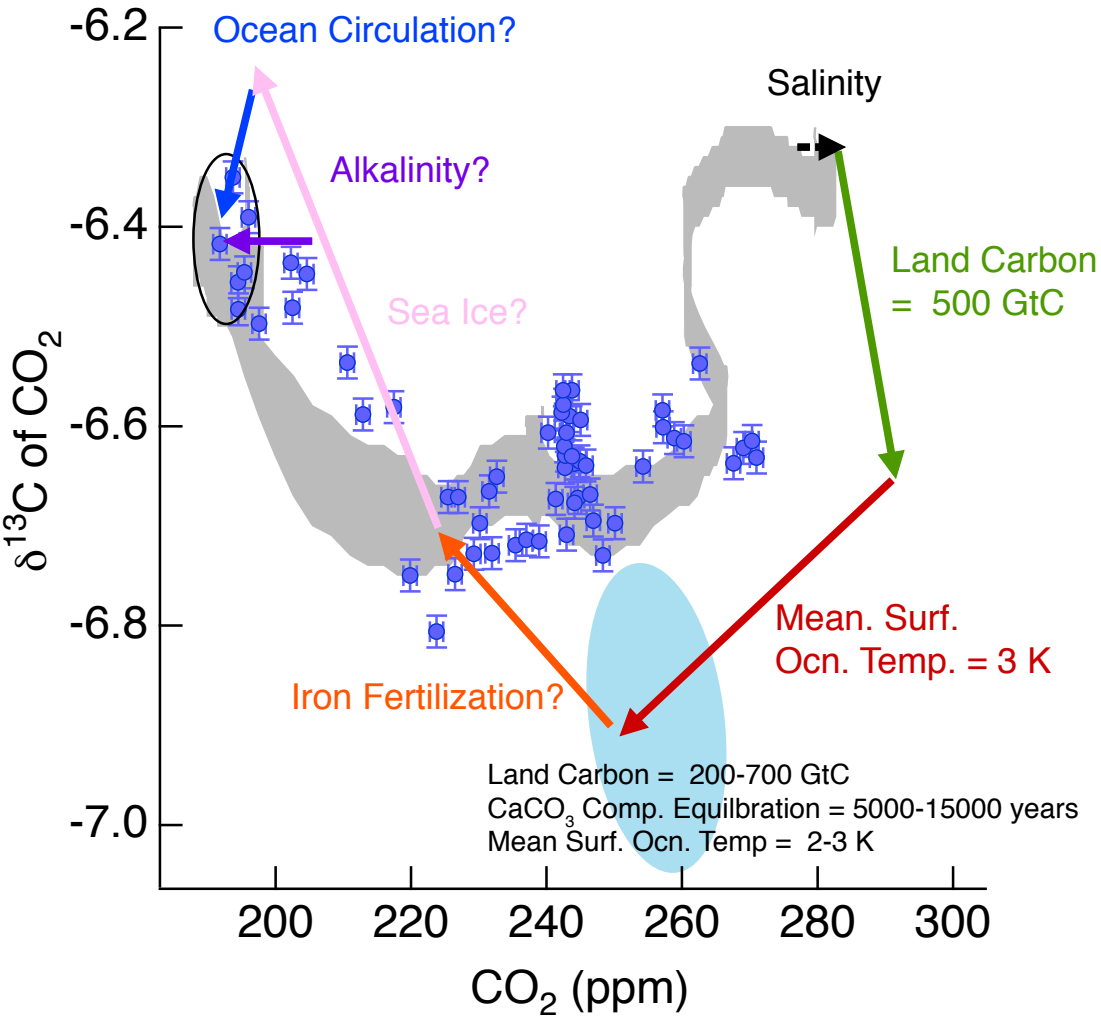

Figure 5.2 Glacier-Interglacial CO_2 and $\delta^{13}C$ of CO_2 relationship
CO_2 plotted against $\delta^{13}C$ of CO_2 with a composite of other records (grey shading, uncertainty from *Schmitt et al., 2012*) spanning a time interval from the Last Glacial Maximum (~24 ka) to the pre-Industrial (~0.5 ka). See Figure 3 for the data displayed in time-domain. The colored arrows indicate the possible data-consistent glacial-to-interglacial mechanisms for lowering CO_2. The path of the arrows is additive with the ending point of each arrow indicating the model state after about 15,000 years of spinup after a 4,000 year transition to glacial boundary conditions. The line between the endpoints thus contains no time information, but the slope of each line approximates the steady-state relationship between CO_2 and $\delta^{13}C$ of CO_2 for the various processes. The light blue ellipse indicates the approximate uncertainty introduced by uncorrelated errors in the assumed equilibration time and estimates of SST and land carbon at the LGM.

Figure 5.3 Deglacial drivers of CO_2 with modeling results
CO_2 (offset by -6 ppm for consistency with the other records), and $\delta^{13}C$ of CO_2 data and modeling results spanning the LGM to pre-Industrial with proxies for some of the dominant factors hypothesized to be important for the deglaciation. Model parameters used to drive the carbon cycle and output are indicated by solid black lines. Temperature proxies from Greenland (NGRIP Community Members, 2004), Antarctica (Pedro et al., 2011; EPICA Community Members, 2006), and stacks of globally disturbed records from the deglaciation (pink shading: Shakun et al., 2012) and the Holocene (orange shading: Marcott et al., 2013) are imposed the surface ocean boxes. The EDML ice core provides the nssCa flux (orange line), a possible indicator of continental dust (Fischer et al., 2007), which controls the preformed nutrient concentration in the Southern Ocean that dominates the early CO_2 rise. The iron flux from Talos Dome (Vallelonga et al., 2013) is also plotted to substantiate the nssCa-to-iron fertilization relantionship. Pa/Th is used to roughly modulate NADW formation (McManus et al., 2004). Also from EDML, ssNA is plotted against the model fraction of sea-ice free area around Antarctica (log scale). Other assumptions, such as the re-growth of the terrestrial biosphere and reef building in the Holocene, as well as important feedbacks such as $CaCO_3$ are described in the text.

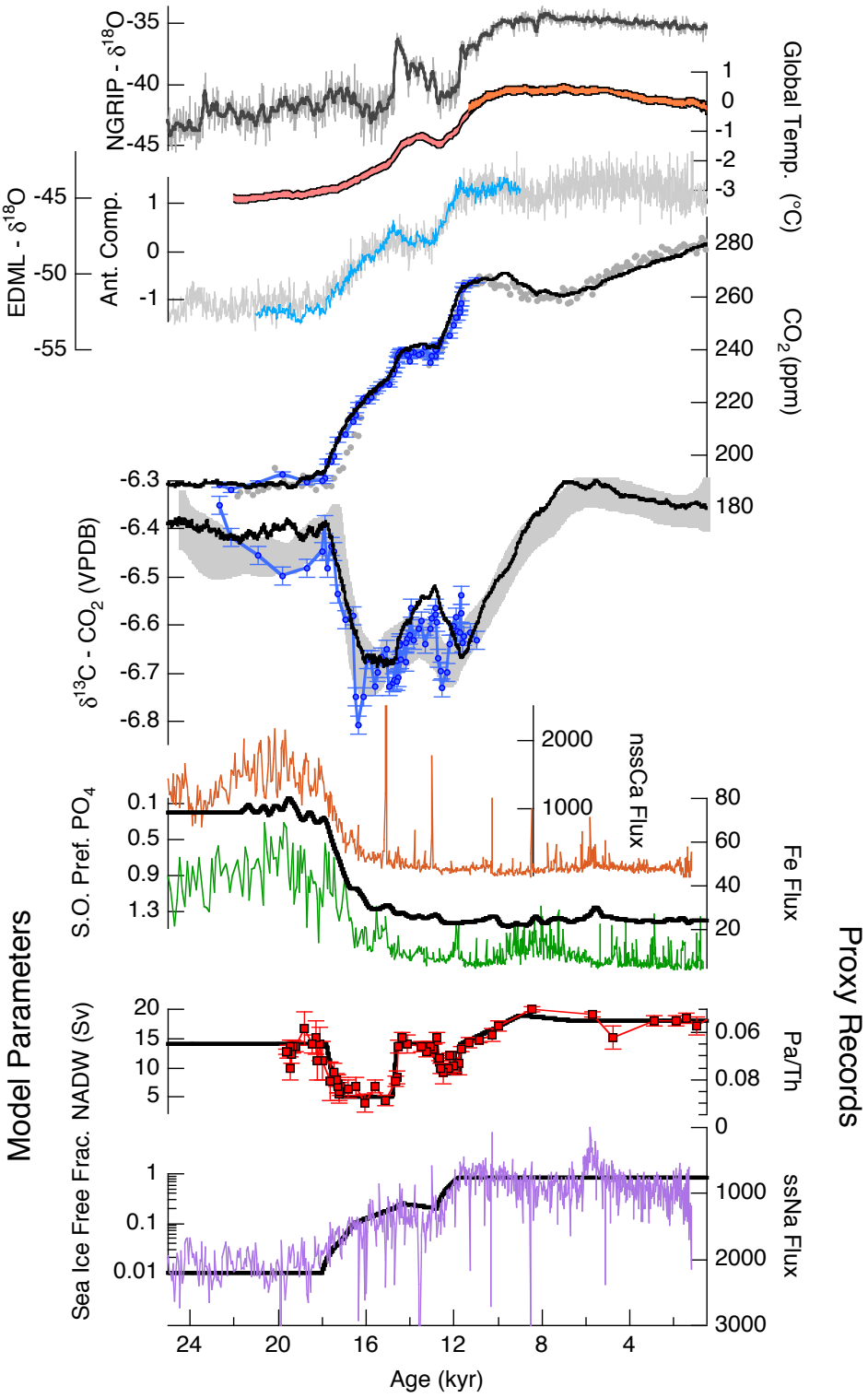

Figure 5.3 (see caption on preceding page)

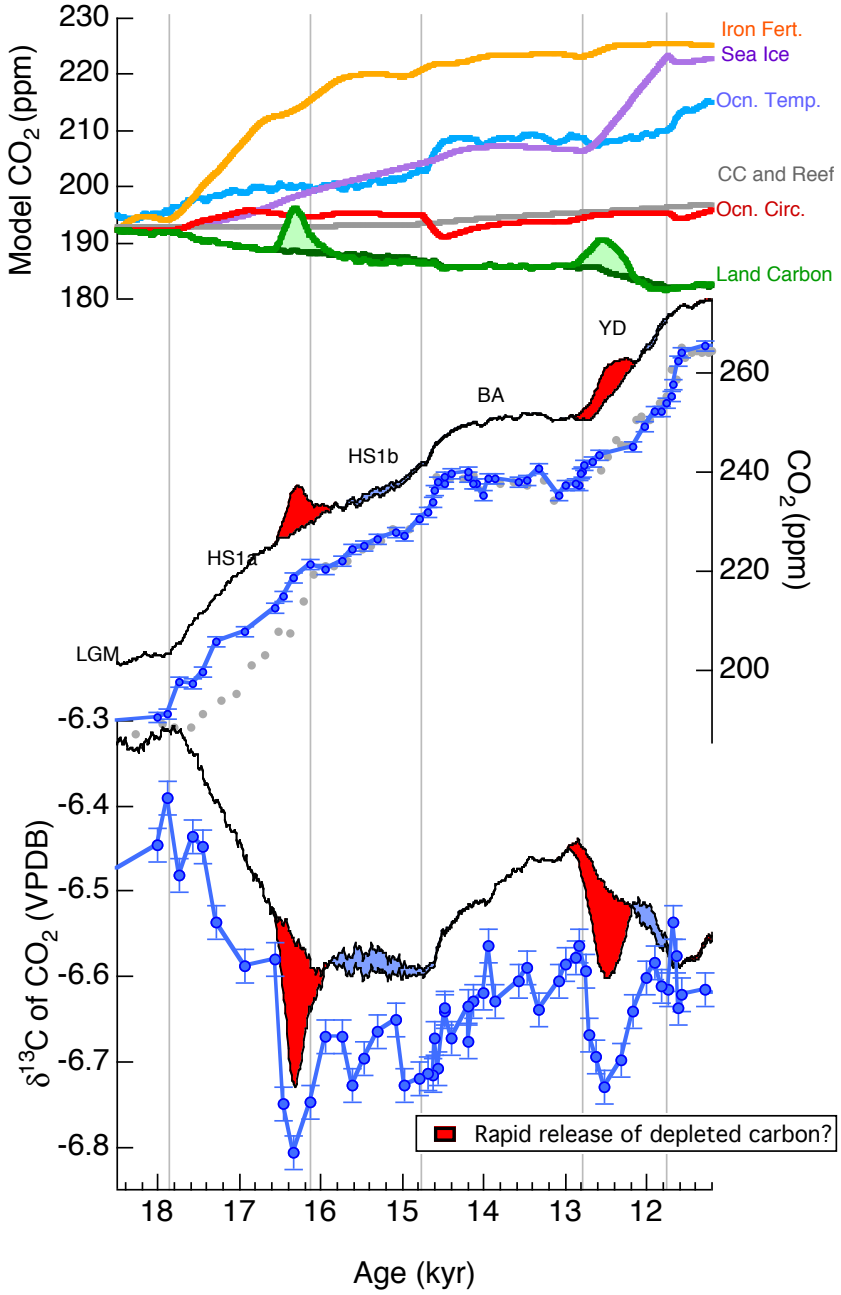

Figure 5.4 Modeled components of the CO_2 rise

A finer-scale view of the data and modeling results over the deglaciation with a delineation of the hypothesized factors driving the CO_2 rise (iron fertilization: orange; sea-ice: purple; ocean temperature: light blue; $CaCO_3$ compensation and reef building: grey; ocean circulation: red; land carbon with no rapid losses: dark green; land carbon with rapid losses at ~16.3 and 12.9 ka: light green). The contribution of an individual factor is calculated by starting at the glacial state and excluding all other factors. The thin black line indicates the modeling results with the red shading indicating the additional CO_2 and $\delta^{13}C$ of CO_2 changes from the release of land carbon to the atmosphere.

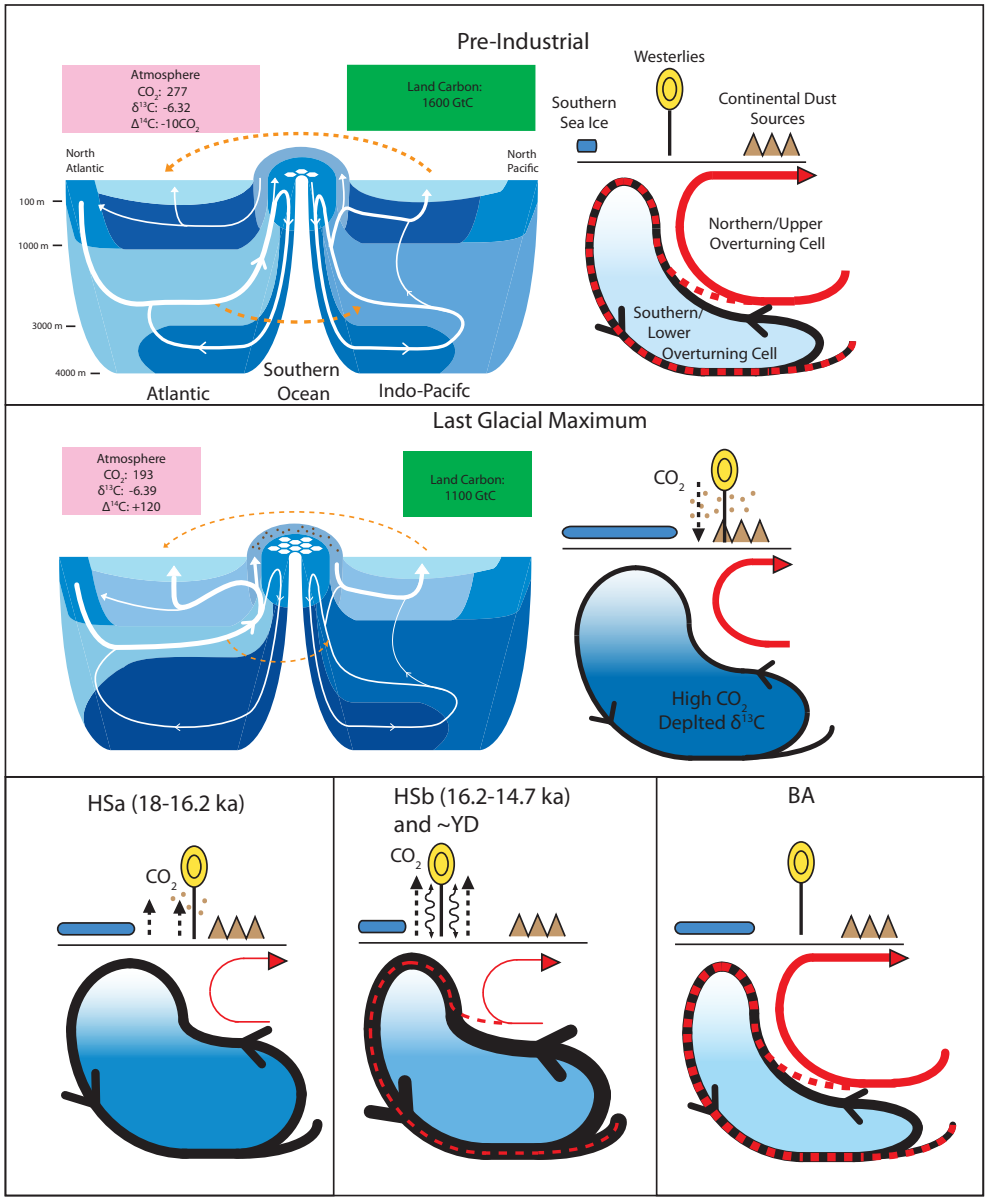

Figure 5.5 Conceptual model of deglacial CO_2
A schematic of the evolution of the carbon cycle during the deglaciation as described in the text. The illustrations of the glacial and pre-Industrial ocean circulation scenarios are a simplified representation of the box model used in the analysis (see Figure B.1 for model parameters). The darker shading is used to qualitatively indicate water with carbon content and greater ventilation ages, and generally higher nutrient and lower oxygen levels. The snap-shots show the proposed evolution and interaction of the Southern Hemisphere westerlies, dust flux, sea ice front and overturning cells and their effect on the carbon cycle during HS1 (both phases), the BA, and the YD.

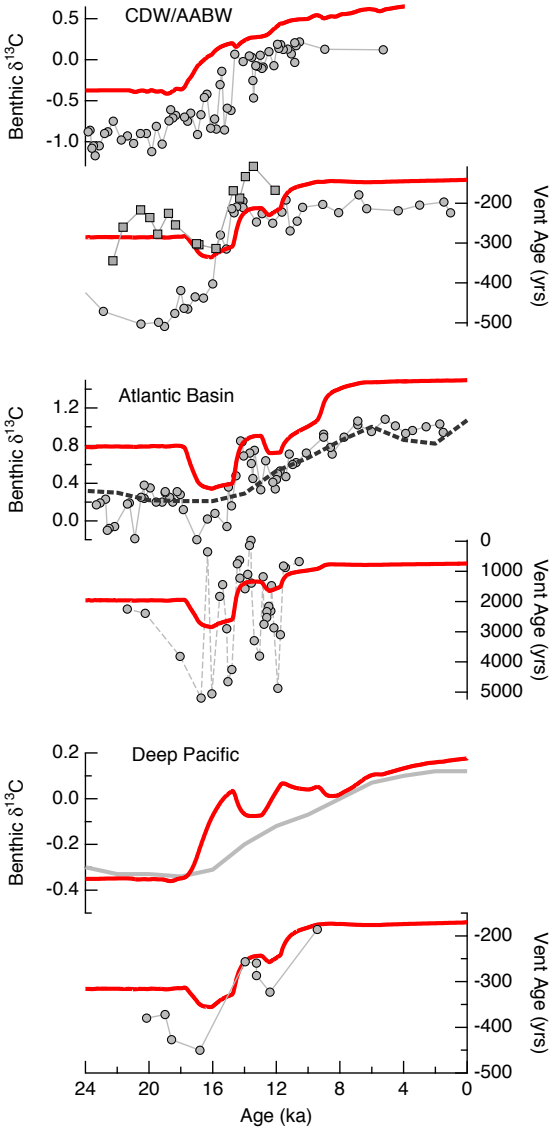

Figure 5.6 Deglacial Ocean Basin Evolution
A selection of benthic carbon isotopes (^{13}C and ^{14}C) records from the major deep ocean basins with the corresponding model simulations (red line). Data for CDW/AABW: $\delta^{13}C$ from *Piotrowski et al., 2005* and $\Delta\Delta^{14}C$ from *Skinner et al., 2010* (grey circles) and *Barker et al., 2010* (grey squares). For the deep Atlantic: $\delta^{13}C$ from *Skinner et al., 2004* and ventilation age from *Thornalley et al, 2011.* For the deep Pacific, a $\delta^{13}C$ benthic stack from *Lisieck, Raymo and Curry, 2008* and $\Delta\Delta^{14}C$ from *Galbraith et al., 2007*. $\Delta\Delta^{14}C$ was compiled in *Burke and Robinson, 2012*. To first order, the model captures many of the major features, though probably underestimates most of the changes. Data-model offsets may be related inaccurate carbon isotopes budgets in the model or the inability of the box model to capture sub-basin water mass properties. A complete evaluation of the data-model mismatch would require much more extensive data synthesis.

5.7 References

Adkins, J. F., et al. (2002), The salinity, temperature, and delta O-18 of the glacial deep ocean, *Science*, *298*(5599), 1769-1773.

Archer, D., et al. (1997), Multiple timescales for neutralization of fossil fuel CO_2, *Geophysical Research Letters*, *24*(4), 405-408.

Archer, D. E., et al. (2003), Model sensitivity in the effect of Antarctic sea ice and stratification on atmospheric pCO_2, *Paleoceanography*, *18*(1).

Barker, S., et al. (2010), Extreme deepening of the Atlantic overturning circulation during deglaciation, *Nature Geosci*, *3*(8), 567-571.

Blunier, T., et al. (2007), Synchronization of ice core records via atmospheric gases, *Climate of the Past*, *3*(2), 325-330.

Bouttes, N., et al. (2011), Last Glacial Maximum CO_2 and delta C-13 successfully reconciled, *Geophysical Research Letters*, *38*.

Bouttes, N., et al. (2012), Impact of oceanic processes on the carbon cycle during the last termination, *Climate of the Past*, *8*(1), 149-170.

Broecker, W., et al. (1999), How strong is the Harvardton-Bear Constraint?, *Global Biogeochemical Cycles*, *13*(4), 817-820.

Broecker, W. S. (1998), Paleocean circulation during the Last Deglaciation: A bipolar seesaw?, *Paleoceanography*, *13*(2), 119-121.

Broecker, W. S., and D. McGee (2013), The ^{13}C record for atmospheric CO_2: What is it trying to tell us?, *Earth and Planetary Science Letters*, *368*(0), 175-182.

Burke, A., and L. F. Robinson (2012), The Southern Ocean's Role in Carbon Exchange During the Last Deglaciation, *Science*, *335*(6068), 557-561.

Calvo, E., et al. (2011), Eastern Equatorial Pacific productivity and related-CO2 changes since the last glacial period, *Proceedings of the National Academy of Sciences*.

Cheng, H., et al. (2009), Ice Age Terminations, *Science*, *326*(5950), 248-252.

Ciais, P., et al. (2012), Large inert carbon pool in the terrestrial biosphere during the Last Glacial Maximum, *Nature Geosci*, *5*(1), 74-79.

Clark, P. U., and A. C. Mix (2002), Ice sheets and sea level of the Last Glacial Maximum, *Quaternary Science Reviews*, *21*(1-3), 1-7.

CLIMAP Project Members (1976), The Surface of the Ice-Age Earth, *Science*, *191*(4232), 1131-1137.

Curry, W. B., and D. W. Oppo (2005), Glacial water mass geometry and the distribution of delta C-13 of Sigma CO2 in the western Atlantic Ocean, *Paleoceanography*, *20*(1).

Denton, G. H., et al. (2010), The Last Glacial Termination, *Science*, *328*(5986), 1652-1656.

Elsig, J., et al. (2009), Stable isotope constraints on Holocene carbon cycle changes from an Antarctic ice core, *Nature*, *461*(7263), 507-510.

EPICA Community Members (2006), One-to-one coupling of glacial climate variability in Greenland and Antarctica, *Nature*, *444*(7116), 195-198.

Fischer, H., et al. (2007), Reconstruction of millennial changes in dust emission, transport

and regional sea ice coverage using the deep EPICA ice cores from the Atlantic and Indian Ocean sector of Antarctica, *Earth and Planetary Science Letters*, *260*(1-2), 340-354.

Friedlingstein, P., et al. (2006), Climate-carbon cycle feedback analysis: Results from the C(4)MIP model intercomparison, *J. Clim.*, *19*(14), 3337-3353.

Galbraith, E. D., et al. (2007), Carbon dioxide release from the North Pacific abyss during the last deglaciation, *Nature*, *449*(7164), 890-U899.

Gersonde, R., et al. (2005), Sea-surface temperature and sea ice distribution of the Southern Ocean at the EPILOG Last Glacial Maximum - A circum-Antarctic view based on siliceous microfossil records, *Quaternary Science Reviews*, *24*(7-9), 869-896.

Grachev, A. M., et al. (2007), Abrupt changes in atmospheric methane at the MIS 5b-5a transition, *Geophysical Research Letters*, *34*(20), 5.

Hendry, K. R., et al. (2012), Abrupt changes in high-latitude nutrient supply to the Atlantic during the last glacial cycle, *Geology*, *40*(2), 123-126.

Huybers, P., and C. Langmuir (2009), Feedback between deglaciation, volcanism, and atmospheric CO2, *Earth and Planetary Science Letters*, *286*(3-4), 479-491.

Jaccard, S. L., and E. D. Galbraith (2011), Large climate-driven changes of oceanic oxygen concentrations during the last deglaciation, *Nature Geoscience*, *5*(2), 151-156.

Joos, F., et al. (2004), Transient simulations of Holocene atmospheric carbon dioxide and terrestrial carbon since the Last Glacial Maximum, *Global Biogeochemical Cycles*, *18*(2).

Kaplan, J. O., et al. (2002), Modeling the dynamics of terrestrial carbon storage since the Last Glacial Maximum, *Geophysical Research Letters*, *29*(22), 4.

Kohler, P., et al. (2005), Quantitative interpretation of atmospheric carbon records over the last glacial termination, *Global Biogeochemical Cycles*, *19*(4), 24.

Lamy, F., et al. (1999), High-resolution marine record of climatic change in mid-latitude Chile during the last 28,000 years based on terrigenous sediment parameters, *Quat. Res.*, *51*(1), 83-93.

Lee, S.-Y., et al. (2011), Southern Ocean wind response to North Atlantic cooling and the rise in atmospheric CO_2: Modeling perspective and paleoceanographic implications, *Paleoceanography*, *26*.

Lemieux-Dudon, B., et al. (2010), Consistent dating for Antarctic and Greenland ice cores, *Quaternary Science Reviews*, *29*(1-2), 8-20.

Leuenberger, M., et al. (1992), Carbon isotope composition of atmospheric CO_2 during the last ice-age from an Antarctic ice core, *Nature*, *357*(6378), 488-490.

Lisiecki, L. E., et al. (2008), Atlantic overturning responses to Late Pleistocene climate forcings, *Nature*, *456*(7218), 85-88.

Lourantou, A., et al. (2010), Constraint of the CO_2 rise by new atmospheric carbon isotopic measurements during the last deglaciation, *Global Biogeochemical Cycles*, *24*, 15.

Marchal, O., et al. (1998), Impact of oceanic reorganizations on the ocean carbon cycle and atmospheric carbon dioxide content, *Paleoceanography*, *13*(3), 225-244.

Marcott, S. A., et al. (2013), A Reconstruction of Regional and Global Temperature for the Past 11,300 Years, *Science*, *339*(6124), 1198-1201.

Marinov, I., et al. (2006), The Southern Ocean biogeochemical divide, *Nature*, *441*(7096), 964-967.

Martin, J. H. (1990), Glacial-interglacial CO2 change: The Iron Hypothesis, *Paleoceanography*, *5*(1), 1-13.

McManus, J. F., et al. (2004), Collapse and rapid resumption of Atlantic meridional circulation linked to deglacial climate changes, *Nature*, *428*(6985), 834-837.

Meckler, A. N., et al. (2013), Deglacial pulses of deep-ocean silicate into the subtropical North Atlantic Ocean, *Nature*, *495*(7442), 495-498.

Monnin, E., et al. (2001), Atmospheric CO_2 concentrations over the last glacial termination, *Science*, *291*(5501), 112-114.

Monnin, E., et al. (2004), Evidence for substantial accumulation rate variability in Antarctica during the Holocene, through synchronization of CO_2 in the Taylor Dome, Dome C and DML ice cores, *Earth and Planetary Science Letters*, *224*(1-2), 45-54.

NGRIP Project Members (2004), High-resolution record of Northern Hemisphere climate extending into the last interglacial period, *Nature*, *431*(7005), 147-151.

Pedro, J. B., et al. (2011), The last deglaciation: timing the bipolar seesaw, *Climate of the Past*, *7*(2), 671-683.

Piotrowski, A. M., et al. (2005), Temporal relationships of carbon cycling and ocean circulation at glacial boundaries, *Science*, *307*(5717), 1933-1938.

Roth, R., and F. Joos (2012), Model limits on the role of volcanic carbon emissions in regulating glacial-interglacial CO_2 variations, *Earth and Planetary Science Letters*, *329*, 141-

149.

Santrock, J., et al. (1985), Isotopic analyses based on the mass-spectrum of carbon-dioxide *Analytical Chemistry*, *57*(7), 1444-1448.

Schmitt, J., et al. (2012), Carbon Isotope Constraints on the Deglacial CO_2 Rise from Ice Cores, *Science*, *336*(6082), 711-714.

Schmittner, A., and E. D. Galbraith (2008), Glacial greenhouse-gas fluctuations controlled by ocean circulation changes, *Nature*, *456*(7220), 373-376.

Shakun, J. D., et al. (2012), Global warming preceded by increasing carbon dioxide concentrations during the last deglaciation, *Nature*, *484*(7392), 49-54.

Skinner, L. C., et al. (2010), Ventilation of the Deep Southern Ocean and Deglacial CO2 Rise, *Science*, *328*(5982), 1147-1151.

Skinner, L. C., and N. J. Shackleton (2004), Rapid transient changes in northeast Atlantic deep water ventilation age across Termination I, *Paleoceanography*, *19*(2), 12.

Smith, H. J., et al. (1999), Dual modes of the carbon cycle since the Last Glacial Maximum, *Nature*, *400*(6741), 248-250.

Stephens, B. B., and R. F. Keeling (2000), The influence of Antarctic sea ice on glacial-interglacial CO_2 variations, *Nature*, *404*(6774), 171-174.

Thornalley, D. J. R., et al. (2011), The Deglacial Evolution of North Atlantic Deep Convection, *Science*, *331*(6014), 202-205.

Toggweiler, J. R., et al. (2006), Midlatitude westerlies, atmospheric CO_2, and climate change

during the ice ages, *Paleoceanography*, *21*(2), 15.

Vallelonga, P., et al. (2013), Iron fluxes to Talos Dome, Antarctica, over the past 200 kyr, *Climate of the Past*, *9*(2), 597-604.

Vecsei, A., and W. H. Berger (2004), Increase of atmospheric CO_2 during deglaciation: Constraints on the coral reef hypothesis from patterns of deposition, *Global Biogeochemical Cycles*, *18*(1).

Waelbroeck, C., et al. (2002), Sea-level and deep water temperature changes derived from benthic foraminifera isotopic records, *Quaternary Science Reviews*, *21*(1-3), 295-305.

Waelbroeck, C., et al. (2009), Constraints on the magnitude and patterns of ocean cooling at the Last Glacial Maximum, *Nature Geoscience*, *2*(2), 127-132.

WAIS Divide Community Members (2013), Onset of deglacial warming in West Antarctica driven by local orbital forcing, *Nature*, *500*(7463), 440-+.

Yu, J., et al. (2010), Loss of Carbon from the Deep Sea Since the Last Glacial Maximum, *Science*, *330*(6007), 1084-1087.

6 Conclusions

This dissertation presents three advancements at the intersection of geochemistry and paleoclimatology by providing better constraints on atmospheric $\delta^{13}C$ of CO_2 during the last deglaciation and last millennium.

Chapter III presents a new method for measuring $\delta^{13}C$ of CO_2 from polar ice. The analytical precision of the method is demonstrated to be significant advancement on other techniques. As described in Chapters IV and V, the method has yielded some of the best quality records of $\delta^{13}C$ of CO_2 to date. By providing a technical description of the analytical procedures, the method can now be widely replicated and improved on by other researches. In the future, the impact of this work may be greatly enhanced through additional data collection at Oregon State University and possibly elsewhere.

Chapter IV presents a new high-resolution record of $\delta^{13}C$ of CO_2 during the late Holocene from about 770-1900 C.E. The data strongly suggests that land carbon controlled atmospheric CO_2 variability from 770-1850 C.E.. A deconvolution of the atmospheric CO_2 and $\delta^{13}C$-CO_2 provides a well-constrained estimate of the evolution of land carbon stocks. The relationship between temperature and land carbon for this time period used to test the hypothesis that climate change can affect the carbon cycle. The data are demonstrated to be consistent with land carbon decreasing by about 60 gigatons for every one degree of Northern Hemisphere warming, in agreement with most models projecting future climate-carbon cycle feedbacks. However, an additional process affecting land carbon is required to explain the data. This missing process may be related to patterns of drought or early anthropogenic land cover change. The data thus provide an important constraint on future climate change while also opening up additional questions about natural variability.

Chapter V presents record a new record of $\delta^{13}C$ of CO_2 spanning the last deglaciation (~22,000 to 10,000 years B.P.). The data strongly confirm previous $\delta^{13}C$ of CO_2 studies. The unprecedented precision and resolution of the measurements, however, defines new types of variability and more strongly constrains the timing of changes. A box model is used to understand the constraints the data place on the evolution of carbon cycle variability from the LGM to late Holocene. The non-linear relationship between CO_2 and $\delta^{13}C$ of CO_2 during the deglaciation is reconciled with a new model of the carbon cycle that calls upon ocean temperature, iron fertilization and sea-ice as the dominant controls on atmospheric CO_2.

The new data presented in this dissertation have significantly advanced our understanding of past carbon cycle variability. In time, as additional data constraints are produced and new models are applied, the interpretations that accompany the data may be proven incorrect. The data, however, will likely stand as major benchmarks for future work, providing a gauge for model performance and a test-bed for new ideas.

Appendix A: Last Millennium

A.1. Comparison with Law Dome

The WAIS Divide $\delta^{13}C\text{-}CO_2$ data are very consistent with the lower resolution Law Dome data (as originally published in *Francey et al., 1999*) and the late Holocene values from the reconstruction of *Schmitt et al., 2012* (Figure A.1). Very recently, though, the $\delta^{13}C\text{-}CO_2$ measurements from Law Dome were revised such that pre-Industrial values were changed by more than 0.10 per mil (Rubino et al., 2013). The reason for the offset between WAIS Divide and the revised Law Dome is currently unknown but we suspect differences in the experimental methods. While the superior resolution and precision of the WAIS Divide data allows us to more robustly define the relative changes in the carbon cycle during the pre-Industrial, we stress that the accuracy of the pre-Industrial $\delta^{13}C\text{-}CO_2$ will require further study.

Not all the CO_2 features in the Law Dome record have a counterpart in the WAIS Divide record, even if the slightly greater smoothing of gases by diffusion in the firn at WAIS Divide is considered (Ahn et al., 2012). Assuming WAIS Divide is accurate would require only few data points in the Law Dome record to be spurious. On the other hand, assuming that Law Dome is the more accurate representation of the atmosphere opens up the possibility that some of the features in WAIS Divide are non-atmospheric in origin.

Focusing on the new observation of a $\delta^{13}C\text{-}CO_2$ excursion between 1470 and 1550 C.E., we argue that WAIS Divide is precisely recording atmospheric changes on the multi-decadal scale. First, the excursion is accompanied by a CH_4 peak that is recorded in multiple Greenland and Antarctic ice cores from a variety of methods (Rhodes et al., 2013; Mitchell et al., 2011), suggesting that the CO_2 change is related to a global biogeochemical change and not in situ processes. Furthermore, the excellent agreement with the mixed layer $\delta^{13}C$ reconstruction from a coral in the

Caribbean (Böhm et al., 2002), albeit the only highly resolved, pristine record spanning the pre-Industrial, suggests that the record is atmospheric in origin. Finally, if the signal is contaminated by closed system mixing within the ice (e.g. *in situ* production), while atmospheric $\delta^{13}C\text{-}CO_2$ is mostly constant (as implied by the Law Dome data), the $\delta^{13}C\text{-}CO_2$-to-CO_2 relationship would be one-to-one. Instead, the $\delta^{13}C\text{-}CO_2$ enrichment leads the CO_2 decrease, a sign of equilibration between the atmosphere and the rest of the carbon cycle immediately following a spike of isotopically depleted carbon (Siegenthaler and. Oeschger, 1987).

Previous work using the sparse Law Dome data deduced little change in biospheric carbon fluxes from about 1200-1500 C.E. followed by an interval of increased uptake by the biosphere of up to 0.3 GtC yr^{-1} at about 1600 C.E,, with a large uncertainty (0.5- 1.2 GtC yr^{-1}) (Joos et al., 1999; Trudinger et al., 2002). An additional ocean sink was needed to explain a sharp drop in CO_2 in the Law Dome record at this time, although this mechanism was not constrained by $\delta^{13}C$ of CO_2 measurements.

A.2. Discussion of Deconvolution Assumptions

The deconvolution of carbon fluxes from CO_2 and $\delta^{13}C$ of CO_2 data was performed in a number of different ways to test the sensitivity of the results to various assumptions.

A.2.1 Single Deconvolution

In the single deconvolution, the CO_2 mixing ratio was used to solve the land-carbon to atmosphere flux (Figure A.2). The ocean acts as passive sink/source, following the air-sea gas exchange and ocean mixing of the given model, and the $\delta^{13}C\text{-}CO_2$ and the ocean to atmosphere flux evolves freely. We used both the High-Latitude Exchange/Interior Diffusion-Advection (HILDA) ocean model coupled to 4-box model of the terrestrial biosphere (Joos and Bruno, 1998) and the Bern3D dynamic ocean–sediment model. The good agreement between the modeled and data $\delta^{13}C\text{-}CO_2$ suggests that land carbon drives most of the CO_2 variability with the ocean

needed as an additional source/sink at a few specific times (most notably 1500-1600 CE).

Some of the disagreement between in the $\delta^{13}C$-CO_2 with the Bern 3D model arises because the model also includes solar and volcanic forcing. This highlights a fundamental limitation of the ice core data. For example, the sub-decadal carbon cycle response to a series of large volcanic eruptions in the early 13th century (*Brovkin et al., 2010*) is likely not captured in the ice core due to smoothing in the firn, but the model simulates a sharp cooling in the surface ocean and thus an increase in solubility. The data do not show any sharp drop and the deconvolution thus requires a spurious increase in the land carbon flux to the atmosphere to balance the modeled flux into the ocean (note the ^{13}C depleted excursion around 1240 C.E.). Exploring this type of variability would require a second deconvolution step where the ice core data is deconvolved to the atmospheric history, though this would provide a non-unique solution. Also, chronological errors on the sub-decadal scale would have to be addressed.

In the approach presented here, we smoothed the data input (including the temperature reconstructions) with a spline that retains only information on multi-decadal and longer timescales, circumventing the problems of spurious results at the decadal timescale at the cost of losing some of the fine-scale information.

A.2.2 Double Deconvolution

In a double deconvolution, the CO_2 and $\delta^{13}C$-CO_2 are used to solve for the land carbon and ocean fluxes to the atmosphere. We employ the HILDA Ocean model coupled to a 4-box model of vegetation and soil. In this case, additional information about the isotopic signature of the ocean flux is required. The carbon isotope flux form the ocean is primarily controlled by the SST dependent fractionation during air-

sea gas exchange and the flux of biologic carbon in and out of the surface ocean (i.e. the strength of the biological pump).

The effect of SST on the double deconvolution was addressed with three distinct approaches (Figure A.2). First, the SST was held constant. Second, the deconvolution was solved for an SST history that reconciled the modeled atmosphere CO_2 and surface ocean pCO_2 (i.e. the ocean flux was driven by changes in SST). Third, the SST was forced with a number of different temperature reconstructions described in the main text (Figure A.3).

The multi-decadal/centennial scale variability in the flux history is insensitive to these different SST assumptions, but the long-term trend in land carbon is partially governed by the long-term trend in SST. For example, land carbon stocks are about 25 GtC larger at 1700 C.E when the MN08 reconstruction is used to drive SST than with constant SST.

Additionally, the various temperature reconstructions lead to significant divergence in the deconvolved land carbon stocks during the MCA. For example, the large warming around 1000 C.E. in *Christiansen and Ljungqvist, 2012* leads to a much larger and sharper loss of land carbon compared to the other reconstructions.

Because of the greater surface area of the ocean in the Southern Hemisphere and strong air-sea gas exchange in the Southern Ocean we choose to use the Global Land and Ocean temperature reconstruction from MN08 as the best representation of global SST. Additionally, the magnitude of temperature variations in the MN08 is smaller than most of other Northern Hemisphere, land based reconstructions and thus provide the most conservative estimate of carbon fluxes.

A.3 Regression Analysis

In the linear model, land carbon stocks are regressed against temperature following:

$$C_s = \gamma T + \varepsilon \qquad (1)$$

where *Cs* is the land carbon stocks, γ is land carbon-climate sensitivity (GtC K^{-1}), *T* is the temperature reconstruction, and ε is the error term.

In the one box model land-carbon stocks are driven by temperature such that:

$$\frac{\partial C}{\partial t} = \left(\gamma \Delta T - C\right)\frac{1}{\tau} \qquad (2)$$

where *C* is land carbon stocks, γ is the equilibrium land carbon-climate sensitivity (GtC K^{-1}), ΔT is the temperature change from proxy reconstructions, and τ is e-folding lifetime of carbon in the well-mixed box. The model parameter γ is varied and fit with iterative least-squares method.

In both cases, uncertainty is addressed with a monte-carlo approach by varying the temperature records within their stated error and using a random selection of the land carbon stocks to obtain a suite of solutions (n = 10,000)

See figures A.5 and A.6 for illustrations of the two models and A.8 for a demonstration of the sensitivity of the analysis to the assumption about the lag between temperature and land carbon.

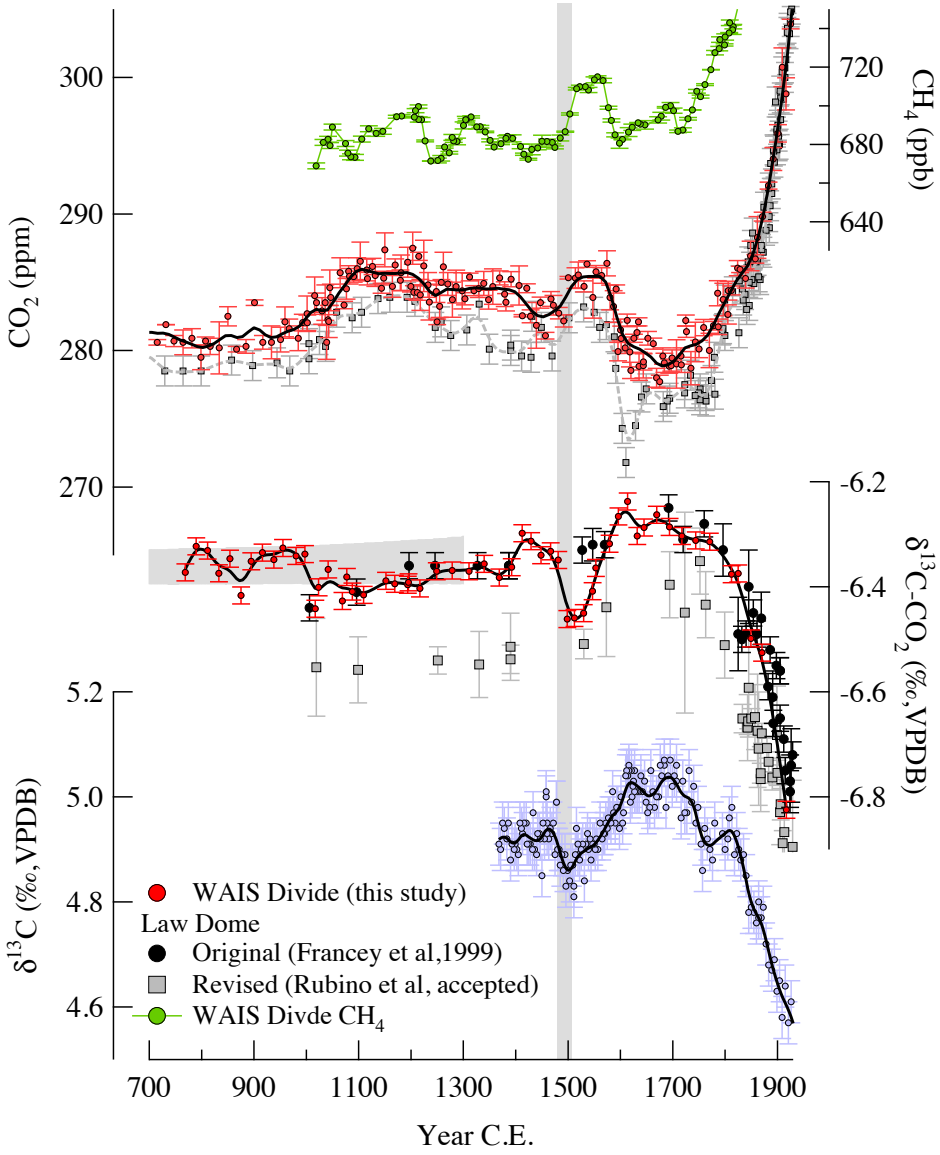

Figure A.1 WAIS Divide and Law Dome Gas Records
Comparison of new WAIS Divide data (red markers, this study) with previous results from the Law Dome ice core. Law Dome CO_2 (*Macfarling-Meure et al., 2006*), $\delta^{13}C$-CO_2 as originally published in *Francey et al., 1999* (black circles) and the same data as recently revised by *Rubino et al., 2013* (grey squares). Also shown are CH_4 from WAIS Divide (green markers, Mitchell et al., 2011) and a record of Caribbean mixed layer $\delta^{13}C$ (light blue markers, Böhm et al., 2002). The grey bar highlights the $\delta^{13}C$-CO_2 depletion discussed in the text that is coincident with the mixed layer depletion and CH_4 increase but not resolved in the Law Dome $\delta^{13}C$-CO_2 records.

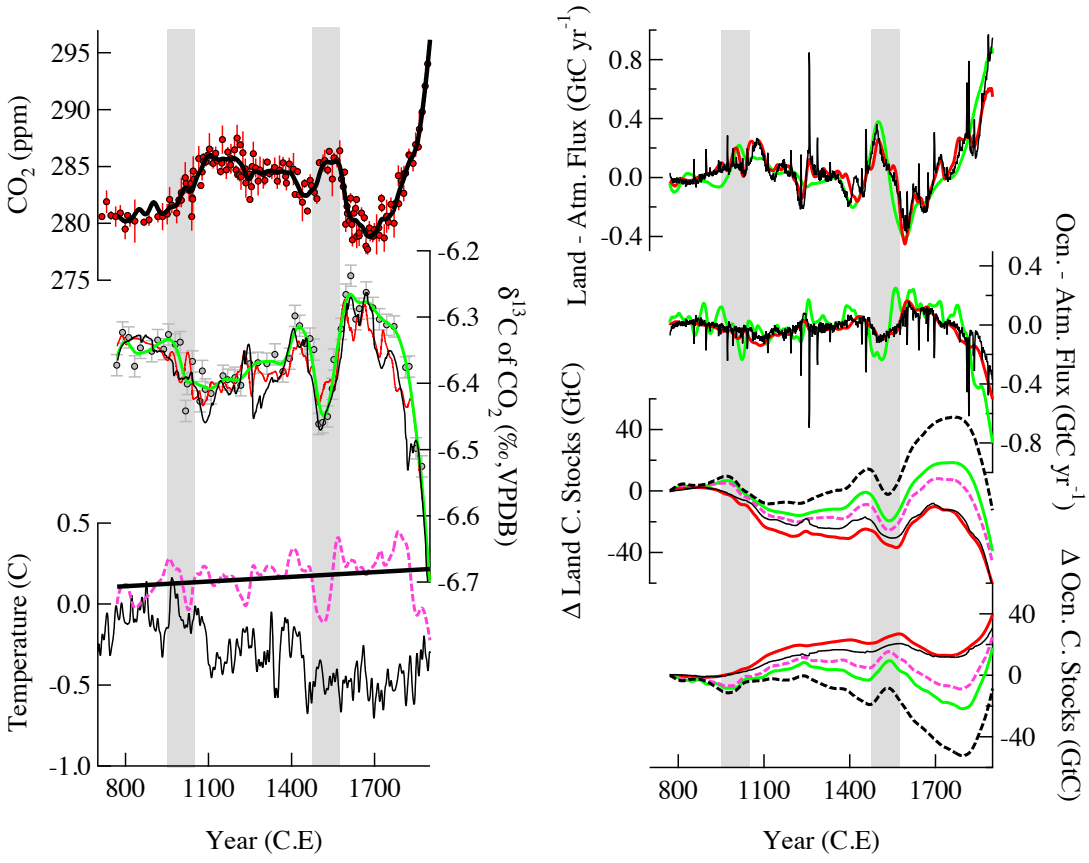

Figure A.2 Deconvolution Approaches
An example of single and double deconvolutions of the data with the HILDA and the Bern3D dynamic ocean–sediment model. Left panel: CO_2 axis shows data (red markers) used as model input. $\delta^{13}C$-CO_2 axis shows data (grey markers) with the single deconvolution predictions with Bern3D (thin black line) and HILDA (red line) models as well as data input used in the double deconvolution results (green line). The temperature axis shows the reconstruction from MN08 (thin black line) used to drive the model and calculated SST that would be required to close the atmospheric budget (dashed red line). Right panel: the carbon fluxes and stocks as calculated from the following methods the single deconvolution with Bern 3D model (thin black line), single deconvolution with the HILDA model (red line), double deconvolution with SST held constant (green line), SST calculated to close the atmospheric budget (dashed red line), and SST prescribed the temperature reconstruction MN08 (dashed black line).

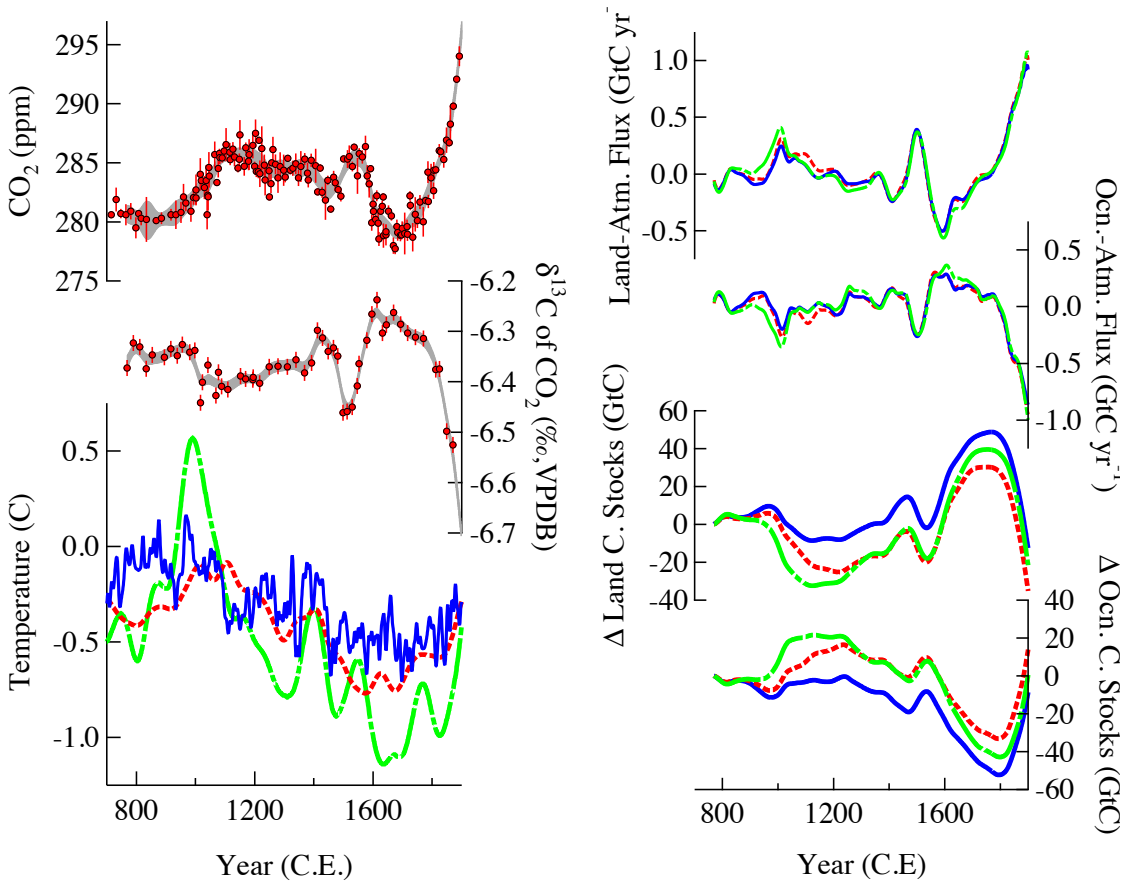

Figure A.3 Double Deconvolution SST sensitivity
The sensitivity of the double deconvolution results to assumptions about SST. Left panel: CO_2, $\delta^{13}C$-CO_2 data (red markers) and temperature data used as model input. Right panel: results using MN09 (solid blue), MG05 (dashed red), and *Christiansen and Ljungqvist, 2012* (stippled green).

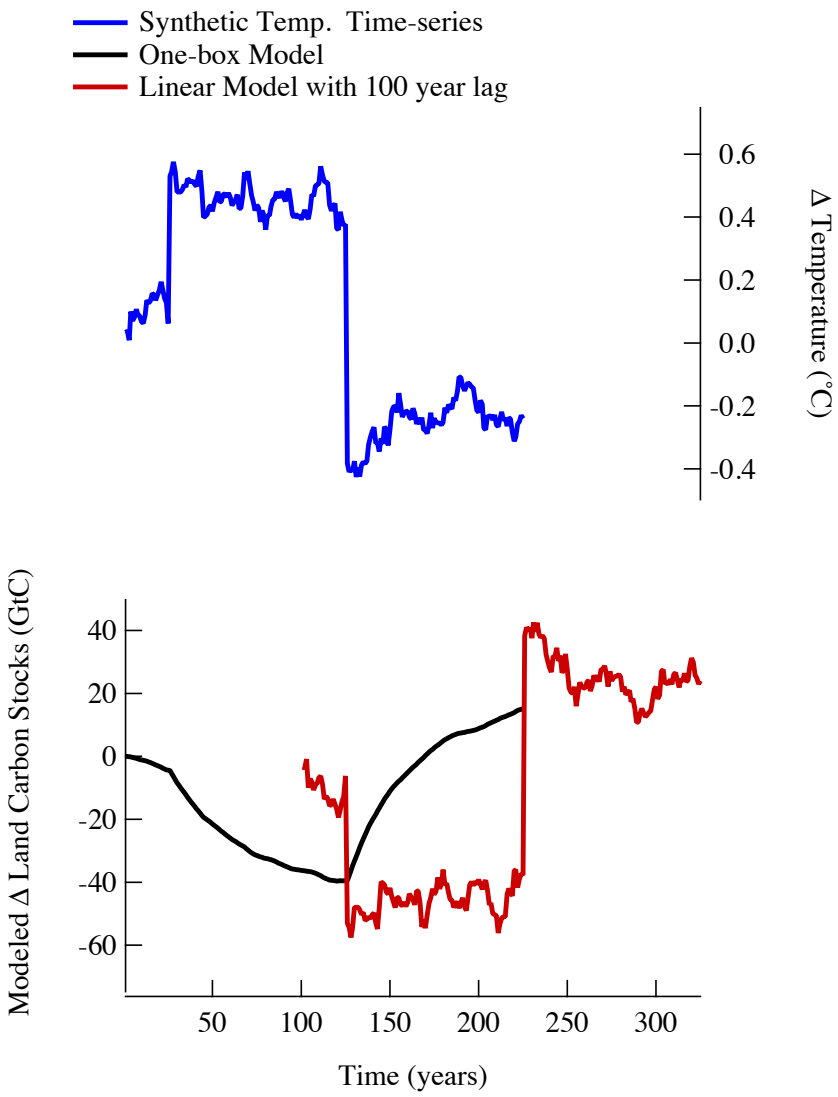

Figure A.4 Regression Models
Example of the linear and one-box models used in the temperature-land carbon regression. Both models were driven by a synthetic time-series of temperature with a land carbon-climate sensitivity of -100 GtC K^{-1}. The one box model approaches equilibrium with a time constant of 50 years, while the linear model employs a 100 year lag.

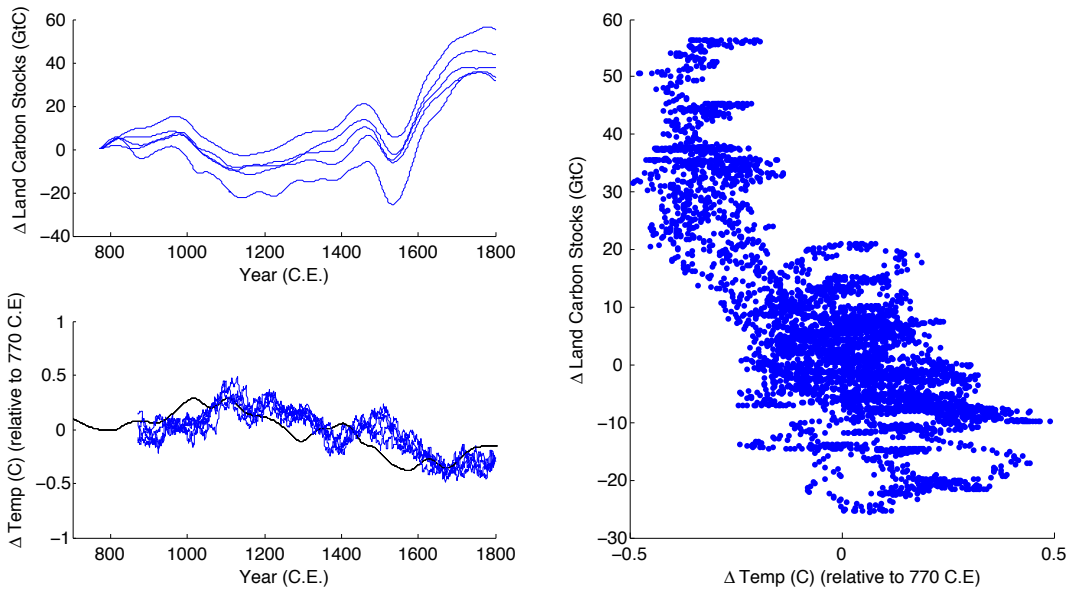

Figure A.5 Linear Regression Model Examples
Examples of the regression analysis using the linear model with a lag of 100 years. Randomly selected land carbon stock histories and the MG05 temperature (black line) reconstruction (with red-noise) are indicated by blue lines (left panel). The linear regressions for the same data are shown in the right panel.

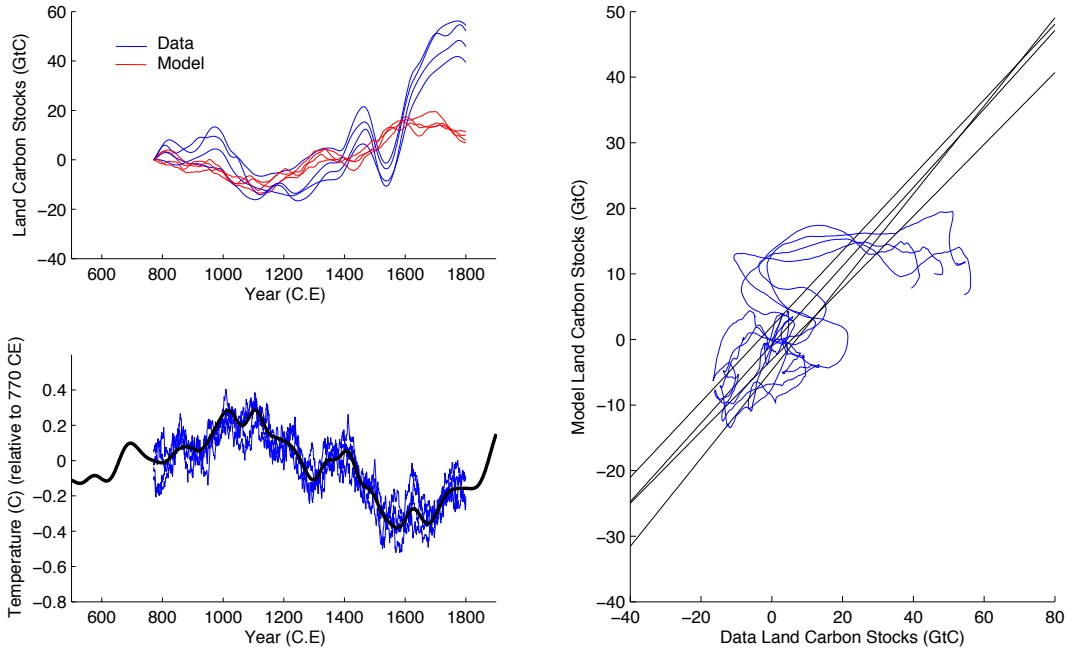

Figure A.6 One-Box Regression Model Examples
Examples of regression analysis using the one-box model. Randomly selected land carbon stock histories and the MG05 temperature reconstruction (with red noise) are indicated by blue lines. The modeled land carbon stocks are shown in red and plotted against the data estimated land carbon stocks (right panel).

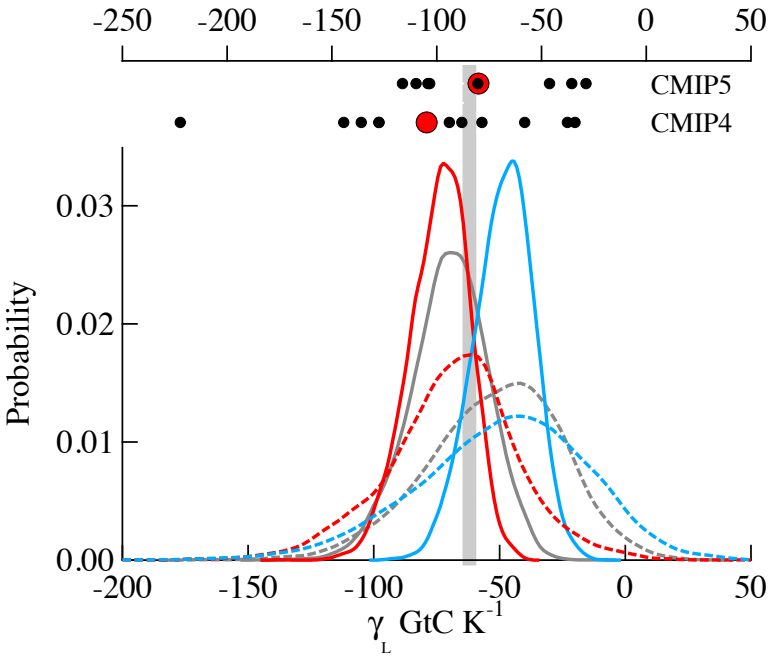

Figure A.7 Carbon-Climate Sensitivity Constraint
The probability density functions from the regression of temperature and land carbon stocks. Colors correspond to regressions using FK10 (grey), MN08 (blue), and MG05 (red). Solid lines indicate the linear model; dashed lines the one-box model. CMIP4 and CMIP5 model sensitivities are represented by the black dots with the ensemble mean indicated by the red dot.

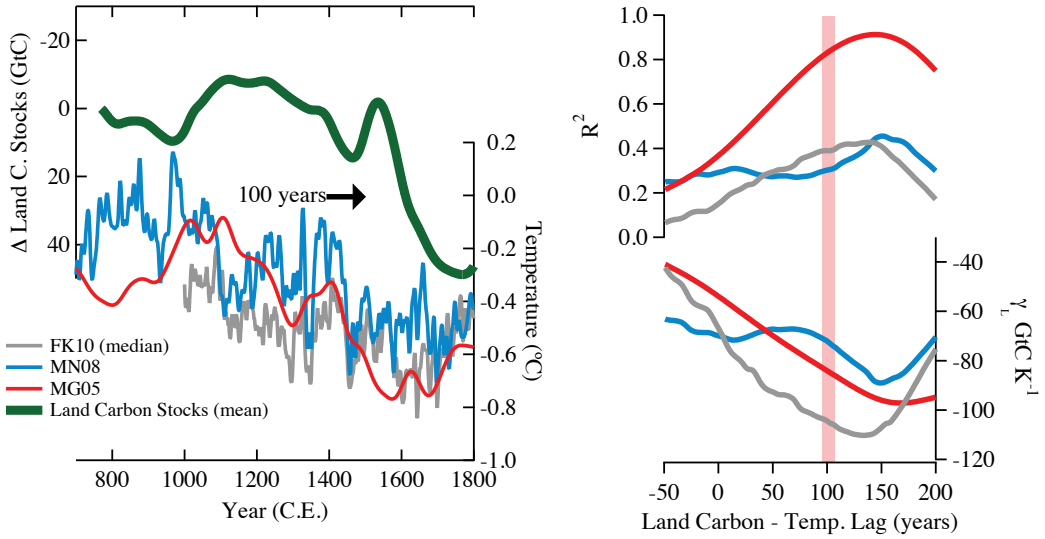

Figure A.8 Carbon-Climate Sensitivity Lag Correlation
A demonstration of the assumption of a lag between the land carbon and temperature records in linear regression analysis. A lag of 100 years was chosen based on the lifetime of carbon in longer-lived carbon pools of the terrestrial biosphere (right panel, red bar). However, the correlation (and inferred sensitivity) reaches a maximum in many of the temperature at around 150 years (right panel, grey bar). While intriguing, this and is mostly due to the alignment of the warm interval around 1400 C.E. with the land carbon excursion around 1550 CE, a likely unrealistically long lag. Note that the median temperature from the FK10 ensemble is used and the errors in the temperature and land carbon reconstructions are not considered in the example so the sensitivities and R^2 values at a 100 year lag are different than those presented in Table 1.

Table A.0.1 Empirical estimates of land carbon-climate sensitivity

Temperature	Regression	R^2	γ_L	95% C.I.
MG05	linear	0.71	-73	[-110,-50]
	one-box	0.58	-67	[-124,-18]
MN08	linear	0.28	-46	[-74,-21]
	one-box	0.35	-47	[-121,10]
FK10	linear	0.28	-69	[-102,-41]
	one-box	0.43	-50	[-108,-4]
Ensemble			-61	[-110,-8]

Table A.0.2 WAIS Divide $\delta^{13}C\text{-}CO_2$ Data

Core	Top Depth (m)	Bottom Depth (m)	Mid-Depth (m)	WDC06A-6 Constant Gas Age (C.E.)	WDC06A-7 Variable Gas Age (C.E.)	$\delta^{13}C\text{-}CO_2$ (per mil, VPDB)
WDC05A	84.41	84.59	84.50	1915.26	1916.37	-6.82
WDC05A	94.82	95.00	94.91	1868.64	1871.58	-6.53
WDC05A	100.34	100.54	100.44	1848.09	1847.24	-6.50
WDC05A	106.06	106.24	106.15	1824.07	1822.16	-6.37
WDC05A	109.02	109.12	109.07	1811.38	1809.02	-6.38
WDC05A	118.52	118.69	118.61	1769.75	1767.04	-6.33
WDC05A	118.53	118.69	118.61	1769.73	1767.02	-6.30
WDC05A	124.55	124.75	124.65	1743.63	1740.19	-6.31
WDC05A	130.55	130.70	130.63	1718.11	1713.95	-6.30
WDC05A	136.06	136.20	136.13	1693.50	1689.38	-6.29
WDC05A	142.25	142.40	142.32	1666.61	1662.22	-6.26
WDC05A	147.02	147.20	147.11	1644.28	1641.56	-6.31
WDC05A	147.03	147.20	147.11	1644.27	1641.56	-6.27
WDC05A	149.82	149.94	149.88	1631.52	1629.15	-6.30
WDC05A	154.17	154.38	154.28	1612.60	1609.47	-6.24
WDC05A	158.32	158.50	158.41	1594.90	1591.06	-6.27
WDC05A	162.14	162.30	162.22	1577.50	1574.16	-6.32
WDC05A	162.14	162.34	162.24	1577.43	1574.09	-6.32
WDC05A	168.73	168.88	168.80	1550.09	1544.89	-6.36
WDC05A	170.07	170.27	170.17	1543.89	1538.94	-6.41
WDC05A	174.10	174.25	174.18	1525.63	1520.94	-6.46
WDC05A	174.10	174.25	174.18	1525.63	1520.94	-6.44
WDC05A	177.78	177.93	177.85	1508.88	1504.38	-6.46
WDC05A	180.73	180.88	180.81	1495.41	1491.24	-6.47
WDC05A	180.73	180.88	180.81	1495.41	1491.24	-6.45
WDC05A	184.55	184.67	184.61	1478.15	1474.33	-6.35
WDC05A	187.80	188.03	187.91	1463.31	1459.45	-6.33
WDC05A	192.02	192.18	192.10	1445.41	1440.57	-6.34
WDC05A	192.26	192.43	192.34	1444.60	1439.63	-6.34
WDC05A	196.25	196.40	196.33	1427.41	1421.86	-6.31
WDC05A	200.19	200.35	200.27	1410.81	1404.46	-6.30
WDC05A	204.64	204.84	204.74	1391.12	1384.84	-6.36
WDC05A	209.88	210.08	209.98	1367.50	1361.29	-6.39
WDC05A	209.88	210.08	209.98	1367.50	1361.29	-6.38
WDC05A	216.21	216.39	216.30	1339.08	1332.81	-6.36
WDC05A	223.09	223.26	223.18	1310.62	1302.47	-6.37
WDC05A	229.94	230.09	230.02	1278.86	1272.02	-6.35
WDC05A	230.12	230.29	230.21	1278.06	1271.24	-6.38
WDC05A	237.09	237.29	237.19	1249.65	1240.45	-6.37

WDC05A	245.07	245.23	245.15	1215.12	1205.36	-6.40
WDC05A	251.58	251.75	251.67	1188.66	1176.73	-6.40
WDC05A	278.35	278.51	278.43	1075.50	1061.44	-6.38
WDC05A	291.92	292.02	291.97	1015.79	1004.07	-6.44
WDC06A	250.03	250.21	250.12	1195.35	1183.63	-6.38
WDC06A	250.21	250.39	250.30	1194.51	1182.75	-6.41
WDC06A	256.00	256.18	256.09	1168.89	1157.24	-6.39
WDC06A	260.11	260.29	260.20	1152.02	1139.45	-6.39
WDC06A	265.24	265.42	265.33	1130.96	1117.44	-6.54
WDC06A	270.23	270.41	270.32	1109.48	1096.00	-6.40
WDC06A	270.41	270.41	270.41	1109.03	1095.56	-6.43
WDC06A	275.24	275.41	275.33	1087.93	1074.71	-6.41
WDC06A	280.11	280.29	280.20	1068.84	1054.17	-6.43
WDC06A	285.63	285.81	285.72	1042.38	1030.74	-6.36
WDC06A	286.00	286.18	286.09	1040.95	1029.25	-6.38
WDC06A	290.00	290.18	290.09	1023.60	1012.10	-6.40
WDC06A	290.18	290.36	290.27	1022.71	1011.14	-6.40
WDC06A	296.00	296.18	296.09	997.33	986.29	-6.34
WDC06A	300.06	300.24	300.15	980.23	968.86	-6.34
WDC06A	306.00	306.18	306.09	955.31	943.01	-6.33
WDC06A	310.00	310.18	310.09	938.05	925.85	-6.35
WDC06A	315.24	315.42	315.33	916.24	902.82	-6.33
WDC06A	320.43	320.61	320.52	894.81	879.92	-6.35
WDC06A	320.61	320.79	320.70	894.11	879.11	-6.35
WDC06A	325.24	325.42	325.33	875.16	859.27	-6.42
WDC06A	330.15	330.33	330.24	853.96	837.96	-6.35
WDC06A	335.24	335.42	335.33	832.92	816.30	-6.37
WDC06A	340.14	340.32	340.23	811.62	795.58	-6.33
WDC06A	340.32	340.50	340.41	810.72	794.74	-6.34
WDC06A	345.24	345.42	345.33	789.40	774.04	-6.32
WDC06A	350.15	350.33	350.24	768.60	753.31	-6.37

A.4 References

Ahn, J., et al. (2012), Atmospheric CO_2 over the last 1000 years: A high-resolution record from the West Antarctic Ice Sheet (WAIS) Divide ice core, *Global Biogeochemical Cycles*, *26*.

Böhm, F., et al. (2002), Evidence for preindustrial variations in the marine surface water carbonate system from coralline sponges, *Geochem. Geophys. Geosyst.*, *3*, 13.

Brovkin, V., et al. (2010), Sensitivity of a coupled climate-carbon cycle model to large volcanic eruptions during the last millennium, *Tellus Series B-Chemical and Physical Meteorology*, *62*(5), 674-681.

Francey, R. J., et al. (1999), A 1000-year high precision record of $\delta^{13}C$ in atmospheric CO_2, *Tellus Series B-Chemical and Physical Meteorology*, *51*(2), 170-193.

Gerber, S., et al. (2004), Sensitivity of a dynamic global vegetation model to climate and atmospheric CO2, *Glob. Change Biol.*, *10*(8), 1223-1239.

Joos, F., and M. Bruno (1998), Long-term variability of the terrestrial and oceanic carbon sinks and the budgets of the carbon isotopes C-13 and C-14, *Global Biogeochemical Cycles*, *12*(2), 277-295.

Joos, F., et al. (1999), The variability in the carbon sinks as reconstructed for the last 1000 years, *Geophysical Research Letters*, *26*(10), 1437-1440.

Mitchell, L. E., et al. (2011), Multidecadal variability of atmospheric methane, 1000-1800 CE, *Journal of Geophysical Research-Biogeosciences*, *116*, 16.

Rhodes, R. H., et al. (2013), Continuous methane measurements from a late Holocene

Greenland ice core: Atmospheric and in-situ signals, *Earth and Planetary Science Letters*, *368*(0), 9-19.

Siegenthaler, U., and H. Oeschger (1987), Biospheric CO_2 emissions during the past 200 years reconstructed by deconvolution of ice core data, *Tellus B*, *39B*(1-2), 140-154.

Trudinger, C. M., et al. (2002), Kalman filter analysis of ice core data - 2. Double deconvolution of CO_2 and delta C-13 measurements, *J. Geophys. Res.-Atmos.*, *107*(D20).

Appendix B: Last Deglaciation

B.1 Taylor Glacier Data

The paleoatmospheric records were produced from a horizontal ice core on the Taylor Glacier in the Dry Valleys of Antarctica. CH_4, CO_2 $\delta^{13}C$ of CO_2 and N_2O were measured at Oregon State University (*this study*) and $\delta^{18}O$ of O_2 and $\delta^{15}N$ of N_2 were measured at Scripps Institution of Oceanography (Baggenstos et al., in prep).

CH_4 measurements in the laboratory were made following the technique first described in *Grachev et al, 2007*. The field CH_4 measurements were completed with a similar but slightly simplified system designed for field deployment in blue ice regions.

The average 1-sigma standard error of a single CH_4 analysis (i.e. the internal precision) was 1.15 ppb during the analysis period (n = 223). The average 1-sigma standard deviation of replicate analyses taken from adjacent depths (i.e. the external precision) was 4.15 ppb (n = 56). The internal precision of the field measurements of the primary sampling area was 2.75 ppb (n = 84). Too few replicates were made in field to assign an external precision.

The CO_2, N_2O and $\delta^{13}C$ of CO_2 were measured as described in Chapter III. ^{15}N data from nearly identical depths were used to correct the $\delta^{13}C$ of CO_2 for gravitational fractionation in the firn. The magnitude of the correction ranged about 0.1‰ in glacial ice to 0.2‰ in early Holocene ice.

The 1-sigma pooled standard deviation of pseudo replication experiments (n = 9) was 0.022 per mil. The standard deviation was likely biased by two replicates from times of rapid $\delta^{13}C$ change and compressed stratigraphy. We suggest that the overall precision for an individual measurement is best represented by the pooled standard

deviation of replicates from times of slowly changing $\delta^{13}C$ of CO_2 (0.016, n = 7) and assign a relative age uncertainty of up to 25 years based on sampling depth uncertainty during early CO_2 rise from 18-16 ka.

The external precision determined by replicate experiments was 1.05 ppm for CO_2 and 4.1 ppb for N_2O (though significantly better in ice with lower dust concentrations at 1.9 ppb). The uncorrected CO_2 data were consistently offset from the EPICA Dome C data by about 9-10 ppm. Correcting the data for procedural blanks (3-4 ppm) and gravitation fractional (<1 ppm) still leaves a significant offset. We believe this offset could be an artifact of the aliquot trapping system. The procedural blank, which may be due to contamination, does not affect the majority of the air that is processed for isotopic measurement.

B.2 Taylor Glacier Blue Ice Stratigraphy

Over 200 CH_4 measurements made in the field identified the major features in the surface stratigraphy and constrained the subsurface stratigraphy to a depth of 20 meters. The field measurements were confirmed by higher precision and more detailed measurements in the laboratory. By identifying the abrupt transition in CH4 across the surface and at depth, the strike and dip of the isochrones was constrained.

For example, the YD-PB transition in CH_4 is exposed in about 4 meters of ice on the surface, but extends across a length of about 20 meters down core. This translates to dip of about 70-80 degrees. The YD-PB transition was also identified at locations 100 meters up glacier and 1000 meters down glacier, suggesting that the strike is along flow and fairly homogenous.

A broad (100 meter scale hinge-to-hinge, a few kilometers along hinge), shallowly plunging syncline/anticline pair is readily apparent in both satellite imagery and geochemical stratigraphy. The sampling transect for the glacial termination was

chosen to intersect these folds at a doubly plunging anticline to simplify the stratigraphy and allow for a complete deglacial sampling in layers that are steeply dipping. This strategy also allowed for the two sections of the records to be spliced together at the OD-BA transition in CH4.

B.3 Carbon Cycle Modeling

The model traces PO_4, O_2, ALK, ^{12}C, ^{13}C,^{14}C, through eleven ocean boxes, carbon isotopes of CO_2 and oxygen in a well-mixed atmosphere, and carbon isotopes in a two-box terrestrial biosphere (See Figure B.1). At steady-state gross primary production and respiration on land both proceed at 90 GtC yr^{-1}. Air-sea gas exchange proceeds with $k_w = 18$ cm hr^{-1} in the low-latitude ocean and $k_w = 36$ cm hr^{-1} in the high-latitude boxes with some sea-ice limitation in the North Atlantic, North Pacific, and Antarctic Ocean boxes. The carbonate chemistry is calculated at each timestep from Matlab code provided as supplement to *Zeebe, R., and D. Wolf-Gladrow, 2001*. Nutrient utilization is based on restoring PO_4 to set levels at each timestep. The basic chemical cycling describing the organic and $CaCO_3$ pump is taken from *Toggweiller, 1999*. Remineralization in the ocean interior follows a power law formulation (*Martin et al., 1987*) with a b = 1.25. $CaCO_3$ compensation is modeled as an impulse response function to a perturbation from steady-state (Archer, et al., 1997; Joos, et al., 2004) with coefficients $a_1 = 0.6$, $a_2 = 0.1$, $a_3 = 0.3$ and respective time constants $\tau_1 =$ 5500 years, $\tau_2 =$ 8200 years, $\tau_3 =$ 200,000 years. The concept for ocean circulation and geometry follows an upper and lower overturning model feed by northern and southern sourced waters, respectively (*Talley, 2013*) (Figure B.1).

The physical and chemical structure of the model also attempts to simulate, in a highly simplified manner, the influence of sea-ice formation and the distinct biogeochemical divide around Antarctica. The Southern Ocean is divided into two distinct regions based on their water mass properties. Roughly equivalent to the region south of the Antarctic Polar Front (refered to in the model as the Antarctic

Ocean), a surface ocean box extending to 1000 meters and partially covered by sea-ice, contains cold (1.0°C), high preformed nutrient content (PO_4 = 1.8 mmol m^{-3}) water. This water mass functions as the site of deepwater formation around Antarctica (35.5 Sv) and as the region south of the notable biogeochemical divide (*Marinov et al., 2006*). This box is susceptible to variable sea-ice cover. North of this divide (referred to in the model as the Subantarctic Ocean), the model contains another surface water mass with warmer (5.5°C), lower preformed nutrient (PO_4 = 1.4 mmol m^{-3}) water that feeds the intermediate waters of the ocean. This box experiences variable nutrient limitation in the model. Some mixing is allowed between the two Southern Ocean boxes.

The deep Atlantic basin is filled with 18 Sv of cold (3.0°C) low preformed nutrient water (PO_4 = 1.4 mmol m^{-3}) of the North Atlantic. The low-latitude region is comprised of a warm surface boxes (20.5°C), extending to 100 meters, with very low preformed nutrient water (PO_4 = 0.2 mmol m^{-3}).

Below the surface, intermediate waters extend down to 1000 meters, readily mixing with both the surface boxes and conveying waters from the Subantarctic to the low-latitude surface, with a minor mixing between North Pacific surface in the Indo-Pacific.

The deep ocean basins extend from about 1000 meters to 3700 meters. The deep Atlantic basin is feed by a mixture of NADW and AABW (18 and 6 Sv, respectively). The deep Atlantic is either routed directly to the Indo-Pacific or upwelled in the Antarctic Ocean box and returned to the deep in the form of AABW.

The deep Indo-Pacific water originates mainly from the deep Southern sourced water with some direct feed of Atlantic water. Most of the deep Indo-Pacific is returned to the surface by upwelling in the two Southern Ocean boxes, where it can either be returned to the deep or entrained in intermediate waters. The water fed to the

intermediate Indo-Pacific eventually upwells, reaching the low-latitude surface ocean before finally being returned to the surface Atlantic via the "warm route" in the form of Indonesian Flow Through water. Some water is also returned to that North Atlantic via the "cold route" by entrainment in Atlantic intermediate waters from Subantarctic surface waters that have travelled in the ACC.

Figure B.1 and Table B.1 provide the pre-Industrial steady-state solution for most of the model parameters.

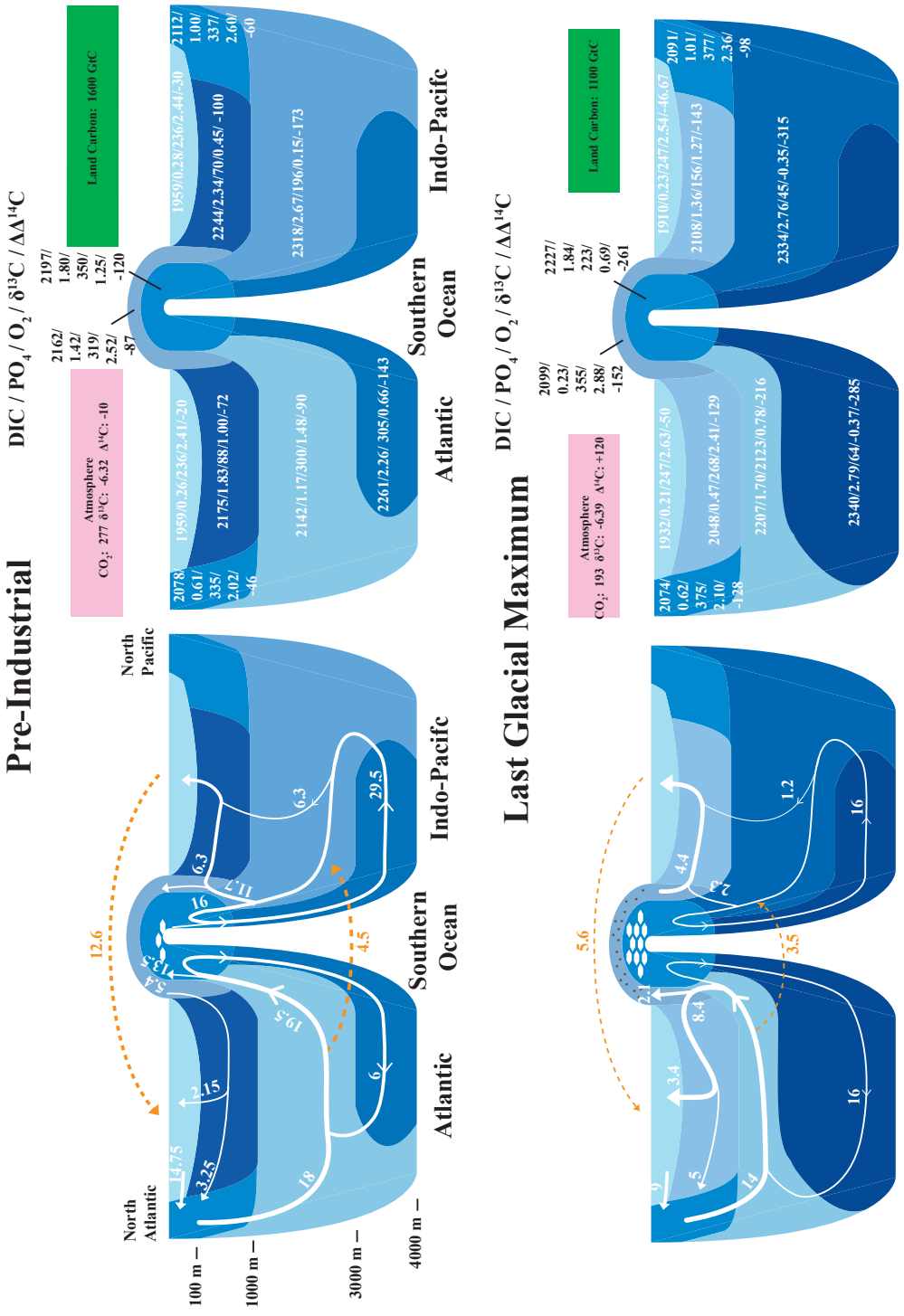

Figure B.1 Box Model
A schematic of the box model at pre-Industrial and LGM steady states. The overturning circulation rates are report in Sv. The biogeochemical variables for each box are reported as: DIC (μmol kg^{-1}) / PO_4 (mmol m^{-3})/ O_2 (mmol m^{-3})/ $\delta^{13}C$ (‰) / $\Delta\Delta^{14}C$ (‰). The darker colors of the boxes are qualitative representations of DIC concentration.

Table B.0.1 Steady-State Box Model Solutions

Pre-Industrial	CO_2 (ppm)	$\delta^{13}C$-CO_2 (per mil)	$\Delta\Delta^{14}C$ (per mil)			
Atmosphere	277	-6.32	-9.8			
Ocean Basin	DIC (µmol kg^{-1})	ALK (µmol kg^{-1})	PO_4 (mmol m^{-3})	O_2 (mmol m^{-3})	$\delta^{13}C$ (per mil)	$\Delta\Delta^{14}C$ (per mil)
Atlantic Surf.	1958.99	2292.00	0.26	236.30	2.41	-19.67
Pacific Surf.	1958.69	2290.60	0.28	236.48	2.44	-29.72
N. Atlantic	2078.50	2308.61	0.61	335.54	2.02	-46.28
N. Pacific	2112.10	2307.93	1.02	337.73	2.60	-58.71
Antarctic Surf.	2196.78	2357.66	1.80	349.87	1.25	-118.59
Subantarctic Surf.	2162.76	2383.03	1.42	318.87	2.52	-87.06
Atlantic Int.	2175.48	2331.35	1.83	88.40	0.99	-72.20
Pacific Int.	2244.21	2338.65	2.34	68.93	0.45	-100.79
Pacific Deep	2318.79	2387.37	2.67	196.63	0.15	-172.77
Atlantic Deep	2142.89	2330.68	1.17	299.24	1.48	-90.18
S.O. Deep	2261.42	2373.53	2.26	305.04	0.66	-143.50
LGM	CO_2 (ppm)	$\delta^{13}C$-CO_2 (per mil)	$\Delta\Delta^{14}C$ (per mil)			
Atmosphere	193	-6.39	117			
Ocean Basin	DIC (µmol kg^{-1})	ALK (µmol kg^{-1})	PO_4 (mmol m^{-3})	O_2 (mmol m^{-3})	$\delta^{13}C$ (per mil)	$\Delta\Delta^{14}C$ (per mil)
Atlantic Surf.	1931.72	2327.59	0.21	247.27	2.63	-49.89
Pacific Surf.	1909.74	2302.82	0.23	247.29	2.54	-46.67
N. Atlantic	2074.12	2340.81	0.62	375.00	2.10	-127.53
N. Pacific	2090.59	2320.90	1.01	376.84	2.36	-97.88
Antarctic Surf.	2227.32	2367.20	1.84	222.87	0.69	-260.72
Subantarctic Surf.	2098.52	2361.84	0.23	354.64	2.88	-151.71
Atlantic Int.	2048.33	2346.24	0.47	268.09	2.41	-128.85
Pacific Int.	2107.78	2329.09	1.36	156.35	1.27	-143.35
Pacific Deep	2333.78	2377.67	2.76	45.12	-0.35	-315.35
Atlantic Deep	2206.83	2357.39	1.70	212.90	0.78	-216.02
S.O. Deep	2340.10	2373.16	2.79	63.72	-0.37	-284.62

Table B.0.2 Taylor Glacier Data

Transect Location (m)	Age from CH_4 and $\delta^{18}O$ sync to WDC06A-7 timescale (ka, BP)	CH_4 (ppb) (solub+grav)	CO_2 (ppm) (grav)	N_2O (ppb) (grav)	$\delta^{13}C$-CO_2 (per mil, VPDB)
-130.00	22.66	383.87	193.70	225.08	-6.350
-128.00	22.11	380.49	191.79	220.60	-6.417
-126.00	20.92	377.90	194.45	221.71	-6.456
-124.00	19.78	376.47	197.56	213.57	-6.497
-122.00	18.67	389.05	194.50	212.00	-6.483
-120.00	18.00	398.42	195.41	224.58	-6.446
-119.00	17.89	389.67	196.02	224.68	-6.390
-118.00	17.73	417.67	202.52	219.36	-6.481
-117.00	17.58	420.12	202.28	203.82	-6.436
-116.00	17.44	425.52	204.60	205.34	-6.447
-115.00	17.28	431.21	210.57	208.55	-6.536
-114.00	16.94	436.20	212.91	200.96	-6.588
-113.00	16.71	444.03			
-112.00	16.57	453.17	217.45	205.91	-6.581
-111.00	16.45	465.88	219.88	203.79	-6.750
-110.00	16.34	452.20	223.75	230.82	-6.806
-108.00	16.13	465.13	226.49	200.32	-6.748
-106.00	15.94	464.22	225.43	200.73	-6.671
-104.00	15.75	476.28	226.97	202.28	-6.671
-102.00	15.61	477.35	229.27	206.57	-6.728
-100.00	15.47	474.47	230.14	205.75	-6.697
-98.00	15.30	482.85	231.51	212.55	-6.665
-96.00	15.09	497.48	232.68	215.62	-6.651
-95.00	14.97		231.96	212.98	-6.727
-94.00	14.87	491.56			
-93.00	14.78	476.19	235.41	219.86	-6.719
-92.00	14.73	521.67			
-91.00	14.69	549.68	237.01	226.11	-6.714
-90.00	14.65	556.30			
-89.00	14.60	604.04	241.36	240.27	-6.673
-88.00	14.56	604.56	242.97	241.63	-6.709
-86.00	14.48	626.32	244.08	248.42	-6.637
-84.00	14.40	597.11	244.61	250.88	-6.672

-82.00	14.35	581.58	244.14	255.12	-6.677
-80.00	14.05	601.38	242.78	254.36	-6.630
10.00		446.76			
20.00	15.63	475.91			
22.00	15.49	481.86			
24.00	15.24	487.79			
26.00	15.00	485.48			
28.00	14.85	486.25			
30.00	14.62	590.12	238.90	228.87	-6.716
33.00	14.52	601.42	242.72	247.67	-6.642
36.00	14.25	611.53	244.95	257.19	-6.635
40.00	14.09	545.32	242.62	255.66	
42.00	14.00	621.84	240.41	254.97	-6.620
44.00	13.93	631.33	243.75	258.02	-6.564
46.00	13.85	625.61	243.76	255.19	-6.630
50.00	13.57	647.76	242.97	258.01	-6.606
53.00	13.47	677.31	243.36	265.99	-6.590
56.00	13.33	626.82	245.82	265.19	-6.640
60.00	13.14	625.97			
63.00	13.07	621.51	240.22	260.88	-6.606
66.00	13.00	629.33	242.25	261.31	-6.586
70.00	12.87	608.65	242.50	263.57	-6.578
71.00	12.84	570.50	242.45	262.39	-6.564
72.00	12.82	507.03	244.76	264.64	
73.00	12.75	496.18	245.00	259.70	-6.594
74.00	12.71	511.33	246.42	259.66	-6.669
75.00	12.66	479.21			
76.00	12.62	461.14	246.89	256.48	-6.695
78.00	12.53	445.19	248.34	249.75	-6.730
80.00	12.44	476.47			
83.00	12.31		250.10	236.41	-6.697
86.00	12.17	456.84	254.25	241.11	-6.640
90.00	12.00	467.80	257.21	242.13	-6.601
92.00	11.91	469.55	257.11	240.73	-6.584
94.00	11.82	458.95	258.84	247.32	-6.612
95.00	11.77				
96.00	11.73	465.49	260.26	241.03	-6.615
97.00	11.68	491.80	262.63	248.80	-6.537
98.00	11.64	591.37			-6.576
99.00	11.61	655.13	267.60	248.81	-6.637
100.00	11.57	746.85	269.08	256.52	-6.622
101.00	11.52	710.99			
105.00	11.28	666.87	270.33	263.45	-6.615
110.00	11.17	698.34			

115.00	10.98	688.45	271.00	260.95	-6.631
120.00	10.78	681.14			
125.00	10.63	697.62			
140.00	10.30	682.79			
150.00	9.92	693.46			
170.00	9.54	697.51			
180.00	9.27	676.29			
190.00	9.00	690.67			
200.00	8.79	681.42			
210.00	8.40	645.98			
220.00	8.20	579.97			
230.00	7.80	633.40			

B.4 Carbon Cycle Model Code

To run the box model code, including spinning up the model to steady-state (for example to LGM conditions) and then simulating a transient run (for example the deglaciation) requires the following matlab scripts:

- BBCM_11Box_LGM_N2O.m
- BBCM_11Box_Deglacial_Core.m
- Core_11Box_N2O_CACO3_Comp.m
- Core_11Box_N2O_no_CACO3_Comp.m
- csys3_hack.m
- equic.m
- O2a_O2oc.m

BBCM_11Box_LGM_N2O.m initializes the model (e.g. calculates box geometry, pre-allocates all variables, provides initial conditions, etc) and calls the "core" code that solves the model variables in a series of loops. First a spin-up loop, nominally 2000 years, is run at pre-Industrial conditions with no $CaCO_3$ compensation by calling Core_11Box_N2O_no_CACO3_Comp.m. Below the spin-up loop, the

boundary conditions are changed to the "perturbed state", nominally for a period spanning 4000 years. At this point $CaCO_3$ is included by calling Core_11Box_N2O_CACO3_Comp.m. After that, a spin-down loop is called for 15,000 years. The code is also set up to pre-allocate space for an additional 25,000 years, referred to as the deglacial interval, though this space is not used until "Deglacial Core" is called in a separate piece of code with BBCM_11Box_Deglacial_Core.m

The “Deglacial Core” is used to run the model in a transient experiment. Some code in the preamble calls time series used to drive the model. The important thing is to create a vector of the time series, interpolated to the space of model timestep that equals the total time in the model run. Below the interpolation code, there are also some matrixes that can be manipulated by hand to prescribe the changing boundary conditions. These are also interpolated to the model timestep. The code then calls the Core_11Box_N2O_CACO3_Comp.m code in a loop. Inside the loop, the boundary condition variables are prescribed by overwriting them at each timestep. In order to change what boundary conditions the model actually uses, the variables have to be commented in or out.

The core code called in each loop requires three scripts of code to solve the solubility of CO_2 and O_2: csys3_hack.m; equic.m; O2a_O2oc.m. : The basis for csys3_hack.m and equic.m are taken from a supplement to *CO_2 in Seawater: Equilibrium, Kinetics, Isotopes (*Zeebe and Wolf-Gladrow, 2001) (http://www.soest.hawaii.edu/oceanography/faculty/zeebe_files/CO2_System_in_Seawater/csys.html)

In order to run the model with O_2 and N_2O, the timestep (dt) must be decreased to 0.1 years. The rate-limiting timestep in the model comes from calling the carbonate chemistry code as it requires a function to solve the roots of a polynomial. If the carbon chemistry is not required in the run, or many runs with O_2 are needed, one

should comment out the code that calls csys3_hack.m. Both csys3_hack.m and equic.m are not provided in the dissertation, but can easily be reconstructed from the Zeebe and Wolf-Gladrow supplement. Core_11Box_N2O_no_CACO3_Comp.m code is also not provided but is essentially identical to Core_11Box_N2O_CACO3_Comp.m with the flux in out of the sediments (Fsed) set to zero.

File: BBCM_11Box_LGM_N2O.m

```
%=========================================================================%
%------------------Carbon Cycle Model BBCM---------------------%
%=========================================================================%
%Notes:
%HBEI Index Tested March 18th 2013 ~=0.17-1.19
clear all
tic
iterations = 1;
output = zeros(iterations,33);

nobio = 1;
zeroO2 = 1;
zeroCaCO3 =1;

dt = .5;                          %timestep (years)
spinup_time =2000/dt;             %spinup time (years)
pert_time = 4000/dt;              %perturbation time (years)
spindown_time = 15000/dt;         %spindown time (years)
deglacial_time =25000/dt;
totaltime = spinup_time+pert_time+spindown_time+deglacial_time+1;
%totaltime = spinup_time;

%%
%=========================================================================%
%Conversions
%=========================================================================%
moles = 6.022*10^23;              %Avogadro's number
dSW = 1020;                       %density of seawater (kgm-3)
molmassC = 12.01;                 %molecular mass of carbon
umol2GtC =  molmassC/(10^6*10^15);     %umol Ckg-1 to gigatons of carbon
mol2GtC = molmassC/(10^15);
mmol2mol = 1/1000;
umol2mmol = 1/1000;
GtC2ppm = 2.1276;                 %gigatons of carbon to ppm
Sv2Kg = 10^6*60*60*24*365*dSW;         %Sverdrups to kilograms of water per year
RPDB = .0112020968;               %13C/12C ratio of PDB
R14Cstd = 1.176e-12;              %radiocarbon standard abundance in Muller et al, 2008 GBC
quoting Siegenthaler, 1989
slfactor = 0.0;
%slfactor = rand(1)*.03;
```

```
%%
%=================================================================%
%Physical Parameters and Ocean Geometry
%=================================================================%
lamda = log(2)/5730;                %radiocarbon decay constant
saofearth = 5.1007200e8;
secondsperyear = 365*24*60*60;
%C14P=(2.5e26/moles)*mol2GtC;          %radiocarbon production GtC
C14P = (1.5/moles)*mol2GtC*saofearth*100000^2*secondsperyear;
%2.25 atoms per cm2 per s


LGMDelT = 2.8;
NHLGMDelT = 4.5;
AntLGMDelT = 3.0;
SHLGMDelT = 4.5;
LGMCooling = 0;
SSTMO = 20.5-LGMDelT*LGMCooling;                        %low-latitude SST (C)
SSTPO = 5.5-SHLGMDelT*LGMCooling;
SSTAO = 1.0-AntLGMDelT*LGMCooling;   %polar ocean SST (C)
SSTNA = 3.0-NHLGMDelT*LGMCooling;
%geometry of the ocean

%(oceans by size)
% Total 335,258,000 sq km
%Pacific (155,557,000 sq km) larger map
%Atlantic (76,762,000 sq km) larger map
%Indian (68,556,000 sq km) larger map
%Southern (20,327,000 sq km) larger map
%Arctic (14,056,000 sq km) larger map
%2*pi*6371000^2*(sin(60*(pi/180))-sin(50*(pi/180)))  area of latitude bands
fracPacific = 0.6;                  %fraction ocnea boxes
fracAtlantic = 0.25;
fracPO = 0.08;
fracAO = 0.02;
fracPD = 0.2;
fracNA = 0.025;
fracNP = 0.025;
fracPINTofSurface = 0.75;
Aoc = 3.62e14;                      %area of low-latitude ocean (m2)
hmix = 100;                         %mixed layer depth (m)
hint = 1000;
oceandepth = 3700;                  %depth of interior ocean (m)
%boxnum = 50;                       %number of boxes
%dx = oceandepth/boxnum;            %depth step in meters
Vatmix = Aoc*(fracAtlantic)*hmix;      %volume of ocean boxes
Vpo = Aoc*fracPO*hint;
Vao = Aoc*fracAO*hint;
Vna = Aoc*fracNA*hint;
Vpacificmix = Aoc*(fracPacific)*hmix;
Vnp = Aoc*fracNP*hint;
```

```
Apo = Aoc*fracPO;
Aao = Aoc*fracAO;
Ana = Aoc*fracNA;
Anp = Aoc*fracNP;
Aatlantic = Aoc*fracAtlantic;
Apacific = Aoc*fracPacific;

Vaint = Aoc*fracAtlantic*(hint-hmix);
Vpint = Aoc*fracPacific*(hint-hmix)*fracPINTofSurface;

Vatdeep = Aoc*(1-fracPD)*(fracAtlantic+fracNA)*(oceandepth-hmix)-Vaint;
Vpadeep = Aoc*(1-fracPD)*(fracPacific+fracPO+fracAO)*(oceandepth-hmix)-Vpint;
Vpd = (Aoc*oceandepth)-(Vatmix+Vpo+Vna+Vpacificmix+Vatdeep+Vpadeep+Vpint+Vaint+Vnp);

%Air-sea gas exchange paraemters
kw = 18*365*24*(1/100)*1;                    %kw = 23.5 cm hr-1 = kg =0.065
kwpo = 36*365*24*(1/100)*1;

kg = 0.05*1;      %0.065 bulk  coefficient (mol m-2yr-1uatm-1) Broecker, 1974 via Maier-Reimer and
Hasselmann,1987
kgpo = 0.1*1;
kgpos = 0.1*1;
salinity = 34.72;


%%
%=================================================================%
%Gross Fluxes, Mixing, Nutrient Limitation, Sea-ice coverage
%=================================================================%
Ff = 0*dt;                          %Fossil Fuel Combustion Gt C yr-1

Flph = 45*dt;                        %terrestrial net primary production
Flb = 45*dt;                         %terrestrial ecosystem respiration plus destruction
Flph2 = 45*dt;
Flb2 = 45*dt;

AMOC = 18*dt*Sv2Kg;    %AMOC formation

PFTfrac     =0.7;      %Flow relative to AMOC
NADW2Indfrac=0.25;     %13/18 must feed into AABW
NADW2AOfrac =0.75;
NADW2CDWfrac=0.0;
NADW2SOfrac =0.0;

PFT  = AMOC*PFTfrac;
NADW2Ind = AMOC*NADW2Indfrac;
NADW2AO = AMOC*NADW2AOfrac;
NADW2CDW = AMOC*NADW2CDWfrac;
NADW2SO = AMOC*NADW2SOfrac;
NADW2IndPac = NADW2Ind+NADW2AO+NADW2CDW;


AMOCLow = (AMOC-PFT)*.6;
AAIWP = NADW2IndPac *.35;
```

```
CDWP = 16*dt*Sv2Kg;  %CDW overturning to Pacific
CDWA = 6*dt*Sv2Kg;   %CDW overturning to Atlantic

CDW = CDWA+CDWP;


Fnppint = 5*dt*Sv2Kg;  %Mixing between boxes
Fnaod = 10*dt*Sv2Kg;

Fpaspint = 15*dt*Sv2Kg;
Fosaint =8*dt*Sv2Kg;

Fso2ao = 2*dt*Sv2Kg;
Fpaspad = 0*dt*Sv2Kg;

Fpint2pad = 4*dt*Sv2Kg;
Faint2od = 1*dt*Sv2Kg;

Fpd2pad =8*dt*Sv2Kg;
Fpd2od = 3*dt*Sv2Kg;

b = 1.25;      %reminerlization exponent

PO4starAT = 0.2;  %restoring PO4
PO4starPAC = 0.2;
PO4starPO = 1.4;
PO4starAO = 1.8;
PO4starNA = 0.6;
PO4starNP = 1;


fracbiopo2pac = 0.0;   %sending export to deeper boxes
fracbioop2atl = 0.0;
frac2pd = 0;
effdepthAABW = 3000;
fracseaiceSO = 1;       %Fraction sea-ice free
fracseaiceAO = .85;
fracseaiceNA = .85;
fracseaiceNP = .85;

Reef = 0;
rO2PO4 = 170;      %ratios of O2,PO4, CaCO3, C, etc
rALKPO4 = 50;      %taken from Toggweiller, 1999
FCA = 0.0;
rCorgPO4 = 117;
rCPO4p = rCorgPO4/(1-FCA);
rCorgO2 = rCPO4p/rO2PO4;
%rALKC = rCPO4p/rALKPO4;
rALKC = .5;

FCAlowlat = 0.1*zeroCaCO3; %dissolution of CaCO3 at depth
FCANA = .05*zeroCaCO3;
FCASO = .00*zeroCaCO3;
FCANP = 0.1*zeroCaCO3;
```

```
FCAremin = 0.1;

ased1 = 0.6;     %impulse response function for CaCO3 comp.
taused1 = 5500;
ased2 = 0.1;
taused2 = 8200;
ased3 = 0.3;
taused3 = 200000;

zscale  = 3000;   %N2O production parameters
RNO2  = 16/170;
O2crit = 4;
a1 = 0.26;
a2 = -0.0004;



%%
%=================================================================%
%Preallocating array space
%=================================================================%
Fatao =zeros(1,totaltime);
Fatoa=zeros(1,totaltime);

Fsoao=zeros(1,totaltime);
Fsooa=zeros(1,totaltime);

Faoao=zeros(1,totaltime);
Faooa=zeros(1,totaltime);

Fnaao=zeros(1,totaltime);
Fnaoa=zeros(1,totaltime);


Fpaao=zeros(1,totaltime);
Fpaoa=zeros(1,totaltime);

PO4deepPre=zeros(1,totaltime);
PO4PDPre=zeros(1,totaltime);
PO4PADPre=zeros(1,totaltime);
PO4PINTPre=zeros(1,totaltime);
PO4AINTPre=zeros(1,totaltime);

Fnpao=zeros(1,totaltime);
Fnpoa=zeros(1,totaltime);

FO2atao=zeros(1,totaltime);
FO2atoa=zeros(1,totaltime);


FO2soao=zeros(1,totaltime);
FO2sooa=zeros(1,totaltime);

FO2naao=zeros(1,totaltime);
```

```
FO2naoa=zeros(1,totaltime);

FO2paao=zeros(1,totaltime);
FO2paoa=zeros(1,totaltime);

FO2aoao=zeros(1,totaltime);
FO2aooa=zeros(1,totaltime);

FO2npao=zeros(1,totaltime);
FO2npoa=zeros(1,totaltime);

O2atm = zeros(1,totaltime);
Ca= zeros(1,totaltime);
Ra= zeros(1,totaltime);
C13a= zeros(1,totaltime);
d13Ca= zeros(1,totaltime);
R14a= zeros(1,totaltime);
C14a= zeros(1,totaltime);

Rb= zeros(1,totaltime);
C13b= zeros(1,totaltime);
d13Cb= zeros(1,totaltime);
R14b= zeros(1,totaltime);
C14b= zeros(1,totaltime);

Rb2= zeros(1,totaltime);
C13b2= zeros(1,totaltime);
d13Cb2= zeros(1,totaltime);
R14b2= zeros(1,totaltime);
C14b2= zeros(1,totaltime);

Cos= zeros(1,totaltime);
Ros= zeros(1,totaltime);
C13os= zeros(1,totaltime);
d13Cos= zeros(1,totaltime);
R14os= zeros(1,totaltime);
C14os= zeros(1,totaltime);

Cpaos= zeros(1,totaltime);
Rpaos= zeros(1,totaltime);
C13paos= zeros(1,totaltime);
d13Cpaos= zeros(1,totaltime);
R14paos= zeros(1,totaltime);
C14paos= zeros(1,totaltime);

Cod= zeros(1,totaltime);
Rod= zeros(1,totaltime);
C13od= zeros(1,totaltime);
d13Cod= zeros(1,totaltime);
R14od= zeros(1,totaltime);
C14od= zeros(1,totaltime);

Caint= zeros(1,totaltime);
Raint= zeros(1,totaltime);
```

```
C13aint= zeros(1,totaltime);
d13Caint= zeros(1,totaltime);
R14aint= zeros(1,totaltime);
C14aint= zeros(1,totaltime);

Cpint= zeros(1,totaltime);
Rpint= zeros(1,totaltime);
C13pint= zeros(1,totaltime);
d13Cpint= zeros(1,totaltime);
R14pint= zeros(1,totaltime);
C14pint= zeros(1,totaltime);

Cpaod= zeros(1,totaltime);
Rpaod= zeros(1,totaltime);
C13paod= zeros(1,totaltime);
d13Cpaod= zeros(1,totaltime);
R14paod= zeros(1,totaltime);
C14paod= zeros(1,totaltime);

Cao= zeros(1,totaltime);
Rao= zeros(1,totaltime);
C13ao= zeros(1,totaltime);
d13Cao= zeros(1,totaltime);
R14ao= zeros(1,totaltime);
C14ao= zeros(1,totaltime);


Cpo= zeros(1,totaltime);
Rpo= zeros(1,totaltime);
C13po= zeros(1,totaltime);
d13Cpo= zeros(1,totaltime);
R14po= zeros(1,totaltime);
C14po= zeros(1,totaltime);

Cpd= zeros(1,totaltime);
Rpd= zeros(1,totaltime);
C13pd= zeros(1,totaltime);
d13Cpd= zeros(1,totaltime);
R14pd= zeros(1,totaltime);
C14pd= zeros(1,totaltime);

Cna= zeros(1,totaltime);
Rna= zeros(1,totaltime);
C13na= zeros(1,totaltime);
d13Cna= zeros(1,totaltime);
R14na= zeros(1,totaltime);
C14na= zeros(1,totaltime);

Cnp= zeros(1,totaltime);
Rnp= zeros(1,totaltime);
C13np= zeros(1,totaltime);
d13Cnp= zeros(1,totaltime);
R14np= zeros(1,totaltime);
C14np= zeros(1,totaltime);
```

```
Catm = zeros(1,totaltime);
d14Ca= zeros(1,totaltime);
d14Cb = zeros(1,totaltime);
d14Cb2 = zeros(1,totaltime);
d14Cos= zeros(1,totaltime);
d14Cpo= zeros(1,totaltime);
d14Cod= zeros(1,totaltime);
d14Cpd= zeros(1,totaltime);
d14Cna= zeros(1,totaltime);
d14Cpaos= zeros(1,totaltime);
d14Cpaod= zeros(1,totaltime);
d14Cpint= zeros(1,totaltime);
d14Caint= zeros(1,totaltime);
d14Cao= zeros(1,totaltime);
d14Cnp= zeros(1,totaltime);

Cb = zeros(1,totaltime);
Cb2= zeros(1,totaltime);

DICsurf = zeros(1,totaltime);
ALKsurf = zeros(1,totaltime+1);

DICpaosurf = zeros(1,totaltime);
ALKPAS = zeros(1,totaltime+1);

DICNA = zeros(1,totaltime);
ALKNA = zeros(1,totaltime+1);
DICPO = zeros(1,totaltime);
ALKPO = zeros(1,totaltime+1);

DICPD = zeros(1,totaltime);
ALKPD = zeros(1,totaltime+1);

DICPINT = zeros(1,totaltime);
ALKPINT = zeros(1,totaltime+1);

DICAINT = zeros(1,totaltime);
ALKAINT = zeros(1,totaltime+1);


DICdeep = zeros(1,totaltime);
pCO2s = zeros(1,totaltime);
pCO2paos = zeros(1,totaltime);
pCO2PO = zeros(1,totaltime);
pCO2AO = zeros(1,totaltime);

CO2 = zeros(1,totaltime);
CO3 = zeros(1,totaltime);

PO4surf = zeros(1,totaltime);
O2surf = zeros(1,totaltime);
```

```
ALKdeep= zeros(1,totaltime+1);
PO4deep= zeros(1,totaltime);
O2deep= zeros(1,totaltime);
pCO2PD = zeros(1,totaltime);



PO4PO= zeros(1,totaltime);
O2PO= zeros(1,totaltime);

PO4PINT= zeros(1,totaltime);
O2PINT= zeros(1,totaltime);

PO4AINT= zeros(1,totaltime);
O2AINT= zeros(1,totaltime);

PO4PD= zeros(1,totaltime);
O2PD= zeros(1,totaltime);

PO4NA= zeros(1,totaltime);
O2NA= zeros(1,totaltime);
pCO2NA = zeros(1,totaltime);

PO4PAS= zeros(1,totaltime);
O2PAS= zeros(1,totaltime);

DICPAD= zeros(1,totaltime);
PO4PAD= zeros(1,totaltime);
O2PAD= zeros(1,totaltime);
ALKPAD= zeros(1,totaltime);


DICAO= zeros(1,totaltime);
PO4AO= zeros(1,totaltime);
O2AO= zeros(1,totaltime);
ALKAO= zeros(1,totaltime);

DICNP= zeros(1,totaltime);
PO4NP= zeros(1,totaltime);
O2NP= zeros(1,totaltime);
pCO2NP = zeros(1,totaltime);
ALKNP = zeros(1,totaltime);

Fsed = zeros(1,totaltime);
dN2OPINT = zeros(1,totaltime);
dN2OAINT= zeros(1,totaltime);
dN2OPD= zeros(1,totaltime);
dN2OPAD= zeros(1,totaltime);
dN2Odeep= zeros(1,totaltime);
TotalN2O =zeros(1,totaltime);
TotalC =zeros(1,totaltime);
TotalC13 =zeros(1,totaltime);
TotalC14 =zeros(1,totaltime);
TotalO2 = zeros(1,totaltime);
```

```
TotalPO4 = zeros(1,totaltime);
TotalALK = zeros(1,totaltime);
TotalPO4Pre = zeros(1,totaltime);


%%
%=================================================================%
%  Initial Conditions
%=================================================================%
%d13C and Fractionation Factors  (mostly from Tans, 1993, GBC)
initiald13C = 0.65;
dos = initiald13C;              %delta of surface waters
dod = initiald13C;              %delta of interior ocean
dpo = initiald13C;              %delta of polar ocean
dao = initiald13C;              %delta of polar ocean
dpd = initiald13C;              %delta of polar ocean
dna = initiald13C;              %delta of polar ocean
dpas = initiald13C;             %delta of polar ocean
dpad = initiald13C;             %delta of polar ocean
dpint = initiald13C;
daint = initiald13C;
dnp = initiald13C;


df = -60;                     %delta of fossil fuel
Rf = (df/(10^3)+1)*RPDB;
da = -6.5;                    %delta of atmosphere
dlb = -24.2;                   %delta of biosphere
dlb2 = -24.2;


d14os = 0;                     %delta of surface waters
d14od = -70;                    %delta of interior ocean
d14po = -70;                    %delta of polar ocean
d14ao = -70;
d14pd = -180;                   %delta of polar ocean
d14na = -30;                   %delta of polar ocean
d14paos = 0;                   %delta of polar ocean
d14paod = -180;                  %delta of polar ocean
d14pint = -120;
d14aint = -120;
d14np = -120;



d14f = -1000;                   %delta of fossil fuel
R14f = (d14f/(10^3)+1)*R14Cstd;
d14a = 0;                     %delta of atmosphere
d14lb = -45;                    %delta of biosphere
d14lb2 = -38;


%aao = (.0049*SSTMO-1.31)/(10^3)+1;
```

```
%eao = -2.05;                %kinetic frationation during air-sea transfer
%aao = eao/(10^3)+1;
%aoa = -(-0.1141*SSTMO+10.78)/(10^3)+1;
%aoa = -(-0.1141*SSTPO+10.78)/(10^3)+1;
%eoa = -10.83;

%aoa = (1.02389-9.483/(SSTMO+273.15)); %kinetic fractionation during sea-air transfer (Trudinger,
2001)
%apoa = (1.02389-9.483/(SSTPO+273.15));

elph = -18.0;                %fractionation of terrestrial photosynthesis
alph = elph/(10^3)+1;
eoph = -24.0;                %fractionation of oceanic photosynthesis
aoph = eoph/(10^3)+1;


molesatm = 1.77e20;          %moles of O2 in the atmosphere 1.77e20 moles of dry air Schlesinger
1997 in Headley and Severinghaus
O2atm(1) = 0.20946;
Catm(1) = 280;               %Atmosphere CO2 (ppm)
Cb(1) = 1100;                %Terrestrial Biosphere  C (GtC)
Cb2(1) = 500;


DICsurf(1) = 2249;           %Ocean Box DIC (umolkg-1)
ALKsurf(1)=2364*(1+slfactor);    %Ocean Box ALK(umolkg-1)
PO4surf(1) = 2.17;           %Ocean Box PO4
O2surf(1) = 180;             %Ocean Box O2

DICdeep(1) = 2249;
ALKdeep(1) = 2364*(1+slfactor);
PO4deep(1)  = 2.17;
O2deep(1) = 180;

DICPO(1) = 2249;
ALKPO(1) = 2364*(1+slfactor);
PO4PO(1)  =2.17;
O2PO(1) = 180;

DICAO(1) = 2249;
ALKAO(1) = 2364*(1+slfactor);
PO4AO(1)  =2.17;
O2AO(1) = 180;

DICNA(1) = 2249;
ALKNA(1) = 2364*(1+slfactor);
PO4NA(1)  =2.17;
O2NA(1) = 180;

DICPD(1) = 2249;
ALKPD(1) = 2364;
PO4PD(1)  =2.17;
O2PD(1) = 180;
```

```
DICpaosurf(1) = 2249;
ALKPAS(1) =2364*(1+slfactor);
PO4PAS(1) = 2.17;
O2PAS(1) = 180;

DICPAD(1) = 2249;
ALKPAD(1) =2364*(1+slfactor);
PO4PAD(1) = 2.17;
O2PAD(1) = 180;


DICPINT(1) = 2249;
ALKPINT(1) =2364*(1+slfactor);
PO4PINT(1) = 2.17;
O2PINT(1) = 180;

DICAINT(1) = 2249;
ALKAINT(1) =2364*(1+slfactor);
PO4AINT(1) = 2.17;
O2AINT(1) = 180;

DICNP(1) = 2249;
ALKNP(1) = 2364*(1+slfactor);
PO4NP(1)  =2.17;
O2NP(1) = 180;


%Conversions to calculate isotope ratios, total C in ocean in boxes, set initial conditions, etc

clear DICs ALKs SST pCO2init
DICs = DICsurf(1);
ALKs = ALKsurf(1);
SST = SSTMO;
csys3_hack; %function takes DICs, ALKs, SST and calculates carbonate parameters.  Namely, pCO2
(ppm)
CO2_init = CO2_r;
pCO2s_init = PC02_r;
pCO2s(1) = pCO2s_init;


clear DICs ALKs SST pCO2init
DICs = DICPO(1);
ALKs = ALKPO(1);
SST = SSTPO;
csys3_hack;
pCO2po_init = PC02_r;
pCO2PO(1) = pCO2po_init;

clear DICs ALKs SST pCO2init
DICs = DICNA(1);
ALKs = ALKNA(1);
SST = SSTNA;
csys3_hack;
pCO2na_init = PC02_r;
```

```
pCO2NA(1) = pCO2na_init;

clear DICs ALKs SST pCO2init
DICs = DICpaosurf(1);
ALKs = ALKPAS(1);
SST = SSTMO;
csys3_hack;
pCO2paos_init = PC02_r;
pCO2paos(1) = pCO2paos_init;

clear DICs ALKs SST pCO2init
DICs = DICAO(1);
ALKs = ALKAO(1);
SST = SSTPO;
csys3_hack;
pCO2AO_init = PC02_r;
pCO2AO(1) = pCO2AO_init;

clear DICs ALKs SST pCO2init
DICs = DICNP(1);
ALKs = ALKNP(1);
SST = SSTNA;
csys3_hack;
pCO2np_init = PC02_r;
pCO2NP(1) = pCO2np_init;

Ca(1) = Catm(1)*GtC2ppm;
Ra(1) = (da/(10^3)+1)*RPDB;
C13a(1) = Ra(1)*Ca(1);
d13Ca(1) = (((Ra(1)*Ca(1))/Ca(1))/RPDB-1)*10^3;
R14a(1) = (d14a/(10^3)+1)*R14Cstd;
C14a(1) = R14a(1)*Ca(1);

Rb(1) = (dlb/(10^3)+1)*RPDB;
C13b(1) = Rb(1)*Cb(1);
d13Cb(1) = (((Rb(1)*Cb(1))/Cb(1))/RPDB-1)*10^3;
R14b(1) = (d14lb/(10^3)+1)*R14Cstd;
C14b(1) = R14b(1)*Cb(1);

Rb2(1) = (dlb2/(10^3)+1)*RPDB;
C13b2(1) = Rb2(1)*Cb2(1);
d13Cb2(1) = (((Rb2(1)*Cb2(1))/Cb2(1))/RPDB-1)*10^3;
R14b2(1) = (d14lb2/(10^3)+1)*R14Cstd;
C14b2(1) = R14b2(1)*Cb2(1);

Cos(1) = DICsurf(1)*Vatmix*dSW*umol2GtC;
Ros(1) = (dos/(10^3)+1)*RPDB;
C13os(1) = Ros(1)*Cos(1);
d13Cos(1) = (((Ros(1)*Cos(1))/Cos(1))/RPDB-1)*10^3;
R14os(1) = (d14os/(10^3)+1)*R14Cstd;
C14os(1) = R14os(1)*Cos(1);

Cpaos(1) = DICpaosurf(1)*Vpacificmix*dSW*umol2GtC;
Rpaos(1) = (dpas/(10^3)+1)*RPDB;
```

```
C13paos(1) = Rpaos(1)*Cpaos(1);
d13Cpaos(1) = (((Rpaos(1)*Cpaos(1))/Cpaos(1))/RPDB-1)*10^3;
R14paos(1) = (d14paos/(10^3)+1)*R14Cstd;
C14paos(1) = R14paos(1)*Cpaos(1);

Cod(1) = DICdeep(1)*Vatdeep*dSW*umol2GtC;
Rod(1) = (dod/(10^3)+1)*RPDB;
C13od(1) = Rod(1)*Cod(1);
d13Cod(1) = (((Rod(1)*Cod(1))/Cod(1))/RPDB-1)*10^3;
R14od(1) = (d14od/(10^3)+1)*R14Cstd;
C14od(1) = R14od(1)*Cod(1);

Cpaod(1) = DICPAD(1)*Vpadeep*dSW*umol2GtC;
Rpaod(1) = (dpad/(10^3)+1)*RPDB;
C13paod(1) = Rpaod(1)*Cpaod(1);
d13Cpaod(1) = (((Rpaod(1)*Cpaod(1))/Cpaod(1))/RPDB-1)*10^3;
R14paod(1) = (d14paod/(10^3)+1)*R14Cstd;
C14paod(1) = R14paod(1)*Cpaod(1);

Cpo(1) = DICPO(1)*Vpo*dSW*umol2GtC;
Rpo(1) = (dpo/(10^3)+1)*RPDB;
C13po(1) = Rpo(1)*Cpo(1);
d13Cpo(1) = (((Rpo(1)*Cpo(1))/Cpo(1))/RPDB-1)*10^3;
R14po(1) = (d14po/(10^3)+1)*R14Cstd;
C14po(1) = R14po(1)*Cpo(1);


Cao(1) = DICAO(1)*Vao*dSW*umol2GtC;
Rao(1) = (dao/(10^3)+1)*RPDB;
C13ao(1) = Rao(1)*Cao(1);
d13Cao(1) = (((Rao(1)*Cao(1))/Cao(1))/RPDB-1)*10^3;
R14ao(1) = (d14ao/(10^3)+1)*R14Cstd;
C14ao(1) = R14ao(1)*Cao(1);


Cpd(1) = DICPD(1)*Vpd*dSW*umol2GtC;
Rpd(1) = (dpd/(10^3)+1)*RPDB;
C13pd(1) = Rpd(1)*Cpd(1);
d13Cpd(1) = (((Rpd(1)*Cpd(1))/Cpd(1))/RPDB-1)*10^3;
R14pd(1) = (d14pd/(10^3)+1)*R14Cstd;
C14pd(1) = R14pd(1)*Cpd(1);

Cna(1) = DICNA(1)*Vna*dSW*umol2GtC;
Rna(1) = (dna/(10^3)+1)*RPDB;
C13na(1) = Rna(1)*Cna(1);
d13Cna(1) = (((Rna(1)*Cna(1))/Cna(1))/RPDB-1)*10^3;
R14na(1) = (d14na/(10^3)+1)*R14Cstd;
C14na(1) = R14na(1)*Cna(1);

Cnp(1) = DICNP(1)*Vnp*dSW*umol2GtC;
Rnp(1) = (dnp/(10^3)+1)*RPDB;
C13np(1) = Rnp(1)*Cnp(1);
d13Cnp(1) = (((Rnp(1)*Cnp(1))/Cnp(1))/RPDB-1)*10^3;
R14np(1) = (d14np/(10^3)+1)*R14Cstd;
```

```
C14np(1) = R14np(1)*Cnp(1);

Cpint(1) = DICPINT(1)*Vpint*dSW*umol2GtC;
Rpint(1) = (dpint/(10^3)+1)*RPDB;
C13pint(1) = Rpint(1)*Cpint(1);
d13Cpint(1) = (((Rpint(1)*Cpint(1))/Cpint(1))/RPDB-1)*10^3;
R14pint(1) = (d14pint/(10^3)+1)*R14Cstd;
C14pint(1) = R14pint(1)*Cpint(1);

Caint(1) = DICAINT(1)*Vaint*dSW*umol2GtC;
Raint(1) = (daint/(10^3)+1)*RPDB;
C13aint(1) = Raint(1)*Caint(1);
d13Caint(1) = (((Raint(1)*Caint(1))/Caint(1))/RPDB-1)*10^3;
R14aint(1) = (d14aint/(10^3)+1)*R14Cstd;
C14aint(1) = R14aint(1)*Caint(1);

%%
%=================================================================%
%Spin-up Loop
%=================================================================%

for t = 1:spinup_time
eval('Core_11Box_N2O_no_CaCO3_Comp')
%eval('Core_11Box_N2O_no_CO2')
end
%%
%=================================================================%
%Perturbation Loop
%=================================================================%
salinity = 34.72*(1+(110/3700));

LGMDelT = 2.8;
NHLGMDelT = 4.5;
AntLGMDelT = 3.0;
SHLGMDelT = 4.5;

LGMCooling = 1;
SSTMO = 20.5-LGMDelT*LGMCooling;
SSTPO = 5.5-SHLGMDelT*LGMCooling;
SSTAO = 1.0-AntLGMDelT*LGMCooling;
SSTNA = 3.0-NHLGMDelT*LGMCooling;


landcarbonloss = 500;

Flb = 45*dt+landcarbonloss/pert_time;


AMOC = 14*dt*Sv2Kg;
PFTfrac =     0.4;
NADW2Indfrac= 0.25;     %13/18 must feed into AABW
NADW2AOfrac=  0.0;
NADW2CDWfrac= 0.0;
NADW2SOfrac=  0.75;
```

```
PFT  = AMOC*PFTfrac;
NADW2Ind = AMOC*NADW2Indfrac;
NADW2AO = AMOC*NADW2AOfrac;
NADW2CDW = AMOC*NADW2CDWfrac;
NADW2SO = AMOC*NADW2SOfrac;
NADW2IndPac = NADW2Ind+NADW2AO+NADW2CDW;


AMOCLow = (AMOC-PFT)*.6;
AAIWP = NADW2IndPac *.35;

CDWP = 16*dt*Sv2Kg;
CDWA = 16*dt*Sv2Kg;

CDW = CDWA+CDWP;

%Fpd2pad =0*dt*Sv2Kg;
%Fpd2od = 0*dt*Sv2Kg;


PO4starAT = 0.2;
PO4starPAC = 0.2;
PO4starPO = 0.2;
%PO4starAO = 1.6;
%PO4starNA = 0.6;
%PO4starNP = 1;
%kgpos = 0.1*(1-0.25^.5);
fracseaiceSO = 1;
fracseaiceAO = .01;
fracseaiceNA = .85;
fracseaiceNP = .85;

%kg = 0.1*(1+0.25^.5);

for t = spinup_time+1:spinup_time+pert_time
eval('Core_11Box_N2O_CaCO3_Comp')
%eval('Core_11Box_N2O_no_CO2')
end
Flb = 45*dt;

%%
%=================================================================%
%Spindown Loop
%=================================================================%
for t = spinup_time+pert_time+1:spinup_time+pert_time+spindown_time
eval('Core_11Box_N2O_CaCO3_Comp')
%eval('Core_11Box_N2O_no_CO2')
end

%for t = spinup_time+pert_time+spindown_time+1:totaltime
%eval('Core_11Box_no_CaCO3_Comp_Testing_NADW')
%end
```

```
%%
%================================================================%
%Output
%================================================================%


      [DICsurf(end) ALKsurf(end-1) PO4surf(end) O2surf(end) d13Cos(end) d14Ca(end)-
d14Cos(end);...
       DICpaosurf(end) ALKPAS(end-1) PO4PAS(end) O2PAS(end) d13Cpaos(end) d14Ca(end)-
d14Cpaos(end);...
       DICNA(end) ALKNA(end-1) PO4NA(end) O2NA(end) d13Cna(end) d14Ca(end)-
d14Cna(end);...
       DICNP(end) ALKNP(end-1) PO4NP(end) O2NP(end) d13Cnp(end) d14Ca(end)-d14Cnp(end);...
       DICAO(end) ALKAO(end-1) PO4AO(end) O2AO(end) d13Cao(end) d14Ca(end)-
d14Cao(end);...
       DICPO(end) ALKPO(end-1) PO4PO(end) O2PO(end) d13Cpo(end) d14Ca(end)-d14Cpo(end);...
       DICAINT(end) ALKAINT(end-1) PO4AINT(end) O2AINT(end) d13Caint(end) d14Ca(end)-
d14Caint(end);...
       DICPINT(end) ALKPINT(end-1) PO4PINT(end) O2PINT(end) d13Cpint(end) d14Ca(end)-
d14Cpint(end);...
       DICPAD(end) ALKPAD(end-1) PO4PAD(end) O2PAD(end) d13Cpaod(end) d14Ca(end)-
d14Cpaod(end);...
       DICdeep(end) ALKdeep(end-1) PO4deep(end) O2deep(end) d13Cod(end) d14Ca(end)-
d14Cod(end);...
       DICPD(end) ALKPD(end-1) PO4PD(end) O2PD(end) d13Cpd(end) d14Ca(end)-d14Cpd(end)]
%    DICPD(end) PO4PD(end) O2PD(end) d13Cpd(end) d14Cpd(end)];


Catm(21000/dt)
d13Ca(21000/dt)

%(PO4NP(end)-PO4starNP)*rCPO4p*umol2GtC*Vnp*dSW*nobio+(PO4PAS(end)-
PO4starPAC)*rCPO4p*umol2GtC*Vpacificmix*dSW*nobio+(PO4NA(end)-
PO4starNA)*rCPO4p*umol2GtC*Vna*dSW*nobio+(PO4surf(end)-
PO4starAT)*rCPO4p*umol2GtC*Vatmix*dSW*nobio+(PO4PO(end)-
PO4starPO)*rCPO4p*umol2GtC*Vpo*dSW*nobio+(PO4AO(end)-
PO4starAO)*rCPO4p*umol2GtC*Vao*dSW*nobio

%[PO4AO(end) PO4PO(end) PO4PAS(end) PO4surf(end) PO4NA(end) PO4NP(end) PO4PD(end)
PO4PAD(end) PO4deep(end) PO4PINT(end) PO4AINT(end)]
if (PO4NA(end)-PO4starNA)<0
  display('zero PO4 in the north atlantic')

else
end
if (PO4AO(t)-PO4starAO)<0
   display('zero PO4 in antarctic southern ocean')
else
end
%[O2PO(end) O2PD(end) O2PAD(end) O2PAS(end) O2deep(end) O2surf(end) O2NA(end)]
%(O2PD(end)*Vpd+O2PO(end)*Vpo+O2deep(end)*Vatdeep+O2surf(end)*Vatmix+O2NA(end)*Vn
a+O2PAS(end)*Vpacificmix+O2PAD(end)*Vpadeep)/(Aoc*3700)
```

```
%(O2PD(end)*Vpd+O2deep(end)*Vatdeep+O2PAD(end)*Vpadeep)/(Vpadeep+Vatdeep+Vpd)
%(PO4PD(end)*Vpd+PO4deep(end)*Vatdeep+PO4PAD(end)*Vpadeep)/(Vpadeep+Vatdeep+Vpd)
%(O2PO(end)*Vpo+O2surf(end)*Vatmix+O2NA(end)*Vna+O2PAS(end)*Vpacificmix)/(Vpo+Vatm
ix+Vna+Vpacificmix)
%(PO4PO(end)*Vpo+PO4surf(end)*Vatmix+PO4NA(end)*Vna+PO4PAS(end)*Vpacificmix)/(Vpo+
Vatmix+Vna+Vpacificmix)

toc


subplot(6,1,1)
hold on
plot(d13Ca(2000:20000/dt), 'r')
subplot(6,1,2)
hold on
plot(Catm(2000:20000/dt), 'r')
subplot(6,1,3)
hold on
plot(d14Ca(2000:20000/dt), 'r')
subplot(6,1,4)
hold on
plot(d13Cpd(2000:20000/dt), 'r')
subplot(6,1,5)
hold on
plot(d13Cpaod(2000:20000/dt), 'r')
subplot(6,1,6)
hold on
plot(d13Cod(2000:20000/dt), 'r')
```

File: BBCM_11Box_Deglacial_Core.m

```
%================================================================%
%------------Running Deglacial Scenarios from LGM--------------%
%================================================================%

load('Stacks_wzero_age.txt')
load('30degree_means.txt')
load('waelbroeck2002.txt')
load('AntComp_Mod4Model.txt')
load('EDML_Dust_Mod4Model.txt')          %no smoothing, NANs removed in excel, 25 and 0 ka
normalized to mean from 25-24 ka and 2-1 ka, respectively
load('EDML_Dust_Mod4Model_Smoothed.txt')   %interpolated with cubic spline in IGOR, 25 and 0
ka normalized to mean from 25-24 ka and 2-1 ka, respectively
load('EDML_Dust_Mod4Model_Smoothed_nospikes.txt')
load('EDML_Smoothed_nssCA_mod4Model.txt')
load('TalosDome_FeFlux_mod4model.txt')
load('NGRIP_mod4model_deglacial.txt')
load('EDML_Dust_Agemodel1.txt')
load('EDML_LD_2011.txt')
load('EDML_Smoothed_nssCA_mod4Model.txt')
%================================================================%
%Re-prescribing LGM SST boundary conditions
%================================================================%
```

```
LGMDelT = 2.8;
NHLGMDelT = 4.5;
AntLGMDelT = 3.0;
SHLGMDelT = 4.5;
LGMCooling = 1;
SSTMO = 20.5-LGMDelT*LGMCooling;
SSTPO = 5.5-SHLGMDelT*LGMCooling;
SSTAO = 1.0-AntLGMDelT*LGMCooling;
SSTNA = 3.0-NHLGMDelT*LGMCooling;

%=========================================================================%
%Constructing SST/Dust/Sealevel Stacks to drive mode
%=========================================================================%

SSTMOstack = [X30degree_means(:,1)
(X30degree_means(:,4)*0.11+X30degree_means(:,6)*0.34+X30degree_means(:,8)*0.36+X30degree_
means(:,10)*0.19)-
(X30degree_means(end,4)*0.11+X30degree_means(end,6)*0.34+X30degree_means(end,8)*0.36+X3
0degree_means(end,10)*0.19)];

SSTPOstack = [X30degree_means(:,1) (X30degree_means(:,10)-X30degree_means(end,10))];

SSTNAstack = [NGRIP_mod4model_deglacial(:,1) (NGRIP_mod4model_deglacial(:,2)-
NGRIP_mod4model_deglacial(end,2))];
int = (0.0:(dt/1000):25)';
SSTMOyi = flipud(interp1(SSTMOstack(:,1),SSTMOstack(:,2)/(3/LGMDelT),int, 'linear'));
SSTPOyi = flipud(interp1(SSTPOstack(:,1),SSTPOstack(:,2),int, 'linear'));
%SSTNAyi = flipud(interp1(SSTNAstack(:,1),SSTNAstack(:,2),int, 'linear'));
SSTNAyi = flipud(interp1(SSTNAstack(:,1),SSTNAstack(:,2)/(9/NHLGMDelT),int, 'linear'));
%SSTAOyi = flipud(interp1(SSTPOstack(:,1),SSTPOstack(:,2)/(4.5/AntLGMDelT),int, 'linear'));
SSTAOyi =flipud(interp1(AntComp_Mod4Model(:,1),(AntComp_Mod4Model(:,2)-
AntComp_Mod4Model(end,2))*AntLGMDelT/(AntComp_Mod4Model(1,2)-
AntComp_Mod4Model(end,2)),int, 'linear'));

%normAntComp4seaice =
flipud(interp1(AntComp_Mod4Model(:,1),AntComp_Mod4Model(:,2)/((AntComp_Mod4Model(1,2)-
AntComp_Mod4Model(end,2))/.7),int, 'linear'));
%fracseaiceyi = normAntComp4seaice-normAntComp4seaice(1)+.05;

%normEDMLDust4seaice =
flipud(interp1(EDML_Dust_Mod4Model_Smoothed(:,1),EDML_Dust_Mod4Model_Smoothed(:,2)/((
EDML_Dust_Mod4Model_Smoothed(1,2)-EDML_Dust_Mod4Model_Smoothed(end,2))/.7),int,
'linear'));
%fracseaiceyi = normEDMLDust4seaice-normEDMLDust4seaice(1)+.05;

EDML_Smoothed_nssCa_LD2011 = [EDML_LD_2011(:,2)/1000
interp1(EDML_Dust_Agemodel1(:,1),interp1(EDML_Smoothed_nssCA_mod4Model(:,1),EDML_Sm
oothed_nssCA_mod4Model(:,2),EDML_Dust_Agemodel1(:,2)),EDML_LD_2011(:,1))];

normEDMLDust4iron = flipud(interp1(EDML_Smoothed_nssCa_LD2011(:,1)-
.2,EDML_Smoothed_nssCa_LD2011(:,2)/((EDML_Smoothed_nssCa_LD2011(1,2)-
EDML_Smoothed_nssCa_LD2011(700,2))/1.2),int, 'linear'));
ironfertyi = normEDMLDust4iron-normEDMLDust4iron(1)+.20;
```

```
%normEDMLDust4iron = flipud(interp1(EDML_Smoothed_nssCA_mod4Model(:,1)-
.2,EDML_Smoothed_nssCA_mod4Model(:,2)/((EDML_Smoothed_nssCA_mod4Model(1,2)-
EDML_Smoothed_nssCA_mod4Model(end,2))/1.2),int, 'linear'));
%ironfertyi = normEDMLDust4iron-normEDMLDust4iron(1)+.20;

%normEDMLDust4iron =
flipud(interp1(TalosDome_FeFlux_mod4model(:,1),TalosDome_FeFlux_mod4model(:,2)/((TalosDom
e_FeFlux_mod4model(1,2)-TalosDome_FeFlux_mod4model(end,2))/.9),int, 'linear'));
%ironfertyi = normEDMLDust4iron-normEDMLDust4iron(1)+.40;

sealevel = flipud(interp1(waelbroeck2002(:,1),waelbroeck2002(:,5),int, 'linear'));

%=================================================================%
%Re-prescribing LGM boundary conditions
%=================================================================%

Flph = 45*dt;                    %terrestrial net primary production
Flb = 45*dt;                     %terrestrial ecosystem respiration plus destruction
Flph2 = 45*dt;
Flb2 = 45*dt;

Ff = 0*dt;                       %Fossil Fuel Combustion Gt C yr-1

salinity = 34.72*(1+(110/3700));
%salinity = 34.72;

AMOC = 14*dt*Sv2Kg;
PFTfrac =     0.4;
NADW2Indfrac= 0.25;     %13/18 must feed into AABW
NADW2AOfrac=  0.0;
NADW2CDWfrac= 0.0;
NADW2SOfrac=  0.75;
PFT  = AMOC*PFTfrac;
NADW2Ind = AMOC*NADW2Indfrac;
NADW2AO = AMOC*NADW2AOfrac;
NADW2CDW = AMOC*NADW2CDWfrac;
NADW2SO = AMOC*NADW2SOfrac;
NADW2IndPac = NADW2Ind+NADW2AO+NADW2CDW;


AMOCLow = (AMOC-PFT)*.6;
AAIWP = NADW2IndPac *.35;

CDWP = 16*dt*Sv2Kg;
CDWA = 16*dt*Sv2Kg;
CDW = CDWA+CDWP;

PO4starPO = 0.2;

fracseaiceSO = 1;
fracseaiceAO = .01;
fracseaiceNA = .85;
fracseaiceNP = .85;
```

```
Reef = 0;
rO2PO4 = 170;
rALKPO4 = 50;
FCA = 0.0;
rCorgPO4 = 117;
rCPO4p = rCorgPO4/(1-FCA);
rCorgO2 = rCPO4p/rO2PO4;
%rALKC = rCPO4p/rALKPO4;
rALKC = .5;

FCAlowlat = 0.1*zeroCaCO3;
FCANA = .05*zeroCaCO3;
FCASO = .00*zeroCaCO3;
FCANP = 0.1*zeroCaCO3;
FCAremin = 0.1;


%=================================================================%
%Matrices used to guide the evolution of some of the parameters
%not all are used and must be called in the loop
%=================================================================%

LGM_start = spinup_time+pert_time+spindown_time;


CDWPRG = [1                         CDWP;
      (25-18)*1000/dt+LGM_start     CDWP;
      (25-17.6)*1000/dt+LGM_start   CDWP+2*dt*Sv2Kg;
      (25-16.0)*1000/dt+LGM_start   CDWP+6*dt*Sv2Kg;
      (25-15.5)*1000/dt+LGM_start   CDWP+20*dt*Sv2Kg;
      (25-14.8)*1000/dt+LGM_start   CDWP+20*dt*Sv2Kg;
      (25-14.6)*1000/dt+LGM_start   CDWP-0*dt*Sv2Kg;
      (25-13.00)*1000/dt+LGM_start  CDWP-0*dt*Sv2Kg;
      (25-12.80)*1000/dt+LGM_start  CDWP+6*dt*Sv2Kg;
      (25-11.75)*1000/dt+LGM_start   CDWP+6*dt*Sv2Kg;
      (25-11.7)*1000/dt+LGM_start   CDWP+4*dt*Sv2Kg;
      (25-9.5)*1000/dt+LGM_start    CDWP+4*dt*Sv2Kg;
      (25-9.1)*1000/dt+LGM_start    CDWP+0*dt*Sv2Kg;
      totaltime                  CDWP+0*dt*Sv2Kg;];

CDWARG = [1                         CDWA;
      (25-18)*1000/dt+LGM_start     CDWA;
      (25-17.6)*1000/dt+LGM_start   CDWA+2*dt*Sv2Kg;
      (25-16.0)*1000/dt+LGM_start   CDWA+5*dt*Sv2Kg;
      (25-15.5)*1000/dt+LGM_start   CDWA+12*dt*Sv2Kg;
      (25-14.8)*1000/dt+LGM_start   CDWA+12*dt*Sv2Kg;
      (25-14.6)*1000/dt+LGM_start   CDWA-3*dt*Sv2Kg;
      (25-13.00)*1000/dt+LGM_start  CDWA-3*dt*Sv2Kg;
      (25-12.80)*1000/dt+LGM_start  CDWA+2*dt*Sv2Kg;
      (25-11.75)*1000/dt+LGM_start   CDWA+2*dt*Sv2Kg;
      (25-11.7)*1000/dt+LGM_start   CDWA+2*dt*Sv2Kg;
      (25-9.5)*1000/dt+LGM_start     CDWA+2*dt*Sv2Kg;
```

```
      (25-9.1)*1000/dt+LGM_start     CDWA-10*dt*Sv2Kg;
      totaltime                  CDWA-10*dt*Sv2Kg;];


ModNADWRG = [1                        0.4;
      (25-17.5)*1000/dt+LGM_start   0.4;
      (25-16.1)*1000/dt+LGM_start   0.4;
      (25-16.0)*1000/dt+LGM_start   0.7;
      (25-14.8)*1000/dt+LGM_start   0.7;
      (25-14.6)*1000/dt+LGM_start   0.5;
      (25-13.00)*1000/dt+LGM_start   0.5;
      (25-12.5)*1000/dt+LGM_start   0.5;
      (25-12.4)*1000/dt+LGM_start   0.7;
      (25-11.75)*1000/dt+LGM_start   0.7;
      totaltime                  0.7;];

NADW2IndRG = [1                       0.25;
      (25-14.7)*1000/dt+LGM_start   0.25;
      (25-14.5)*1000/dt+LGM_start   0.25;
      totaltime                  0.25;];


NADW2CDWRG =  [1                      0.0;
      (25-17.5)*1000/dt+LGM_start   0.0;
      (25-16.1)*1000/dt+LGM_start   0.0;
      (25-16.0)*1000/dt+LGM_start   0.75;
      (25-14.8)*1000/dt+LGM_start   0.75;
      (25-14.6)*1000/dt+LGM_start   0.5;
      (25-13.00)*1000/dt+LGM_start   0.5;
      (25-12.5)*1000/dt+LGM_start   0.5;
      (25-12.4)*1000/dt+LGM_start   0.75;
      (25-11.75)*1000/dt+LGM_start   0.75;
      totaltime                  0.75;];


NADW2SORG =[1                         0.75;
      (25-17.5)*1000/dt+LGM_start   0.75;
      (25-16.1)*1000/dt+LGM_start   0.75;
      (25-16.0)*1000/dt+LGM_start   0.0;
      (25-14.8)*1000/dt+LGM_start   0.0;
      (25-14.6)*1000/dt+LGM_start   0.25;
      (25-13.00)*1000/dt+LGM_start   0.25;
      (25-12.5)*1000/dt+LGM_start   0.25;
      (25-12.4)*1000/dt+LGM_start   0.0;
      (25-11.75)*1000/dt+LGM_start   0.0;
      totaltime                  0.0;];

AMOCRG = [1                        AMOC;
      (25-17.8)*1000/dt+LGM_start   AMOC;
      (25-17.6)*1000/dt+LGM_start   AMOC-4*dt*Sv2Kg;
      (25-17.0)*1000/dt+LGM_start   AMOC-9*dt*Sv2Kg;
```

```
        (25-14.8)*1000/dt+LGM_start   AMOC-9*dt*Sv2Kg;
        (25-14.6)*1000/dt+LGM_start   AMOC+0*dt*Sv2Kg;
        (25-13.00)*1000/dt+LGM_start  AMOC+0*dt*Sv2Kg;
        (25-12.80)*1000/dt+LGM_start  AMOC-3*dt*Sv2Kg;
        (25-12.60)*1000/dt+LGM_start  AMOC-5*dt*Sv2Kg;
        (25-11.75)*1000/dt+LGM_start   AMOC-5*dt*Sv2Kg;
        (25-11.7)*1000/dt+LGM_start   AMOC+0*dt*Sv2Kg;
        (25-10.)*1000/dt+LGM_start    AMOC+3*dt*Sv2Kg;
        (25-9.0)*1000/dt+LGM_start    AMOC+5*dt*Sv2Kg;
        (25-6.5)*1000/dt+LGM_start    AMOC+4*dt*Sv2Kg;
        totaltime                 AMOC+4*dt*Sv2Kg;];

PO4starPORG = [1                    0.2;
        (25-17.3)*1000/dt+LGM_start   0.2;
        (25-17.0)*1000/dt+LGM_start   0.7;
        (25-16.2)*1000/dt+LGM_start   1.3;
        (25-16.1)*1000/dt+LGM_start   1.3;
        (25-15.5)*1000/dt+LGM_start   1.4;
        (25-13.00)*1000/dt+LGM_start  1.4;
        (25-12.75)*1000/dt+LGM_start  1.4;
        totaltime                 1.4;];

PO4starAORG = [1                    1.6;
        (25-17.6)*1000/dt+LGM_start   1.6;
        (25-17.0)*1000/dt+LGM_start   1.6;
        (25-16.4)*1000/dt+LGM_start   1.7;
        (25-16.1)*1000/dt+LGM_start   1.7;
        (25-16.0)*1000/dt+LGM_start   1.8;
        (25-13.00)*1000/dt+LGM_start  1.8;
        (25-12.75)*1000/dt+LGM_start  1.8;
        totaltime                 1.8;];



PO4starNARG = [1                    0.6;
        (25-17.8)*1000/dt+LGM_start   0.6;
        (25-17.6)*1000/dt+LGM_start   0.6;
        (25-17.4)*1000/dt+LGM_start   0.6;
        (25-16.5)*1000/dt+LGM_start   0.6;
        (25-13.00)*1000/dt+LGM_start  0.6;
        (25-12.80)*1000/dt+LGM_start  0.6;
        totaltime                 0.6;];


PO4starAt_PacRG = [1                .2;
        (25-18)*1000/dt+LGM_start     .2;
        (25-17.8)*1000/dt+LGM_start   .2;
%       (25-17.6)*1000/dt+LGM_start   .05;
%       (25-14.7)*1000/dt+LGM_start   .05;
%       (25-14.5)*1000/dt+LGM_start   .05;
%       (25-12.90)*1000/dt+LGM_start  .05;
%       (25-12.80)*1000/dt+LGM_start  .05;
%       (25-11.6)*1000/dt+LGM_start   .05;
%       (25-11.5)*1000/dt+LGM_start   .05;
```

```
        (25-10.)*1000/dt+LGM_start    .4;
        totaltime                     .4;];


fracseaiceAORG = [1                       0.01;
        (25-18.0)*1000/dt+LGM_start   0.01;
        (25-17.0)*1000/dt+LGM_start   0.05;
        (25-16.5)*1000/dt+LGM_start   0.1;
        (25-15.5)*1000/dt+LGM_start   0.15;
        (25-14.7)*1000/dt+LGM_start   0.2;
        (25-14.4)*1000/dt+LGM_start   0.25;
        (25-12.8)*1000/dt+LGM_start  0.20;
  %     (25-12.5)*1000/dt+LGM_start  0.70;
        (25-11.75)*1000/dt+LGM_start  0.85;
        (25-11.0)*1000/dt+LGM_start  0.85;
        totaltime                    0.85;];

fracseaiceNARG = [1                   .85;
        (25-17.8)*1000/dt+LGM_start   .85;
        (25-17.6)*1000/dt+LGM_start   .85;
        (25-17.4)*1000/dt+LGM_start   .85;
       (25-14.7)*1000/dt+LGM_start    .85;
        (25-14.6)*1000/dt+LGM_start   .85;
        (25-12.8)*1000/dt+LGM_start  .85;
   %    (25-12.60)*1000/dt+LGM_start  .50;
        (25-11.75)*1000/dt+LGM_start   .50;
        (25-11.7)*1000/dt+LGM_start   .85;
        (25-10.)*1000/dt+LGM_start    .85;
        (25-9.5)*1000/dt+LGM_start    .85;
        totaltime                     .85;];


kgSOpercentRG = [1                      .1;
        (25-17.8)*1000/dt+LGM_start   .1;
        (25-17.6)*1000/dt+LGM_start   .15;
        (25-17.4)*1000/dt+LGM_start   .15;
        (25-16.2)*1000/dt+LGM_start   .15;
        (25-14.8)*1000/dt+LGM_start   .15;
        (25-14.7)*1000/dt+LGM_start   .1;
        (25-13.00)*1000/dt+LGM_start  .1;
        (25-12.70)*1000/dt+LGM_start  .15;
        (25-12.50)*1000/dt+LGM_start  .15;
        (25-12.0)*1000/dt+LGM_start  .15;
        (25-11.75)*1000/dt+LGM_start   .15;
        (25-11.7)*1000/dt+LGM_start   0.1;
        totaltime                     0.1;];


FlphRG = [1                           Flph;
        (25-17.5)*1000/dt+LGM_start       Flph+.00*dt;
        (25-17.0)*1000/dt+LGM_start       Flph+.01*dt;
        (25-15.0)*1000/dt+LGM_start       Flph+.0125*dt;
        (25-11.0)*1000/dt+LGM_start       Flph+.015*dt;
        (25-9.0)*1000/dt+LGM_start        Flph+.06*dt;
```

```
        (25-7)*1000/dt+LGM_start         Flph+.08*dt;
        (25-6)*1000/dt+LGM_start         Flph+.01*dt;
        (25-5)*1000/dt+LGM_start         Flph+.01*dt;
        totaltime                    Flph+.0*dt;];


Flph2RG = [1                             Flph2;
        (25-16.6)*1000/dt+LGM_start      Flph2+.00*dt;
        (25-16.4)*1000/dt+LGM_start      Flph2-.25*dt;
        (25-16.2)*1000/dt+LGM_start      Flph2+.07*dt;
        (25-15.0)*1000/dt+LGM_start      Flph2+.0*dt;
%       (25-14.8)*1000/dt+LGM_start      Flph2-.1*dt;
        (25-14.6)*1000/dt+LGM_start      Flph2+.0*dt;
        (25-13.00)*1000/dt+LGM_start     Flph2+.00*dt;
        (25-12.6)*1000/dt+LGM_start      Flph2-.13*dt;
       (25-12.2)*1000/dt+LGM_start      Flph2+.1*dt;
        (25-11.75)*1000/dt+LGM_start     Flph2+.0*dt;
        (25-10.0)*1000/dt+LGM_start      Flph2+.00*dt;
        totaltime                    Flph2+.00*dt;];



FCAlowlatRG = [1                 .1;
        (25-18)*1000/dt+LGM_start    .1;
        (25-17.6)*1000/dt+LGM_start  .025;
        (25-17.4)*1000/dt+LGM_start  .025;
        (25-14.7)*1000/dt+LGM_start  .025;
        (25-14.6)*1000/dt+LGM_start  .1;
        (25-13.00)*1000/dt+LGM_start .1;
        (25-12.80)*1000/dt+LGM_start .025;
        (25-11.6)*1000/dt+LGM_start  .025;
        (25-11.5)*1000/dt+LGM_start  .1;
        (25-10.)*1000/dt+LGM_start   .1;
        (25-9.5)*1000/dt+LGM_start   .1;
        totaltime                .1;];

ReefRG = [1                          0;
        (25-14.70)*1000/dt+LGM_start     0;
        (25-14.60)*1000/dt+LGM_start     0.009;
        (25-9)*1000/dt+LGM_start         0.009;
        (25-8)*1000/dt+LGM_start         0.029;
        (25-6)*1000/dt+LGM_start         0.029;
        (25-5)*1000/dt+LGM_start         0.019;
        totaltime                    0.019;];


%=================================================================%
%interpolating guides to model time steps
%=================================================================%
CDWPguide = interp1(CDWPRG(:,1),CDWPRG(:,2),1:totaltime);
CDWAguide = interp1(CDWARG(:,1),CDWARG(:,2),1:totaltime);
AMOCguide = interp1(AMOCRG(:,1),AMOCRG(:,2),1:totaltime);
PO4starPOguide = interp1(PO4starPORG(:,1),PO4starPORG(:,2),1:totaltime);
PO4starAOguide = interp1(PO4starAORG(:,1),PO4starAORG(:,2),1:totaltime);
```

```
PO4starNAguide = interp1(PO4starNARG(:,1),PO4starNARG(:,2),1:totaltime);
fracseaiceAOguide = interp1(fracseaiceAORG(:,1),fracseaiceAORG(:,2),1:totaltime);
fracseaiceNAguide = interp1(fracseaiceNARG(:,1),fracseaiceNARG(:,2),1:totaltime);
Reefguide = interp1(ReefRG(:,1),ReefRG(:,2),1:totaltime).*dt;
Flphguide = interp1(FlphRG(:,1),FlphRG(:,2),1:totaltime);
Flph2guide = interp1(Flph2RG(:,1),Flph2RG(:,2),1:totaltime);
ModNADWFRAC = interp1(ModNADWRG(:,1),ModNADWRG(:,2),1:totaltime);
NADW2Indguide = interp1(NADW2IndRG(:,1),NADW2IndRG(:,2),1:totaltime);
NADW2CDWguide = interp1(NADW2CDWRG(:,1),NADW2CDWRG(:,2),1:totaltime);
NADW2SOguide = interp1(NADW2SORG(:,1),NADW2SORG(:,2),1:totaltime);
PO4starAt_Pacguide= interp1(PO4starAt_PacRG(:,1),PO4starAt_PacRG(:,2),1:totaltime);
kgSOguide= interp1(kgSOpercentRG(:,1),kgSOpercentRG(:,2),1:totaltime);
FCAlowlatguide= interp1(FCAlowlatRG(:,1),FCAlowlatRG(:,2),1:totaltime);

ModeNADWsave = zeros(1,totaltime);
Fsed = zeros(1,totaltime);
%Fsedsave= zeros(1,totaltime);



%=================================================================%
%calling core equation in deglacial loop. a prescribed variable
%is overwritten at each time step.  comment in or out a variable
%to turn it on or off.
%=================================================================%
tic
for t = spinup_time+pert_time+spindown_time+1:totaltime

AMOC = AMOCguide(t);
PFTfrac =     ModNADWFRAC(t);
%NADW2Indfrac= NADW2Indguide(t);
NADW2AOfrac=  NADW2CDWguide(t);
%NADW2CDWfrac= NADW2CDWguide(t);
NADW2SOfrac=  NADW2SOguide(t);


ModeNADWsave(t)  = NADW2AOfrac;
PFT  = AMOC*PFTfrac;
NADW2Ind = AMOC*NADW2Indfrac;
NADW2AO = AMOC*NADW2AOfrac;
NADW2CDW = AMOC*NADW2CDWfrac;
NADW2SO = AMOC*NADW2SOfrac;
NADW2IndPac = NADW2Ind+NADW2AO+NADW2CDW;


AMOCLow = (AMOC-PFT)*.6;
AAIWP = NADW2IndPac *.35;

CDWP = CDWPguide(t);
CDWA = CDWAguide(t);
CDW = CDWA+CDWP;

fracseaiceAO = fracseaiceAOguide(t);
```

```
fracseaiceNA = fracseaiceNAguide(t);

PO4starPO = ironfertyi(t-(spinup_time+pert_time+spindown_time));
PO4starPOguide(t) = PO4starPO;


Kfert = 1.35;
lag = 100;
Flph = Flphguide(t)+(Catm(t-lag/dt)-Catm(t-1-lag/dt))*Kfert;
%Flph3(t)  = (Catm(t-lag/dt)-Catm(t-1-lag/dt))*Kfert;  used to save the
%CO2 fertilization effect in a full run
%Flph = Flphguide(t)+Flph3(t);
%Flph2 =Flph2guide(t);

Reef = Reefguide(t);

salinity = 34.72*(1+(-sealevel(t-(spinup_time+pert_time+spindown_time)))/3700);

SSTMO = 20.5-LGMDelT*LGMCooling+SSTMOyi(t-(spinup_time+pert_time+spindown_time));
SSTPO = 5.5-SHLGMDelT*LGMCooling+SSTPOyi(t-(spinup_time+pert_time+spindown_time));
SSTAO = 1.0-AntLGMDelT*LGMCooling+SSTAOyi(t-(spinup_time+pert_time+spindown_time));
SSTNA = 3.0-NHLGMDelT*LGMCooling+SSTNAyi(t-(spinup_time+pert_time+spindown_time));



eval('Core_11Box_N2O_CaCO3_Comp')
%eval('Core_11Box_N2O_no_CaCO3_Comp')
%eval('Core_11Box_N2O_no_CO2')
bioflux(t) = FbaopdOrg;
%bioflux(t) = FbsopdOrg;
end


%=====================================================================%
%plotting results
%=====================================================================%
load('d13C_Schmitt.txt')
load('CO2_Monnin.txt')
load('d13C_TG.txt')
load('CO2_TG.txt')
timeoff = -42000;

figure(2)
subplot(3,1,1)
hold on
plot(-flipud(int),Catm(spinup_time+pert_time+spindown_time+1:totaltime), 'b')
plot(-CO2_TG(:,1),CO2_TG(:,2), 'k')
plot(-CO2_Monnin(1:110,2),CO2_Monnin(1:110,3), 'k')
subplot(3,1,2)
hold on
plot(-flipud(int),d13Ca(spinup_time+pert_time+spindown_time+1:totaltime), 'b')
plot(-d13C_TG(:,1),d13C_TG(:,2), 'k')
plot(-d13C_Schmitt(:,1),d13C_Schmitt(:,2), 'r')
subplot(3,1,3)
```

```
hold on
plot(-flipud(int),d14Ca(spinup_time+pert_time+spindown_time+1:totaltime), 'b')

%=================================================================%
%compiling  variables for output. however output file is not
%defined at this time
%=================================================================%

outputdt = 0.01;
toc
CO2_model =
interp1(flipud(int),Catm(spinup_time+pert_time+spindown_time+1:totaltime),0:outputdt:25);
%O2_pint_model =
interp1(flipud(int),(O2PINT(spinup_time+pert_time+spindown_time+1:totaltime)),0:outputdt:25);
%O2_aint_model =
interp1(flipud(int),(O2AINT(spinup_time+pert_time+spindown_time+1:totaltime)),0:outputdt:25);
%O2_pd_model =
interp1(flipud(int),(O2PD(spinup_time+pert_time+spindown_time+1:totaltime)),0:outputdt:25);
%O2_od_model =
interp1(flipud(int),(O2deep(spinup_time+pert_time+spindown_time+1:totaltime)),0:outputdt:25);
%O2_paod_model =
interp1(flipud(int),(O2PAD(spinup_time+pert_time+spindown_time+1:totaltime)),0:outputdt:25);

PO4_pint_model =
interp1(flipud(int),(PO4PINT(spinup_time+pert_time+spindown_time+1:totaltime)),0:outputdt:25);
PO4_aint_model =
interp1(flipud(int),(PO4AINT(spinup_time+pert_time+spindown_time+1:totaltime)),0:outputdt:25);
PO4_pd_model =
interp1(flipud(int),(PO4PD(spinup_time+pert_time+spindown_time+1:totaltime)),0:outputdt:25);
PO4_od_model =
interp1(flipud(int),(PO4deep(spinup_time+pert_time+spindown_time+1:totaltime)),0:outputdt:25);
PO4_paod_model =
interp1(flipud(int),(PO4PAD(spinup_time+pert_time+spindown_time+1:totaltime)),0:outputdt:25);

%N2O_model = interp1(flipud(int),
(TotalN2O(spinup_time+pert_time+spindown_time+1:totaltime)),0:outputdt:25);
d13C_model =
interp1(flipud(int),d13Ca(spinup_time+pert_time+spindown_time+1:totaltime),0:outputdt:25);
d14C_model =
interp1(flipud(int),d14Ca(spinup_time+pert_time+spindown_time+1:totaltime),0:outputdt:25);
dd14Cpd_model = interp1(flipud(int),d14Ca(spinup_time+pert_time+spindown_time+1:totaltime)-
d14Cpd(spinup_time+pert_time+spindown_time+1:totaltime),0:outputdt:25);
d13Cpd_model =
interp1(flipud(int),d13Cpd(spinup_time+pert_time+spindown_time+1:totaltime),0:outputdt:25);
dd14Cpaod_model = interp1(flipud(int),d14Ca(spinup_time+pert_time+spindown_time+1:totaltime)-
d14Cpaod(spinup_time+pert_time+spindown_time+1:totaltime),0:outputdt:25);
d13Cpaod_model =
interp1(flipud(int),d13Cpaod(spinup_time+pert_time+spindown_time+1:totaltime),0:outputdt:25);
dd14Cod_model = interp1(flipud(int),d14Ca(spinup_time+pert_time+spindown_time+1:totaltime)-
d14Cod(spinup_time+pert_time+spindown_time+1:totaltime),0:outputdt:25);
d13Cod_model =
interp1(flipud(int),d13Cod(spinup_time+pert_time+spindown_time+1:totaltime),0:outputdt:25);
d13Cpaos_model =
interp1(flipud(int),d13Cpaos(spinup_time+pert_time+spindown_time+1:totaltime),0:outputdt:25);
```

```
Cb2_model =
interp1(flipud(int),Cb2(spinup_time+pert_time+spindown_time+1:totaltime),0:outputdt:25);
Cb_model =
interp1(flipud(int),Cb(spinup_time+pert_time+spindown_time+1:totaltime),0:outputdt:25);

TotalCbmodel = Cb2_model+Cb_model;

Reefmodel  =
(1/dt)*interp1(flipud(int),Reefguide(spinup_time+pert_time+spindown_time+1:totaltime),0:outputdt:2
5);
Fsedmodel =
(1/dt)*interp1(flipud(int),Fsed(spinup_time+pert_time+spindown_time+1:totaltime),0:outputdt:25);
PO4starPOmodel =
interp1(flipud(int),PO4starPOguide(spinup_time+pert_time+spindown_time+1:totaltime),0:outputdt:2
5);
Antseaicemodel =
interp1(flipud(int),fracseaiceAOguide(spinup_time+pert_time+spindown_time+1:totaltime),0:outputdt
:25);
NAseaicemodel =
interp1(flipud(int),fracseaiceNAguide(spinup_time+pert_time+spindown_time+1:totaltime),0:outputdt
:25);
windspeedmodel =
interp1(flipud(int),kgSOguide(spinup_time+pert_time+spindown_time+1:totaltime),0:outputdt:25);
AMOCmodel
=1/(Sv2Kg*dt)*interp1(flipud(int),AMOCguide(spinup_time+pert_time+spindown_time+1:totaltime),
0:outputdt:25);
SOUpwellingmodel=1/(Sv2Kg*dt)*interp1(flipud(int),CDWPguide(spinup_time+pert_time+spindown
_time+1:totaltime)+CDWAguide(spinup_time+pert_time+spindown_time+1:totaltime)+ModeNADWs
ave(spinup_time+pert_time+spindown_time+1:totaltime),0:outputdt:25);
PreformedPO4 =
interp1(flipud(int),TotalPO4Pre(spinup_time+pert_time+spindown_time+1:totaltime)./TotalPO4(spinu
p_time+pert_time+spindown_time+1:totaltime),0:outputdt:25);
biofluxmodel =
interp1(flipud(int),bioflux(spinup_time+pert_time+spindown_time+1:totaltime)./dt,0:outputdt:25);

PFTmodel
=1/(Sv2Kg*dt)*interp1(flipud(int),ModNADWFRAC(spinup_time+pert_time+spindown_time+1:total
time).*AMOCguide(spinup_time+pert_time+spindown_time+1:totaltime),0:outputdt:25);
NADW2Indmodel
=1/(Sv2Kg*dt)*interp1(flipud(int),NADW2Indguide(spinup_time+pert_time+spindown_time+1:totalti
me).*AMOCguide(spinup_time+pert_time+spindown_time+1:totaltime),0:outputdt:25);
NADW2AOmodel
=1/(Sv2Kg*dt)*interp1(flipud(int),NADW2CDWguide(spinup_time+pert_time+spindown_time+1:tot
altime).*AMOCguide(spinup_time+pert_time+spindown_time+1:totaltime),0:outputdt:25);
NADW2SOmodel
=1/(Sv2Kg*dt)*interp1(flipud(int),NADW2SOguide(spinup_time+pert_time+spindown_time+1:totalti
me).*AMOCguide(spinup_time+pert_time+spindown_time+1:totaltime),0:outputdt:25);
NADW2IndPacmodel = NADW2Indmodel+NADW2AOmodel+NADW2SOmodel;


%FCAlowlat =FCAlowlatguide(t);
salinitymodel = interp1(flipud(int),(34.72*(1+(-sealevel)/3700)),0:outputdt:25);
SSTMOmodel = interp1(flipud(int),(20.5-LGMDelT*LGMCooling+SSTMOyi),0:outputdt:25);
SSTPOmodel = interp1(flipud(int),(5.5-SHLGMDelT*LGMCooling+SSTPOyi),0:outputdt:25);
```

```
SSTAOmodel = interp1(flipud(int),(1.0-AntLGMDelT*LGMCooling+SSTAOyi),0:outputdt:25);
SSTNAmodel = interp1(flipud(int),(3.0-NHLGMDelT*LGMCooling+SSTNAyi),0:outputdt:25);

[(0:outputdt:25)' SSTMOmodel' SSTNAmodel' SSTNAmodel' SSTPOmodel' SSTAOmodel'
salinitymodel' TotalCbmodel' Reefmodel' Fsedmodel'  Antseaicemodel' NAseaicemodel'
PO4starPOmodel' AMOCmodel' SOUpwellingmodel' NADW2SOmodel' NADW2AOmodel'
NADW2Indmodel' PFTmodel'];


[(0:outputdt:25)' CO2_model' d13C_model' d14C_model' -dd14Cpd_model' d13Cpd_model' -
dd14Cpaod_model' d13Cpaod_model' -dd14Cod_model' d13Cod_model'];
%[-dd14Cpd_model' d13Cpd_model' -dd14Cpaod_model' d13Cpaod_model' ventage(-
dd14Cod_model)' d13Cod_model' d13Cpaos_model'];

sstcorrTGCO2 =  CO2_TG(:,2)+interp1(flipud(int),Catm(spinup_time+pert_time+spindown_time+1)-
Catm(spinup_time+pert_time+spindown_time+1:totaltime),CO2_TG(:,1));
sstcorrTGd13C =
d13C_TG(:,2)+interp1(flipud(int),d13Ca(spinup_time+pert_time+spindown_time+1)-
d13Ca(spinup_time+pert_time+spindown_time+1:totaltime),d13C_TG(:,1));

sstcorrMonninCO2 =
CO2_Monnin(1:110,3)+interp1(flipud(int),Catm(spinup_time+pert_time+spindown_time+1)-
Catm(spinup_time+pert_time+spindown_time+1:totaltime),CO2_Monnin(1:110,2));
sstcorrSchmittd13C=
d13C_Schmitt(:,2)+interp1(flipud(int),d13Ca(spinup_time+pert_time+spindown_time+1)-
d13Ca(spinup_time+pert_time+spindown_time+1:totaltime),d13C_Schmitt(:,1));
```

File: Core_11Box_N2O_CACO3_Comp.m

```
%=========================================================================%
%%Core Equations for 11 Box Model with CaCO3 compensation and
%N2O producion
%4.05.13
%=========================================================================%

%-------------------------------------------------------------
%Atmosphere Box
%-------------------------------------------------------------
Fatao(t)=kg*Catm(t)*Aatlantic*dt*mol2GtC;
Fatoa(t)=kg*pCO2s(t)*Aatlantic*dt*mol2GtC;


Fsoao(t)=kgpos*Catm(t)*Apo*dt*mol2GtC*fracseaiceSO;
Fsooa(t)=kgpos*pCO2PO(t)*Apo*dt*mol2GtC*fracseaiceSO;

Faoao(t)=kgpos*Catm(t)*Aao*dt*mol2GtC*fracseaiceAO;
Faooa(t)=kgpos*pCO2AO(t)*Aao*dt*mol2GtC*fracseaiceAO;

Fnaao(t)=kgpo*Catm(t)*Ana*dt*mol2GtC*fracseaiceNA;
Fnaoa(t)=kgpo*pCO2NA(t)*Ana*dt*mol2GtC*fracseaiceNA;

Fpaao(t)=kg*Catm(t)*Apacific*dt*mol2GtC;
```

```
Fpaoa(t)=kg*pCO2paos(t)*Apacific*dt*mol2GtC;

Fnpao(t)=kgpo*Catm(t)*Anp*dt*mol2GtC*fracseaiceNP;
Fnpoa(t)=kgpo*pCO2NP(t)*Anp*dt*mol2GtC*fracseaiceNP;



FO2atao(t)=kw*O2a_O2oc(O2atm(t),SSTMO,salinity)*Aatlantic*dt*zeroO2;
FO2atoa(t)=kw*O2surf(t)*Aatlantic*dt*zeroO2;


FO2soao(t)=kwpo*O2a_O2oc(O2atm(t),SSTPO,salinity)*Apo*dt*zeroO2*fracseaiceSO;
FO2sooa(t)=kwpo*O2PO(t)*Apo*dt*zeroO2*fracseaiceSO;


FO2aoao(t)=kwpo*O2a_O2oc(O2atm(t),SSTAO,salinity)*Aao*dt*zeroO2*fracseaiceAO;
FO2aooa(t)=kwpo*O2AO(t)*Aao*dt*zeroO2*fracseaiceAO;

FO2naao(t)=kwpo*O2a_O2oc(O2atm(t),SSTNA,salinity)*Ana*dt*zeroO2*fracseaiceNA;
FO2naoa(t)=kwpo*O2NA(t)*Ana*dt*zeroO2*fracseaiceNA;

FO2paao(t)=kw*O2a_O2oc(O2atm(t),SSTMO,salinity)*Apacific*dt*zeroO2;
FO2paoa(t)=kw*O2PAS(t)*Apacific*dt*zeroO2;

FO2npao(t)=kwpo*O2a_O2oc(O2atm(t),SSTNA,salinity)*Anp*dt*zeroO2*fracseaiceNP;
FO2npoa(t)=kwpo*O2NP(t)*Anp*dt*zeroO2*fracseaiceNP;

aoa = ((.99915*.998764)/(1.01051-1.05e-4*SSTMO));   %Schmittner Manuscript
aao = ((.99915*.998764));


apoa = ((.99915*.998764)/(1.01051-1.05e-4*SSTPO));
apao = ((.99915*.998764));

aaoa = ((.99915*.998764)/(1.01051-1.05e-4*SSTAO));
aaao = ((.99915*.998764));

anaa = ((.99915*.998764)/(1.01051-1.05e-4*SSTNA));
anao = ((.99915*.998764));



%sum of fluxes
Ca(t+1) = Ff-Flph+Flb-Flph2+Flb2...
   -Fatao(t)+Fatoa(t)...
   -Fsoao(t)+Fsooa(t)...
   -Fnaao(t)+Fnaoa(t)...
   -Fpaao(t)+Fpaoa(t)...
   -Faoao(t)+Faooa(t)...
   -Fnpao(t)+Fnpoa(t)...
   +Ca(t);

Catm(t+1) = Ca(t+1)/2.12;
```

```
C13a(t+1) = Ff*Rf-alph*Flph*Ra(t)+Flb*Rb(t)-alph*Flph2*Ra(t)+Flb2*Rb2(t)...
   -aao*Fatao(t)*Ra(t)+aoa*Fatoa(t)*Ros(t)...
   -apao*Fsoao(t)*Ra(t)+apoa*Fsooa(t)*Rpo(t)...
   -anao*Fnaao(t)*Ra(t)+anaa*Fnaoa(t)*Rna(t)...
   -aao*Fpaao(t)*Ra(t)+aoa*Fpaoa(t)*Rpaos(t)...
   -aaao*Faoao(t)*Ra(t)+aaoa*Faooa(t)*Rao(t)...
   -anao*Fnpao(t)*Ra(t)+anaa*Fnpoa(t)*Rnp(t)...
    +C13a(t);

d13Ca(t+1) = ((C13a(t+1)/Ca(t+1))/RPDB-1)*10^3;
Ra(t+1) = (C13a(t+1)/Ca(t+1));

C14a(t+1) = exp(-lamda*dt)*(C14P*dt+Ff*R14f-alph^2*Flph*R14a(t)+Flb*R14b(t)-
alph^2*Flph2*R14a(t)+Flb2*R14b2(t)...
   -aao^2*Fatao(t)*R14a(t)+aoa^2*Fatoa(t)*R14os(t)...
   -apao^2*Fsoao(t)*R14a(t)+apoa^2*Fsooa(t)*R14po(t)...
   -anao^2*Fnaao(t)*R14a(t)+anaa^2*Fnaoa(t)*R14na(t)...
   -aao^2*Fpaao(t)*R14a(t)+aoa^2*Fpaoa(t)*R14paos(t)...
   -aaao^2*Faoao(t)*R14a(t)+aaoa^2*Faooa(t)*R14ao(t)...
   -anao^2*Fnpao(t)*R14a(t)+anaa^2*Fnpoa(t)*R14np(t)...
   +C14a(t));

d14Ca(t+1) = ((C14a(t+1)/Ca(t+1))/R14Cstd-1)*10^3;
R14a(t+1) = (C14a(t+1)/Ca(t+1));

O2atm(t+1) = (1/molesatm)*mmol2mol*(-FO2atao(t)+FO2atoa(t)...
   -FO2soao(t)+FO2sooa(t)...
   -FO2naao(t)+FO2naoa(t)...
   -FO2npao(t)+FO2npoa(t)...
   -FO2paao(t)+FO2paoa(t)...
   -FO2aoao(t)+FO2aooa(t))...
   +O2atm(t);


%-----------------------------------------------------------------
%polar ocean box balance
%-----------------------------------------------------------------
if (PO4PO(t)-PO4starPO)<0
   display('zero PO4 in surface southern ocean')
  OrgFluxz0 = 0;
else


OrgFluxz0 = (PO4PO(t)-PO4starPO)*rCPO4p*umol2GtC*Vpo*dSW*nobio*dt;
end
FbsopadOrg = fracbiopo2pac*(OrgFluxz0*(hmix/100)^-b);
FbsoodOrg = fracbioop2atl*(OrgFluxz0*(hmix/100)^-b);
FbsopdOrg = (1-fracbiopo2pac-fracbioop2atl)*(OrgFluxz0*(hmix/100)^-b);

FbsopadCaCO3 = fracbiopo2pac*(OrgFluxz0*(hmix/100)^-b)*FCASO;
FbsoodCaCO3 = fracbioop2atl*(OrgFluxz0*(hmix/100)^-b)*FCASO;
FbsopdCaCO3 = (1-fracbiopo2pac-fracbioop2atl)*(OrgFluxz0*(hmix/100)^-b)*FCASO;
```

```
Cpo(t+1) = Fsoao(t)-Fsooa(t)-FbsopdOrg-FbsoodOrg-FbsopadOrg-FbsopdCaCO3-FbsopadCaCO3-
FbsoodCaCO3...
   +umol2GtC*((NADW2IndPac-AAIWP)*DICPAD(t)...
   +NADW2SO*DICdeep(t)...
   -((NADW2IndPac-AAIWP+NADW2SO))*DICPO(t)...
   +Fso2ao*(DICAO(t)-DICPO(t)))...
   +Cpo(t);

DICPO(t+1) = Cpo(t+1)/(Vpo*dSW*umol2GtC);
%ALKPO(t+1) = (-Fsoas*(ALKPO(t)-ALKsurf(t))+Fsopd*(ALKPD(t)-
ALKPO(t)))/(Vpo*dSW)+ALKPO(t);
PO4PO(t+1) = ((NADW2IndPac-AAIWP)*PO4PAD(t)...
      +NADW2SO*PO4deep(t)...
   -(NADW2IndPac-AAIWP+NADW2SO)*PO4PO(t)...
   +Fso2ao*(PO4AO(t)-PO4PO(t))...
   -(FbsopdOrg+FbsoodOrg+FbsopadOrg)/(rCPO4p*umol2GtC))/(Vpo*dSW)...
   +PO4PO(t);

ALKPO(t+1) = ((NADW2IndPac-AAIWP)*ALKPAD(t)...
      +NADW2SO*ALKdeep(t)...
   -(NADW2IndPac-AAIWP+NADW2SO)*ALKPO(t)...
   +Fso2ao*(ALKAO(t)-ALKPO(t))...
   -(FbsopdCaCO3+FbsopadCaCO3+FbsoodCaCO3)/(rALKC*umol2GtC))/(Vpo*dSW)...
   +ALKPO(t);


O2PO(t+1) = ((NADW2IndPac-AAIWP)*O2PAD(t)...
      +NADW2SO*O2deep(t)...
   -(NADW2IndPac-AAIWP+NADW2SO)*O2PO(t)...
   +Fso2ao*(O2AO(t)-O2PO(t))...
   +(FbsopdOrg+FbsoodOrg+FbsopadOrg)/(rCorgO2*umol2GtC))/(Vpo*dSW)...
   +(FO2soao(t)-FO2sooa(t))/Vpo...
   +O2PO(t);


   clear DICs ALKs SST PC02_r
   SST = SSTPO;
   DICs = DICPO(t+1);
   ALKs = ALKPO(t+1);
   csys3_hack;
   pCO2PO(t+1) = PC02_r;


C13po(t+1) = apao*Fsoao(t)*Ra(t)-apoa*Fsooa(t)*Rpo(t)...
   -aoph*(FbsopdOrg+FbsoodOrg+FbsopadOrg)*Rpo(t)-
(FbsopdCaCO3+FbsopadCaCO3+FbsoodCaCO3)*Rpo(t)...
   +umol2GtC*((NADW2IndPac-AAIWP)*DICPAD(t)*Rpaod(t)...
    +NADW2SO*DICdeep(t)*Rod(t)...
   +Fso2ao*(DICAO(t)*Rao(t)-DICPO(t)*Rpo(t))...
   -(NADW2IndPac-AAIWP+NADW2SO)*DICPO(t)*Rpo(t))...
   +C13po(t);

d13Cpo(t+1) = ((C13po(t+1)/Cpo(t+1))/RPDB-1)*10^3;
```

```
Rpo(t+1) = (C13po(t+1)/Cpo(t+1));

C14po(t+1) = exp(-lamda*dt)*(apao^2*Fsoao(t)*R14a(t)-apoa^2*Fsooa(t)*R14po(t)...
   -aoph^2*(FbsopdOrg+FbsoodOrg+FbsopadOrg)*R14po(t)-
(FbsopdCaCO3+FbsopadCaCO3+FbsoodCaCO3)*R14po(t)...
   +umol2GtC*((NADW2IndPac-AAIWP)*DICPAD(t)*R14paod(t)...
    +NADW2SO*DICdeep(t)*R14od(t)...
   +Fso2ao*(DICAO(t)*R14ao(t)-DICPO(t)*R14po(t))...
   -(NADW2IndPac-AAIWP+NADW2SO)*DICPO(t)*R14po(t))...
   +C14po(t));

d14Cpo(t+1) = ((C14po(t+1)/Cpo(t+1))/R14Cstd-1)*10^3;
R14po(t+1) = (C14po(t+1)/Cpo(t+1));



%---------------------------------------------------------------
%Antarctic ocean box balance
%---------------------------------------------------------------
if (PO4AO(t)-PO4starAO)<0
%    display('zero PO4 in antarctic southern ocean')
  OrgFluxz0 = 0;
else


OrgFluxz0 = (PO4AO(t)-PO4starAO)*rCPO4p*umol2GtC*Vao*dSW*nobio*dt;
end
FbaopdOrg = (OrgFluxz0*(hmix/100)^-b);

Cao(t+1) = Faoao(t)-Faooa(t)-FbaopdOrg...
   +umol2GtC*((CDWA+NADW2AO)*DICdeep(t)...
   +CDWP*DICPAD(t)...
   -Fso2ao*(DICAO(t)-DICPO(t))...
   -(CDW+NADW2AO)*DICAO(t))...
   +Cao(t);

DICAO(t+1) = Cao(t+1)/(Vao*dSW*umol2GtC);
%ALKPO(t+1) = (-Fsoas*(ALKPO(t)-ALKsurf(t))+Fsopd*(ALKPD(t)-
ALKPO(t)))/(Vpo*dSW)+ALKPO(t);
PO4AO(t+1) = (-Fso2ao*(PO4AO(t)-
PO4PO(t))+(CDWA+NADW2AO)*PO4deep(t)+CDWP*PO4PAD(t)-
(CDW+NADW2AO)*PO4AO(t)...
   -(FbaopdOrg)/(rCPO4p*umol2GtC))/(Vao*dSW)...
   +PO4AO(t);

ALKAO(t+1) = (-Fso2ao*(ALKAO(t)-
ALKPO(t))+(CDWA+NADW2AO)*ALKdeep(t)+CDWP*ALKPAD(t)-
(CDW+NADW2AO)*ALKAO(t))/(Vao*dSW)...
   +ALKAO(t);


O2AO(t+1) = (-Fso2ao*(O2AO(t)-O2PO(t))+(CDWA+NADW2AO)*O2deep(t)+CDWP*O2PAD(t)-
(CDW+NADW2AO)*O2AO(t)...
   +(FbaopdOrg)/(rCorgO2*umol2GtC))/(Vao*dSW)...
```

```
    +(FO2aoao(t)-FO2aooa(t))/Vao...
    +O2AO(t);


    clear DICs ALKs SST PC02_r
    SST = SSTAO;
    DICs = DICAO(t+1);
    ALKs = ALKAO(t+1);
    csys3_hack;
    pCO2AO(t+1) = PC02_r;


C13ao(t+1) = aaao*Faoao(t)*Ra(t)-aaoa*Faooa(t)*Rao(t)-aoph*FbaopdOrg*Rao(t)...
    +umol2GtC*((CDWA+NADW2AO)*DICdeep(t)*Rod(t)...
    +CDWP*DICPAD(t)*Rpaod(t)...
     -Fso2ao*(DICAO(t)*Rao(t)-DICPO(t)*Rpo(t))...
    -(CDW+NADW2AO)*DICAO(t)*Rao(t))...
    +C13ao(t);

d13Cao(t+1) = ((C13ao(t+1)/Cao(t+1))/RPDB-1)*10^3;
Rao(t+1) = (C13ao(t+1)/Cao(t+1));

C14ao(t+1) = exp(-lamda*dt)*(aaao^2*Faoao(t)*R14a(t)-aaoa^2*Faooa(t)*R14ao(t)-
aoph^2*FbaopdOrg*R14ao(t)...
    +umol2GtC*((CDWA+NADW2AO)*DICdeep(t)*R14od(t)...
    +CDWP*DICPAD(t)*R14paod(t)...
    -Fso2ao*(DICAO(t)*R14ao(t)-DICPO(t)*R14po(t))...
    -(CDW+NADW2AO)*DICAO(t)*R14ao(t))...
    +C14ao(t));

d14Cao(t+1) = ((C14ao(t+1)/Cao(t+1))/R14Cstd-1)*10^3;
R14ao(t+1) = (C14ao(t+1)/Cao(t+1));



%-------------------------------------------------------------
%Surface Atlantic Ocean
%-------------------------------------------------------------
if (PO4surf(t)-PO4starAT)<0
    display('zero PO4 in surface atlantic')
   OrgFluxz0 = 0;
else

OrgFluxz0 = (PO4surf(t)-PO4starAT)*rCPO4p*umol2GtC*Vatmix*dSW*nobio*dt;
end
FbatpdOrg = frac2pd*(OrgFluxz0*(effdepthAABW/100)^-b);

FbatadOrg = (OrgFluxz0*((hint+hmix)/100)^-b)-FbatpdOrg;

FbataiOrg = (OrgFluxz0*(hmix/100)^-b)-FbatpdOrg-FbatadOrg;



FbataiCaCO3 = FbataiOrg*FCAlowlat*FCAremin;
```

```
FbatpdCaCO3 = FbatpdOrg*FCAlowlat+(FbataiOrg*FCAlowlat*(1-FCAremin))/2;
FbatadCaCO3 = FbatadOrg*FCAlowlat+(FbataiOrg*FCAlowlat*(1-FCAremin))/2;



Cos(t+1) = Reef-
(FbataiOrg+FbatadOrg+FbatpdOrg+FbatpdCaCO3+FbatadCaCO3+FbataiCaCO3)+Fatao(t)-Fatoa(t)...
   +umol2GtC*((AMOC-PFT-AMOCLow)*(DICAINT(t))...
   +PFT*DICpaosurf(t)...
   +Fosaint*(DICAINT(t)-DICsurf(t))...
   -(AMOC-AMOCLow)*DICsurf(t))...
   +Cos(t);

DICsurf(t+1) = Cos(t+1)/(Vatmix*dSW*umol2GtC);

PO4surf(t+1) = ((AMOC-PFT-AMOCLow)*(PO4AINT(t))...
   +PFT*PO4PAS(t)...
   -(AMOC-AMOCLow)*PO4surf(t)...
   +Fosaint*(PO4AINT(t)-PO4surf(t))....
   -(FbataiOrg+FbatadOrg+FbatpdOrg)/(rCPO4p*umol2GtC))/(Vatmix*dSW)...
   +PO4surf(t);


ALKsurf(t+1) = ((AMOC-PFT-AMOCLow)*(ALKAINT(t))...
   +PFT*ALKPAS(t)...
   -(AMOC-AMOCLow)*ALKsurf(t)...
   +Fosaint*(ALKAINT(t)-ALKsurf(t))....
   -(FbatpdCaCO3+FbatadCaCO3+FbataiCaCO3)/(rALKC*umol2GtC))/(Vatmix*dSW)...
   +ALKsurf(t);


O2surf(t+1) = ((AMOC-PFT-AMOCLow)*(O2AINT(t))...
   +PFT*O2PAS(t)...
   -(AMOC-AMOCLow)*O2surf(t)...
   +Fosaint*(O2AINT(t)-O2surf(t))...
   +(FbataiOrg+FbatadOrg+FbatpdOrg)/(rCorgO2*umol2GtC))/(Vatmix*dSW)...
   +(FO2atao(t)-FO2atoa(t))/Vatmix...
   +O2surf(t);

   clear DICs ALKs SST PC02_r
   SST = SSTMO;
   DICs = DICsurf(t+1);
   ALKs = ALKsurf(t+1);
   csys3_hack;
   pCO2s(t+1) = PC02_r;


C13os(t+1) = Reef*Ros(t)-aoph*(FbataiOrg+FbatadOrg+FbatpdOrg)*Ros(t)-
(FbatpdCaCO3+FbatadCaCO3+FbataiCaCO3)*Ros(t)+aao*Fatao(t)*Ra(t)-aoa*Fatoa(t)*Ros(t)...
   +umol2GtC*((AMOC-PFT-AMOCLow)*(DICAINT(t))*Raint(t)...
   +PFT*DICpaosurf(t)*Rpaos(t)...
   +Fosaint*(DICAINT(t)*Raint(t)-DICsurf(t)*Ros(t))...
   -(AMOC-AMOCLow)*DICsurf(t)*Ros(t))...
   +C13os(t);
```

```
d13Cos(t+1) = ((C13os(t+1)/Cos(t+1))/RPDB-1)*10^3;
Ros(t+1) = (C13os(t+1)/Cos(t+1));

C14os(t+1) = exp(-lamda*dt)*(Reef*R14os(t)-aoph^2*(FbataiOrg+FbatadOrg+FbatpdOrg)*R14os(t)-
(FbatpdCaCO3+FbatadCaCO3+FbataiCaCO3)*R14os(t)+aao^2*Fatao(t)*R14a(t)-
aoa^2*Fatoa(t)*R14os(t)...
   +umol2GtC*((AMOC-PFT-AMOCLow)*(DICAINT(t))*R14aint(t)...
   +PFT*DICpaosurf(t)*R14paos(t)...
   +Fosaint*(DICAINT(t)*R14aint(t)-DICsurf(t)*R14os(t))...
   -(AMOC-AMOCLow)*DICsurf(t)*R14os(t))...
   +C14os(t));

d14Cos(t+1) = ((C14os(t+1)/Cos(t+1))/R14Cstd-1)*10^3;
R14os(t+1) = (C14os(t+1)/Cos(t+1));


%-----------------------------------------------------------------
%North Atlantic ocean box balance
%-----------------------------------------------------------------
if (PO4NA(t)-PO4starNA)<0
%    display('zero PO4 in the north atlantic')
  OrgFluxz0 = 0;
else

OrgFluxz0 = (PO4NA(t)-PO4starNA)*rCPO4p*umol2GtC*Vna*dSW*nobio*dt;
end
FbnaodOrg = (OrgFluxz0*(hmix/100)^-b);
FbnaodCaCO3 = (OrgFluxz0*(hmix/100)^-b)*FCANA;


Cna(t+1) = Fnaao(t)-Fnaoa(t)-FbnaodOrg-FbnaodCaCO3...
   +umol2GtC*(-AMOC*DICNA(t)...
   +(AMOC-AMOCLow)*DICsurf(t)...
   +Fnaod*(DICdeep(t)-DICNA(t))...
   +AMOCLow*DICAINT(t))...
   +Cna(t);

DICNA(t+1) = Cna(t+1)/(Vna*dSW*umol2GtC);

PO4NA(t+1) = ((AMOC-AMOCLow)*(PO4surf(t))...
   -AMOC*(PO4NA(t))...
   +Fnaod*(PO4deep(t)-PO4NA(t))...
   +AMOCLow*PO4AINT(t)...
   -(FbnaodOrg)/(rCPO4p*umol2GtC))/(Vna*dSW)...
   +PO4NA(t);

ALKNA(t+1) = ((AMOC-AMOCLow)*(ALKsurf(t))...
   -AMOC*(ALKNA(t))...
   +Fnaod*(ALKdeep(t)-ALKNA(t))...
   +AMOCLow*ALKAINT(t)...
   -(FbnaodCaCO3)/(rALKC*umol2GtC))/(Vna*dSW)...
   +ALKNA(t);
```

```
O2NA(t+1) = ((AMOC-AMOCLow)*(O2surf(t))...
   -AMOC*(O2NA(t))...
   +AMOCLow*O2AINT(t)...
   +Fnaod*(O2deep(t)-O2NA(t))...
   +(FbnaodOrg)/(rCorgO2*umol2GtC))/(Vna*dSW)...
   +(FO2naao(t)-FO2naoa(t))/Vna...
   +O2NA(t);

   clear DICs ALKs SST PC02_r
   SST = SSTNA;
   DICs = DICNA(t+1);
   ALKs = ALKNA(t+1);
   csys3_hack;
   pCO2NA(t+1) = PC02_r;

C13na(t+1) = anao*Fnaao(t)*Ra(t)-anaa*Fnaoa(t)*Rna(t)...
   -aoph*FbnaodOrg*Rna(t)-FbnaodCaCO3*Rna(t)...
   +umol2GtC*(-AMOC*(DICNA(t)*Rna(t))...
   +Fnaod*(DICdeep(t)*Rod(t)-DICNA(t)*Rna(t))...
   +(AMOC-AMOCLow)*(DICsurf(t)*Ros(t))...
   +AMOCLow*(DICAINT(t)*Raint(t)))...
   +C13na(t);

d13Cna(t+1) = ((C13na(t+1)/Cna(t+1))/RPDB-1)*10^3;
Rna(t+1) = (C13na(t+1)/Cna(t+1));

C14na(t+1) = exp(-lamda*dt)*(anao^2*Fnaao(t)*R14a(t)-anaa^2*Fnaoa(t)*R14na(t)...
   -aoph^2*FbnaodOrg*R14na(t)-FbnaodCaCO3*R14na(t)...
   +umol2GtC*(-AMOC*(DICNA(t)*R14na(t))...
    +Fnaod*(DICdeep(t)*R14od(t)-DICNA(t)*R14na(t))...
   +(AMOC-AMOCLow)*(DICsurf(t)*R14os(t))...
   +AMOCLow*(DICAINT(t)*R14aint(t)))...
   +C14na(t));

d14Cna(t+1) = ((C14na(t+1)/Cna(t+1))/R14Cstd-1)*10^3;
R14na(t+1) = (C14na(t+1)/Cna(t+1));



%-----------------------------------------------------------------
%North Pacific ocean box balance
%-----------------------------------------------------------------
if (PO4NP(t)-PO4starNP)<0
%    display('zero PO4 in the north atlantic')
  OrgFluxz0 = 0;
else

OrgFluxz0 = (PO4NP(t)-PO4starNP)*rCPO4p*umol2GtC*Vnp*dSW*nobio*dt;
end
FbnppaodOrg = (OrgFluxz0*(hmix/100)^-b);
FbnppaodCaCO3 = (OrgFluxz0*(hmix/100)^-b)*FCANP;


Cnp(t+1) = Fnpao(t)-Fnpoa(t)-FbnppaodOrg-FbnppaodCaCO3...
```

```
   +umol2GtC*(Fnppint*(DICPINT(t)-DICNP(t)))...
   +Cnp(t);

DICNP(t+1) = Cnp(t+1)/(Vnp*dSW*umol2GtC);

PO4NP(t+1) = (Fnppint*(PO4PINT(t)-PO4NP(t))...
   -(FbnppaodOrg)/(rCPO4p*umol2GtC))/(Vnp*dSW)...
   +PO4NP(t);

ALKNP(t+1) = (Fnppint*(ALKPINT(t)-ALKNP(t))...
   -(FbnppaodCaCO3)/(rALKC*umol2GtC))/(Vnp*dSW)...
   +ALKNP(t);

O2NP(t+1) = (Fnppint*(O2PINT(t)-O2NP(t))...
   +(FbnppaodOrg)/(rCorgO2*umol2GtC))/(Vnp*dSW)...
   +(FO2npao(t)-FO2npoa(t))/Vnp...
   +O2NP(t);

   clear DICs ALKs SST PC02_r
   SST = SSTNA;
   DICs = DICNP(t+1);
   ALKs = ALKNP(t+1);
   csys3_hack;
   pCO2NP(t+1) = PC02_r;

C13np(t+1) = anao*Fnpao(t)*Ra(t)-anaa*Fnpoa(t)*Rnp(t)...
   -aoph*FbnppaodOrg*Rnp(t)-FbnppaodCaCO3*Rnp(t)...
   +umol2GtC*(Fnppint*(DICPINT(t)*Rpint(t)-DICNP(t)*Rnp(t)))...
   +C13np(t);

d13Cnp(t+1) = ((C13np(t+1)/Cnp(t+1))/RPDB-1)*10^3;
Rnp(t+1) = (C13np(t+1)/Cnp(t+1));

C14np(t+1) = exp(-lamda*dt)*(anao^2*Fnpao(t)*R14a(t)-anaa^2*Fnpoa(t)*R14np(t)...
   -aoph^2*FbnppaodOrg*R14np(t)-FbnppaodCaCO3*R14np(t)...
   +umol2GtC*(Fnppint*(DICPINT(t)*R14pint(t)-DICNP(t)*R14np(t)))...
   +C14np(t));

d14Cnp(t+1) = ((C14np(t+1)/Cnp(t+1))/R14Cstd-1)*10^3;
R14np(t+1) = (C14np(t+1)/Cnp(t+1));



%---------------------------------------------------------------
%Deep Atlantic Ocean
%---------------------------------------------------------------
%Fsed(t+1) = Fsed(t)*exp(-dt/taused)+(dt*ased)/taused*((-Fatao(t)+Fatoa(t)-Fsoao(t)+Fsooa(t)-
Fnaao(t)+Fnaoa(t)-Fpaao(t)+Fpaoa(t)-Faoao(t)+Faooa(t)-Fnpao(t)+Fnpoa(t))*exp(-dt/taused));
Fsed(t+1) = ased1*Fsed(t)*exp(-dt/taused1)+ased2*Fsed(t)*exp(-dt/taused2)+ased3*Fsed(t)*exp(-
dt/taused3)+(((dt*ased1)/taused1)*exp(-dt/taused1)+((dt*ased2)/taused2)*exp(-
dt/taused2)+((dt*ased3)/taused3)*exp(-dt/taused3))*(-Fatao(t)+Fatoa(t)-Fsoao(t)+Fsooa(t)-
Fnaao(t)+Fnaoa(t)-Fpaao(t)+Fpaoa(t)-Faoao(t)+Faooa(t)-Fnpao(t)+Fnpoa(t));
%Fsedsave(t+1) = Fsed(t+1);
%Fsed(t+1) = Fsedsave(t+1);
```

```
Cod(t+1) =
0.4*Fsed(t)+FbatadOrg+FbatadCaCO3+FbnaodOrg+FbnaodCaCO3+FbsoodOrg+FbsoodCaCO3...
   +umol2GtC*(AMOC*DICNA(t)...
   +CDWA*DICPD(t)...
   -Fnaod*(DICdeep(t)-DICNA(t))...
   +Faint2od*(DICAINT(t)-DICdeep(t))...
   +Fpd2od*(DICPD(t)-DICdeep(t))...
   -(AMOC+CDWA)*DICdeep(t))...
   +Cod(t);

DICdeep(t+1) = Cod(t+1)/(Vatdeep*dSW*umol2GtC);

%ALKdeep(t+1) = (-Fasad*(ALKdeep(t)-ALKsurf(t))-Fadpd*(ALKdeep(t)-
ALKPD(t)))/(Vatdeep*dSW)+ALKdeep(t);
PO4deep(t+1) = (AMOC*PO4NA(t)...
   +CDWA*PO4PD(t)...
   -Fnaod*(PO4deep(t)-PO4NA(t))...
   +Faint2od*(PO4AINT(t)-PO4deep(t))...
   +Fpd2od*(PO4PD(t)-PO4deep(t))...
   -(AMOC+CDWA)*PO4deep(t)...
   +(FbatadOrg+FbnaodOrg+FbsoodOrg)/(rCPO4p*umol2GtC))/(Vatdeep*dSW)+PO4deep(t);


PO4deepPre(t+1) = (AMOC*PO4starNA...
   +CDWA*PO4PDPre(t)...
   +Faint2od*(PO4AINTPre(t)-PO4deepPre(t))...
   +Fpd2od*(PO4PDPre(t)-PO4deepPre(t))...
   -Fnaod*(PO4deepPre(t)-PO4starNA)...
   -(AMOC+CDWA)*PO4deepPre(t))/(Vatdeep*dSW)+PO4deepPre(t);

ALKdeep(t+1) = (AMOC*ALKNA(t)...
   +CDWA*ALKPD(t)...
   +Faint2od*(ALKAINT(t)-ALKdeep(t))...
   +Fpd2od*(ALKPD(t)-ALKdeep(t))...
   -(AMOC+CDWA)*ALKdeep(t)...
   -Fnaod*(ALKdeep(t)-ALKNA(t))...

+(FbatadCaCO3+FbnaodCaCO3+FbsoodCaCO3)/(rALKC*umol2GtC))/(Vatdeep*dSW)+ALKdeep(t)
;
O2deep(t+1) = (AMOC*O2NA(t)...
   +CDWA*O2PD(t)...
    +Faint2od*(O2AINT(t)-O2deep(t))...
    +Fpd2od*(O2PD(t)-O2deep(t))...
   -(AMOC+CDWA)*O2deep(t)...
   -Fnaod*(O2deep(t)-O2NA(t))...
   -(FbatadOrg+FbnaodOrg+FbsoodOrg)/(rCorgO2*umol2GtC))/(Vatdeep*dSW)+O2deep(t);
dN2Odeep(t+1) = RNO2*(a1./(O2deep(t)+a2))*exp(-
3000/zscale)*((FbatadOrg+FbnaodOrg+FbsoodOrg)/(rCorgO2));


C13od(t+1) =
0.4*Fsed(t)*Rod(t)+aoph*(FbatadOrg*Ros(t)+FbnaodOrg*Rna(t)+FbsoodOrg*Rpo(t))+FbatadCaCO3
*Ros(t)+FbnaodCaCO3*Rna(t)+FbsoodCaCO3*Rpo(t)...
   +umol2GtC*(AMOC*DICNA(t)*Rna(t)...
```

```
   +CDWA*DICPD(t)*Rpd(t)...
   +Faint2od*(DICAINT(t)*Raint(t)-DICdeep(t)*Rod(t))...
   +Fpd2od*(DICPD(t)*Rpd(t)-DICdeep(t)*Rod(t))...
   -Fnaod*(DICdeep(t)*Rod(t)-DICNA(t)*Rna(t))...
   -(AMOC+CDWA)*DICdeep(t)*Rod(t))...
   +C13od(t);

d13Cod(t+1) = ((C13od(t+1)/Cod(t+1))/RPDB-1)*10^3;
Rod(t+1) = (C13od(t+1)/Cod(t+1));

C14od(t+1) = exp(-
lamda*dt)*(0.4*Fsed(t)*R14od(t)+aoph^2*(FbatadOrg*R14os(t)+FbnaodOrg*R14na(t)+FbsoodOrg*
R14po(t))+FbatadCaCO3*R14os(t)+FbnaodCaCO3*R14na(t)+FbsoodCaCO3*R14po(t)...
   +umol2GtC*(AMOC*DICNA(t)*R14na(t)...
   +Faint2od*(DICAINT(t)*R14aint(t)-DICdeep(t)*R14od(t))...
   +Fpd2od*(DICPD(t)*R14pd(t)-DICdeep(t)*R14od(t))...
   +CDWA*DICPD(t)*R14pd(t)...
   -Fnaod*(DICdeep(t)*R14od(t)-DICNA(t)*R14na(t))...
   -(AMOC+CDWA)*DICdeep(t)*R14od(t))...
   +C14od(t));

d14Cod(t+1) = ((C14od(t+1)/Cod(t+1))/R14Cstd-1)*10^3;
R14od(t+1) = (C14od(t+1)/Cod(t+1));


%-----------------------------------------------------------------
%Surface Pacific Ocean
%-----------------------------------------------------------------
if (PO4PAS(t)-PO4starPAC)<0
   display('zero PO4 in surface pacific')
  OrgFluxz0 = 0;
else

OrgFluxz0 = (PO4PAS(t)-PO4starPAC)*rCPO4p*umol2GtC*Vpacificmix*dSW*nobio*dt;
end
FbpapdOrg = frac2pd*(OrgFluxz0*(effdepthAABW/100)^-b);
FbpapadOrg = (OrgFluxz0*((hint+hmix)/100)^-b)-frac2pd*(OrgFluxz0*(effdepthAABW/100)^-b)+(1-
fracPINTofSurface)*(OrgFluxz0*(hmix/100)^-b);
FbpapiOrg =fracPINTofSurface*(OrgFluxz0*(hmix/100)^-b)-(OrgFluxz0*((hint+hmix)/100)^-b)-
frac2pd*(OrgFluxz0*(effdepthAABW/100)^-b);


FbpapiCaCO3 =FbpapiOrg*FCAlowlat*FCAremin;
FbpapdCaCO3 = FbpapdOrg*FCAlowlat+(FbpapiOrg*FCAlowlat*(1-FCAremin))/2;
FbpapadCaCO3 = FbpapadOrg*FCAlowlat+(FbpapiOrg*FCAlowlat*(1-FCAremin))/2;



Cpaos(t+1) = -
(FbpapiOrg+FbpapadOrg+FbpapdOrg+FbpapdCaCO3+FbpapadCaCO3+FbpapiCaCO3)+Fpaao(t)-
Fpaoa(t)...
   +umol2GtC*(PFT*DICPINT(t)...
   -PFT*DICpaosurf(t)...
   +Fpaspint*(DICPINT(t)-DICpaosurf(t))...
```

```
    +Fpaspad*(DICPAD(t)-DICpaosurf(t)))...
    +Cpaos(t);

DICpaosurf(t+1) = Cpaos(t+1)/(Vpacificmix*dSW*umol2GtC);

PO4PAS(t+1) = (PFT*PO4PINT(t)...
    -PFT*PO4PAS(t)...
    +Fpaspint*(PO4PINT(t)-PO4PAS(t))...
    +Fpaspad*(PO4PAD(t)-PO4PAS(t))...
    -(FbpapiOrg+FbpapadOrg+FbpapdOrg)/(rCPO4p*umol2GtC))/(Vpacificmix*dSW)...
    +PO4PAS(t);
ALKPAS(t+1) = (PFT*ALKPINT(t)...
    -PFT*ALKPAS(t)...
    +Fpaspint*(ALKPINT(t)-ALKPAS(t))...
    +Fpaspad*(ALKPAD(t)-ALKPAS(t))...
    -(FbpapdCaCO3+FbpapadCaCO3+FbpapiCaCO3)/(rALKC*umol2GtC))/(Vpacificmix*dSW)...
    +ALKPAS(t);
O2PAS(t+1) = (PFT*O2PINT(t)...
    -PFT*O2PAS(t)...
    +Fpaspint*(O2PINT(t)-O2PAS(t))...
    +Fpaspad*(O2PAD(t)-O2PAS(t))...
    +(FbpapiOrg+FbpapadOrg+FbpapdOrg)/(rCorgO2*umol2GtC))/(Vpacificmix*dSW)...
    +(FO2paao(t)-FO2paoa(t))/Vpacificmix...
    +O2PAS(t);


    clear DICs ALKs SST PC02_r
    SST = SSTMO;
    DICs = DICpaosurf(t+1);
    ALKs = ALKPAS(t+1);
    csys3_hack;
    pCO2paos(t+1) = PC02_r;


C13paos(t+1) = -aoph*(FbpapiOrg+FbpapadOrg+FbpapdOrg)*Rpaos(t)...
    -(FbpapdCaCO3+FbpapadCaCO3+FbpapiCaCO3)*Rpaos(t)...
    +aao*Fpaao(t)*Ra(t)-aoa*Fpaoa(t)*Rpaos(t)...
    +umol2GtC*(PFT*DICPINT(t)*Rpint(t)...
    -PFT*DICpaosurf(t)*Rpaos(t)...
    +Fpaspint*(DICPINT(t)*Rpint(t)-DICpaosurf(t)*Rpaos(t))...
    +Fpaspad*(DICPAD(t)*Rpaod(t)-DICpaosurf(t)*Rpaos(t)))...
    +C13paos(t);

d13Cpaos(t+1) = ((C13paos(t+1)/Cpaos(t+1))/RPDB-1)*10^3;
Rpaos(t+1) = (C13paos(t+1)/Cpaos(t+1));

C14paos(t+1) = exp(-lamda*dt)*(-aoph^2*(FbpapiOrg+FbpapadOrg+FbpapdOrg)*R14paos(t)...
    -(FbpapdCaCO3+FbpapadCaCO3+FbpapiCaCO3)*R14paos(t)...
    +aao^2*Fpaao(t)*R14a(t)-aoa^2*Fpaoa(t)*R14paos(t)...
    +umol2GtC*(PFT*DICPINT(t)*R14pint(t)...
    -PFT*DICpaosurf(t)*R14paos(t)...
    +Fpaspint*(DICPINT(t)*R14pint(t)-DICpaosurf(t)*R14paos(t))...
    +Fpaspad*(DICPAD(t)*R14paod(t)-DICpaosurf(t)*R14paos(t)))...
    +C14paos(t));
```

```
d14Cpaos(t+1) = ((C14paos(t+1)/Cpaos(t+1))/R14Cstd-1)*10^3;
R14paos(t+1) = (C14paos(t+1)/Cpaos(t+1));


%------------------------------------------------------------
%Deep Polar Ocean
%------------------------------------------------------------
Cpd(t+1) =
FbatpdOrg+FbsopdOrg+FbpapdOrg+FbatpdCaCO3+FbsopdCaCO3+FbpapdCaCO3+FbaopdOrg...
   +umol2GtC*((CDW+NADW2AO)*DICAO(t)...
   +NADW2CDW*DICdeep(t)...
   +Fpd2pad*(DICPAD(t)-DICPD(t))...
   +Fpd2od*(DICdeep(t)-DICPD(t))...
   -(CDW+NADW2CDW+NADW2AO)*DICPD(t))...
   +Cpd(t);

DICPD(t+1) = Cpd(t+1)/(Vpd*dSW*umol2GtC);

PO4PD(t+1) = ((CDW+NADW2AO)*PO4AO(t)...
   +NADW2CDW*PO4deep(t)...
   +Fpd2pad*(PO4PAD(t)-PO4PD(t))...
   +Fpd2od*(PO4deep(t)-PO4PD(t))...
   -(CDW+NADW2CDW+NADW2AO)*PO4PD(t)...
   +(FbatpdOrg+FbsopdOrg+FbpapdOrg+FbaopdOrg)/(rCPO4p*umol2GtC))/(Vpd*dSW)...
   +PO4PD(t);

PO4PDPre(t+1) = ((CDW+NADW2AO)*PO4starAO...
   +NADW2CDW*PO4deepPre(t)...
   +Fpd2pad*(PO4PADPre(t)-PO4PDPre(t))...
   +Fpd2od*(PO4deepPre(t)-PO4PDPre(t))...
   -(CDW+NADW2CDW+NADW2AO)*PO4PDPre(t))/(Vpd*dSW)...
   +PO4PDPre(t);


ALKPD(t+1) = ((CDW+NADW2AO)*ALKAO(t)...
   +NADW2CDW*ALKdeep(t)...
   +Fpd2pad*(ALKPAD(t)-ALKPD(t))...
   +Fpd2od*(ALKdeep(t)-ALKPD(t))...
   -(CDW+NADW2CDW+NADW2AO)*ALKPD(t)...
   +(FbatpdCaCO3+FbsopdCaCO3+FbpapdCaCO3)/(rALKC*umol2GtC))/(Vpd*dSW)...
   +ALKPD(t);

O2PD(t+1) = ((CDW+NADW2AO)*O2AO(t)...
   +NADW2CDW*O2deep(t)...
   +Fpd2pad*(O2PD(t)-O2PAD(t))...
   +Fpd2od*(O2deep(t)-O2PAD(t))...
   -(CDW+NADW2CDW+NADW2AO)*O2PD(t)...
   -(FbatpdOrg+FbsopdOrg+FbpapdOrg+FbaopdOrg)/(rCorgO2*umol2GtC))/(Vpd*dSW)...
   +O2PD(t);
dN2OPD(t+1) = RNO2*(a1./(O2PD(t)+a2))*exp(-
4000/zscale)*((FbatpdOrg+FbsopdOrg+FbpapdOrg+FbaopdOrg)/(rCorgO2));
```

```
C13pd(t+1) =
aoph*(FbatpdOrg*Ros(t)+FbsopdOrg*Rpo(t)+FbpapdOrg*Rpaos(t)+FbaopdOrg*Rao(t))...
   +FbatpdCaCO3*Ros(t)+FbsopdCaCO3*Rpo(t)+FbpapdCaCO3*Rpaos(t)...
   +umol2GtC*((CDW+NADW2AO)*DICAO(t)*Rao(t)...
   +NADW2CDW*DICdeep(t)*Rod(t)...
   +Fpd2pad*(DICPAD(t)*Rpaod(t)-DICPD(t)*Rpd(t))...
   +Fpd2od*(DICdeep(t)*Rod(t)-DICPD(t)*Rpd(t))...
   -(CDW+NADW2CDW+NADW2AO)*DICPD(t)*Rpd(t))...
   +C13pd(t);

d13Cpd(t+1) = ((C13pd(t+1)/Cpd(t+1))/RPDB-1)*10^3;
Rpd(t+1) = (C13pd(t+1)/Cpd(t+1));

C14pd(t+1) = exp(-
lamda*dt)*(aoph^2*(FbatpdOrg*R14os(t)+FbsopdOrg*R14po(t)+FbpapdOrg*R14paos(t)+FbaopdOrg
*R14ao(t))...
    +FbatpdCaCO3*R14os(t)+FbsopdCaCO3*R14po(t)+FbpapdCaCO3*R14paos(t)...
   +umol2GtC*((CDW+NADW2AO)*DICAO(t)*R14ao(t)...
   +NADW2CDW*DICdeep(t)*R14od(t)...
   +Fpd2pad*(DICPAD(t)*R14paod(t)-DICPD(t)*R14pd(t))...
   +Fpd2od*(DICdeep(t)*R14od(t)-DICPD(t)*R14pd(t))...
   -(CDW+NADW2CDW+NADW2AO)*DICPD(t)*R14pd(t))...
   +C14pd(t));

d14Cpd(t+1) = ((C14pd(t+1)/Cpd(t+1))/R14Cstd-1)*10^3;
R14pd(t+1) = (C14pd(t+1)/Cpd(t+1));



%---------------------------------------------------------------
%Deep Pacific Ocean
%---------------------------------------------------------------
Cpaod(t+1) =
0.6*Fsed(t)+FbpapadOrg+FbsopadOrg+FbpapadCaCO3+FbsopadCaCO3+FbnppaodOrg+FbnppaodC
aCO3...
   +umol2GtC*((CDWP+NADW2CDW+NADW2AO)*DICPD(t)...
   +NADW2Ind*DICdeep(t)...
   +Fpint2pad*(DICPINT(t)-DICPAD(t))...
   +Fpd2pad*(DICPD(t)-DICPAD(t))...
   -(NADW2IndPac+CDWP)*DICPAD(t))...
   +Cpaod(t);

DICPAD(t+1) = Cpaod(t+1)/(Vpadeep*dSW*umol2GtC);

PO4PAD(t+1) = ((CDWP+NADW2CDW+NADW2AO)*PO4PD(t)...
     +NADW2Ind*PO4deep(t)...
   -(NADW2IndPac+CDWP)*PO4PAD(t)...
    +Fpint2pad*(PO4PINT(t)-PO4PAD(t))...
    +Fpd2pad*(PO4PD(t)-PO4PAD(t))...
   +(FbpapadOrg+FbsopadOrg+FbnppaodOrg)/(rCPO4p*umol2GtC))/(Vpadeep*dSW)...
   +PO4PAD(t);

PO4PADPre(t+1) = ((CDWP+NADW2CDW+NADW2AO)*PO4PDPre(t)...
     +NADW2Ind*PO4deepPre(t)...
```

```
    +Fpint2pad*(PO4PINTPre(t)-PO4PADPre(t))...
     +Fpd2pad*(PO4PDPre(t)-PO4PADPre(t))...
   -(NADW2IndPac+CDWP)*PO4PADPre(t))/(Vpadeep*dSW)...
   +PO4PADPre(t);


ALKPAD(t+1) = ((CDWP+NADW2CDW+NADW2AO)*ALKPD(t)...
     +NADW2Ind*ALKdeep(t)...
   -(NADW2IndPac+CDWP)*ALKPAD(t)...
    +Fpint2pad*(ALKPINT(t)-ALKPAD(t))...
    +Fpd2pad*(ALKPD(t)-ALKPAD(t))...
   +(FbpapadCaCO3+FbsopadCaCO3+FbnppaodCaCO3)/(rALKC*umol2GtC))/(Vpadeep*dSW)...
   +ALKPAD(t);


O2PAD(t+1) = ((CDWP+NADW2CDW+NADW2AO)*O2PD(t)...
     +NADW2Ind*O2deep(t)...
   -(NADW2IndPac+CDWP)*O2PAD(t)...
    +Fpint2pad*(O2PINT(t)-O2PAD(t))...
    +Fpd2pad*(O2PD(t)-O2PAD(t))...
   -(FbpapadOrg+FbsopadOrg+FbnppaodOrg)/(rCorgO2*umol2GtC))/(Vpadeep*dSW)...
   +O2PAD(t);
dN2OPAD(t+1) = RNO2*(a1./(O2PAD(t)+a2))*exp(-
3000/zscale)*((FbpapadOrg+FbsopadOrg+FbnppaodOrg)/(rCorgO2));

C13paod(t+1) =
0.6*Fsed(t)*Rpaod(t)+aoph*FbpapadOrg*Rpaos(t)+FbpapadCaCO3*Rpaos(t)+aoph*FbsopadOrg*Rp
o(t)+FbsopadCaCO3*Rpo(t)+aoph*FbnppaodOrg*Rnp(t)+FbnppaodCaCO3*Rnp(t)...
   +umol2GtC*((CDWP+NADW2CDW+NADW2AO)*DICPD(t)*Rpd(t)...
     +NADW2Ind*DICdeep(t)*Rod(t)...
    +Fpint2pad*(DICPINT(t)*Rpint(t)-DICPAD(t)*Rpaod(t))...
     +Fpd2pad*(DICPD(t)*Rpd(t)-DICPAD(t)*Rpaod(t))...
   -(NADW2IndPac+CDWP)*DICPAD(t)*Rpaod(t))...
   +C13paod(t);

d13Cpaod(t+1) = ((C13paod(t+1)/Cpaod(t+1))/RPDB-1)*10^3;
Rpaod(t+1) = (C13paod(t+1)/Cpaod(t+1));

C14paod(t+1) = exp(-
lamda*dt)*(0.6*Fsed(t)*R14paod(t)+aoph^2*FbpapadOrg*R14paos(t)+FbpapadCaCO3*R14paos(t)+
aoph^2*FbsopadOrg*R14po(t)+FbsopadCaCO3*R14po(t)+aoph^2*FbnppaodOrg*R14np(t)+Fbnppao
dCaCO3*R14np(t)...
   +umol2GtC*((CDWP+NADW2CDW+NADW2AO)*DICPD(t)*R14pd(t)...
      +NADW2Ind*DICdeep(t)*R14od(t)...
      +Fpint2pad*(DICPINT(t)*R14pint(t)-DICPAD(t)*R14paod(t))...
      +Fpd2pad*(DICPD(t)*R14pd(t)-DICPAD(t)*R14paod(t))...
   -(NADW2IndPac+CDWP)*DICPAD(t)*R14paod(t))...
   +C14paod(t));

d14Cpaod(t+1) = ((C14paod(t+1)/Cpaod(t+1))/R14Cstd-1)*10^3;
R14paod(t+1) = (C14paod(t+1)/Cpaod(t+1));

%-------------------------------------------------------------
%Intermediate Pacific Ocean
```

```
%-------------------------------------------------------------

Cpint(t+1) = +FbpapiOrg+FbpapiCaCO3...
   +umol2GtC*((PFT-AAIWP)*DICPO(t)...
   +AAIWP*DICPAD(t)...
   +Fpaspint*(DICpaosurf(t)-DICPINT(t))...
   +Fpint2pad*(DICPAD(t)-DICPINT(t))...
   +Fnppint*(DICNP(t)-DICPINT(t))...
   -PFT*DICPINT(t))...
   +Cpint(t);

DICPINT(t+1) = Cpint(t+1)/(Vpint*dSW*umol2GtC);

PO4PINT(t+1) = ((PFT-AAIWP)*PO4PO(t)...
   +AAIWP*PO4PAD(t)...
   -PFT*PO4PINT(t)...
   +Fpaspint*(PO4PAS(t)-PO4PINT(t))...
   +Fpint2pad*(PO4PAD(t)-PO4PINT(t))...
   +Fnppint*(PO4NP(t)-PO4PINT(t))...
   +(FbpapiOrg)/(rCPO4p*umol2GtC))/(Vpint*dSW)...
   +PO4PINT(t);

PO4PINTPre(t+1) = ((PFT-AAIWP)*PO4starPO...
   +AAIWP*PO4PADPre(t)...
   -PFT*PO4PINTPre(t)...
   +Fnppint*(PO4starNP-PO4PINTPre(t))...
   +Fpint2pad*(PO4PADPre(t)-PO4PINTPre(t))...
   +Fpaspint*(PO4starPAC-PO4PINTPre(t)))/(Vpint*dSW)...
   +PO4PINTPre(t);

ALKPINT(t+1) = ((PFT-AAIWP)*ALKPO(t)...
   +AAIWP*ALKPAD(t)...
   -PFT*ALKPINT(t)...
   +Fpaspint*(ALKPAS(t)-ALKPINT(t))...
   +Fpint2pad*(ALKPAD(t)-ALKPINT(t))...
   +Fnppint*(ALKNP(t)-ALKPINT(t))...
   +(FbpapiCaCO3)/(rALKC*umol2GtC))/(Vpint*dSW)...
   +ALKPINT(t);

O2PINT(t+1) = ((PFT-AAIWP)*O2PO(t)...
   +AAIWP*O2PAD(t)...
   -PFT*O2PINT(t)...
   +Fpaspint*(O2PAS(t)-O2PINT(t))...
   +Fpint2pad*(O2PAD(t)-O2PINT(t))...
   +Fnppint*(O2NP(t)-O2PINT(t))...
   -(FbpapiOrg)/(rCorgO2*umol2GtC))/(Vpint*dSW)...
   +O2PINT(t);

dN2OPINT(t+1) = RNO2*(a1./(O2PINT(t)+a2))*exp(-100/zscale)*((FbpapiOrg)/(rCorgO2));

C13pint(t+1) = aoph*FbpapiOrg*Rpaos(t)+FbpapiCaCO3*Rpaos(t)...
   +umol2GtC*((PFT-AAIWP)*DICPO(t)*Rpo(t)...
   +AAIWP*DICPAD(t)*Rpaod(t)...
   +Fpaspint*(DICpaosurf(t)*Rpaos(t)-DICPINT(t)*Rpint(t))...
```

```
   +Fpint2pad*(DICPAD(t)*Rpaod(t)-DICPINT(t)*Rpint(t))...
   +Fnppint*(DICNP(t)*Rnp(t)-DICPINT(t)*Rpint(t))...
   -PFT*DICPINT(t)*Rpint(t))...
   +C13pint(t);

d13Cpint(t+1) = ((C13pint(t+1)/Cpint(t+1))/RPDB-1)*10^3;
Rpint(t+1) = (C13pint(t+1)/Cpint(t+1));

C14pint(t+1) = exp(-lamda*dt)*(aoph^2*FbpapiOrg*R14paos(t)+FbpapiCaCO3*R14paos(t)...
   +umol2GtC*((PFT-AAIWP)*DICPO(t)*R14po(t)...
   +AAIWP*DICPAD(t)*R14paod(t)...
   +Fpaspint*(DICpaosurf(t)*R14paos(t)-DICPINT(t)*R14pint(t))...
   +Fpint2pad*(DICPAD(t)*R14paod(t)-DICPINT(t)*R14pint(t))...
   +Fnppint*(DICNP(t)*R14np(t)-DICPINT(t)*R14pint(t))...
   -PFT*DICPINT(t)*R14pint(t))...
   +C14pint(t));

d14Cpint(t+1) = ((C14pint(t+1)/Cpint(t+1))/R14Cstd-1)*10^3;
R14pint(t+1) = (C14pint(t+1)/Cpint(t+1));

%---------------------------------------------------------------
%Intermediate Atlantic Ocean
%---------------------------------------------------------------
Caint(t+1) = FbataiOrg+FbataiCaCO3...
   +umol2GtC*((AMOC-PFT)*DICPO(t)...
   +Fosaint*(DICsurf(t)-DICAINT(t))...
   +Faint2od*(DICdeep(t)-DICAINT(t))...
   -(AMOC-PFT)*DICAINT(t))...
   +Caint(t);

DICAINT(t+1) = Caint(t+1)/(Vaint*dSW*umol2GtC);

PO4AINT(t+1) = ((AMOC-PFT)*PO4PO(t)...
   -(AMOC-PFT)*PO4AINT(t)...
   +Fosaint*(PO4surf(t)-PO4AINT(t))...
   +Faint2od*(PO4deep(t)-PO4AINT(t))...
   +(FbataiOrg)/(rCPO4p*umol2GtC))/(Vaint*dSW)...
   +PO4AINT(t);


PO4AINTPre(t+1) = ((AMOC-PFT)*PO4starPO...
   -(AMOC-PFT)*PO4AINTPre(t)...
   +Faint2od*(PO4deepPre(t)-PO4AINTPre(t))...
   +Fosaint*(PO4starAT-PO4AINTPre(t)))/(Vaint*dSW)...
   +PO4AINTPre(t);

ALKAINT(t+1) = ((AMOC-PFT)*ALKPO(t)...
   -(AMOC-PFT)*ALKAINT(t)...
   +Fosaint*(ALKsurf(t)-ALKAINT(t))...
   +Faint2od*(ALKdeep(t)-ALKAINT(t))...
   +(FbataiCaCO3)/(rALKC*umol2GtC))/(Vaint*dSW)...
   +ALKAINT(t);

O2AINT(t+1) = ((AMOC-PFT)*O2PO(t)...
```

```
   -(AMOC-PFT)*O2AINT(t)...
   +Fosaint*(O2surf(t)-O2AINT(t))...
   +Faint2od*(O2deep(t)-O2AINT(t))...
   -(FbataiOrg)/(rCorgO2*umol2GtC))/(Vaint*dSW)...
   +O2AINT(t);

dN2OAINT(t+1) = RNO2*(a1./(O2AINT(t)+a2))*exp(-100/zscale)*((FbataiOrg)/(rCorgO2));

C13aint(t+1) = aoph*FbataiOrg*Ros(t)+FbataiCaCO3*Ros(t)...
   +umol2GtC*((AMOC-PFT)*DICPO(t)*Rpo(t)...
   +Fosaint*(DICsurf(t)*Ros(t)-DICAINT(t)*Raint(t))...
    +Faint2od*(DICdeep(t)*Rod(t)-DICAINT(t)*Raint(t))...
   -(AMOC-PFT)*DICAINT(t)*Raint(t))...
   +C13aint(t);


d13Caint(t+1) = ((C13aint(t+1)/Caint(t+1))/RPDB-1)*10^3;
Raint(t+1) = (C13aint(t+1)/Caint(t+1));

C14aint(t+1) = exp(-lamda*dt)*(aoph^2*FbataiOrg*R14os(t)+FbataiCaCO3*R14os(t)...
   +umol2GtC*((AMOC-PFT)*DICPO(t)*R14po(t)...
   +Fosaint*(DICsurf(t)*R14os(t)-DICAINT(t)*R14aint(t))...
   +Faint2od*(DICdeep(t)*R14od(t)-DICAINT(t)*R14aint(t))...
   -(AMOC-PFT)*DICAINT(t)*R14aint(t))...
   +C14aint(t));

d14Caint(t+1) = ((C14aint(t+1)/Caint(t+1))/R14Cstd-1)*10^3;
R14aint(t+1) = (C14aint(t+1)/Caint(t+1));



%-------------------------------------------------------------
%long lived terrestrial biosphere box balance
%-------------------------------------------------------------
Cb(t+1) = Flph-Flb+Cb(t);
C13b(t+1) = alph*Flph*Ra(t)-Flb*Rb(t)+C13b(t);
d13Cb(t+1) = ((C13b(t+1)/Cb(t+1))/RPDB-1)*10^3;
Rb(t+1) = (C13b(t+1)/Cb(t+1));

C14b(t+1) = exp(-lamda*dt)*(alph^2*Flph*R14a(t)-Flb*R14b(t)+C14b(t));
d14Cb(t+1) = ((C14b(t+1)/Cb(t+1))/R14Cstd-1)*10^3;
R14b(t+1) = (C14b(t+1)/Cb(t+1));
%-------------------------------------------------------------
%short lived terrestrial biosphere box balance
%-------------------------------------------------------------
Cb2(t+1) = Flph2-Flb2+Cb2(t);
C13b2(t+1) = alph*Flph2*Ra(t)-Flb2*Rb2(t)+C13b2(t);
d13Cb2(t+1) = ((C13b2(t+1)/Cb2(t+1))/RPDB-1)*10^3;
Rb2(t+1) = (C13b2(t+1)/Cb2(t+1));

C14b2(t+1) = exp(-lamda*dt)*(alph^2*Flph2*R14a(t)-Flb2*R14b2(t)+C14b2(t));
d14Cb2(t+1) = ((C14b2(t+1)/Cb2(t+1))/R14Cstd-1)*10^3;
R14b2(t+1) = (C14b2(t+1)/Cb2(t+1));
%-------------------------------------------------------------
```

```
%Conservation of Mass Checks
%---------------------------------------------------------------
TotalN2O(t) =
((((dN2OPINT(t)+dN2OAINT(t)+dN2OPAD(t)+dN2OPD(t)+dN2Odeep(t))*10)/(mol2GtC))*28)/(1e1
2);
TotalC(t) =
Ca(t)+Cb(t)+Cos(t)+Cod(t)+Cpo(t)+Cb2(t)+Cpd(t)+Cna(t)+Cpaos(t)+Cpaod(t)+Cpint(t)+Caint(t)+Cao
(t)+Cnp(t);
TotalC13(t) =
C13a(t)+C13os(t)+C13od(t)+C13b(t)+C13po(t)+C13b2(t)+C13pd(t)+C13na(t)+C13paod(t)+C13paos(
t)+C13pint(t)+C13aint(t)+C13ao(t)+C13np(t);
TotalC14(t) =
C14a(t)+C14os(t)+C14od(t)+C14b(t)+C14po(t)+C14b2(t)+C14pd(t)+C14na(t)+C14paod(t)+C14paos(
t)+C14pint(t)+C14aint(t)+C14ao(t)+C14np(t);
TotalO2(t) =
O2PD(t)*Vpd+O2PO(t)*Vpo+O2deep(t)*Vatdeep+O2surf(t)*Vatmix+O2NA(t)*Vna+O2PAS(t)*Vpa
cificmix+O2PAD(t)*Vpadeep+O2PINT(t)*Vpint+O2AINT(t)*Vaint+O2AO(t)*Vao+O2NP(t)*Vnp+(
molesatm*1000)*O2atm(t);
TotalPO4(t) =
PO4PD(t)*Vpd+PO4PO(t)*Vpo+PO4deep(t)*Vatdeep+PO4surf(t)*Vatmix+PO4NA(t)*Vna+PO4PA
S(t)*Vpacificmix+PO4PAD(t)*Vpadeep+PO4PINT(t)*Vpint+PO4AINT(t)*Vaint+PO4AO(t)*Vao+P
O4NP(t)*Vnp;
TotalALK(t) =
ALKPD(t)*Vpd+ALKPO(t)*Vpo+ALKdeep(t)*Vatdeep+ALKsurf(t)*Vatmix+ALKNA(t)*Vna+ALK
PAS(t)*Vpacificmix+ALKPAD(t)*Vpadeep+ALKPINT(t)*Vpint+ALKAINT(t)*Vaint+ALKAO(t)*V
ao+ALKNP(t)*Vnp;
TotalPO4Pre(t)  =
PO4PDPre(t)*Vpd+PO4starPO*Vpo+PO4deepPre(t)*Vatdeep+PO4starAT*Vatmix+PO4starNA*Vna
+PO4starPAC*Vpacificmix+PO4PADPre(t)*Vpadeep+PO4PINTPre(t)*Vpint+PO4AINTPre(t)*Vaint
+PO4starAO*Vao+PO4starNA*Vnp;
```

File: O2a_O2oc.m

```
function O2oc = O2a_O2oc(O2atmosphere,temp,salinityO2)

tempK = temp+273.15;

A1 = -58.3877;
A2 = 85.8079;
A3 = 23.8439;
B1 = -.034892;
B2 = .015568;
B3 = -.0019387;

Bunsenconv = 22.4136; %l mol-1
Sa =
(exp(A1+A2*(100/tempK)+A3*log(tempK/100)+salinityO2*(B1+B2*(tempK/100)+B3*(tempK/100)
^2))/Bunsenconv)*10e5;
O2oc = O2atmosphere*Sa;
```

B.5 References

Archer, D., et al. (1997), Multiple timescales for neutralization of fossil fuel CO_2, *Geophysical Research Letters*, *24*(4), 405-408.

Grachev, A. M., et al. (2007), Abrupt changes in atmospheric methane at the MIS 5b-5a transition, *Geophysical Research Letters*, *34*(20), 5.

Joos, F., et al. (2004), Transient simulations of Holocene atmospheric carbon dioxide and terrestrial carbon since the Last Glacial Maximum, *Global Biogeochemical Cycles*, *18*(2).

Martin, J. H., et al. (1987), VERTEX: carbon cycling in the northeast Pacific, *Deep Sea Research Part A. Oceanographic Research Papers*, *34*(2), 267-285.

Mitchell, L. E., et al. (2011), Multidecadal variability of atmospheric methane, 1000-1800 CE, *Journal of Geophysical Research-Biogeosciences*, *116*.

Talley, L. D. (2013), Closure of the global overturning circulation through the Indian, Pacific, and Southern Oceans: Schematics and transports, *Oceanography*, *26*(1), 80-97.

Toggweiler, J. R. (1999), Variation of atmospheric CO_2 by ventilation of the ocean's deepest water, *Paleoceanography*, *14*(5), 571-588.

Zeebe, R., and D. Wolf-Gladrow (2001), *CO_2 in Seawater: Equilibrium, Kinetics, Isotopes* 346 pp., Amsterdam.

Bibliography

Adkins, J. F., et al. (2002), The salinity, temperature, and delta O-18 of the glacial deep ocean, *Science*, *298*(5599), 1769-1773.

Ahmed, M., et al. (2013), Continental-scale temperature variability during the past two millennia, *Nature Geoscience*.

Ahn, J., et al. (2009), A high-precision method for measurement of paleoatmospheric CO_2 in small polar ice samples, *J. Glaciol.*, *55*(191), 499-506.

Ahn, J., et al. (2012), Atmospheric CO_2 over the last 1000 years: A high-resolution record from the West Antarctic Ice Sheet (WAIS) Divide ice core, *Global Biogeochemical Cycles*, *26*.

Archer, D., et al. (1997), Multiple timescales for neutralization of fossil fuel CO_2, *Geophysical Research Letters*, *24*(4), 405-408.

Archer, D. E., et al. (2003), Model sensitivity in the effect of Antarctic sea ice and stratification on atmospheric pCO_2, *Paleoceanography*, *18*(1).

Arora, V. K., et al. (2013), Carbon-Concentration and Carbon-Climate Feedbacks in CMIP5 Earth System Models, *J. Clim.*, *26*(15), 5289-5314.

Assonov, S. S., and C. A. M. Brenninkmeijer (2006), On the N_2O correction used for mass spectrometric analysis of atmospheric CO_2, *Rapid Communications In Mass Spectrometry*, *20*(11), 1809-1819.

Assonov, S. S., et al. (2005), The ^{18}O isotope exchange rate between firn air CO_2 and the firn matrix at three Antarctic sites, *Journal of Geophysical Research: Atmospheres*, *110*(D18).

Barker, S., et al. (2010), Extreme deepening of the Atlantic overturning circulation during deglaciation, *Nature Geosci*, *3*(8), 567-571.

Blunier, T., et al. (2007), Synchronization of ice core records via atmospheric gases, *Climate of the Past*, *3*(2), 325-330.

Böhm, F., et al. (2002), Evidence for preindustrial variations in the marine surface water carbonate system from coralline sponges, *Geochem. Geophys. Geosyst.*, *3*, 13.

Bottinga, Y., and H. Craig (1968), Oxygen isotope fractionation between CO_2 and water, and the isotopic composition of marine atmospheric CO_2, *Earth and Planetary Science Letters*, *5*, 285-295.

Bouttes, N., et al. (2011), Last Glacial Maximum CO_2 and delta C-13 successfully reconciled, *Geophysical Research Letters*, *38*.

Bouttes, N., et al. (2012), Impact of oceanic processes on the carbon cycle during the last termination, *Climate of the Past*, *8*(1), 149-170.

Brenninkmeijer, C. A. M., et al. (1983), Oxygen Isotope Fractionation Between CO_2 and H2O, *Isotope Geoscience*, *1*(2), 181-190.

Broecker, W., et al. (1999), How strong is the Harvardton-Bear Constraint?, *Global Biogeochemical Cycles*, *13*(4), 817-820.

Broecker, W. S. (1998), Paleocean circulation during the Last Deglaciation: A bipolar seesaw?, *Paleoceanography*, *13*(2), 119-121.

Broecker, W. S. (2000), Was a change in thermohaline circulation responsible for the Little

Ice Age?, *Proceedings of the National Academy of Sciences*, *97*(4), 1339-1342.

Broecker, W. S., and D. McGee (2013), The 13C record for atmospheric CO_2: What is it trying to tell us?, *Earth and Planetary Science Letters*, *368*(0), 175-182.

Brovkin, V., et al. (2010), Sensitivity of a coupled climate-carbon cycle model to large volcanic eruptions during the last millennium, *Tellus Series B-Chemical and Physical Meteorology*, *62*(5), 674-681.

Brzezinski, M. A., et al. (2002), A switch from Si $(OH)_4$ to NO_3 depletion in the glacial Southern Ocean, *Geophysical Research Letters*, *29*(12), 5-1-5-4.

Buizert, C., et al. (2013), Assessment of diffusive isotopic fractionation in polar firn, and application to ice core trace gas records, *Earth and Planetary Science Letters*, *361*(0), 110-119.

Burke, A., and L. F. Robinson (2012), The Southern Ocean's Role in Carbon Exchange During the Last Deglaciation, *Science*, *335*(6068), 557-561.

Calvo, E., et al. (2011), Eastern Equatorial Pacific productivity and related-CO_2 changes since the last glacial period, *Proceedings of the National Academy of Sciences*

Cheng, H., et al. (2009), Ice Age Terminations, *Science*, *326*(5950), 248-252.

Chikamoto, M. O., et al. (2012), Quantifying the ocean's role in glacial CO_2 reductions, *Climate of the Past*, *8*(2), 545-563.

Christiansen, B., and F. C. Ljungqvist (2012), The extra-tropical Northern Hemisphere temperature in the last two millennia: reconstructions of low-frequency variability, *Climate*

of the Past, *8*(2), 765-786.

Ciais, P., et al. (2012), Large inert carbon pool in the terrestrial biosphere during the Last Glacial Maximum, *Nature Geosci*, *5*(1), 74-79.

Clark, P. U., et al. (2009), The Last Glacial Maximum, *Science*, *325*(5941), 710-714.

Clark, P. U., and A. C. Mix (2002), Ice sheets and sea level of the Last Glacial Maximum, *Quaternary Science Reviews*, *21*(1-3), 1-7.

CLIMAP Project Members (1976), The Surface of the Ice-Age Earth, *Science*, *191*(4232), 1131-1137.

Cook, E. R., et al. (2010), Asian Monsoon Failure and Megadrought During the Last Millennium, *Science*, *328*(5977), 486-489.

Cook, E. R., et al. (2004), Long-term aridity changes in the western United States, *Science*, *306*(5698), 1015-1018.

Cox, P., and C. Jones (2008), Illuminating the Modern Dance of Climate and CO_2, *Science*, *321*(5896), 1642-1644.

Craig H. (1953), The geochemistry of the stable carbon isotopes *Geochimica et Cosmochimica Acta*, *3*, 53-92.

Curry, W. B., and D. W. Oppo (2005), Glacial water mass geometry and the distribution of delta C-13 of ΣCO_2 in the western Atlantic Ocean, *Paleoceanography*, *20*(1).

Davidson, E. A., and I. A. Janssens (2006), Temperature sensitivity of soil carbon decomposition and feedbacks to climate change, *Nature*, *440*(7081), 165-173.

Denton, G. H., et al. (2010), The Last Glacial Termination, *Science*, *328*(5986), 1652-1656.

Ellehoj, M. D., et al. (2013), Ice-vapor equilibrium fractionation factor of hydrogen and oxygen isotopes: Experimental investigations and implications for stable water isotope studies, *Rapid Communications In Mass Spectrometry*, *27*(19), 2149-2158.

Elsig, J., et al. (2009), Stable isotope constraints on Holocene carbon cycle changes from an Antarctic ice core, *Nature*, *461*(7263), 507-510.

EPICA Community Members (2006), One-to-one coupling of glacial climate variability in Greenland and Antarctica, *Nature*, *444*(7116), 195-198.

Fischer, H., et al. (2007), Reconstruction of millennial changes in dust emission, transport and regional sea ice coverage using the deep EPICA ice cores from the Atlantic and Indian Ocean sector of Antarctica, *Earth and Planetary Science Letters*, *260*(1,Äì2), 340-354.

Fischer, H., et al. (2013), Where to find 1.5 million yr old ice for the IPICS "Oldest Ice" ice core, *Clim. Past Discuss.*, *9*(3), 2771-2815.

Francey, R. J., et al. (1999), A 1000-year high precision record of $\delta_{13}C$ in atmospheric CO_2, *Tellus Series B-Chemical and Physical Meteorology*, *51*(2), 170-193.

Frank, D. C., et al. (2010), Ensemble reconstruction constraints on the global carbon cycle sensitivity to climate, *Nature*, *463*(7280), 527-U143.

Friedli, H., Fischer, H., Oeschger, H., Siegenthaler, U., , and B. Stauffer (1986), Ice core record of the $^{13}C/^{12}C$ ratio of atmospheric CO_2 in the past two centuries, *Nature*, *324*(20), 237-238.

Friedlingstein, P., et al. (2006), Climate-carbon cycle feedback analysis: Results from the C(4)MIP model intercomparison, *J. Clim.*, *19*(14), 3337-3353.

Galbraith, E. D., et al. (2007), Carbon dioxide release from the North Pacific abyss during the last deglaciation, *Nature*, *449*(7164), 890-U899.

Gerber, S., et al. (2004), Sensitivity of a dynamic global vegetation model to climate and atmospheric CO2, *Glob. Change Biol.*, *10*(8), 1223-1239.

Gersonde, R., et al. (2005), Sea-surface temperature and sea ice distribution of the Southern Ocean at the EPILOG Last Glacial Maximum - A circum-Antarctic view based on siliceous microfossil records, *Quaternary Science Reviews*, *24*(7-9), 869-896.

Goldewijk, K. K., et al. (2011), The HYDE 3.1 spatially explicit database of human-induced global land-use change over the past 12,000 years, *Glob. Ecol. Biogeogr.*, *20*(1), 73-86.

Grachev, A. M., et al. (2007), Abrupt changes in atmospheric methane at the MIS 5b-5a transition, *Geophysical Research Letters*, *34*(20), 5.

Halsted, R. E., and A. O. Nier (1950), Gas Flow through the Mass Spectrometer Viscous Leak, *Review of Scientific Instruments*, *21*(12), 1019-1021.

Haug, G. H., et al. (2001), Southward migration of the intertropical convergence zone through the Holocene, *Science*, *293*(5533), 1304-1308.

Helama, S., et al. (2009), Multicentennial megadrought in northern Europe coincided with a global El Nino-Southern Oscillation drought pattern during the Medieval Climate Anomaly, *Geology*, *37*(2), 175-178.

Hendry, K. R., et al. (2012), Abrupt changes in high-latitude nutrient supply to the Atlantic during the last glacial cycle, *Geology*, *40*(2), 123-126.

Hopkins, F. M., et al. (2012), Warming accelerates decomposition of decades-old carbon in forest soils, *Proceedings of the National Academy of Sciences*, *109*(26), 1753-1761.

Horita, J., and D. J. Wesolowski (1994), Liquid-vapor fractionation of oxygen and hydrogen isotopes of water from the freezing to the critical temperature, *Geochimica et Cosmochimica Acta*, *58*(16), 3425-3437.

Huybers, P., and C. Langmuir (2009), Feedback between deglaciation, volcanism, and atmospheric CO_2, *Earth and Planetary Science Letters*, *286*(3-4), 479-491.

Indermuhle, A., et al. (1999), Holocene carbon-cycle dynamics based on CO_2 trapped in ice at Taylor Dome, Antarctica, *Nature*, *398*(6723), 121-126.

Jaccard, S. L., and E. D. Galbraith (2011), Large climate-driven changes of oceanic oxygen concentrations during the last deglaciation, *Nature Geoscience*, *5*(2), 151-156.

Joos, F., and M. Bruno (1998), Long-term variability of the terrestrial and oceanic carbon sinks and the budgets of the carbon isotopes C-13 and C-14, *Global Biogeochemical Cycles*, *12*(2), 277-295.

Joos, F., et al. (2004), Transient simulations of Holocene atmospheric carbon dioxide and terrestrial carbon since the Last Glacial Maximum, *Global Biogeochemical Cycles*, *18*(2).

Joos, F., et al. (1999), The variability in the carbon sinks as reconstructed for the last 1000 years, *Geophysical Research Letters*, *26*(10), 1437-1440.

Kaplan, J. O., et al. (2002), Modeling the dynamics of terrestrial carbon storage since the Last Glacial Maximum, *Geophysical Research Letters*, *29*(22), 4.

Keeling, R. F. (1995), The atmospheric oxygen cycle: The oxygen isotopes of atmospheric

CO_2 and O_2 and the O_2/N_2 ratio, *Rev. Geophys.*, *33*(S2), 1253-1262.

Kennett, D. J., et al. (2012), Development and Disintegration of Maya Political Systems in Response to Climate Change, *Science*, *338*(6108), 788-791.

Kohler, P., et al. (2005), Quantitative interpretation of atmospheric carbon records over the last glacial termination, *Global Biogeochemical Cycles*, *19*(4), 24.

Lamy, F., et al. (1999), High-resolution marine record of climatic change in mid-latitude Chile during the last 28,000 years based on terrigenous sediment parameters, *Quat. Res.*, *51*(1), 83-93.

Lee, S.-Y., et al. (2011), Southern Ocean wind response to North Atlantic cooling and the rise in atmospheric CO_2: Modeling perspective and paleoceanographic implications, *Paleoceanography*, *26*.

Lemieux-Dudon, B., et al. (2010), Consistent dating for Antarctic and Greenland ice cores, *Quaternary Science Reviews*, *29*(1-2), 8-20.

Leuenberger, M., et al. (1992), Carbon isotope compositoin of atmospheric CO_2 during the last ice-age from an Antarctic ice core, *Nature*, *357*(6378), 488-490.

Leuenberger, M. C., et al. (2003), High-resolution delta C-13 measurements on ancient air extracted from less than 10 cm^3 of ice, *Tellus Series B-Chemical and Physical Meteorology*, *55*(2), 138-144.

Lisiecki, L. E., et al. (2008), Atlantic overturning responses to Late Pleistocene climate forcings, *Nature*, *456*(7218), 85-88.

Lourantou, A., et al. (2010), Constraint of the CO_2 rise by new atmospheric carbon isotopic measurements during the last deglaciation, *Global Biogeochemical Cycles*, *24*, 15.

Luthi, D., et al. (2008), High-resolution carbon dioxide concentration record 650,000-800,000 years before present, *Nature*, *453*(7193), 379-382.

Lynch-Stieglitz, J., et al. (1995), The influence of air-sea exchange on the isotopic composition of oceanic carbon: Observations and modeling, *Global Biogeochemical Cycles*, *9*(4), 653-665.

MacDonald, G. M., et al. (2006), Rapid early development of circumarctic peatlands and atmospheric CH_4 and CO_2 variations, *Science*, *314*(5797), 285-288.
MacFarling-Meure, C., et al. (2006), Law Dome CO_2, CH_4 and N_2O ice core records extended to 2000 years BP, *Geophysical Research Letters*, *33*(14).

Mader, H. M. (1992), Observations of the water-vein system in polycrystalline ice, *J. Glaciol.*, *38*(130), 333-347.

Majoube, M. (1971), Oxygen-18 and Deuterium Fractionation Between Water and Steam, *Journal De Chimie Physique Et De Physico-Chimie Biologique*, *68*(10), 1423-1436.

Mann, M. E., et al. (2008), Proxy-based reconstructions of hemispheric and global surface temperature variations over the past two millennia, *Proc. Natl. Acad. Sci. U. S. A.*, *105*(36), 13252-13257.

Marchal, O., et al. (1998), Impact of oceanic reorganizations on the ocean carbon cycle and atmospheric carbon dioxide content, *Paleoceanography*, *13*(3), 225-244.

Marcott, S. A., et al. (2013), A Reconstruction of Regional and Global Temperature for the Past 11,300 Years, *Science*, *339*(6124), 1198-1201.

Marinov, I., et al. (2006), The Southern Ocean biogeochemical divide, *Nature*, *441*(7096), 964-967.

Martin, J. H. (1990), Glacial-interglacial CO_2 change: The Iron Hypothesis, *Paleoceanography*, *5*(1), 1-13.

Martin, J. H., et al. (1987), VERTEX: carbon cycling in the northeast Pacific, *Deep Sea Research Part A. Oceanographic Research Papers*, *34*(2), 267-285.

McManus, J. F., et al. (2004), Collapse and rapid resumption of Atlantic meridional circulation linked to deglacial climate changes, *Nature*, *428*(6985), 834-837.

Meckler, A. N., et al. (2013), Deglacial pulses of deep-ocean silicate into the subtropical North Atlantic Ocean, *Nature*, *495*(7442), 495-498.

Meheut, M., et al. (2007), Equilibrium isotopic fractionation in the kaolinite, quartz, water system: Prediction from first-principles density-functional theory, *Geochimica et Cosmochimica Acta*, *71*(13), 3170-3181.

Mitchell, L. E., et al. (2011), Multidecadal variability of atmospheric methane, 1000-1800 CE, *Journal of Geophysical Research-Biogeosciences*, *116*, 16.

Moberg, A., et al. (2005), Highly variable Northern Hemisphere temperatures reconstructed from low- and high-resolution proxy data, *Nature*, *439*(7079), 1014-1014.

Monnin, E., et al. (2001), Atmospheric CO_2 concentrations over the last glacial termination, *Science*, *291*(5501), 112-114.

Monnin, E., et al. (2004), Evidence for substantial accumulation rate variability in Antarctica

during the Holocene, through synchronization of CO_2 in the Taylor Dome, Dome C and DML ice cores, *Earth and Planetary Science Letters*, *224*(1-2), 45-54.

NGRIP Community Members (2004), High-resolution record of Northern Hemisphere climate extending into the last interglacial period, *Nature*, *431*(7005), 147-151.

Nye, J. F., and F. C. Frank (1973), Hydrology of the intergranular veins in a temperate glacier, paper presented at Symposium on the Hydrology of Glaciers.

O'Leary, M. H. (1981), Carbon isotope fractionation in plants, *Phytochemistry*, *20*(4), 553-567.

PAGES 2k Consortium. (2013), Continental-scale temperature variability during the past two millennia, *Nature Geosci*, *6*(5), 339-346.

Pedro, J. B., et al. (2011), The last deglaciation: timing the bipolar seesaw, *Climate of the Past*, *7*(2), 671-683.

Petit, J. R., et al. (1999), Climate and atmospheric history of the past 420,000 years from the Vostok ice core, Antarctica, *Nature*, *399*(6735), 429-436.

Piotrowski, A. M., et al. (2005), Temporal relationships of carbon cycling and ocean circulation at glacial boundaries, *Science*, *307*(5717), 1933-1938.

Raich, J. W., and W. H. Schlesinger (1992), The global carbon-dioxide flux in soil respiration and its relationship to vegetations and climate, *Tellus Series B-Chemical and Physical Meteorology*, *44*(2), 81-99.

Revelle, R., and H. E. Suess (1957), Carbon Dioxide Exchange Between Atmosphere and Ocean and the Question of an Increase of Atmospheric CO_2 during the Past Decades, *Tellus*,

9(1), 18-27.

Rhodes, R. H., et al. (2013), Continuous methane measurements from a late Holocene Greenland ice core: Atmospheric and in-situ signals, *Earth and Planetary Science Letters*, *368*(0), 9-19.

Roth, R., and F. Joos (2012), Model limits on the role of volcanic carbon emissions in regulating glacial-interglacial CO_2 variations, *Earth and Planetary Science Letters*, *329*, 141-149.

Rubino, M., et al. (2013), A revised 1000 year atmospheric $\delta^{13}C$-CO_2 record from Law Dome and South Pole, Antarctica, *Journal of Geophysical Research: Atmospheres*, *118*(15), 8482-8499.

Ruddiman, W. F. (2003), The anthropogenic greenhouse era began thousands of years ago, *Clim. Change*, *61*(3), 261-293.

Russell, J. M., and T. C. Johnson (2007), Little Ice Age drought in equatorial Africa: Intertropical Convergence Zone migrations and El Nino-Southern Oscillation variability, *Geology*, *35*(1), 21-24.

Santrock, J., et al. (1985), Isotopic analyses based on the mass-spectrum of carbon-dioxide *Analytical Chemistry*, *57*(7), 1444-1448.

Sarmiento, J. L., and N. Gruber (2006), *Ocean biogeochemical dynamics*, Princeton University Press.

Schaefer, H., et al. (2008), On the suitability of partially clathrated ice for analysis of concentration and $\delta^{13}C$ of palaeo-atmospheric CO_2, *Earth and Planetary Science Letters*, *307*(3-4), 334-340.

Schmitt, J., et al. (2012), Carbon Isotope Constraints on the Deglacial CO_2 Rise from Ice Cores, *Science*, *336*(6082), 711-714.

Schmitt, J., et al. (2011), A sublimation technique for high-precision measurements of $\delta^{13}CO_2$ and mixing ratios of CO_2 and N_2O from air trapped in ice cores, *Atmos. Meas. Tech.*, *4*(7), 1445-1461.

Schmittner, A., and E. D. Galbraith (2008), Glacial greenhouse-gas fluctuations controlled by ocean circulation changes, *Nature*, *456*(7220), 373-376.

Schwalm, C. R., et al. (2012), Reduction in carbon uptake during turn of the century drought in western North America, *Nature Geoscience*, *5*(8), 551-556.

Shakun, J. D., et al. (2012), Global warming preceded by increasing carbon dioxide concentrations during the last deglaciation, *Nature*, *484*(7392), 49-54.

Shanahan, T. M., et al. (2009), Atlantic Forcing of Persistent Drought in West Africa, *Science*, *324*(5925), 377-380.

Siegenthaler, U., et al. (1988), Stable-isotope ratios and concentration of CO_2 in air from polar ice cores, *Annals of Glaciology*, *10*, 151-156.

Siegenthaler, U., and H. Oeschger (1987), Biospheric CO_2 emissions during the past 200 years reconstructed by deconvolution of ice core data, *Tellus B*, *39B*(1-2), 140-154.

Siegenthaler, U., et al. (2005), Stable carbon cycle-climate relationship during the late Pleistocene, *Science*, *310*(5752), 1313-1317.

Sigman, D. M., and E. A. Boyle (2000), Glacial/interglacial variations in atmospheric carbon

dioxide, *Nature*, *407*(6806), 859-869.

Sinha, A., et al. (2011), A global context for megadroughts in monsoon Asia during the past millennium, *Quaternary Science Reviews*, *30*(1-2), 47-62.

Skinner, L. C., et al. (2010), Ventilation of the Deep Southern Ocean and Deglacial CO_2 Rise, *Science*, *328*(5982), 1147-1151.

Skinner, L. C., and N. J. Shackleton (2004), Rapid transient changes in northeast Atlantic deep water ventilation age across Termination I, *Paleoceanography*, *19*(2), 12.

Smith, H. J., et al. (1999), Dual modes of the carbon cycle since the Last Glacial Maximum, *Nature*, *400*(6741), 248-250.

Stephens, B. B., and R. F. Keeling (2000), The influence of Antarctic sea ice on glacial-interglacial CO 2 variations, *Nature*, *404*(6774), 171-174.

Stocker, B. D., et al. (2011), Sensitivity of Holocene atmospheric CO_2 and the modern carbon budget to early human land use: analyses with a process-based model, *Biogeosciences*, *8*(1), 69-88.

Talley, L. D. (2013), Closure of the global overturning circulation through the Indian, Pacific, and Southern Oceans: Schematics and transports, *Oceanography*, *26*(1), 80-97.

Thornalley, D. J. R., et al. (2011), The Deglacial Evolution of North Atlantic Deep Convection, *Science*, *331*(6014), 202-205.

Toggweiler, J. R. (1999), Variation of atmospheric CO_2 by ventilation of the ocean's deepest water, *Paleoceanography*, *14*(5), 571-588.

Toggweiler, J. R., et al. (2006), Midlatitude westerlies, atmospheric CO_2, and climate change during the ice ages, *Paleoceanography*, *21*(2), 15.

Trudinger, C. M., et al. (2002), Kalman filter analysis of ice core data - 2. Double deconvolution of CO_2 and delta C-13 measurements, *J. Geophys. Res.-Atmos.*, *107*(D20).

Trumbore, S. E., and C. I. Czimczik (2008), An Uncertain Future for Soil Carbon, *Science*, *321*(5895), 1455-1456.

Vallelonga, P., et al. (2013), Iron fluxes to Talos Dome, Antarctica, over the past 200 kyr, *Climate of the Past*, *9*(2), 597-604.

van der Molen, M. K., et al. (2011), Drought and ecosystem carbon cycling, *Agric. For. Meteorol.*, *151*(7), 765-773.

Vecsei, A., and W. H. Berger (2004), Increase of atmospheric CO_2 during deglaciation: Constraints on the coral reef hypothesis from patterns of deposition, *Global Biogeochemical Cycles*, *18*(1).

Waelbroeck, C., et al. (2002), Sea-level and deep water temperature changes derived from benthic foraminifera isotopic records, *Quaternary Science Reviews*, *21*(1-3), 295-305.

Waelbroeck, C., et al. (2009), Constraints on the magnitude and patterns of ocean cooling at the Last Glacial Maximum, *Nature Geoscience*, *2*(2), 127-132.

WAIS Divide Community Members (2013), Onset of deglacial warming in West Antarctica driven by local orbital forcing, *Nature*, *500*(7463), 440-+.

Wanninkhof, R. (1992), Relationship between wind speed and gas exchange over the ocean,

Journal of Geophysical Research: Oceans, *97*(C5), 7373-7382.

Wanninkhof, R., and W. R. McGillis (1999), A cubic relationship between air-sea CO_2 exchange and wind speed, *Geophysical Research Letters*, *26*(13), 1889-1892.

Welp, L. R., et al. (2011), Interannual variability in the oxygen isotopes of atmospheric CO_2 driven by El Nino, *Nature*, *477*(7366), 579-582.

Yu, J., et al. (2010), Loss of Carbon from the Deep Sea Since the Last Glacial Maximum, *Science*, *330*(6007), 1084-1087.

Yu, Z. C. (2012), Northern peatland carbon stocks and dynamics: a review, *Biogeosciences*, *9*(10), 4071-4085.

Zeebe, R., and D. Wolf-Gladrow (2001), *CO_2 in Seawater: Equilibrium, Kinetics, Isotopes* 346 pp., Amsterdam.

Zhang, J., et al. (1995), Carbon isotope fractionation during gas-water exchange and dissolution of CO_2, *Geochimica et Cosmochimica Acta*, *59*(1), 107-114.

Zhao, C. L., et al. (1997), A high precision manometric system for absolute calibrations of CO_2 in dry air, *Journal of Geophysical Research: Atmospheres*, *102*(D5), 5885-5894.